

# A Fault Tolerant Motor Drive for Electric Power Steering Systems



**Ari Akbar Hassan AL-JAF**

School of Engineering

Newcastle University

Newcastle upon Tyne, United Kingdoms

A Thesis submitted for the degree of

*Doctor of Philosophy*

October 2019

# Declaration

I, Ari AL-JAF, hereby declare that the work presented in this thesis is genuine, done originally by me under the guidance and supervision of the acknowledged supervisors. To best of my knowledge, I solemnly certify that this work has not been submitted elsewhere for the award of any degree under my name. The contents and materials of this thesis are work generated by me as well as the presented results, except as specified in the text, acknowledgements and references. I certify that the content of this thesis, in future, will not be used for submission under my name for any other degree or diploma in any university, except specified content that will be used for publication either in conferences or scientific journals.

October 2019



## Abstract

---

Electric machines are becoming increasingly prevalent in safety critical transport applications, whether as both the main drive components or in auxiliary systems. An automotive electric power steering system is an auxiliary drive system that replaces conventional hydraulic systems due to its high reliability, low size and cost, high security, good road feeling, control stability and operates when required. Permanent magnet AC motors are one of the most favourable choices for this application due to their high torque and power density, low torque ripple and low acoustic noise. The main challenge with PM machines in a fault situation is the drag torque resulting from short-circuit currents. These currents are induced by fluxes from the permanent magnets.

This research investigates a 12 slot 8 pole interior permanent magnet motor. It investigates different winding arrangements and winding connections for a dual-lane system and compares them to a single-lane system. The baseline motor has 4 coils in parallel per phase for a single-lane system, and 2 coils per lane per phase for a dual lane system. In a dual-lane system, the stator coils can be connected in three different arrangements which are interleaved, half-half and quarter. The half-half arrangement is the best compromise for the baseline motor, as it produces the highest average torque and medium torque ripple under a symmetrical 3-phase short-circuit fault.

A modular winding was implemented on the baseline motor's stator to reduce drag torque and torque ripple under faulted conditions. However, the stator core saturates leading to higher torque ripple and a torque drop under normal conditions. Therefore, a new modular stator was developed to overcome saturation. This gave higher torque capability due to the wider wound teeth tooth arc used, and hence a higher winding factor. The fault-tolerance of the modular stator is significantly improved due to the higher coil inductance and lower drag torque. In the constant power region, the power is significantly compromised. The knee point speed is affected as the high q-axis inductance limits the availability of the supply voltage at a lower speed.

Various approaches are presented that aim to reduce the overall motor inductance or only the q-axis inductance to recover the power drop. Firstly, the baseline motor's rotor is shaped to reduce the q-axis flux. This is not feasible as the power cannot be fully recovered and the torque ripple becomes considerably high. Secondly, the number of turns is reduced, and the input current is increased to keep the MMF input unchanged. Using this approach, the power drop is fully recovered, but a thicker wire diameter should be used for winding, and higher input current means higher ECU losses.

Finally, a novel SPM motor is presented. This overcomes the constant power region torque drop through reducing the q-axis inductance. Compared to the baseline motor, the power and torque density of the motor are considerably higher. The overall stator and rotor stack lengths are shorter. As the end-windings are bigger that affects the motors overall length which might also affect the motor size and packaging. The coils and motor lanes are segregated which helps in reducing the torque ripple under faulted condition. At lower speeds the average torque available within a short circuit or single MOSFET fault within the drive stage is similar to that of the baseline motor. At higher speeds the SPM offers greater average torque capability than the baseline motor.

## Acknowledgements

---

I would like to start by expressing my gratitude to the backers of this research project: Newcastle University and ZF Group.

A project of this nature requires the input of many individuals. Sincere appreciations are given to both my academic and industrial supervisors, Professor Barrie Mecrow and Dr David Moule for their guidance, advice, assistance and support throughout the duration of the work and the thesis review.

I would also like to especially thank Dr Dave Atkinson and Darren Mackie for designing and constructing the electronics of the motor drive for this project, and their continuous guidance and support during the motor testing in Newcastle University.

I would like to express my deepest gratitude to all those who helped me throughout this research work. Sincere thanks to Andrew Houston, Steven Neville and the mechanical team in ZF Group for helping with the motor drawings, construction, winding and testing.

Many thanks to my manager Harvey Smith for his continuous help by allocating me time to write my thesis while working at ZF.

Many thanks to my university colleagues Nicola Chiodetto and Iago Martinez for helping with the software packages and Nazik Nemat for proof reading the thesis.

Finally, I would like to thank parents and siblings for their endless support throughout my studies.

# Contents

---

Abstract.....	ii
Acknowledgements.....	iv
Contents .....	v
List of Figures .....	xi
List of Tables .....	xxiii
Introduction .....	1
1.1.    EPS systems and reliability .....	2
1.1.1.    Failure: .....	3
1.1.1.1.    Causes of failure:.....	3
1.1.1.2.    Time of failure:.....	3
1.1.1.3.    Degree of failure: .....	3
1.1.1.4.    Combination of failure:.....	3
1.2.    What is fault tolerance and why it is needed: .....	3
1.2.1.    Benign Failure: .....	4
1.2.2.    Continuous operation with degraded output:.....	4
1.2.3.    Continuous operation with full capability: .....	4
1.3.    Electrical machine topologies for Electrical power steering systems: .....	5
1.3.1.    Brushed DC (BDC) Motors:.....	6
1.3.2.    Switched Reluctance Motors (SRM): .....	6
1.3.3.    Induction Motors (IM): .....	6
1.3.4.    Brushless DC(BLDC) Motors: .....	7
1.3.5.    Permanent Magnet Synchronous Motors (PMSM):.....	7
Interior Permanent Magnet (IPM) motor:.....	8
1.3.6.    Multi-lane systems: .....	10
1.3.7.    Winding arrangements: .....	11
1.3.8.    Winding connections: .....	13
1.4.    Objective and methodology: .....	14

## Contents

---

1.5. Overview of thesis:.....	16
1.6. Contribution to knowledge:.....	17
1.7. Published work:.....	18
Double-layer winding arrangement and connections.....	19
2.1. Baseline motor characteristics and design parameters:.....	19
2.2. Simulation results under normal operating conditions:.....	20
2.2.1 Cogging torque: .....	21
Skewing: .....	21
2.2.2 Back-emf: .....	25
2.2.3 Loaded Characteristic:.....	27
Test rig:.....	28
2.2.3.1 Torque-current characteristic:.....	30
2.2.3.2 Effect of current phase advance angle: .....	31
2.2.3.3 Torque ripple:.....	33
2.2.4 Inductance calculations: .....	36
2.2.4.1 D-axis inductance: .....	36
Inductance vs rotor position .....	36
Inductance vs current phase advance angle:.....	37
2.2.4.2 Q-axis inductances: .....	38
Inductance vs rotor position .....	38
Inductance vs current phase advance angle:.....	38
2.2.4.3 Magnet Flux linkage:.....	40
Flux-linkage vs rotor position .....	40
Flux-linkage versus current phase advance angle .....	40
2.2.5 Resistance calculation: .....	42
2.3. Faulted condition:.....	44
2.3.1. Fault scenarios: .....	46
2.3.2. Effect of a shorted lane upon the healthy lane back-emf: .....	48

Three-phase short-circuit in one lane: .....	48
2.3.3. Torque, torque ripple and short circuit current:.....	56
Three-phase short-circuit in one lane under loaded condition: .....	56
Single MosFET short-circuit in one lane: .....	62
2.4. Summary: .....	64
Modular winding arrangement and connections .....	67
3.1. Loaded Characteristic:.....	68
3.2. Inductance comparison: .....	71
3.2.1. D-axis inductances:.....	71
3.2.2. Q-axis inductances:.....	73
3.2.3. Magnet Flux linkage: .....	74
3.3. Fault scenarios: .....	76
3.3.1. No-load investigation:.....	76
All coils short: .....	76
Back-emf investigation in the healthy lane and no-load drag torque: .....	77
3.3.2. Loaded investigation: .....	79
3.3.3. Short circuit current: .....	81
3.4. Summary: .....	82
A new modular design .....	83
4.1. Design development process: .....	83
4.2. Stator construction and winding:.....	87
4.3. No-load investigations and comparisons: .....	89
4.3.1. Cogging torque:.....	89
3D results vs practical: .....	91
4.3.2. Back-emf: .....	92
3D results vs practical: .....	94
4.4. Loaded comparisons: .....	95
4.4.1. Torque vs input current: .....	95

## Contents

---

4.4.2. Torque vs Advance angle: .....	96
4.4.3. Torque ripple:.....	97
3D results vs experimental: .....	98
4.4.4. DC torque comparison (3D FE vs experimental): .....	100
4.5. Inductance comparison: .....	101
4.5.1. D-axis inductances: .....	102
4.5.2. Q-axis inductances: .....	103
4.5.3. Magnet flux linkage:.....	104
4.6. Torque capability under fault conditions:.....	106
4.6.1. No-load investigation: .....	107
4.6.2. Loaded investigation:.....	110
4.7. Torque-speed characteristics and phasor diagram at normal conditions: .	113
4.8. Summary:.....	117
Novel SPM design and development .....	119
5.1. Enhancing constant power region capability: .....	119
5.1.1. Changing the number of turns: .....	121
5.1.2. Shaping the baseline rotor: .....	123
5.1.3. A surface mounted magnet alternative and associated demagnetisation issues: .....	125
5.2. The impact of tolerance in the stator construction:.....	129
5.3. Construction of the SPM rotor:.....	136
5.4. Inductance comparison: .....	138
5.5. Choosing an appropriate motor stack for manufacture: .....	139
5.6. Measured capability comparison between designs: .....	140
5.6.1. No-load characteristics:.....	141
5.6.2. Loaded characteristics: .....	143
5.6.3. Performance under faulted conditions:.....	145
5.6.3.1. No-load comparison (Simulation vs Experimental):.....	145

## Contents

---

5.6.3.2. Loaded comparison: .....	146
Experimental results:.....	148
5.6.3.3. Comparison using colour map graphs: .....	148
A) Max power with no failure: .....	149
B) One lane operating, and one lane inactive:.....	152
C) One lane is operating, and one lane is short-circuited through a power module (Single MosFET failure): .....	155
• Edge coil connected to the shorted MosFET.....	157
• Middle coil connected to the shorted MosFET .....	158
D) One lane operational and one lane short-circuited at its terminals to give a balanced three-phase short-circuit: .....	160
E) All fault comparison for the same motor:.....	163
• Baseline motor: .....	164
• Intermediate design:.....	165
• SPM motor: .....	165
5.7. Summary: .....	166
Conclusions and further work .....	168
6.1. Background: .....	168
6.2. Baseline design investigation: .....	169
6.3. Dissimilar teeth stator with modular windings:.....	169
6.4. Segmented rotor SPM motor:.....	170
6.5. Testing and comparison the designs:.....	171
6.6. Segmented surface magnet motor .....	171
6.7. Further work: .....	172
6.7.1. Optimising the wound tooth and insert as a push in tooth:.....	172
6.7.2. Compressed coils:.....	172
6.7.3. Sleeve material and sleeve thickness: .....	173
6.7.4. Vibration and structural analysis: .....	173

## Contents

---

References .....	174
Appendix .....	178
1. Appendix A: .....	178
2. Appendix B: .....	178

## List of Figures

---

Figure 1: Power steering integrated system designs, A: Hydraulic Power Steering (HPS) and B: Electrical Power Steering (EPS). .....	1
Figure 2: EPAS schematic arrangement. Key components of an EPAS system include a torque sensor, electric motor, electronic control unit, and control and diagnostic algorithms implemented in software [3].....	2
Figure 3: The single-unit integrated design can be packaged on the steering column, steering rack, or pinion. (a) Column fitted, (b) rack fitted, and (c) pinion fitted [3]. .....	2
Figure 4: The availability spectrum. ....	4
Figure 5: IPM rotor with: (a) V-shape magnets, (b) multi-layer V-shape magnets .....	8
Figure 6: baseline motor stator with fractional slot concentrated winding representation and actual stator. ....	9
Figure 7: drag torque phasor diagram based on the operational speed .....	10
Figure 8: drag torque and short-circuit current vs speed characteristics.....	10
Figure 9: a typical dual-lane three-phase motor drive schematic.....	11
Figure 10: motor winding arrangements for 12 teeth stator with 8 pole and 10 or 14 pole rotor.....	12
Figure 11: 12:8 motor double-layer arrangement winding connection possibilities for one of two lanes.....	13
Figure 12: 12:10 or 12:14 motor double-layer arrangement winding connection possibilities. ....	13
Figure 13: modular arrangement winding connection possibilities.....	14
Figure 14: baseline motor's torque-speed characteristics.....	15
Figure 15: fractional slot concentrated winding (FSCW) 12:8 IPM motor that is used in this project .....	19
Figure 16: the baseline motor's rotor with skewed rotor pucks. ....	20
Figure 17: Stepped rotor skewing in three modules [53].....	22
Figure 18: 2D FE cogging torque waveform for one electrical cycle. ....	23
Figure 19: 2D FE Cogging torque harmonic content – electrical orders. ....	23
Figure 20: 2D FE Cogging torque harmonic content – electrical orders [Scaled].....	23
Figure 21: 3D FE and experimental cogging torque waveform for one electrical cycle. ....	24
Figure 22: 3D FE Cogging torque harmonic contents – mechanical orders.....	24

## List of Figures

---

Figure 23: line to line back-emf waveform for an electric cycle based on 2D FE simulation. ....	26
Figure 24: line to line back-emf harmonic content based on 2D FE simulation. ....	26
Figure 25: line to line back-emf waveform for an electric cycle based on 3D FE simulation and practical test. ....	26
Figure 26: line to line back-emf harmonic content based on 3D FE simulation and practical tests. ....	27
Figure 27: line to line back-emf harmonic content based on 3D FE simulation and practical tests [scaled]. ....	27
Figure 28: production motor before and after reconnecting the stator for dual-lane system. ....	28
Figure 29: circuit diagram for connecting the motor during DC torque test. ....	29
Figure 30: test rig to measure torque ripple, cogging torque and DC torque experimentally. ....	29
Figure 31: ECU to drive different motors in the lab. ....	29
Figure 32: Torque vs current based on 2D FE simulation. ....	30
Figure 33: flux plot of the baseline motor cross-section based on 2D FE simulation (full-load). ....	30
Figure 34: Phasor diagram of an IPM motor at one per-unit speed [22]. ....	32
Figure 35: torque vs advance angle based on 2D FE simulations at rated current. ...	32
Figure 36: DC torque comparison between the practical and 3D FE simulation at rated current. ....	32
Figure 37: Harmonic content of the DC torque at rated current. ....	33
Figure 38: 3D FE and experimental DC kt comparison at full-load and half-load. ....	33
Figure 39: Motor torque capability for different skewing angle based on 2D FE Simulations. ....	34
Figure 40: Motor torque harmonic content for different skewing angle based on 2D FE Simulations. ....	34
Figure 41: Motor torque harmonic content for different skewing angle based on 2D FE Simulations [Scaled]. ....	34
Figure 42: comparison between practical and 3D FE simulated motor torque. ....	35
Figure 43: comparison between practical and 3D FE simulated motor torque harmonic content. ....	35
Figure 44: simulated d-axis self-inductance ( $L_{dd}$ ) vs rotor position for different input phase current ( $I_s$ ). ....	37

## List of Figures

---

Figure 45: simulated q-axis inductance as a result of d-axis excitation ( $L_{qd}$ ) vs rotor position. ....	37
Figure 46: simulated s-axis inductance ( $L_{dd}$ ) vs current advance angle for different input phase current ( $I_s$ ). ....	38
Figure 47: simulated q-axis self-inductance ( $L_{qq}$ ) vs rotor position for different input phase current ( $I_s$ ) ....	39
Figure 48: simulated q-axis inductance because of q-axis excitation ( $L_{dq}$ ) vs rotor position for different input phase current ( $I_s$ ) ....	39
Figure 49: simulated q-axis inductance ( $L_{qq}$ ) vs current advance angle for different input phase current ( $I_s$ ). ....	40
Figure 50: simulated d-axis magnet flux linkage ( $\psi_{Fd}$ ) vs rotor position for different current ( $I_s$ ). ....	41
Figure 51: simulated q-axis magnet flux linkage ( $\psi_{Fq}$ ) vs rotor position for different current ( $I_s$ ). ....	41
Figure 52: simulated q-axis flux linkage ( $\psi_{Fq}$ ) vs current phase advance angle for different input phase currents ( $I_s$ ). ....	41
Figure 53: simulated d-axis flux linkage ( $\psi_{Fd}$ ) vs current phase advance angle for different input phase current ( $I_s$ ). ....	42
Figure 54: the winding layout of the baseline motor. ....	43
Figure 55: simulated drag torque and short circuit current against speed when all terminals of the machine is short circuited (2D FE). ....	46
Figure 56: dual-lane different winding arrangement: (a) Interleaved (b) Half-half (c) Quarter. ....	47
Figure 57: possible stator coils connections (a) star (b) delta. ....	48
Figure 58: Interaction between motor lanes for Interleaved arrangement (green circles illustrate interactions). ....	49
Figure 59: 2D FE back-emf comparison between faulted and healthy when a lane is short circuited (Interleaved). ....	49
Figure 60: Harmonic components for the back-emf of the healthy lane affected by the faulty lane (Interleaved). ....	50
Figure 61: Harmonic components for back-emf of the healthy lane affected by the faulty lane (Interleaved) [scaled]. ....	50
Figure 62: Interaction between motor lanes for Half-half arrangement. ....	51
Figure 63: 2D FE back-emf comparison for faulted and healthy at no-load when a lane is short circuited (Half-half). ....	51

## List of Figures

---

Figure 64: Harmonic components for the back-emf of the healthy lane affected by the faulty lane (Half-half). .....	51
Figure 65: Harmonic components for the back-emf of the healthy lane affected by the faulty lane (Half-half) [scaled]. .....	52
Figure 66: Interaction between motor lanes for Quarter arrangement. ....	52
Figure 67: 2D FE back-emf comparison for faulted and healthy at no-load when a lane is short circuited (Quarter). .....	53
Figure 68: Harmonic components for the back-emf of the healthy lane affected by the faulty lane (Quarter). .....	53
Figure 69: Harmonic components for the back-emf of the healthy lane affected by the faulty lane (Quarter) [scaled]. .....	53
Figure 70: Drag torque for different arrangements when one lane short circuited and the other inactive. ....	54
Figure 71: Practical and simulation comparison of the back-emf during one lane short-circuited (half-half connection). .....	55
Figure 72: No-load drag torque comparison for Half-half arrangement. ....	56
Figure 73: No-load short circuit current comparison for Half-Split arrangement. ....	56
Figure 74: Motor torque capability under three-phase fault condition in one lane for different winding connections. ....	57
Figure 75: percentage torque ripple for different motor connection type under three-phase fault in one lane. ....	57
Figure 76: torque ripple amplitude for worst case drag torque for different winding connections at 600 rpm. ....	58
Figure 77: harmonic contents for worst case drag torque for different winding connections at 600 rpm. ....	58
Figure 78: Half-half and quarter arrangement representation using coils' numbers and interaction points. ....	59
Figure 79: short-circuit current in the leading phase (phase 2 as in Figure 78). ....	59
Figure 80: short-circuit current in the middle phase (phase 1 as in Figure 78). ....	60
Figure 81: short-circuit current in the trailing phase (phase 3 as in Figure 78). ....	60
Figure 82: induced short-circuit current for all phases ( Interleaved arrangement)...	61
Figure 83: induced short-circuit current for all phases ( Half-half arrangement). ....	61
Figure 84: induced short-circuit current for all phases ( Quarter arrangement). ....	61
Figure 85: Single MosFET failure diagram for a dual-lane three-phase motor. ....	62
Figure 86: Winding connection layouts and coil highlight for MosFET failure. ....	62

## List of Figures

---

Figure 87: Drag torque for double layer winding and different winding connections.	63
Figure 88: Torque ripple for double layer winding and different winding connections. .....	63
Figure 89: Induced short-circuit current for double layer winding and different winding connections.....	64
Figure 90: modular winding arrangement cross-section .....	67
Figure 91: space harmonic comparison between different winding arrangements for similar stator cross-section. ....	68
Figure 92: Baseline motor cross-section with double-layer winding (full-load).....	68
Figure 93: Baseline motor cross-section with modular winding (full-load). ....	69
Figure 94: torque vs current comparison between double layer and modular winding at 1000 rpm.....	69
Figure 95: Torque ripple comparison between double layer and modular winding at full load and 10 elec. degrees current phase advance. ....	70
Figure 96: harmonic contents comparison between double layer and modular winding at full load and 10 elec. degrees current phase advance.....	70
Figure 97: MTPA of the modular winding arrangement.....	71
Figure 98: D-axis self-inductance ( $L_{dd}$ ) comparison for different input phase currents. .....	72
Figure 99: Q-axis inductance as a result of d-axis flux linkage ( $L_{qd}$ ) comparison for different input currents. ....	72
Figure 100: D-axis inductance ( $L_{dd}$ ) vs current advance angle for different input phase currents.....	72
Figure 101: Q-axis self-inductance ( $L_{qq}$ ) comparison for different input phase currents. .....	73
Figure 102: D-axis inductance as a result of q-axis flux linkage ( $L_{dq}$ ) comparison for different input currents. ....	73
Figure 103: Q-axis inductance ( $L_{qq}$ ) vs current advance angle for different input phase currents.....	74
Figure 104: D-axis magnet flux linkage ( $\psi_{Fd}$ ) comparison for different input currents in the d-axis. ....	75
Figure 105: Q-axis magnet flux linkage ( $\psi_{Fq}$ ) comparison for different input currents. .....	75
Figure 106: D-axis flux linkage ( $\psi_{Fd}$ ) vs current phase advance angle for different input phase currents. ....	75

## List of Figures

---

Figure 107: Drag torque and short-circuit current comparison between double layer and modular windings. The torque is normalised against the rated torque of the baseline motor.....	76
Figure 108: back-emf comparison between faulted and unfaulted situation (Interleaved). .....	77
Figure 109: Harmonic content of the back-emf with Interleaved connection for modular arrangement. ....	78
Figure 110: Harmonic content of the back-emf with Interleaved connection for modular arrangement [Scaled]. ....	78
Figure 111: back-emf comparison between faulted and unfaulted situation (Half-half). .....	78
Figure 112: Harmonic contents of the back-emf with Half-half connection for modular arrangement. ....	79
Figure 113: Harmonic contents of the back-emf with Half-half connection for modular arrangement [Scaled]. ....	79
Figure 114: torque comparison between Interleaved and Half-half arrangements of the modular windings. ....	80
Figure 115: torque ripple comparison between Interleaved and Half-half arrangements of the modular windings. ....	81
Figure 116: Short-circuit current comparison for different winding arrangements of the modular winding. ....	81
Figure 117: stator development to restore torque capability and reduce torque ripple: A. Baseline motor (Double Layer), B. Baseline motor (Modular), C. Modified equal tooth design, and D. New design (dissimilar teeth) [full-load].....	84
Figure 118: torque comparison between the developed stator designs for the same rotor with rated current and 10 degrees electrical phase advance angle. ....	85
Figure 119: torque harmonic contents of the developed stator designs with rated current and 10 degrees electrical phase advance angle. ....	85
Figure 120: Cross-section comparison between baseline motor and new designed stator. ....	86
Figure 121: Dissimilar teeth stator as an intermediate design to be combined with baseline motor's rotor.....	88
Figure 122: Rotor from the baseline motor and wound stator assembled in to the housing.....	88

## List of Figures

---

Figure 123: Cogging torque comparison between the baseline motor and new-stator design (2D FE simulations and un-skewed rotor). .....	90
Figure 124: Harmonic content of Figure 123 (2D FE simulations and un-skewed rotor). .....	90
Figure 125: Cogging torque comparison between the baseline motor and new-stator design (2D FE simulations and skewed rotor). .....	91
Figure 126: Harmonic content of Figure 125 (2D FE simulations and skewed rotor). .....	91
Figure 127: Harmonic content comparison of the cogging torque for both baseline and new-stator designs.....	92
Figure 128: 2D FE back-emf comparison between baseline and new-stator designs for skewed rotor. ....	93
Figure 129: Harmonic content of back-emf comparison (Figure 128). ....	93
Figure 130: Harmonic content of back-emf comparison (Figure 128) [scaled].....	93
Figure 131 : Back-emf comparison of the both the motor designs (practical vs simulation). ....	94
Figure 132: Back-emf comparison of the both the motor designs (practical vs simulation) [scaled]. ....	95
Figure 133: 2D FE torque-MMF comparison between the new designed stator and baseline motor. ....	95
Figure 134: 2D FE magnetic flux density in the baseline motor (double-layer) for 10 degrees electrical current phase advance and at rated current (full-load). ....	96
Figure 135: 2D FE magnetic flux density in the new-stator design for 10 degrees electrical current phase advance and at rated current (full-load). ....	96
Figure 136: Comparison between MTPA of both baseline and new-stator designs based on 2D FE analysis. ....	97
Figure 137: 2D FE torque and torque ripple comparison for both designs. ....	97
Figure 138: Harmonic content of 2D FE torque ripple comparison. ....	98
Figure 139: Torque (3D simulation and practical) comparison between baseline design and new-stator design.....	99
Figure 140: Torque ripple (3D simulation and practical) comparison between baseline design and new-stator design. ....	99
Figure 141: New-stator DC torque comparison between half load and full load. ....	100
Figure 142: New-stator DC torque harmonic content comparison between half load and full load. ....	101

## List of Figures

---

Figure 143: Harmonic content comparison of both baseline and New-stator designs. ....	101
Figure 144: 2D FE d-axis self-inductance ( $L_{dd}$ ) comparison for different input phase currents. ....	102
Figure 145: 2D FE q-axis inductance as a result of d-axis flux linkage ( $L_{qd}$ ) comparison for different input currents.....	102
Figure 146: 2D FE d-axis inductance ( $L_{dd}$ ) vs current advance angle for different input phase currents.....	103
Figure 147: 2D FE q-axis self-inductance ( $L_{qq}$ ) comparison for different input phase currents. ....	103
Figure 148: 2D FE d-axis inductance as a result of q-axis flux linkage ( $L_{dq}$ ) comparison for different input currents.....	104
Figure 149: 2D FE q-axis inductance ( $L_{qq}$ ) vs current advance angle for different input phase currents.....	104
Figure 150: 2D FE d-axis magnet flux linkage ( $\psi_{Fd}$ ) comparison for different input currents. ....	105
Figure 151: 2D FE q-axis magnet flux linkage ( $\psi_{Fq}$ ) comparison for different input currents. ....	105
Figure 152: 2D FE d-axis flux linkage ( $\psi_{Fd}$ ) vs current phase advance angle for different input phase currents.....	106
Figure 153: Drag torque and short-circuit current comparison between baseline and new-design. The torque is normalised against the rated torque of the baseline motor. ....	107
Figure 154: 2D FE back-emf comparison of different winding arrangements of the New-stator design under healthy and faulty conditions (solid lines: no-load back-emf, dotted lines: interleaved arrangement and dashed lines: half-half arrangement). This is a lane inactive and a lane 3-phase balanced short. ....	108
Figure 155: back-emf comparison between practical and simulation of the New-stator design (Half-half arrangement).....	108
Figure 156: no-load drag torque comparison between baseline motor and new-stator design.....	109
Figure 157: no-load short circuit current comparison between baseline motor and new-stator design.....	109
Figure 158: 2D FE torque capability under three-phase fault condition in one lane for different winding connections. ....	110

## List of Figures

---

Figure 159: percentage torque ripple for different motor connection type under three-phase fault in one lane (2D FE). .....	110
Figure 160: torque ripple amplitude for worst case drag torque (at 300 rpm) for different winding connections. The healthy lane is operated with full current at 10 degrees electric advance angle. ....	111
Figure 161: Interaction between motor lanes for Half-half arrangement (new-stator design layout). ....	111
Figure 162: short-circuit current in the edge phase as in Figure 161 (coil 4: leading coil in shorted lane) .....	112
Figure 163: short-circuit current in the edge phase as in Figure 161 (coil 6: trailing coil in shorted lane) .....	112
Figure 164: short-circuit current in the edge phase as in Figure 161 (coil 5: middle coil in shorted lane) .....	112
Figure 165: New-stator design's phasor diagram for constant torque region at MTPA (based on 2D FE). ....	114
Figure 166: Baseline motor's phasor diagram for constant torque region at MTPA (based on 2D FE). ....	114
Figure 167: 2D FE torque-speed curve comparison between baseline design and New-stator design. ....	114
Figure 168: practically tested torque-speed curve comparison between baseline design and New-stator design. ....	115
Figure 169: baseline design's phasor diagram at 60° electrical advance angle.....	116
Figure 170: New-stator design's phasor diagram at 60° electrical advance angle..	116
Figure 171: phasor diagram of the motor's operating point at 70 elec. deg. advance angle for (a) Baseline motor at full load _24 turns, and (b) New-stator with Baseline motor's rotor at full load_23 turns and (c) New-stator with baseline motor's rotor at half load_23_turns. ....	120
Figure 172: 2D FE torque-speed curve comparison between baseline design and New-stator design (with different number of turns and different input current). ....	122
Figure 173: q-axis flux path using frozen permeability method (full load). ....	123
Figure 174: introducing flux barriers to the baseline motor's rotor. ....	124
Figure 175: 2D FE torque-speed curve comparison between baseline design and New-stator design (with different number of turns and different input current, and rotor shaping). ....	125
Figure 176: q-axis flux path in SPM motor design with the magnets disabled. ....	126

## List of Figures

---

Figure 177: Demagnetisation check of the SPM magnet under q-axis current (full-load). .....	126
Figure 178: Magnet shapes used to achieve very low torque ripple and cogging torque and lower demagnetisation at the edge of the magnet. ....	126
Figure 179: introducing flux barriers into the rotor core-back to block the q-axis flux and develop the design. ....	127
Figure 180: q-axis flux path in different designs after introducing flux barriers (full-load). .....	128
Figure 181: Magnetic flux density at full-load and demagnetisation area within the magnet (full-load). ....	129
Figure 182: Torque-speed characteristic of three different stator design with different rotors. ....	129
Figure 183: thin tooth assembly methods including mechanical tolerances (full-load). .....	130
Figure 184: 2D FE torque capability for the SPM motor with tolerances for 36 mm stack length. ....	131
Figure 185: 2D FE harmonic content of the SPM motor torque capability. ....	131
Figure 186: 2D FE cogging torque for the SPM motor with tolerances for 36 mm stack length. ....	132
Figure 187: 2D FE harmonic content of the SPM motor cogging torque. ....	132
Figure 188: 2D FE back-emf harmonic content of the SPM motor for different this tooth tolerance shape. ....	133
Figure 189: 2D FE back-emf harmonic content of the SPM motor for different this tooth tolerance shape [scaled]. ....	133
Figure 190: Last stator design for the SPM motor. ....	134
Figure 191: stator construction with push in teeth and ready to be wound. ....	134
Figure 192: unitary stator constructed and ready to be wound. ....	134
Figure 193: last proposed rotor design. ....	136
Figure 194: last constructed rotor shape. ....	137
Figure 195: laminations, toolings and assembly for the rotor. ....	137
Figure 196: manufacturing process of the SPM rotor. ....	138
Figure 197: comparison between q-axis inductance vs input current for all the motor designs. ....	139
Figure 198: comparison between d-axis inductance vs input current for all the motor designs. ....	139

## List of Figures

---

Figure 199: 2D FE and 3D FE comparison of the SPM torque capability for different stack lengths.....	140
Figure 200: Harmonic contents of the SPM torque capability. ....	140
Figure 201: harmonic content comparison of the cogging torque for all the motor designs (measured values).....	141
Figure 202: Harmonic content comparison of the back-emf for all the motor designs. ....	142
Figure 203: Harmonic content comparison of the back-emf for all the motor designs [scaled]. ....	143
Figure 204: DC torque comparison between simulation and practical results of the SPM design. ....	143
Figure 205: experimental DC torque comparison for all the motor designs. ....	144
Figure 206: SPM's torque ripple comparison between practical and simulation results. ....	144
Figure 207: Torque ripple comparison between all the motor designs based on harmonic contents. ....	145
Figure 208: Comparison between all the motors for no-load drag torque. ....	146
Figure 209: Comparison between all the motors for no-load induced short-circuit current.....	146
Figure 210: comparison between all motor design torque capability under three-phase short circuit fault for half-half arrangement.....	147
Figure 211: comparison between torque capability of the SPM for different winding arrangement under three-phase short circuit fault. ....	147
Figure 212: torque ripple comparison between SPM's different winding arrangement under three-phase short circuit fault. ....	147
Figure 213: example of the colour map graphs for torque ripple content of a torque speed characteristic.....	149
Figure 214: Comparison between torque-speed characteristics of all the motor designs for max power tuning. ....	150
Figure 215: colour map of torque ripple harmonic content for different motors: A) baseline, B) intermediate, and C) SPM.....	151
Figure 216: Interaction between motor lanes for Half-half arrangement. ....	152
Figure 217: torque-speed characteristics of all the motor designs when one lane is operated, and one lane is inactive. ....	153

## List of Figures

---

Figure 218: colour map of torque ripple harmonic content for different motors: A) baseline, B) intermediate, and C) SPM. ....	154
Figure 219: circuit diagram of a power module used to create a single MosFET failure. ....	155
Figure 220: power module with reconnected terminals to create a single MosFET failure. ....	155
Figure 221: circuit diagram for single MosFET and direction of current flow. ....	156
Figure 222: 2D FE simulated single MosFET failure time series torque waveform at 800 rpm. ....	156
Figure 223: harmonic contents of the simulated single MosFET failure time series waveform. ....	156
Figure 224: 2D FE simulated single MosFET failure time series current waveform at 800 rpm. ....	157
Figure 225: torque comparison under single MosFET short-circuit fault (edge coil) for all the motor designs (measured). ....	157
Figure 226: Winding connection layouts and coil highlight for MosFET failure. ....	158
Figure 227: torque comparison under single MosFET short-circuit fault (middle coil) for all the motor designs (measured). ....	159
Figure 228: colour map of torque ripple harmonic content for different motors with a single MosFET shorted: A) baseline, B) intermediate, and C) SPM. ....	160
Figure 229: torque capability under three-phase short-circuit in one lane and the other is operated normally (measured). ....	161
Figure 230: colour map of torque ripple harmonic content for different motors with a symmetrical short circuit of one lane: A) baseline, B) intermediate, and C) SPM. ....	162
Figure 231: change over modes between single MosFET failure and symmetrical three-phase fault. ....	163
Figure 232: torque capability of the intermediate design a constant speed experiencing different faults (simulation). ....	164
Figure 233: baseline motor's capability under different conditions (measured) ....	165
Figure 234: intermediate design's capability under different conditions (measured). ....	165
Figure 235: SPM motor's capability under different conditions (measured) ....	166
Figure 236: dynamometer to test torque-speed curve using ramp tests. ....	178
Figure 237: B - H characteristic of the steel material used for all the motor ....	178

## List of Tables

---

Table 1: Motor specification that is used to carry out simulations. ....	20
Table 2: windings parameters calculations based on numerical equations for the baseline motor. ....	43
Table 3: measured winding resistance for three identical baseline motors. ....	44
Table 4: comparison between different arrangements when lane1 is shorted and lane2 is inactive. ....	54
Table 5: measured winding resistance for the new-stator design with modular windings. ....	88
Table 6: windings parameters calculations based on numerical equations for the new-stator design with modular windings. ....	89
Table 7: Comparison of certain harmonic contents of Figure 126 which are cogging torque in mNm. ....	92
Table 8: comparison of certain harmonic contents of torque ripple as in Figure 140.99	
Table 9: comparison of main harmonic contents of DC torque as in Figure 143. ....	101
Table 10: measured winding resistance for the new-stator design with modular windings. ....	135
Table 11: windings parameters calculations based on numerical equations for the SPM stator with modular windings. ....	136
Table 12: comparison between cogging torque certain harmonic contents. ....	142



# Chapter 1

## Introduction

Autonomous vehicles are expected to become the mainstream alternatives to conventional vehicles over the next 20 years. A key challenge is safety. Very high levels of reliability compared to benign failure modes are needed because there is no immediate backup from a human driver. Central to this is the need for very high reliability in the steering mechanism. Most vehicles on the road today include a system to assist the driver in steering the vehicle. Electrical Power Steering (EPS) systems have overtaken conventional Hydraulic Power Steering (HPS) systems as power electronics, electrical motors, digital controllers and sensors have advanced. Diagrammatic sketches of the two systems are shown in Figure 1. EPS is preferable because of its advantages in engine efficiency, environmental compatibility, fuel economy, maintainability, modularity and space efficiency [1-6]. It can also reduce the drag on the engine equivalent to 5 horsepower, as HPS operates continuously whether the steering is needed or not [5].

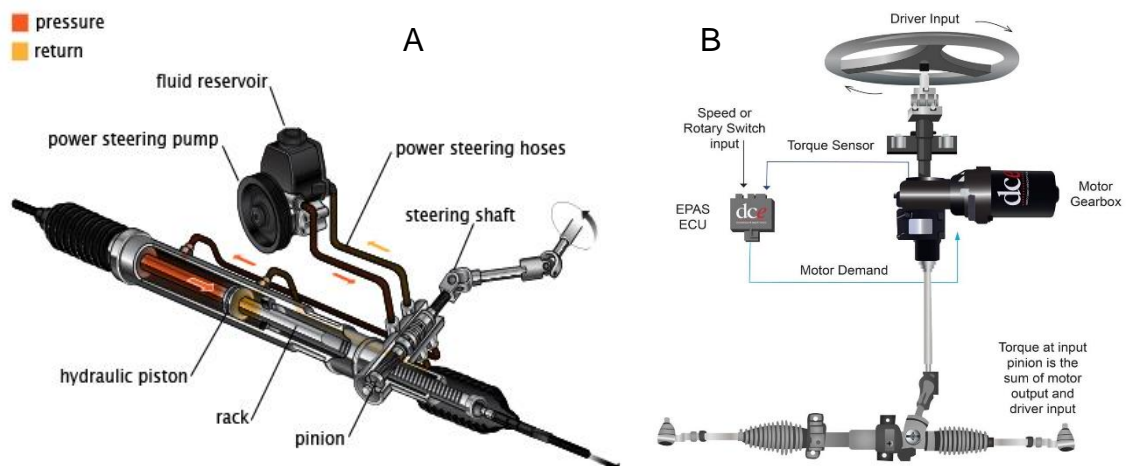


Figure 1: Power steering integrated system designs, A: Hydraulic Power Steering (HPS) and B: Electrical Power Steering (EPS).

This research is undertaken with close collaboration between Newcastle University and ZF, seeking fault tolerant capability of electric drives in EPS systems. It commences by investigating a current system and highlighting any related issues such as drag torque and short-circuit current. This bulk of this thesis discusses a newly designed fault-tolerant motor.

### 1.1. EPS systems and reliability

EPS systems are electromechanical systems widely used in passenger cars. They have superseded their HPS counterparts as they contribute to fuel economy and higher reliability. An EPS system consists of a steering wheel, a motor, a torque sensor, a reduction gear box, rack and pinion and an intermediate shaft to connect the wheel to the other parts [6-8] as in Figure 2. According to the motor placement, there are various types of EPS system, including rack fitted, column fitted, and pinion fitted motors [6, 7, 9], as illustrated in Figure 3. EPS is considered to be one of the safety critical applications that needs a high level of reliability and fault tolerance capability [18]. As driverless cars are becoming prevalent in real life applications, fault tolerance becomes more important.

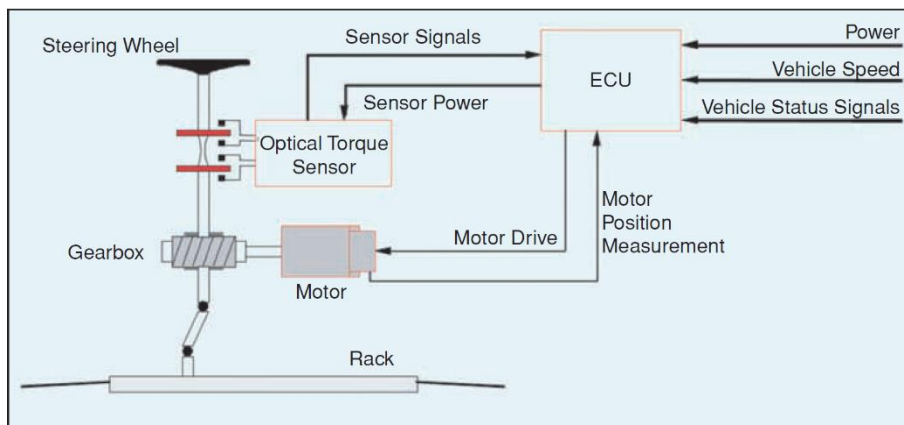


Figure 2: EPAS schematic arrangement. Key components of an EPAS system include a torque sensor, electric motor, electronic control unit, and control and diagnostic algorithms implemented in software [3].

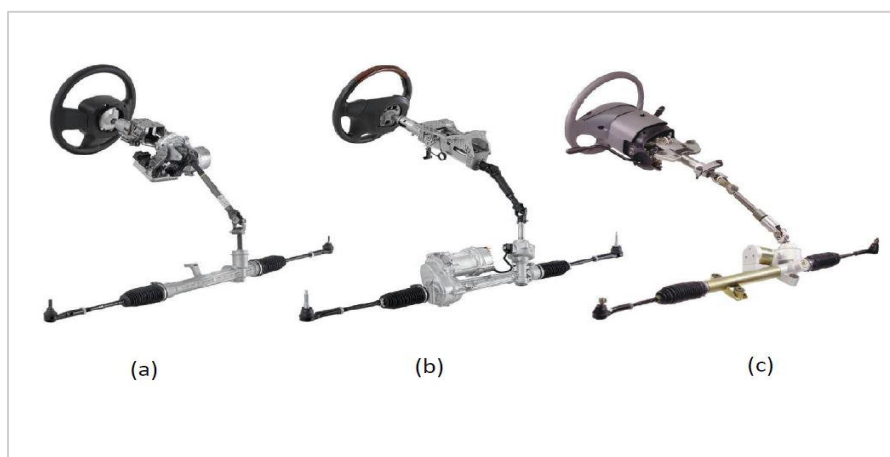


Figure 3: The single-unit integrated design can be packaged on the steering column, steering rack, or pinion. (a) Column fitted, (b) rack fitted, and (c) pinion fitted [3].

Different techniques and approaches have been developed to investigate system dependability. An ARMS (or RAMS) study [7] is one of the techniques to evaluate the

four elements; availability, reliability, maintainability, and safety. Haylock [8] used some definitions based on Caplen [9] that are applicable as follows:

**1.1.1. Failure:**

This is the inability of a system, component or a piece of equipment to operate to its required capability or perform its specific function. According to [9, 10], this can be classified into:

**1.1.1.1. Causes of failure:**

- i. **Misuse failure:** applicable when the system is subjected to stresses beyond the item's stated capability.
- ii. **Inherent weakness failure or latent defect:** applicable when the system is subjected to stresses within the item's stated capability.

**1.1.1.2. Time of failure:**

- i. **Sudden failure:** unexpected failure that cannot be anticipated by prior examination.
- ii. **Gradual failure:** failure that can be anticipated by prior examination.

**1.1.1.3. Degree of failure:**

- i. **Partial failure:** resulting from characteristic deviation beyond a specified limit, however the system does work up to a certain limit but not as well as it should.
- ii. **Complete failure:** resulting from characteristic deviation that causes complete lack of required function beyond a specified limit.

**1.1.1.4. Combination of failure:**

- i. **Catastrophic:** a combination of both sudden and complete failure.
- ii. **Degradation:** a combination of both gradual and partial failure.

As mentioned earlier, safety is an imperative quality for EPS applications. Hence, it is important an EPS system to operate in a degraded manner following a fault.

**1.2. What is fault tolerance and why it is needed:**

As today's technology advances toward intelligent systems, in which human interaction becomes less required, fault tolerance becomes a prevalent quality to avoid loss of control in safety critical systems. Pietrantuono and Russo in [11] describe a system as safety critical when the consequence of its failure results in substantial environmental and property damage or loss of life.

Based on White's [12] spectrum of availability, a system with increased fault tolerance will also have cost, availability and complexity increases as in Figure 4. White also defines a fault tolerant system as one in which "no single failure will cause the system to malfunction". By malfunction, it is implied that the system should be capable of performing under faulted conditions. This also gives the confidence to categorise the failure types as follows as in [8, 13]:

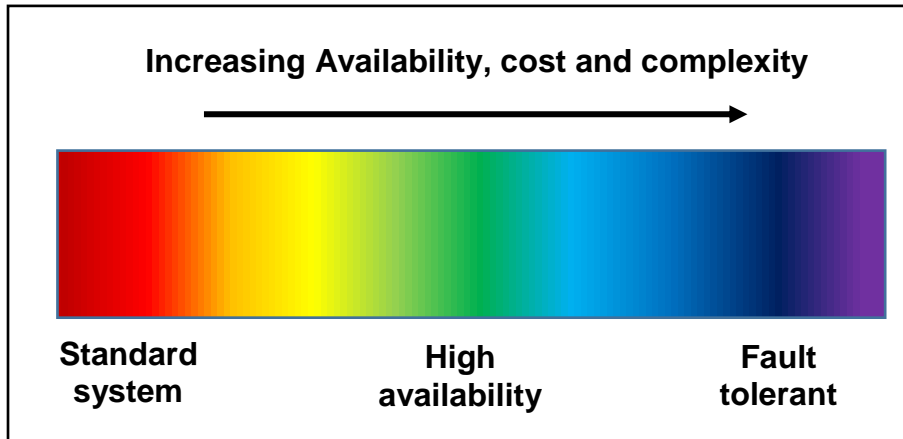


Figure 4: The availability spectrum.

### 1.2.1. Benign Failure:

This type of fault is accepted in a system where sufficient performance can still be obtained after a single module failure. Mellor *et al.* described in [14], a permanent magnet electric vehicle traction drive that can withstand benign failures where a fault in one component does not affect other components and does not lead to a complete system failure, such as sudden braking in the traction system. It is also possible to consider economic repair after a module failure.

### 1.2.2. Continuous operation with degraded output:

It is undesirable for systems to lose full capability after a single failure. This happens when the system is treated as a single unit in which a failure could potentially bring it to a halt. Ifedi *et al.* [15] presents a fault tolerant in-wheel motor that is partitioned to increase the system's fault tolerant capability. It uses an outer rotor permanent magnet motor that is divided into eight sub-motors driven via micro inverters. In case of a failure in any sub-motor, full system failure is unlikely, and it can be operated with a degraded output.

### 1.2.3. Continuous operation with full capability:

Bennett *et al.* [16], developed a fault tolerant drive for the nose wheel steering of an aircraft. The system needed to be operational and fully functional following a single

fault. A dual lane electric drive was produced for a motor prototype that had to produce full torque following a failure. This required each lane of the system to be capable of producing 200% of the full torque as a failed lane could produce a drag torque of half its capability.

### **1.3. Electrical machine topologies for Electrical power steering systems:**

Recent advances in materials and power availability have influenced the best choice for EPS systems. The cost of additional redundant parts in terms of both space and weight is also considered to be a key role player. 12 V systems have limited power capability due to the size of wiring harnesses; with higher voltages such as 48 V power voltage systems, the power capability and efficiency can be increased significantly, as it reduces harness losses.

According to Andrada *et al.* in [17], the following requirements should be fulfilled by a motor to be suitable for EPS:

1. Smooth torque production with minimum ripple.
2. Fault-tolerance.
3. High efficiency.
4. Low inertia.
5. Minimum package size and weight.
6. High power/torque density.

Moreover, researchers [18-20] suggest that the motor may have the following attributes for fault tolerant applications:

1. Similarity between stator slot number and pole number (the range of the slots per pole is between 0.7-1.5). The range of 0.7-1.5 has a coil span of 1 slot-pitch which permits a non-overlapping winding with shortest possible end turns, which is also important for mechanical isolations.
2. The coils of each phase should be separated from the other phases physically and decoupled magnetically. One way of achieving this is that each coil should be wound around alternate tooth.
3. A high number of phases so that in case of losing one phase, there would not be a large torque ripple or extreme disturbance to the converter's DC link current.
4. Each phase may be driven by a single-phase converter, or there may be a multiple set of three phase converters.

5. To limit the short-circuit current, the synchronous reactance per phase should be at least 1 per unit or higher. This value limits the single-phase fault current to rated current value or less.
6. The converter should be capable of detecting a range of faults.

Based on the above requirements and the type of systems, it is important to investigate different motor types and their compatibility for EPS applications.

### **1.3.1. Brushed DC (BDC) Motors:**

This type of motor is considered to be the simplest motor, to understand and for ease of control [21]. Despite their operational simplicity, they are not suitable for many variable speed drives due to low power density, arcing and EMI problems that are associated with the commutating brushes [22]. Their large size, poor efficiency and high inertia [23] are major drawbacks. Higher inertia affects the design of the gearing ratio in the EPS system [24] and the dynamic response of the system in variable speed drive [25]. Reflected inertia of the armature seen through the gear train by the driver as a particular downside.

### **1.3.2. Switched Reluctance Motors (SRM):**

Compared to brushed machines, SRMs are better choices but not used in practice. They have low inertia, high efficiency, rugged rotor construction and natural fault tolerance [17, 26]. These motors can withstand high temperatures and can operate in harsh environments [27]. Mecrow *et al.* [26] proposed a single-tooth segmental rotor SRM and widened the wound tooth maximising the torque by 40% through higher flux linkage, increasing the fault tolerance and reducing the copper volume by 30%. Despite all the aforementioned, SRMs are not considered suitable for EPS systems because of their high acoustic noise and torque ripple [22].

### **1.3.3. Induction Motors (IM):**

Induction motors are used in many industrial applications due to their cost effectiveness and reliability in high speed operation [28-30]. Aroquiadassou *et al.* in [31] describe and compare two rotating electrical motors for EPS systems taking the 42 V power availability into consideration. They explain how a traditional three-phase IM with a 6-switch voltage source inverter (VSI) is not suitable for this application. By referring to Welchko and Lipo [32] and highlighting the poor operating capability of an induction machine following a phase open circuit, they propose a 6 phase IM with a sequenced unidirectional stator current. They also compare the IM to an optimised

permanent magnet synchronous motor (PMSM) with the same torque output. They conclude that the PMSM has a higher torque and power density.

#### **1.3.4. Brushless DC(BLDC) Motors:**

Compared to their counterparts, Brushless (BL) motors have the advantage of no brushing contacts, less iron loss, lower noise, lower torque ripple and lower inertia [23]. The magnets offer an advantage of higher power density. This type of motor is driven through a square wave drive [24]. In the constant power region, the magnet flux must be weakened for the voltage source to accommodate the motor's back-emf. This leads to high torque ripple at high speeds, which is very undesirable [22] due to the trapezoidal nature of the back-emf. Although, its principle of flux-weakening operation is similar to Permanent Magnet Synchronous Motors (PMSM), the current is controlled through commutation and is not continuous, which is the main reason behind higher torque ripple.

#### **1.3.5. Permanent Magnet Synchronous Motors (PMSM):**

Radial PMSMs are generally favoured for EPS applications for their high torque density and low torque ripple [23]. Radial flux machines are important as they have a balanced radial force distribution for most slot/pole combinations, thereby reducing acoustic noise and increasing the bearing life [21]. Most importantly for this research are the requirements of fault tolerance capability, power density, weight and smooth torque [2]. In a safety critical application such as EPS, fault tolerance is needed to increase the system reliability [19].

Faults that might occur within the motor of an EPS system include [33]:

- I. Electromagnetic faults within the machine:
  - Winding short circuit at the terminals.
  - Winding open circuit.
  - Winding short circuit (phase to phase).
  - Magnet faults.
- II. Faults within the power converter:
  - Power device short circuit or open circuit.
  - DC link capacitor failure.
  - Power supply failure.
  - Connector failure.
  - Other components failure, such as microchips or software failure.

For a fault tolerant EPS system, the PM machine must be tolerant of a range of the fault conditions. Fault tolerance is generally produced by introducing redundancy: minimising the number of redundant components whilst enhancing fault tolerance is an objective which minimises system oversizing [34].

In [35], different motor topologies have been investigated in terms of power capability, torque density, operating speed range, efficiency and overload capability for different applications. The paper also specifies the PM machines' major design considerations for fixed PM excitation, including:

- Power factor.
- Torque density.
- Capability of withstanding demagnetization.
- Field-weakening capability.
- Motor losses, including eddy current loss, winding loss, and stator iron losses, the latter being particularly important at high speeds.
- Temperature rise in the magnets.

**Interior Permanent Magnet (IPM) motor:**

The proposed baseline motor for this project is an interior permanent magnet (IPM) motor. An IPM motor can provide up to 30% reluctance torque due to rotor saliency and a broader range of flux weakening capability [24, 33, 35-37]. In [24], the following aspects are discussed:

- ease of manufacture and magnetisation of the magnet both before and after the rotor assembly.
- The elimination of magnet sleeve.
- Design for high speed operation using internal bridges and webs for mechanical integrity.
- increasing the flux/pole and pole area through the use of V-shape magnets as in Figure 5.

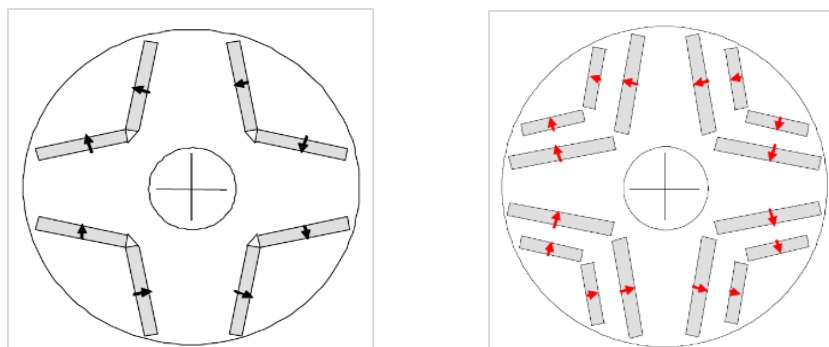


Figure 5: IPM rotor with: (a) V-shape magnets, (b) multi-layer V-shape magnets

In addition, fractional slot concentrated winding (FSCW) machines (as in Figure 6) are proposed for the following reasons [38]:

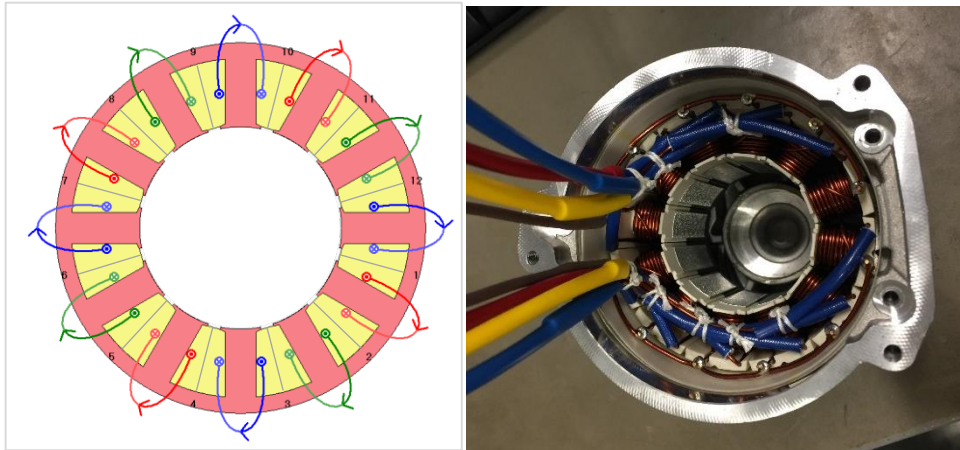


Figure 6: baseline motor stator with fractional slot concentrated winding representation and actual stator.

1. Modularity: manufacturing complexity can be reduced as each tooth holds a coil that can be wound separately. This also helps in labour cost reduction and manufacturing time [39] in comparison to distributed windings.
2. High fill factor that directly leads to lower copper loss by reducing the winding resistance, hence enhancing efficiency and thermal conductivity [40].
3. Higher torque density and lower copper mass. With shorter end-windings compared to a distributed winding a greater proportion of the copper is contained within the active part of the motor [41].

Whilst it has the above advantages, [39] states how FSCW machines can produce stator MMF harmonics, especially 5<sup>th</sup> and 7<sup>th</sup> order, a lower winding factor and excessive torque ripple.

The above considerations for IPM motors play a crucial part in the machine's operation. During field-weakening mode at high speed, the back emf may be larger than the supply voltage. The terminal voltage is regulated through the power electronics and, in the event of an open-circuit failure they may be subject to over voltage. [42, 43].

One of the disadvantages of using permanent magnet motors for fault tolerant applications is the drag torque that results from any shorted lanes in multi-lane systems (this will be covered in later chapters). In applications requiring high reliability and a high level of fault tolerance, the electric machines are often divided into smaller sub-machines, "lanes", and provided with more than one electrical supply.

As described in [15, 16] the losses generated within the shorted lane are dissipated in the relatively small resistance present in the short circuit loop, resulting in creation of

a drag torque. During a short-circuit fault in one lane, the other lane(s) must be able to overcome the drag torque produced; for example, continuous operation with a degraded output. This can be estimated using the following equations, where  $\omega$  is the electrical speed,  $R$  is the resistance of the short circuit loop,  $\psi$  is the flux from the permanent magnet, and  $L$  is the inductance present:

$$i = \frac{\omega\psi}{R+j\omega L} \Rightarrow i_{rms} = \frac{\omega\psi}{\sqrt{R^2+(\omega L)^2}} \quad Loss = drag\ torque = i_{rms}^2 * R = \frac{\omega^2\psi^2 R}{R^2+(\omega L)^2} \frac{1}{\omega}$$

Figure 7 shows three phasor diagrams with speed increasing from left to right. The left diagram shows how at low speed the resistance limits the current as the reactance is small. The short circuit current rises as the speed increases (centre): at high speed (right) the current becomes independent of speed as both back emf and reactance rise linearly with speed and resistance plays an increasingly minor role [37], as shown in Figure 8.

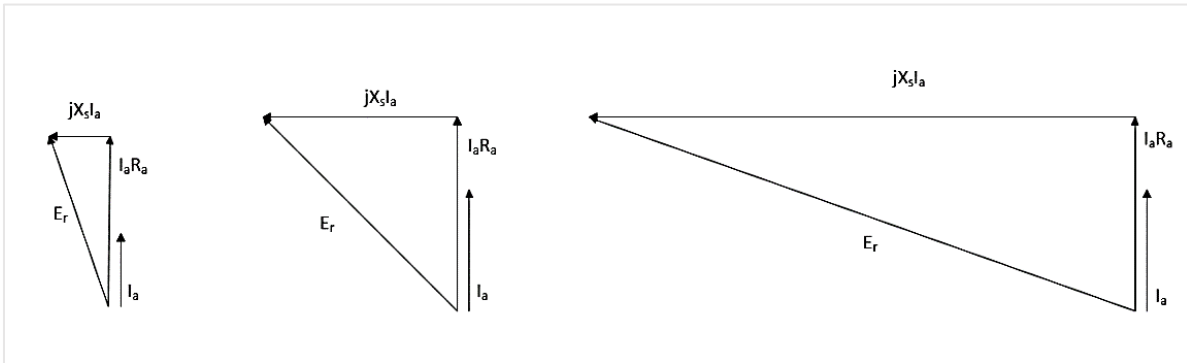


Figure 7: drag torque phasor diagram based on the operational speed

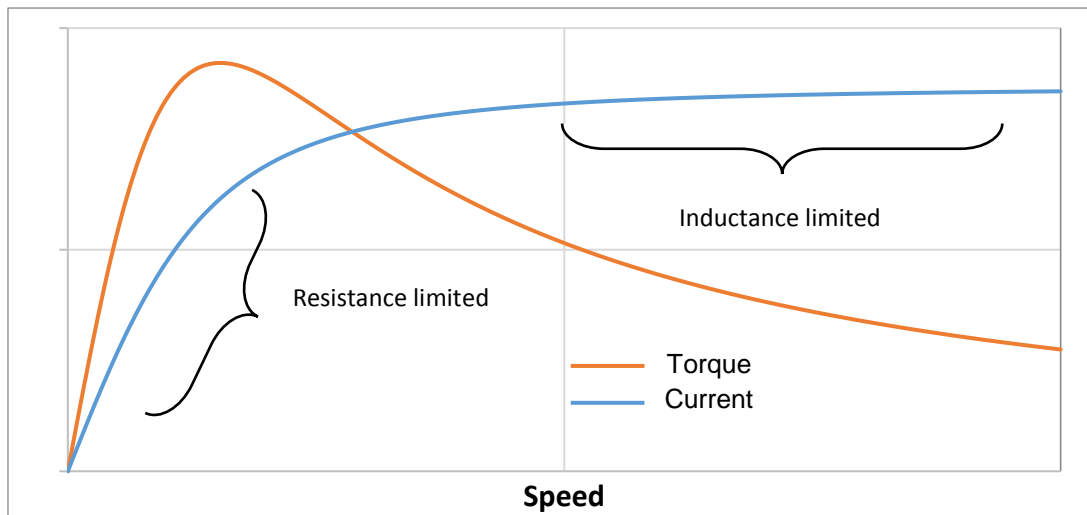


Figure 8: drag torque and short-circuit current vs speed characteristics.

### 1.3.6. Multi-lane systems:

The key requirements of fault tolerant motors are to increase the thermal, magnetic and physical isolation between independent lanes. Atkinson *et al*, in [44], highlight how

lane isolation can depend on making isolated drive units. This can be achieved through either a set of isolated H-bridges or several multi-phase bridges. In the literature [15, 45-49], multi three-phase or single-phase bridges are investigated and suggested to increase the system reliability and fault-tolerant capability. Each inverter supplies a section of the motor as a separate redundant part partitioning the motor into several sub-motors. This helps the system to operate efficiently across a wide range of speeds and, following a short-circuit in one of the sub-motors, minimises the effect of drag torque on the healthy parts of the system. For simplicity and reduced complexity there has been significant interest in dual-lane systems. In [16, 50, 51] there has been considerable investigation of how to split the motor into two separate halves internally (dual-lane systems). Particular attention has been focused on the internal winding arrangements, with connections of two different three-phase and five-phase motors, with each sub-motor fed from separate supply and drive. The winding connections will depend on the motor's slot-pole combination but, regardless of the motor's internal winding connection, the drive schematic of a typical dual-lane motor may be represented in Figure 9 below.

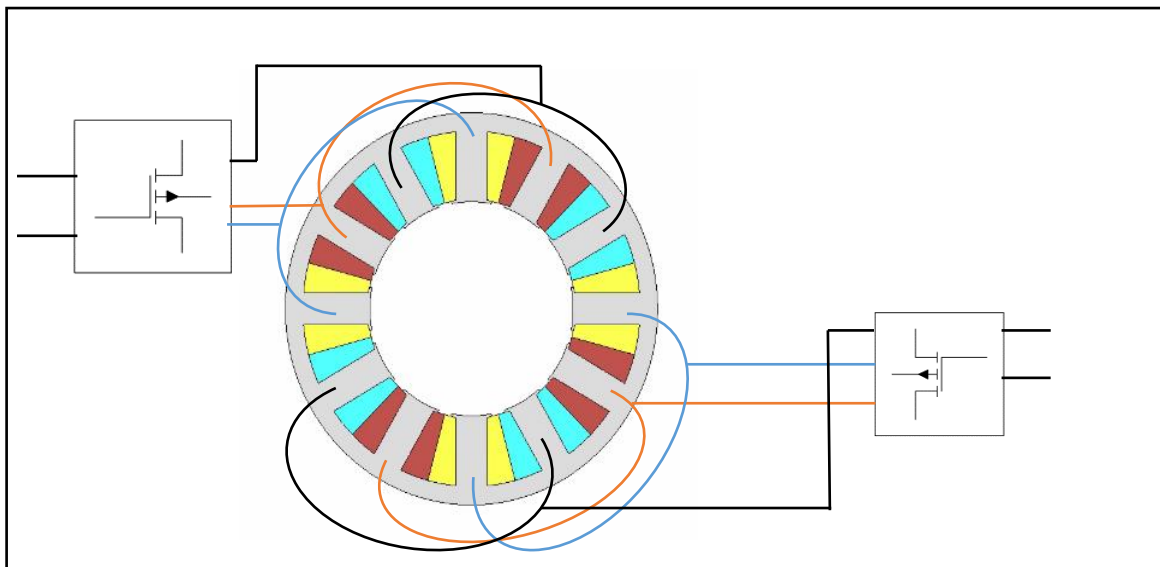


Figure 9: a typical dual-lane three-phase motor drive schematic.

### 1.3.7. Winding arrangements:

If a coil is wound around each tooth, there are conductors from two coils present in each slot. This is categorised as a Double-Layer (DL) winding. Conversely, if only every alternate tooth is wound, there are only conductors from only one coil present in each slot, producing what is termed a Modular, or Single Layer winding. The Modular winding offers better fault tolerance capability by minimising the mutual coupling between the coils [41], greater inductance, and ensuring physical separation of the

windings. With a single layer concentrated winding, the synchronous reactance is higher, limiting the short circuit current and providing a broader constant power region [24, 52].

There are several motor arrangements used in EPS systems, such as 12:10, 12:8 or 9:6 motor slot-pole combinations. As 9:6 motor slot-pole combination is difficult to be divided into two identical systems for dual-lane systems, only 12:10 and 12:8 will be highlighted. Figure 10 shows the different winding arrangements of both the 12:8 and 12:10 slot-pole motor topologies for both modular and double layer arrangement.

Additionally, the winding factors for these topologies are different. Both 9:6 and 12:8 slot-pole combinations have similar winding factor (0.866 for an un-skewed rotor). However, 12:10 and 12:14 slot-pole combinations have higher winding factors (0.966 for an un-skewed rotor) as the pole arcs are smaller, allowing the tooth to gather more magnet flux. However, they have noise and vibration issues due to lower mechanical vibration modes.

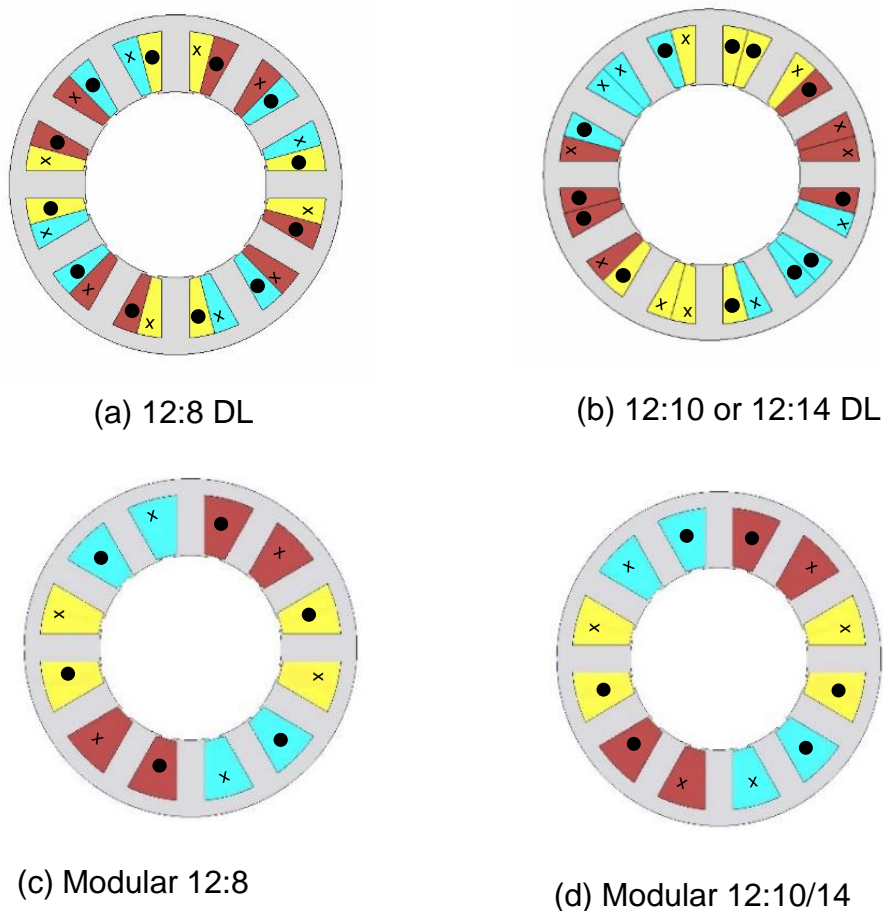


Figure 10: motor winding arrangements for 12 teeth stator with 8 pole and 10 or 14 pole rotor.

**1.3.8. Winding connections:**

For a dual-lane system, in which the machine is split between two equal halves, fed by two different inverters, the above winding arrangements can be connected using different coil connections, according to their slot pole combination. Both 12:8 and 12:10 pole slot combinations have three different winding connections. Figure 11 shows the possible connection for one of two lanes in a 12:8 motor.

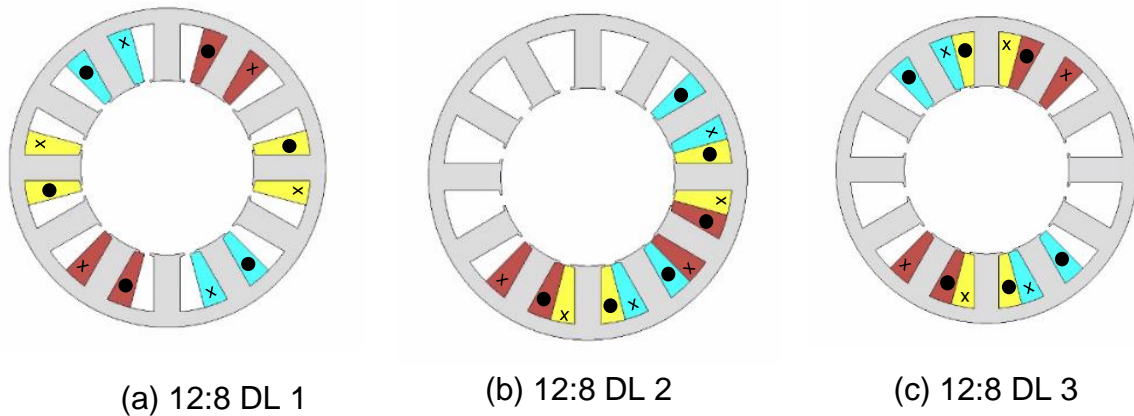


Figure 11: 12:8 motor double-layer arrangement winding connection possibilities for one of two lanes.

Because of its different stator excitation mechanism, the 12:10 and 12:14 motor topology offer slightly different phase for the DL 3 connection type, as shown in Figure 12.

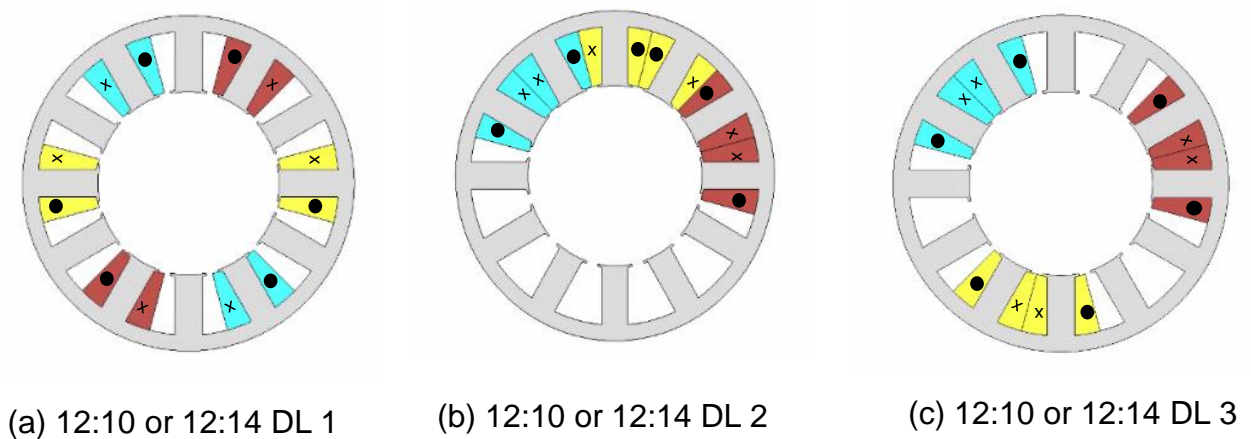


Figure 12: 12:10 or 12:14 motor double-layer arrangement winding connection possibilities.

Due to the nature of the modular winding arrangement, both the 8 and 10 pole motor topologies have the same winding connections but different coil polarities, with the options shown in Figure 13.

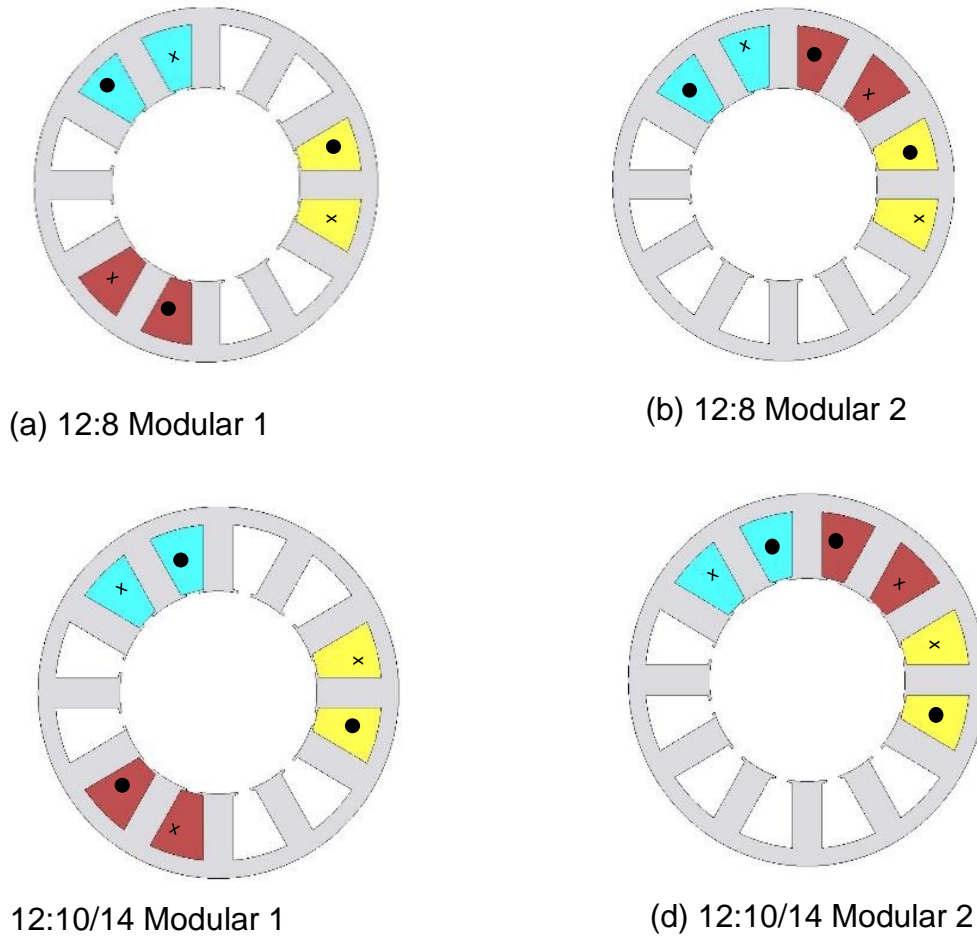


Figure 13: modular arrangement winding connection possibilities.

#### 1.4. Objective and methodology:

This thesis presents a novel fault tolerant power and torque dense SPM motor, designed for an EPS application. The motor is developed and compared to a commercial product, which is termed the “baseline” motor. The baseline motor is a 12 slot 8 pole single lane IPM motor with 85 mm outer diameter and 36mm stack length (both rotor and stator). The winding arrangement is double layer concentrated winding in which each tooth is wound with a coil. The rotor is skewed to fulfil the requirements of having low cogging torque and low torque ripple. The IPM can provide the following torques that fulfil the application requirements (Figure 14):

- 1- The stall torque should be 4.6 Nm or above for a complete mechanical rotor rotation up to the motor torque-speed curve knee point of 1100 rpm.
- 2- The average torque should be or above 3 Nm at 2000 rpm and 2 Nm at 3000 rpm.
- 3- The torque ripple and the cogging torque should be as low as possible.

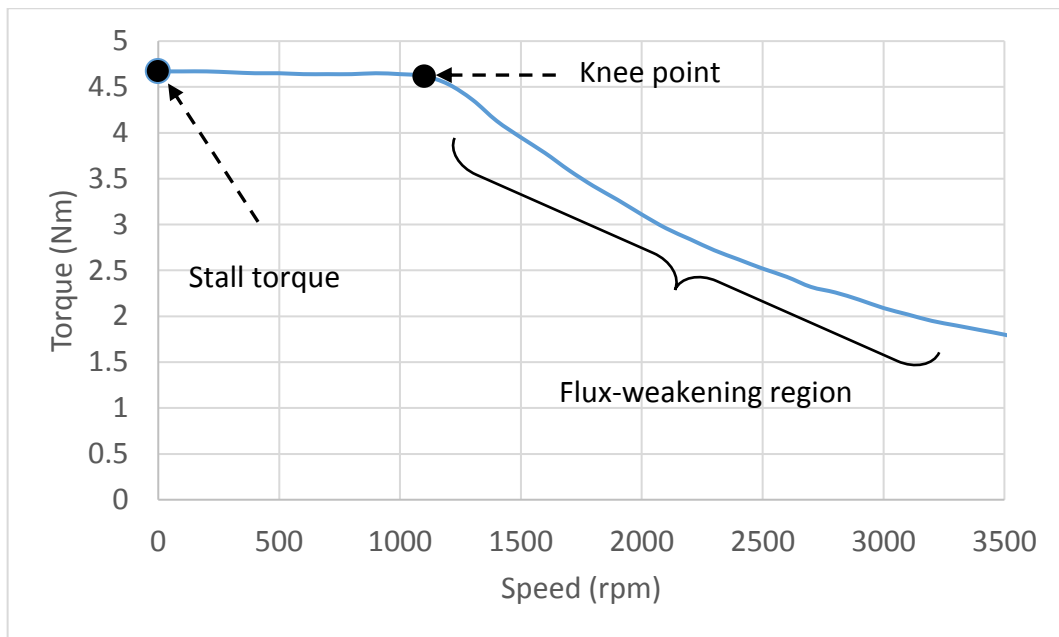


Figure 14: baseline motor's torque-speed characteristics.

As will be covered in later chapters, a failure within the motor leads to a high drag torque compared to the motor's stall torque. If the motor is fed by one power converter, a single failure within the motor or the drive is likely to lead to an unacceptable loss of capability.

The aim of this research is to investigate the fault tolerant quality of this machine by turning it into a multi-lane motor and to reduce the drag torque following a fault (such as three-phase balanced short or single MosFET failure), thereby enabling the motor to have greater capability when faulted.

Different FE software packages were used to carry out the investigation including Infolytica Magnet, JMAG, Ansys Maxwell, and MotorCAD [all trademarks acknowledged]. MATLAB and Visual basic scripting were used to control the finite element simulation software and analyse the resulting data. The different finite element simulation programs provided predictions of motor performance. Use of the different programs allowed answers to be obtained more efficiently through use of the most suitable solver and allowed cross-checking of answers and therefore greater confidence in the results.

The new machine should have similar or smaller dimensions to the current design, without increasing the winding resistance or slot fill factor. The following research has been conducted to achieve the research objectives:

- 1- Investigation of the current design under different fault conditions such as three-phase balanced shorts and single MosFET failure.
- 2- Division of the motor into two equal halves (two lanes) and shorting one lane investigating the subsequent drag torque and torque ripple.
- 3- Evaluation of modular windings (each alternate tooth is wound) to investigate the normal and faulted capability of the motor. Focusing only on electromagnetic rather than structural aspects.
- 4- Design of a new stator to overcome the accumulated issues with modular windings implemented on the baseline motors stator.
- 5- Investigation of the torque capability of the new stator at high speed.
- 6- Design of a new segmented SPM rotor to overcome the challenges of high-speed torque capability and magnet demagnetisation.
- 7- Recommendation for future work, based on simulations and results from experimental models.

### **1.5. Overview of thesis:**

This thesis comprises two main parts. The first part investigates and highlights the un-faulted and faulted performance of the baseline motor, showing the key role the inductance and resistance play in the performance during faulted and un-faulted conditions. The second concerns the design and construction of a novel Segmented Rotor SPM motor that overcomes the issues of having high inductance values affecting the torque speed characteristics. It provides higher torque density and lower inertia that makes the dynamic rotor response higher. Each chapter is described briefly below:

**Chapter 1:** introduces and gives an overview of the whole thesis. It discusses the advantages of EPS systems over their hydraulic counterparts. It also shows several motor candidates for the application and the merits of selecting synchronous PM motors. Several winding arrangements and connections are described and their benefits for fault-tolerant systems highlighted.

**Chapter 2:** investigates the performance of the baseline motor under normal operation and faulted conditions. It also studies the possible winding connections for a dual-lane system having two separate bridges. Simulation, analytical and experimental results are shown and compared for both faulted and un-faulted conditions.

**Chapter 3:** takes the baseline motor's stator to investigate modular windings. It observes the motor performance under both faulted and un-faulted conditions. It also shows the effect of inductance on the drag torque comparing to the baseline motor.

**Chapter 4:** develops the stator to overcome the issues that arises in chapters 2 and 3. It introduces a dissimilar teeth stator that provides higher torque capability compared to the baseline motor. 2D FE and 3D FE results are used to compare the performance. This design offers a very high fault tolerant capability but compromises the torque-speed characteristics due to very high q-axis inductance.

**Chapter 5:** presents the development of a novel segmented rotor SPM motor to tackle the issue addressed in chapter 4. It starts by showing design approaches to shape the rotor introducing the flux barriers to reduce the q-axis inductance. The new design offers a very high torque density and power density compared to both previous designs. However, the compromise is the faulted performance which is still better than the baseline motor but not as good as the intermediate design. Simulation and experimental results are presented to validate results.

**Chapter 6:** concludes the research and suggests future work that can further enhance the fault tolerant capability of the new motor based on the drive availability.

### **1.6. Contribution to knowledge:**

The contributions of this research include:

1. Investigating different winding connections for a 12:8 concentrated wound IPM motor for both double-layer and single-layer winding arrangements. Dual-lane systems were also investigated and compared with the single-lane arrangement. The arrangements were focusing on torque capability and torque ripple under normal and certain faulted conditions.
2. Development from an existing 12:8 concentrated wound IPM motor, a dissimilar teeth stator with modular winding. This increases the fault-tolerant capability and torque density in the constant torque region of the resultant motor. This motor suffers from poorer performance in the constant power region. However, the q-axis inductance was identified as the reason for the power drop.
3. A novel high torque segmented SPM motor was developed that addresses the problem of high q-axis inductance. Flux barriers were introduced to reduce the q-axis flux and improve the motor capability in the constant power region, whilst also ensuring there is no magnet demagnetisation. The measures of performance

focused on higher torque and power density and physical segregation between the motor lanes and phase coils.

### **1.7. Published work:**

The following paper has been published from this research:

1. Al-Jaf A., Mecrow, B., and Moule, D., 'Winding Arrangement and Design Development for Fault Tolerant EPS Systems' The 9th International Conference on Power Electronics, Machines and Drives (PEMD 2018) 17-19 April 2018, Liverpool ACC, Liverpool, UK.

## Chapter 2

# Double-layer winding arrangement and connections

This chapter investigates an interior permanent magnet synchronous motor (PMSM) with pole caps. As highlighted in Chapter 1, PMSMs are suitable for EPS applications, due to their high efficiency and their low torque ripple. An existing production motor used in an electric power steering application is studied in this chapter.

Initially, 2D FE simulation results are presented to show the capability of this baseline motor under both normal and faulted conditions. The fault simulations require intensive computation, so simulations are carried out in 2D. Different winding arrangements and connection types are investigated and compared.

### 2.1. Baseline motor characteristics and design parameters:

The baseline motor is a 12 slot, 8 pole fractional slot concentrated windings interior PMSM with pole caps (Figure 15) that are used to protect the magnet from stator demagnetising fields and can be used to create a sinusoidal induced back-emf. The caps also contribute to cogging torque reduction and minimisation of magnet eddy currents induced by airgap space harmonics [24].

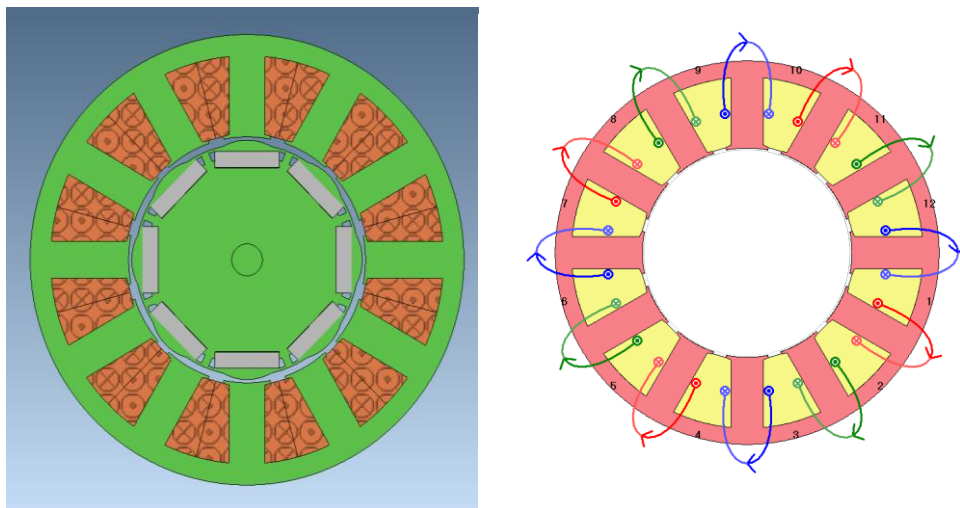


Figure 15: fractional slot concentrated winding (FSCW) 12:8 IPM motor that is used in this project

Because of the different reluctance paths between the d-axis and q-axis of the rotor, the motor has a degree of saliency that results in maximum torque per ampere (MTPA) with some MMF advance angle. For future steering applications, there are various imperative requirements: fault tolerance, power density, small packaging size and

smooth torque [2]. The table below shows the motor parameters that are used in this work. The term rotor pucks refer to the number of axial segments of the rotor which are used for step skewing Figure 16.

Variable	Value	Unit
Motor Rated torque	4.65	Nm
Motor Base speed	1150	rpm
Motor excitation	Three-phase AC machine	
Number of parallel paths per phase	4	
Number of turns per stator segment	24	
Phase peak current	126	A
Current Advance angle	10	Elec-deg
DC link voltage	12	V
RMS current density	21.07	A/mm <sup>2</sup>
Rotor pucks skewed angle	5.4	Mech-deg
Number of pucks	3	
Number of slots	12	
Number of poles	8	
Stator outer diameter	85	mm
Axial length	36	mm

Table 1: Motor specification that is used to carry out simulations.

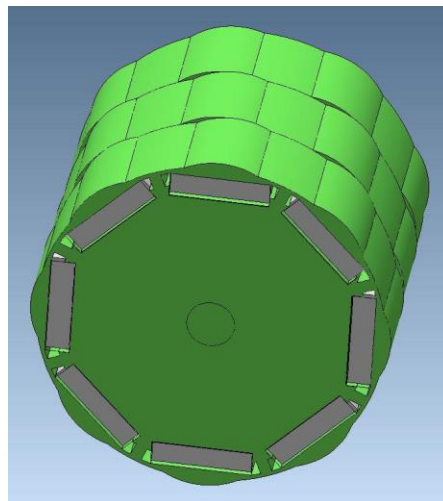


Figure 16: the baseline motor's rotor with skewed rotor pucks.

## 2.2. Simulation results under normal operating conditions:

Simulation results are used for both loaded and un-loaded conditions to show how skewing affects the overall machine performance, including voltage, torque and flux

linkage. Additionally, the effect of current amplitude and phase advance upon torque are presented. The motor specifications are shown in Table 1.

### 2.2.1 Cogging torque:

Cogging torque is an oscillatory torque which exists, even when the machine is unexcited. It occurs because of magnetic attraction between the stator teeth and rotor magnets [24, 53-55]. It does not contribute to the average motor torque but does add to the torque ripple and acoustic noise in the machine. Design choices can lead to reduction of the cogging torque; however, they can also affect the mean torque capability. The cogging torque is expressed in equation (2-1), and the number of the cogging cycles in one mechanical cycle can be calculated using equation (2-2).

$$\tau_{cog}(\vartheta_m) = \sum_{k=1}^{\infty} T_{kN_p} \sin(kN_p Q \vartheta_m + \varphi_k N_p) \quad (2-1)$$

$$N_{period} = \frac{N_p Q}{HCF\{Q, N_p\}} \quad (2-2)$$

Where

$\tau_{cog}(\vartheta_m)$  is the cogging torque in Nm

$T_{kN_p}$  is the torque coefficient

$\vartheta_m$  is the mechanical angular position in (deg or rad)

$N_p$  in number of poles

$Q$  is the number of the stator slots

$N_{period}$  is the number of the repetitive cogging cycles in one mechanical cycle.

In [55] and [53] different approaches are proposed and highlighted to reduce the cogging torque but the main focus in this work is skewing to minimise and smoother output torque.

#### Skewing:

Skewing is a method used to reduce EMF harmonics, cogging torque and torque ripple. It can be applied to either the rotor or the stator of a motor [53, 56, 57]. It can be applied to the stator either before or after winding insertion [24]. The skewing angle should be at least half a slot pitch or one cogging torque cycle, which can be calculated using equation (2-3) [53, 56-58]. However, it has been shown that for some operating conditions skewing can actually result in increased torque ripple.

$$\vartheta_{sk} = \frac{1}{N_p} \frac{2\pi}{Q} \quad (2-3)$$

A general formula regarding cogging torque reduction shown in equation (2-4):

$$\tau_{sk} = \frac{1}{\vartheta_{sk}} \int_0^{\vartheta_{sk}} \tau_{cog}(\vartheta_m) d\vartheta_m \Rightarrow \sum_{k=1}^{\infty} \int_0^{2\pi/(N_p Q)} T_{kN_p} \sin(kN_p Q \vartheta_m + \varphi_k N_p) d\vartheta_m = 0 \quad (2-4)$$

Stator skewing can cause manufacturing difficulties which make automatic slot filling almost impossible. When the rotor is skewed, the magnets require complex shapes or complex magnetisation, adding to the cost of production. Therefore, different studies have proposed segmented or “stepped” rotor skewing. This divides the rotor into a series of axial segments which rotate according to the required skew angle.

The skew angle for each module is  $(\vartheta_{ss} = \vartheta_{sk}/N_s)$  in which  $(\vartheta_{sk})$  in equation (2-3).  $(\vartheta_{ss})$  remains independent of the rotor axial length. With correct choice of step skew, the magnitude of cogging is reduced and the number of cogging cycles per slot pitch increased. In general, the step skewing reduces the back-emf fundamental and harmonics by  $[k_{sk} = \sin(kp\vartheta_{sk})/kp\vartheta_{sk}]$ .

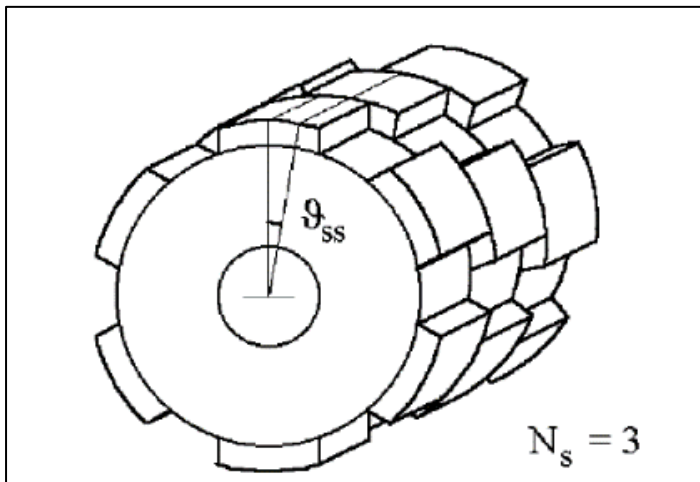


Figure 17: Stepped rotor skewing in three modules [53].

In this application a three-step segmented skew is used. Theoretically, each segment should have a rotational angle difference of 5 mechanical degrees to be effective. Based on Figure 18, Figure 19 and Figure 20, the cogging can be eliminated by skewing the rotor 15 mechanical degrees (5 degrees per puck).

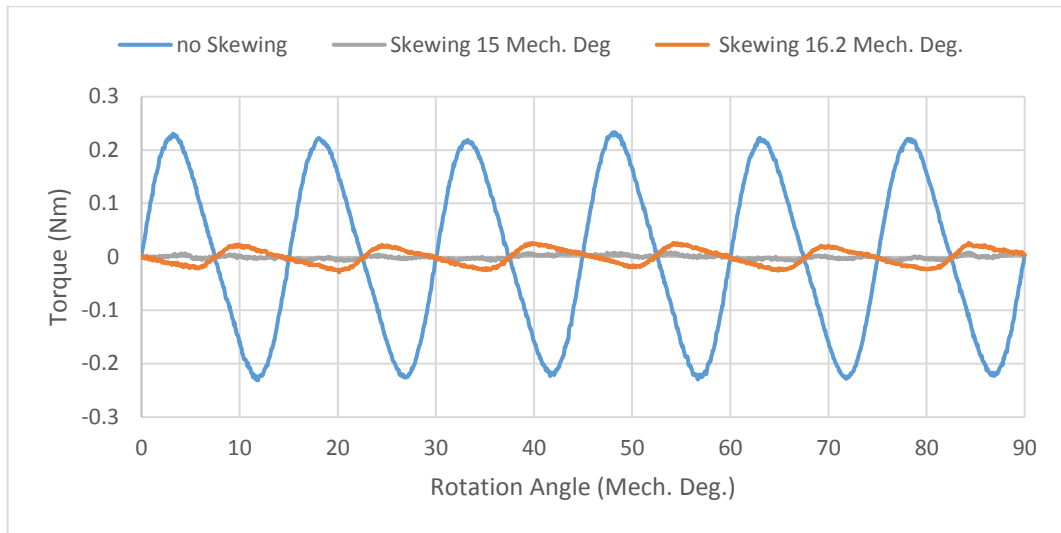


Figure 18: 2D FE cogging torque waveform for one electrical cycle.

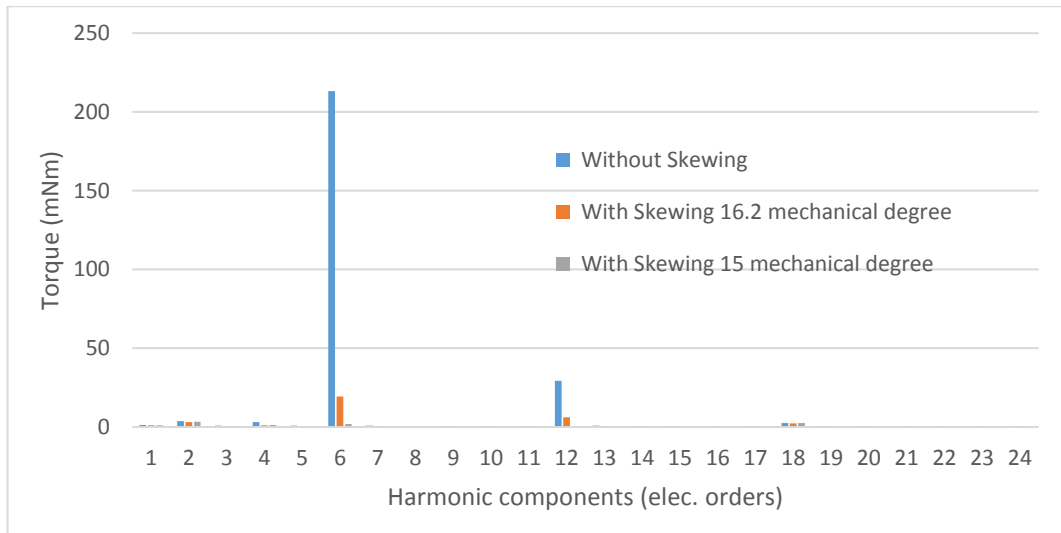


Figure 19: 2D FE Cogging torque harmonic content – electrical orders.

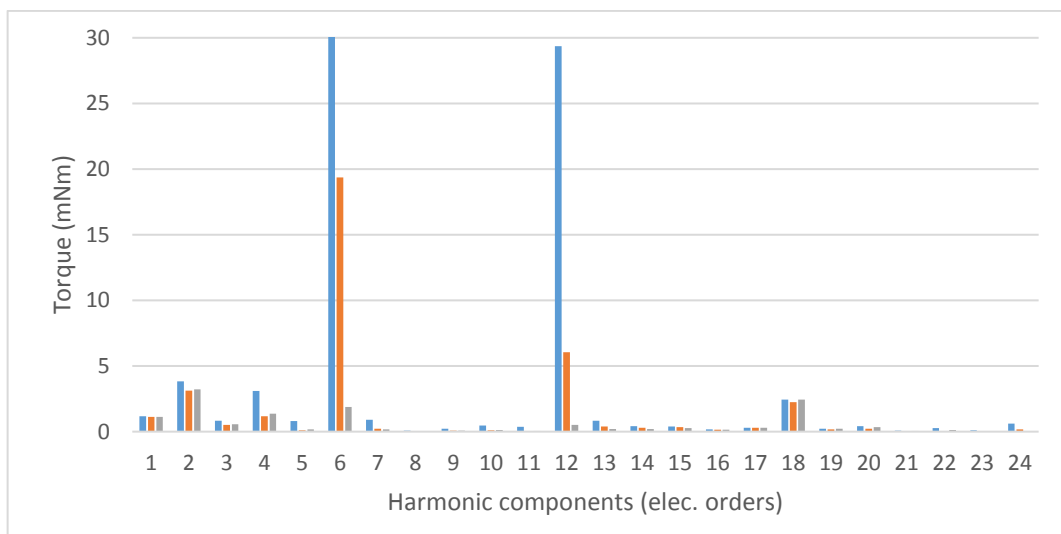


Figure 20: 2D FE Cogging torque harmonic content – electrical orders [Scaled].

This only shows the 2D FE simulation results that neglects the 3D effects that have significant impacts on the cogging torque values. The actual motor is skewed by 16.2 mechanical degrees (5.4 mech. degrees per puck) for reasons explained in [59], which indicates that the motor's cogging torque cannot be eliminated by the theoretical skewing angle due to axial interaction between adjacent rotor pucks and the end flux leakage (Figure 21 and Figure 22). Over skewing is required to minimise the cogging torque. The main harmonic content of the cogging torque is 24<sup>th</sup> mechanical order and is amplified by the gearing ratio in EPS systems. This could be felt by the driver if it is not reduced by a great level. The 6<sup>th</sup> order electrical (24<sup>th</sup> mechanical) cogging torque which can be seen clearly in the above figures could be felt by the driver.

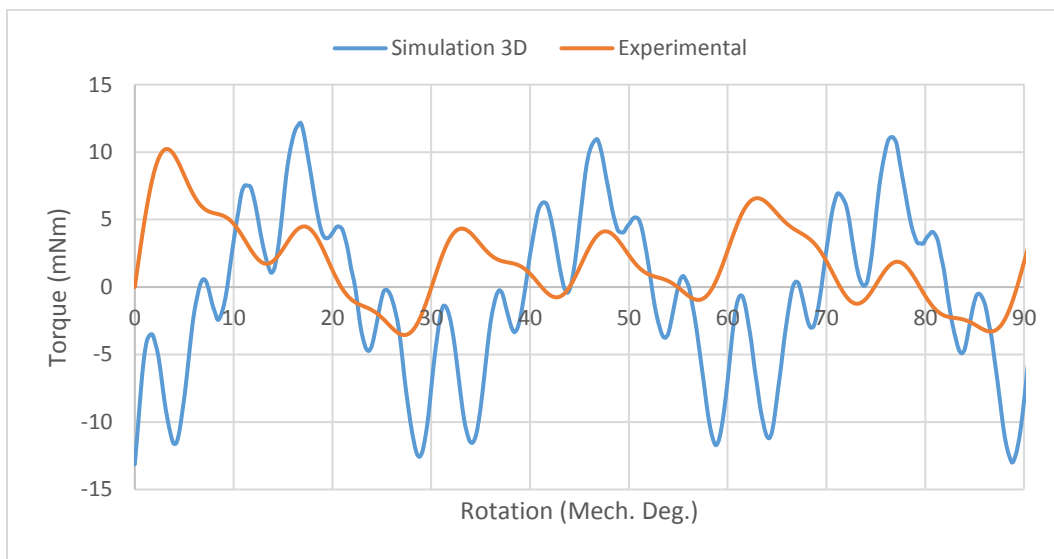


Figure 21: 3D FE and experimental cogging torque waveform for one electrical cycle.

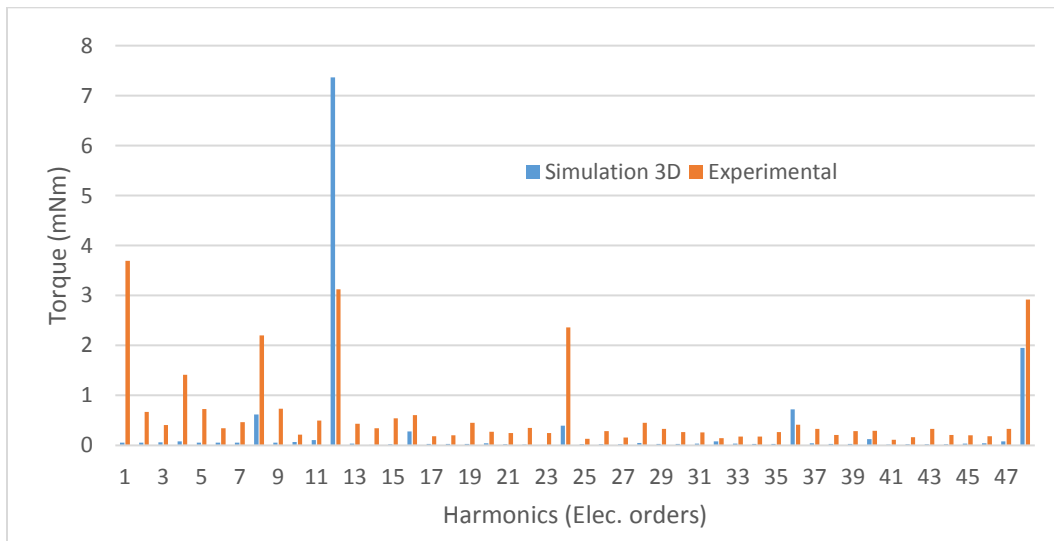


Figure 22: 3D FE Cogging torque harmonic contents – mechanical orders.

As the cogging torque value is very small compared to the motor stall torque (almost 0.2%), the difference between 3D simulation predictions and practical results was expected to be different as construction and assembly tolerances significantly affect the cogging torque values shown in Figure 21.

From Figure 21 and Figure 22, there is a phase shift difference between the two signals as the experimental result doesn't have a reference and they are not aligned. Although, there are some odd harmonic contents in the experimental results which is present due to the stator assembly and the rig setup.

Although, the experimental torque signal in Figure 21 has been reconstructed from the harmonic contents in Figure 22. The phase shift is also due to not having the harmonic angle information of the harmonic content.

### **2.2.2 Back-emf:**

Simulated and measured test results of the back-emf are used to characterise the baseline motor. It is important for the back-emf to be sinusoidal to ensure smooth torque production (assuming a sinusoidal input current). In FE simulations the speed is set to 1000 rpm and the back-emf constant ( $K_e$ ) is determined. The 2D and 3D FE results differ due to small axial gaps between rotor magnet pucks and axial fringing between pucks, which are not included in the 2D simulation. The overall magnet length is 33.45 mm, whilst the rotor overall stack is 36 mm. This leads to approximately 7% reduction in the magnet flux travelling to the stator. The 2D  $K_e$  is 51.2 mV/rad (Figure 23 and Figure 24), while the 3D  $K_e$  is 44.5 mV/rad (Figure 25 and Figure 26). The combined effects result in approximately 13% difference between the 2D and 3D results, however the harmonic contents are not significantly affected (Figure 26 and Figure 27). The phase shift between the practical and experimental results (Figure 25) is due to the rigs speed variation.

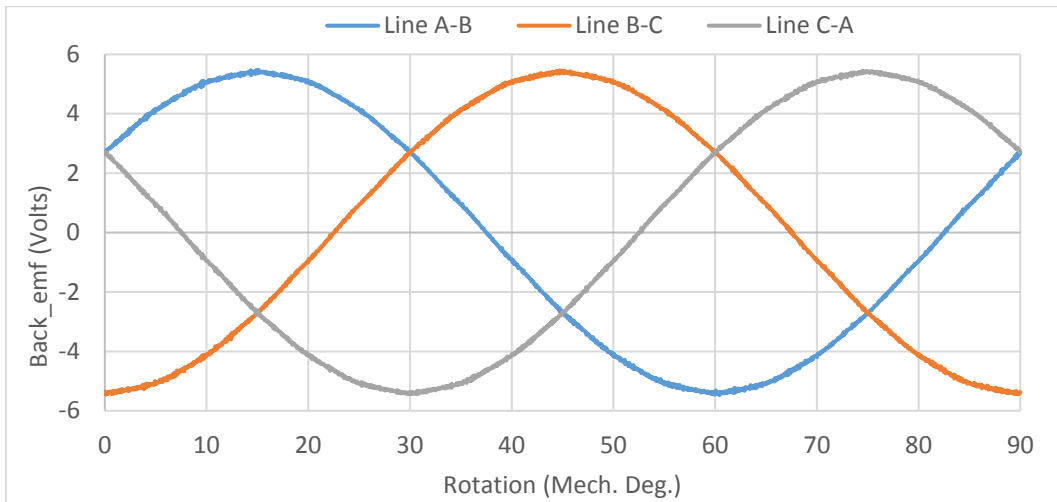


Figure 23: line to line back-emf waveform for an electric cycle based on 2D FE simulation.

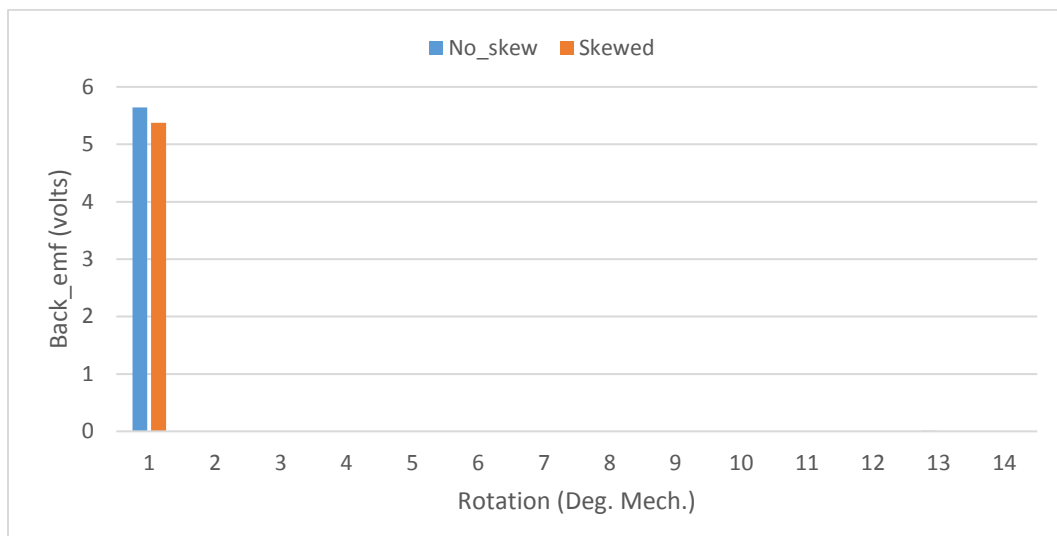


Figure 24: line to line back-emf harmonic content based on 2D FE simulation.

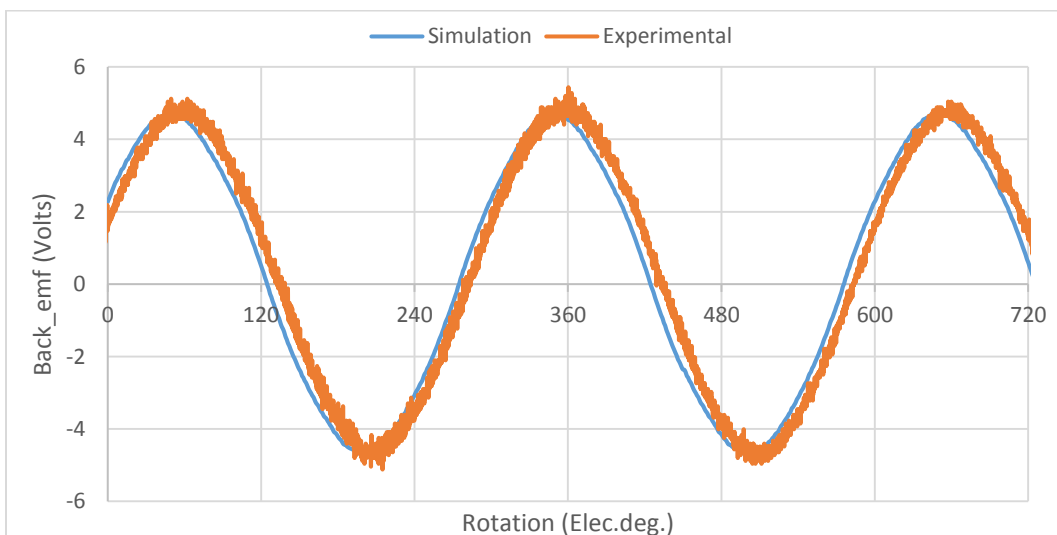


Figure 25: line to line back-emf waveform for an electric cycle based on 3D FE simulation and practical test.

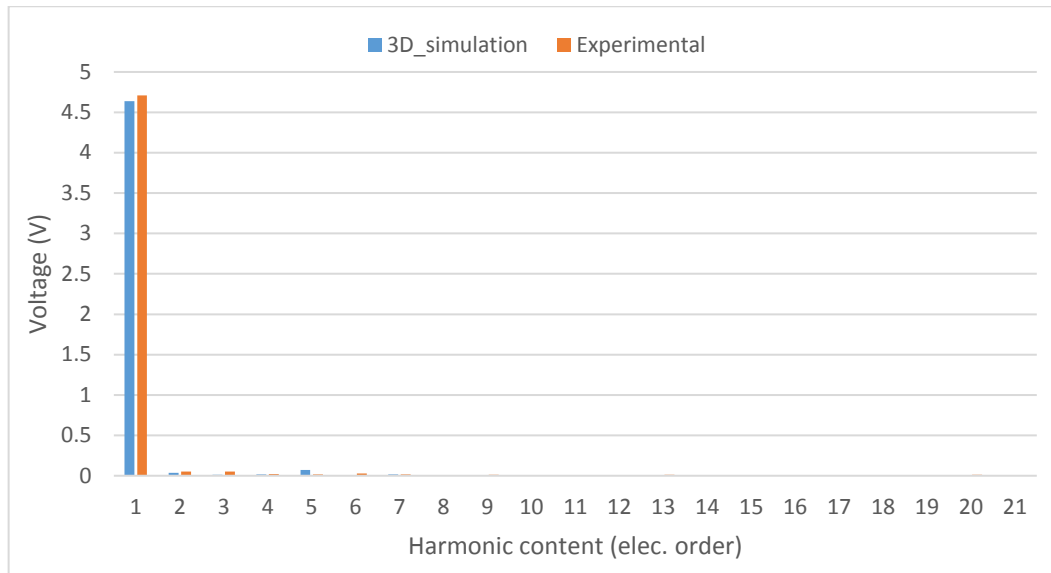


Figure 26: line to line back-emf harmonic content based on 3D FE simulation and practical tests.

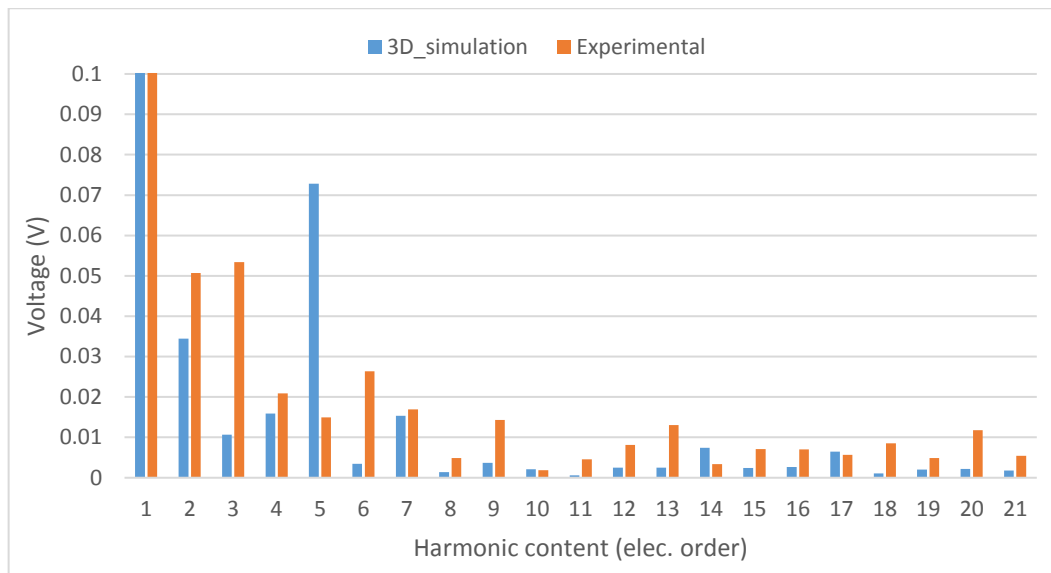


Figure 27: line to line back-emf harmonic content based on 3D FE simulation and practical tests [scaled].

### 2.2.3 Loaded Characteristic:

This section studies the motor behaviour when the windings are excited. It considers the torque constant ( $k_t$ ), which varies with the saturation level of the motor when the input MMF is increased. As the motor has a degree of saliency, the maximum torque per Ampere (MTPA) is investigated and the optimum advance angle is highlighted. Finally, torque ripple and its harmonic content are shown, and the effect of skewing is highlighted.

**Test rig:**

The baseline motor is provided by ZF (Figure 28). Some of the practical tests were carried out in ZF labs including cogging torque, torque ripple, torque-speed characteristics, and loaded fault conditions. All the motors were tested using the same setup for measuring cogging torque. The rig, which consists of a DC motor connected to fly-wheel, is rotated at 50 rpm. A measurement is made with the rig alone so its contribution to the cogging torque can be subtracted from the measurement with the motor connected.

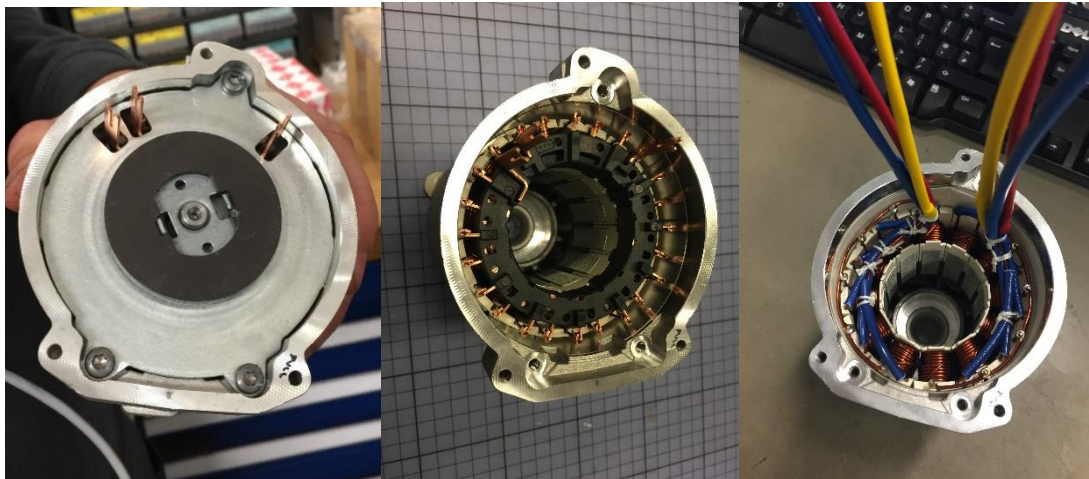


Figure 28: production motor before and after reconnecting the stator for dual-lane system.

For loaded tests, an ECU is used that is provided by ZF. The ECU (Figure 31) is capable of receiving an external encoder signal which is used to align the rotor axis to the input current.

As it is a switching device, time harmonics are expected to affect the torque ripple of the motor. The test was conducted at 50 rpm. As with the cogging torque measurement, the contribution of the rig to the measurement was subtracted from the result.

The setup with and without the motor, as in Figure 30, would be investigated to differentiate the rigs ripple content from the actual motor harmonic contents. This is done for both cogging torque and torque ripple experiments.

The DC torque test is carried out at 10 rpm by inserting a positive rated DC current through a phase and return through the other two phases (Figure 29).

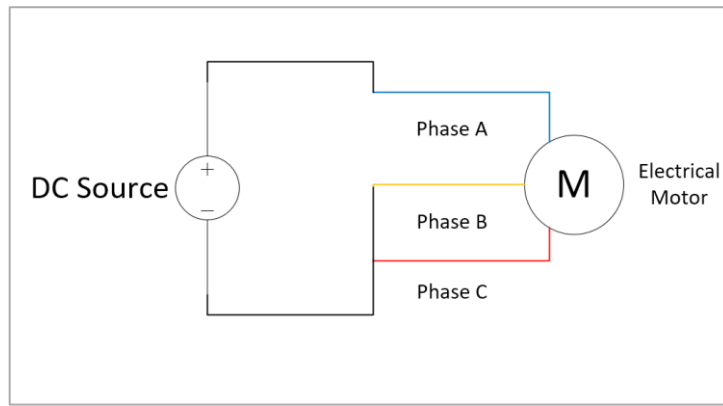


Figure 29: circuit diagram for connecting the motor during DC torque test.

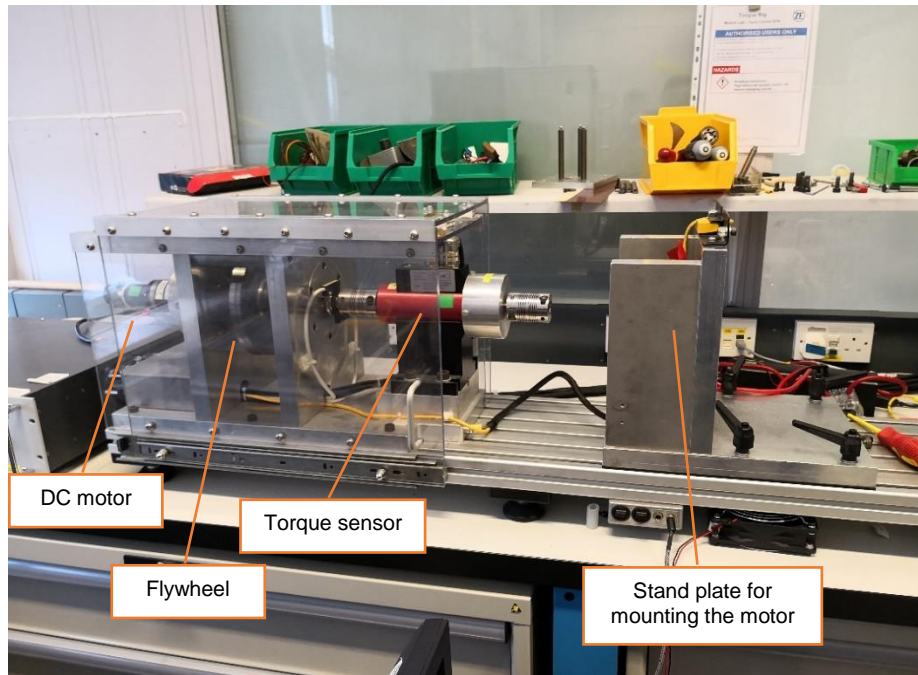


Figure 30: test rig to measure torque ripple, cogging torque and DC torque experimentally.

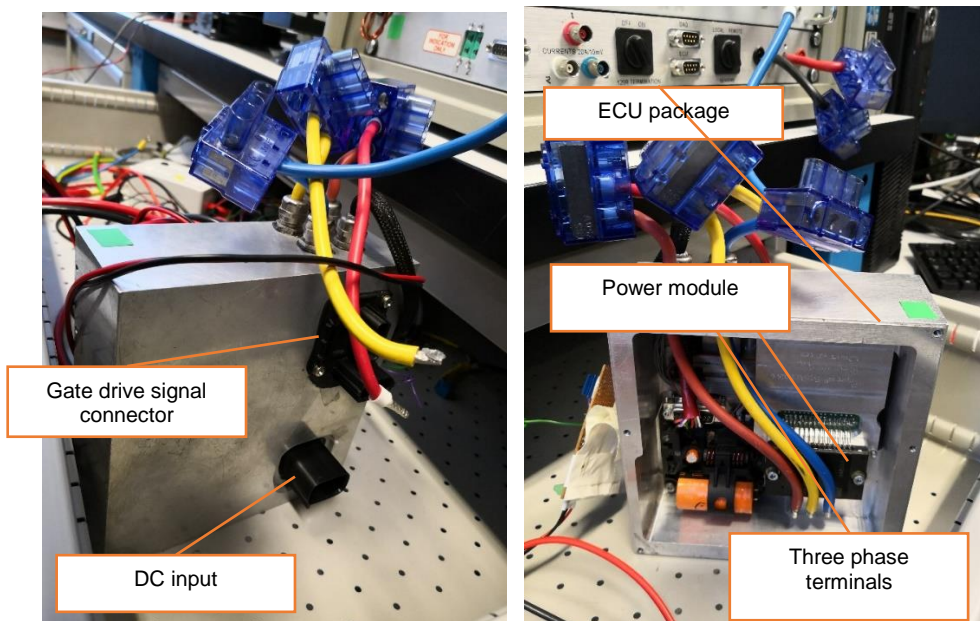


Figure 31: ECU to drive different motors in the lab.

### 2.2.3.1 Torque-current characteristic:

The relationship between the input current and the average torque is used to calculate the torque constant ( $k_t$ ). The variation between the input current and the torque produced is not linear due to the non-linear behaviour of the core material of the motor. The non-linearity leads to saturation within the electromagnetic core of the motor, which reduces the torque constant by approximately 3% between half load and full load (Figure 32). The saturation effect can be reduced by either increasing the cross-sectional area of the saturated sections or enhancing the property of the core material. Increasing the lamination cross-section can lead to reduction of the electric loading due to a smaller slot area for otherwise unchanged dimensions such as outer diameter, whilst using laminations with enhanced material properties may not be cost effective.

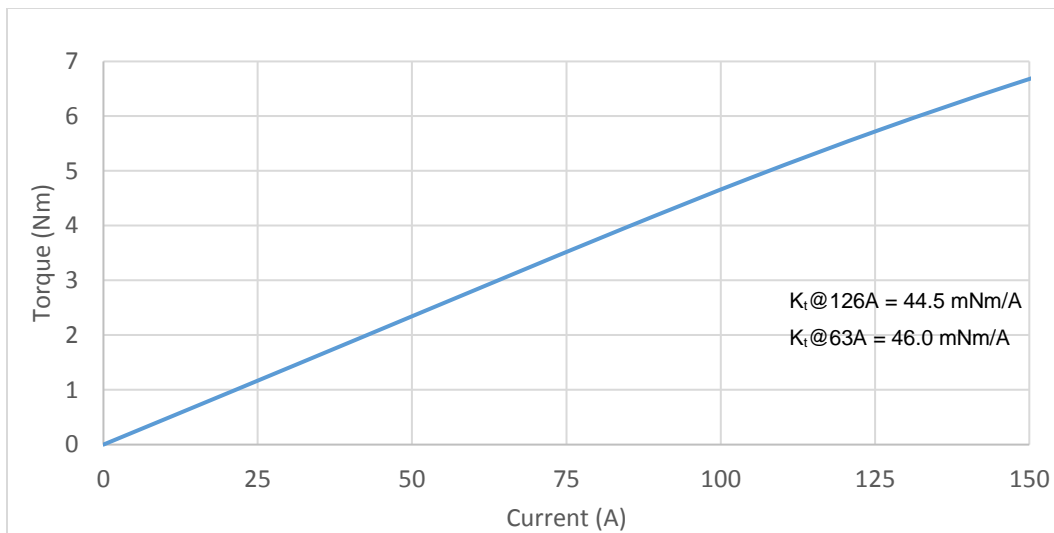


Figure 32: Torque vs current based on 2D FE simulation.

The motor core saturation mostly occurs in the teeth faces and the rotor bridges as shown in Figure 33.

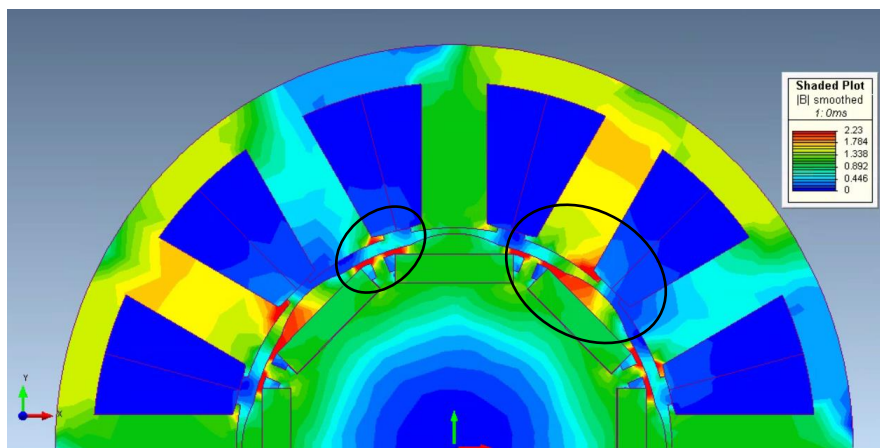


Figure 33: flux plot of the baseline motor cross-section based on 2D FE simulation (full-load).

### 2.2.3.2 Effect of current phase advance angle:

The IPM motor's saliency influences the reluctance torque, flux weakening operation and inverter rating. Because of the non-linear relationship between the current and torque in salient motors [24, 33], the current phase angle must be advanced by a value which is dependent on the load. The following equations describe the reluctance torque and alignment torque components for different speeds, neglecting saturation and losses. The per-unit voltage equations for both d-axis and q-axis are as follows:

$$V_{qs} = n_{pu}(E_0 + X_{ds}I_{ds}) \quad (2-5)$$

$$V_{ds} = -n_{pu}X_{qs}I_{qs} \quad (2-6)$$

Where

$n_{pu}$  = per-unit speed

$E_0$  = per-unit open circuit voltage at one per-unit speed

$X_{ds}$  = per-unit direct axis reactance at one per-unit speed,

$X_{qs}$  = per-unit quadrature axis reactance at one per-unit speed.

By defining  $V_s$  as the stator phase voltage and  $I_s$  as the stator phase current, d-axis and q-axis terms can be related to the stator with following equations:

$$V_s = V_s \angle \delta = V_{qs} - jV_{ds} \quad (2-7)$$

$$I_s = I_s \angle \gamma = I_{qs} - jI_{ds} \quad (2-8)$$

Figure 34 shows the relation between the open circuit voltage ( $E_0$ ) and the stator current phasor ( $I_s$ ). With the assumptions of a lossless motor, the output power equals the power input, derived from equations (2-5 and 2-6):

$$P_{out} = V_{qs}I_{qs} + V_{ds}I_{ds} \quad (2-9)$$

$$P_{out} = n_{pu} \left[ E_0 I_s \cos \gamma + \frac{X_{qs} - X_{ds}}{2} I_s^2 \sin 2\gamma \right] \quad (2-10)$$

The above power equation has a positive value for  $0 < \gamma < 90$ . Suppose the maximum torque occurs at an angle  $\gamma^*$  [37]. The reluctance term is  $(\frac{X_{qs} - X_{ds}}{2} I_s^2 \sin 2\gamma)$  that defines reluctance torque at the maximum torque point. Based on Figure 35 the maximum torque is obtained with a current advance angle of 12 electrical degrees, though it should be noted that peak value is only about 2% greater than when the current is in the q-axis and saliency is not employed. Another way to investigate the motor's saliency is the DC torque. Figure 36 and Figure 37 show both 3D simulations and measurements for the machine in which dc current is placed in the stator and the rotor is rotated. Two things should be noted: the correlation between simulated and

measured currents and the second space harmonic in the torque. This second harmonic is the reluctance torque contribution.

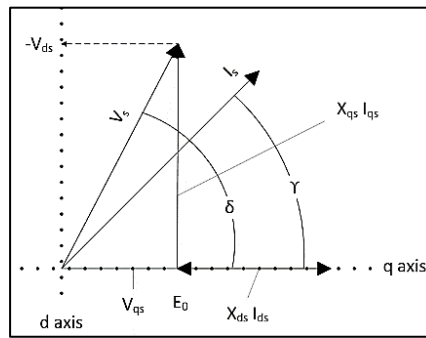


Figure 34: Phasor diagram of an IPM motor at one per-unit speed [22].

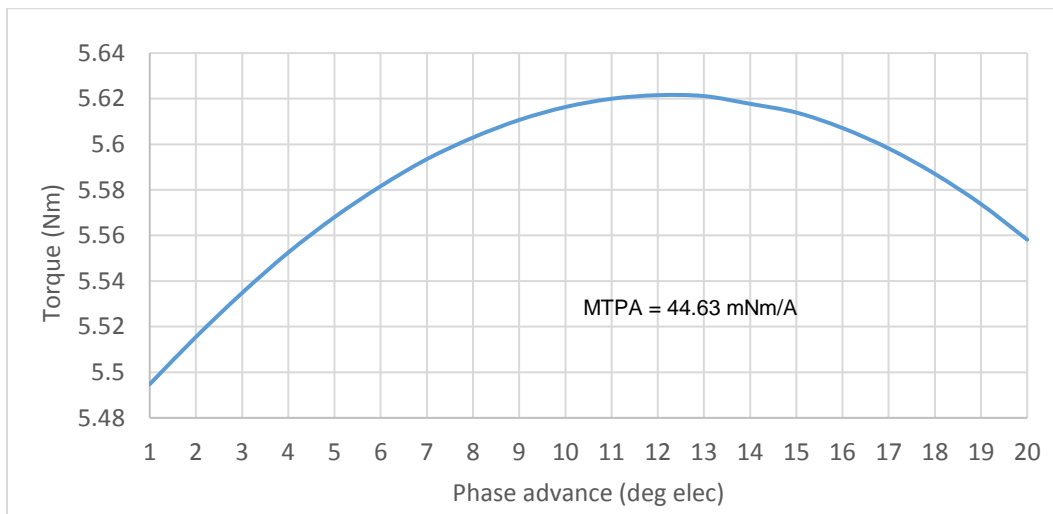


Figure 35: torque vs advance angle based on 2D FE simulations at rated current.

Expectedly, the 8<sup>th</sup> order harmonic in the DC Kt harmonic contents is noticeably lower at half load (Figure 38) as it is due to saturation. Reluctance torque is mainly due to permeance change and it varies with saturation level of the core saturation level.

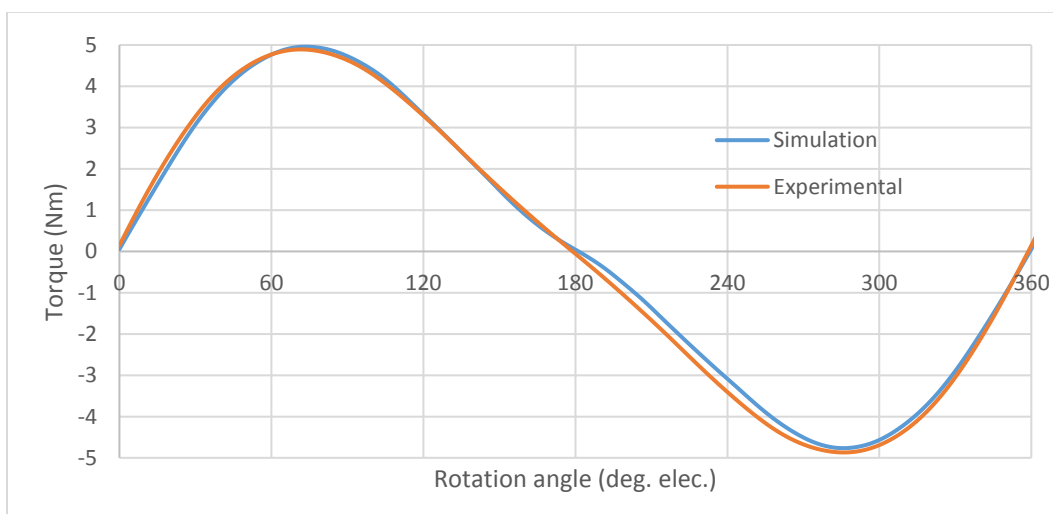


Figure 36: DC torque comparison between the practical and 3D FE simulation at rated current.

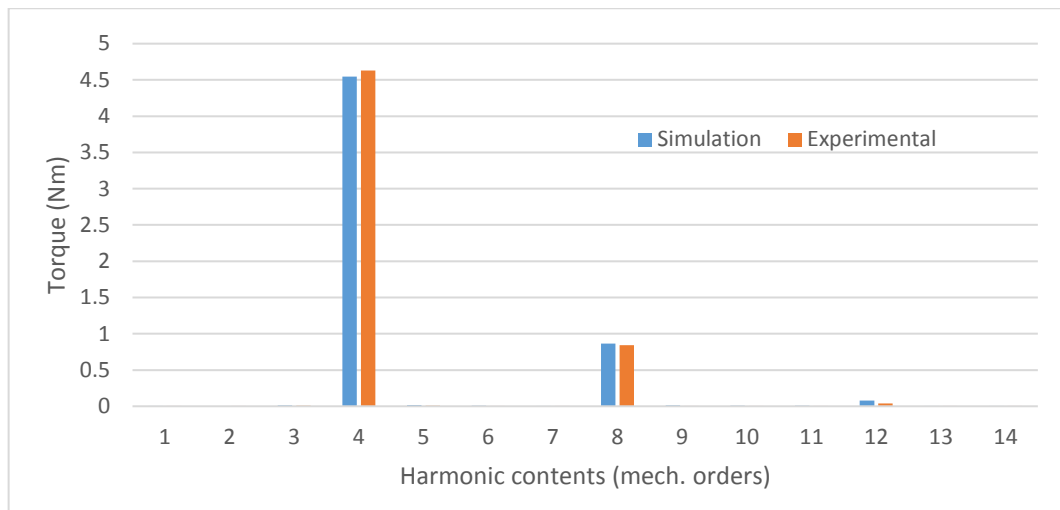


Figure 37: Harmonic content of the DC torque at rated current.

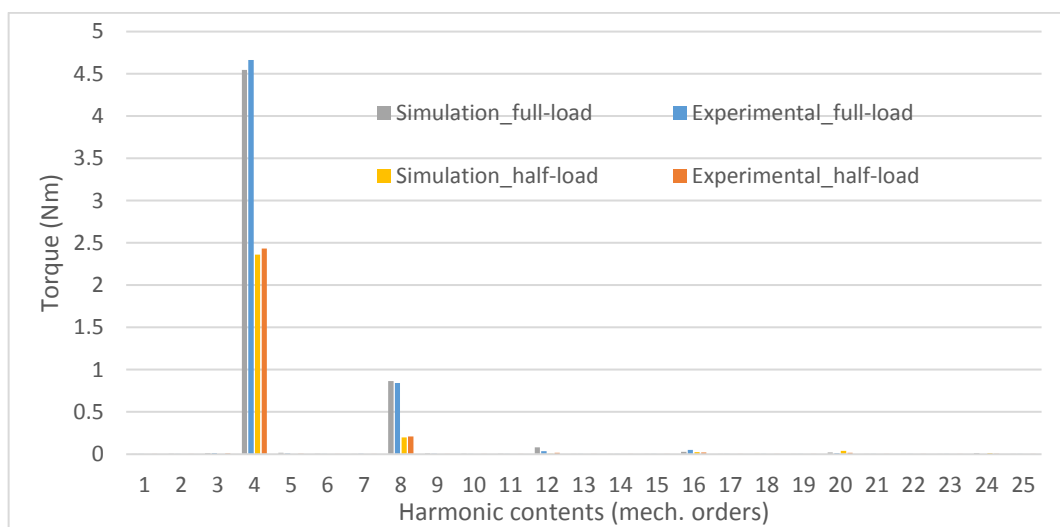


Figure 38: 3D FE and experimental DC kt comparison at full-load and half-load.

### 2.2.3.3 Torque ripple:

Electromagnetic torque is a function of both the input current and the strength of the rotor permanent magnets. The harmonic contents of the produced torque are dependent on both space harmonics due to slotting and time harmonics due to switching frequency of the motor drive. As mentioned earlier, skewing leads to reducing both cogging torque and torque ripple due to slotting. Figure 39 shows how skewing affects the mean torque, which reduces by 5.5% because in effect each rotor puck is at a different current phase advance angle. Hence, each puck produces a different torque and only one puck is producing maximum torque [53, 56-58]. Of course, the torque ripple is significantly reduced, especially 6<sup>th</sup> and 12<sup>th</sup> orders shown in Figure 40 and Figure 41. The motor is simulated with harmonically pure drive currents which resulted in the peak-peak torque ripple of 380 mNm with no-skewing and 50 mNm with 16.2 mechanical degree skewing.

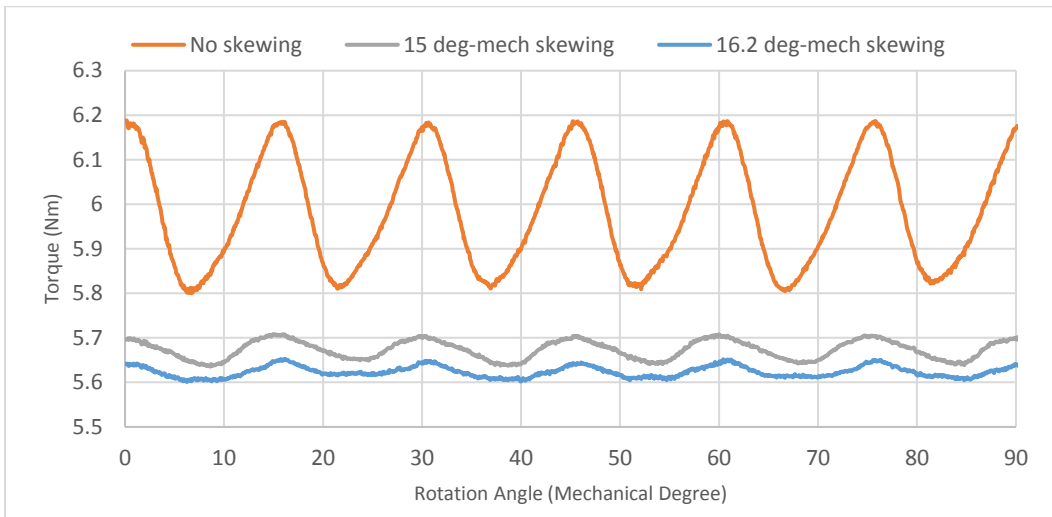


Figure 39: Motor torque capability for different skewing angle based on 2D FE Simulations

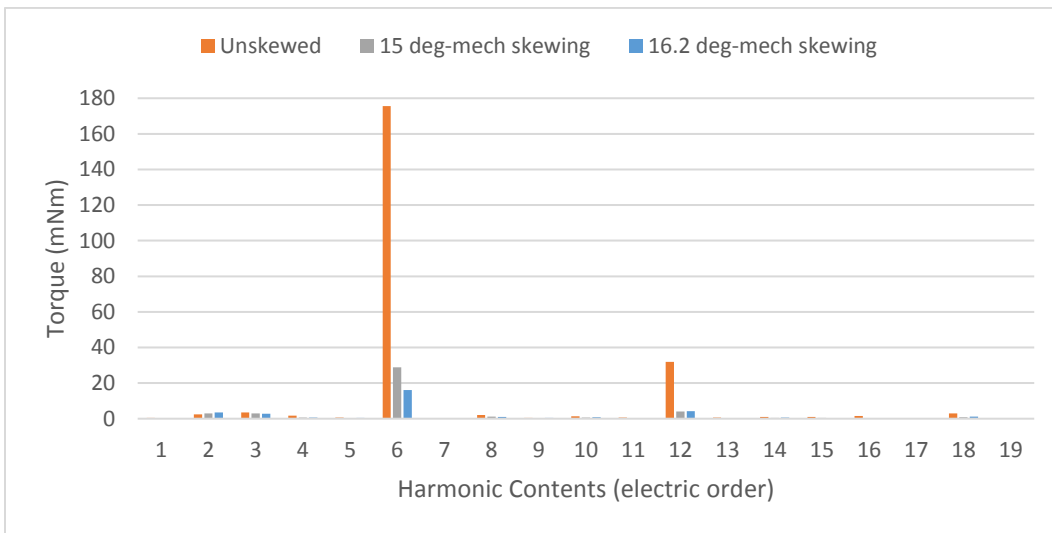


Figure 40: Motor torque harmonic content for different skewing angle based on 2D FE Simulations

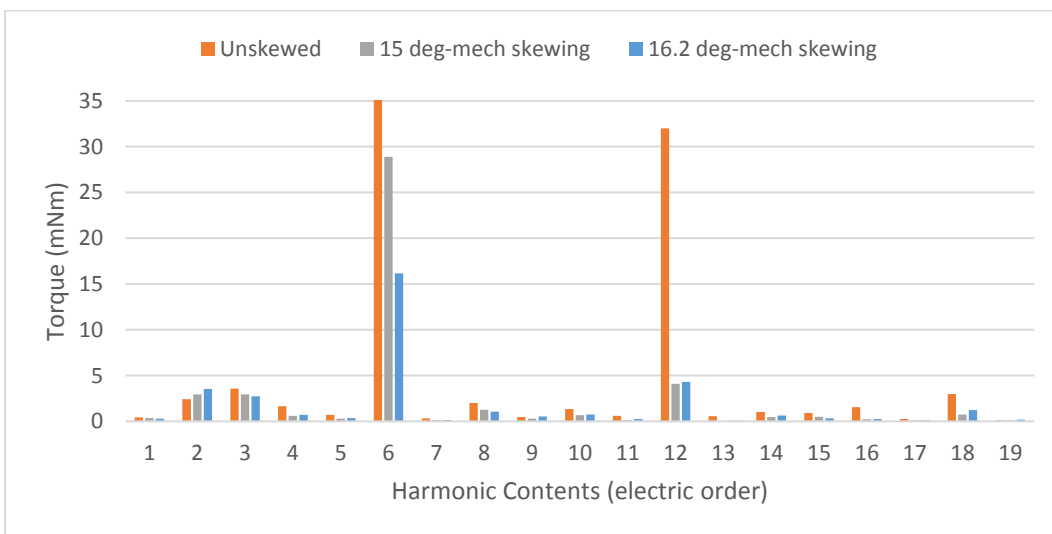


Figure 41: Motor torque harmonic content for different skewing angle based on 2D FE Simulations [Scaled]

## Chapter 2: Winding arrangements and connection types

The difference between 2D and 3D simulations is due to the short magnet pucks mentioned earlier. Additionally, there is approximately 4% difference between the simulated 3D FE average torque and measured average torque. The stator teeth are wound separately, assembled and dropped into the motor housing. This leaves a tolerance gap between the stator segments which, it is believed, leads to the torque drop (Figure 42) due to less magnetic flux travelling through the gaps. This can also lead to mismatching the torque ripple contents as shown in Figure 43. Although, the motor is driven by an ECU which might have introduced additional ripple to the torque due to time harmonics (further described in **Test rig**).

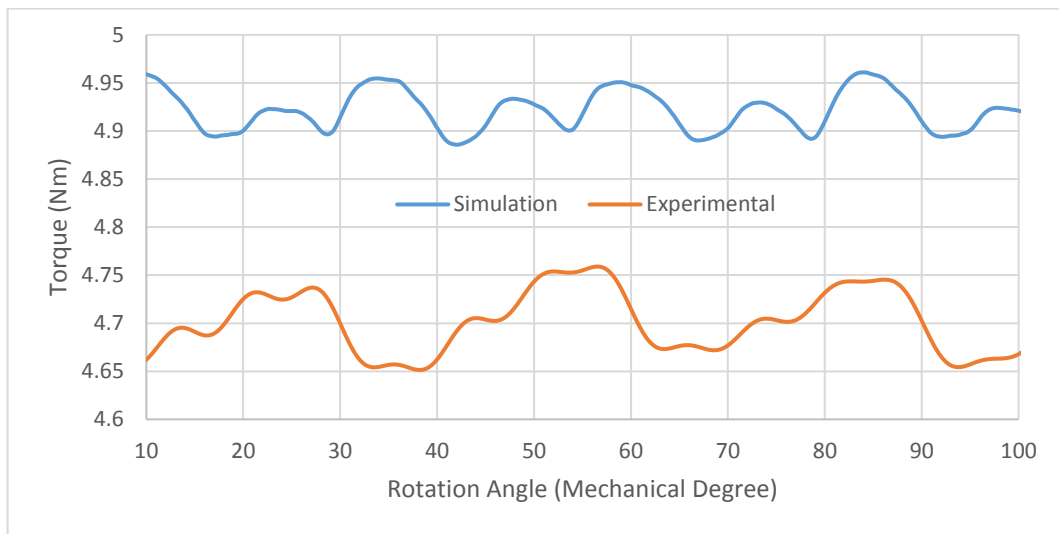


Figure 42: comparison between practical and 3D FE simulated motor torque.

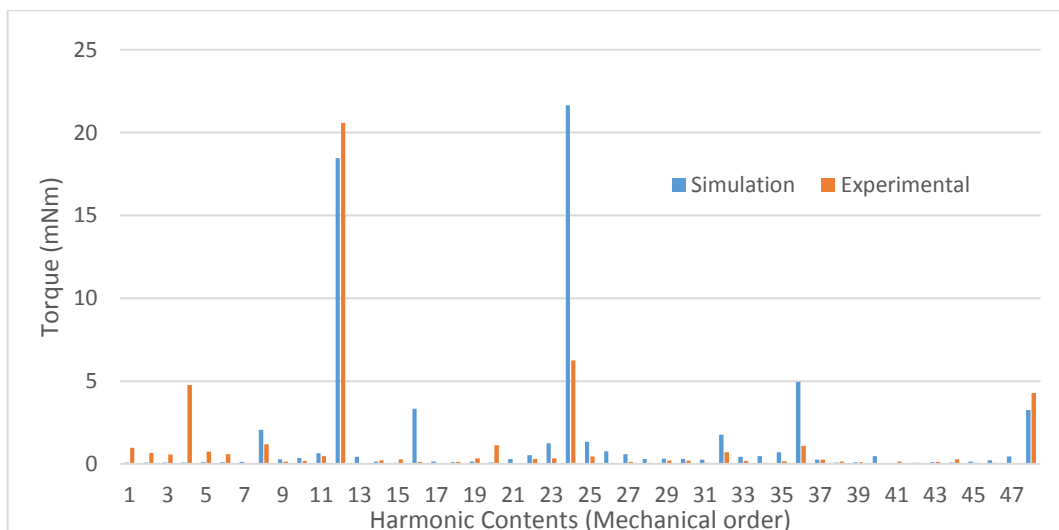


Figure 43: comparison between practical and 3D FE simulated motor torque harmonic content.

### 2.2.4 Inductance calculations:

The inductance is calculated using the “frozen permeability” method [46, 48, 60]. This process enables calculation of individual parameters, with material operating points held as if all sources were combined. The magnetic field is first calculated with both magnets and all currents present. The permeability for the FE mesh elements is stored after solving for a nonlinear calculation for each specific load current and rotor position, before introducing each source in turn to determine the flux it produces.

Investigating the d-axis and q-axis inductance components is important to evaluate the motor’s characteristics such as torque-speed capability, reluctance torque and short circuit current during fault conditions. Some FE software packages provide the frozen permeability technique, which can separate the contribution of the magnet and the current in the total flux-linkage.

After obtaining the required fluxes through the three- phase coils in the simulations, Park’s transformation is used to extract the d-axis, q-axis and magnet flux.

$$\begin{bmatrix} u_d \\ u_q \\ u_0 \end{bmatrix} = \frac{2}{3} \begin{bmatrix} \cos(\omega t) & \cos(\omega t - \frac{2\pi}{3}) & \cos(\omega t + \frac{2\pi}{3}) \\ -\sin(\omega t) & -\sin(\omega t - \frac{2\pi}{3}) & -\sin(\omega t + \frac{2\pi}{3}) \\ \frac{1}{2} & \frac{1}{2} & \frac{1}{2} \end{bmatrix} \begin{bmatrix} u_a \\ u_b \\ u_c \end{bmatrix} \quad (2-11)$$

To avoid any manual calculation errors, scripting is used to automate the process of calculating fluxes at different rotor positions, different current and angles and in different rotor segments.

#### 2.2.4.1 D-axis inductance:

To determine the d-axis inductance, the input current is arranged to give a magnetic field in direct opposition to the magnet in the negative d-axis. This demonstrates a practical situation when the motor is operated in the flux-weakening region at very high speeds. The current reduces the total flux and enables a wider speed range with a constant supply voltage. The phase current varies with the rotor position. However, it is transformed into the rotor and the current is position invariant.

#### Inductance vs rotor position

Current was inserted in the negative d-axis and kept on that axis whilst rotating the rotor. The self and mutual inductances (Figure 44 and Figure 45) versus the rotor position were obtained to investigate the slotting effect of rotor position on the d-axis inductance ripple. From Figure 44 there is clearly about 6% variation in the inductance

at rated current due to the permeance variation caused by slotting. Figure 45 shows the cross-coupling effect in which flux appears in the q – axis, even though all current is in the d axis. This results in a cross-coupling inductance, which is about 4% of the main axis inductances. The negative inductance indicates the magnetic flux path reversal with respect to the rotor position.

**Inductance vs current phase advance angle:**

In this test, the current was advanced from the q-axis towards the negative d-axis (Figure 46). The d-axis inductance was then calculated at every 5 electrical degrees to see how it varied. Note how, as the rotor moves into the negative d-axis there is a position of minimum flux. This is because the rotor bridges start to saturate, the inductance starts to decrease when approaching alignment with the negative d-axis.

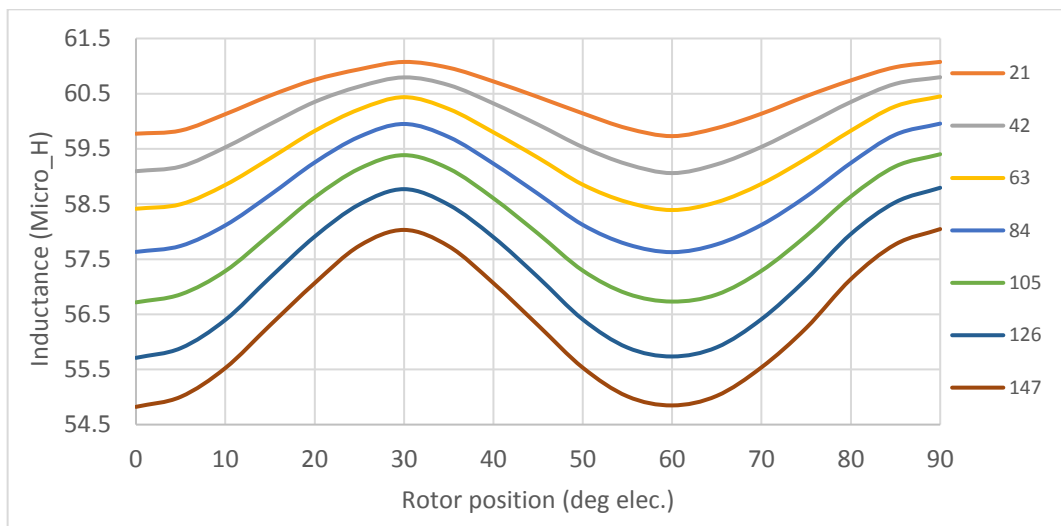


Figure 44: simulated d-axis self-inductance ( $L_{dd}$ ) vs rotor position for different input phase current ( $I_s$ ).

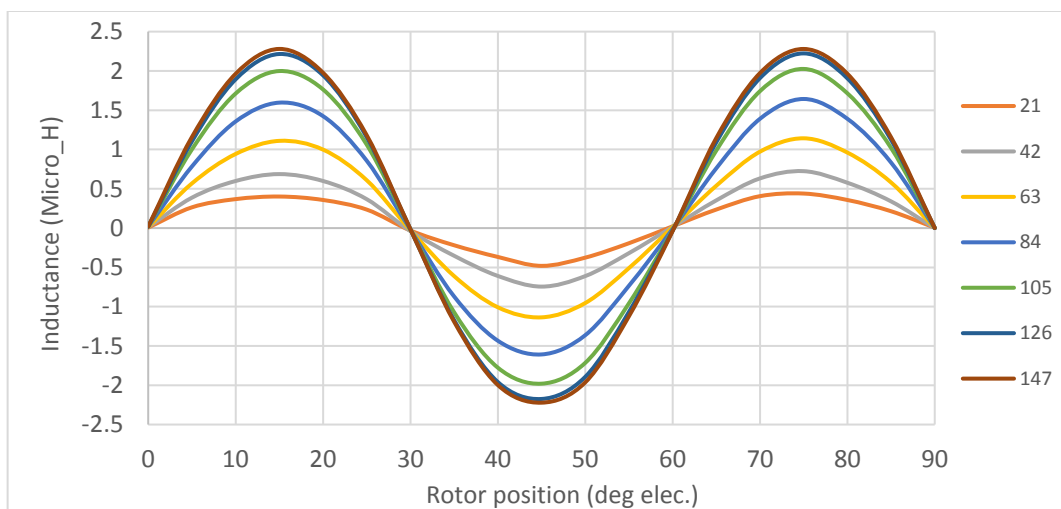


Figure 45: simulated q-axis inductance as a result of d-axis excitation ( $L_{qd}$ ) vs rotor position.

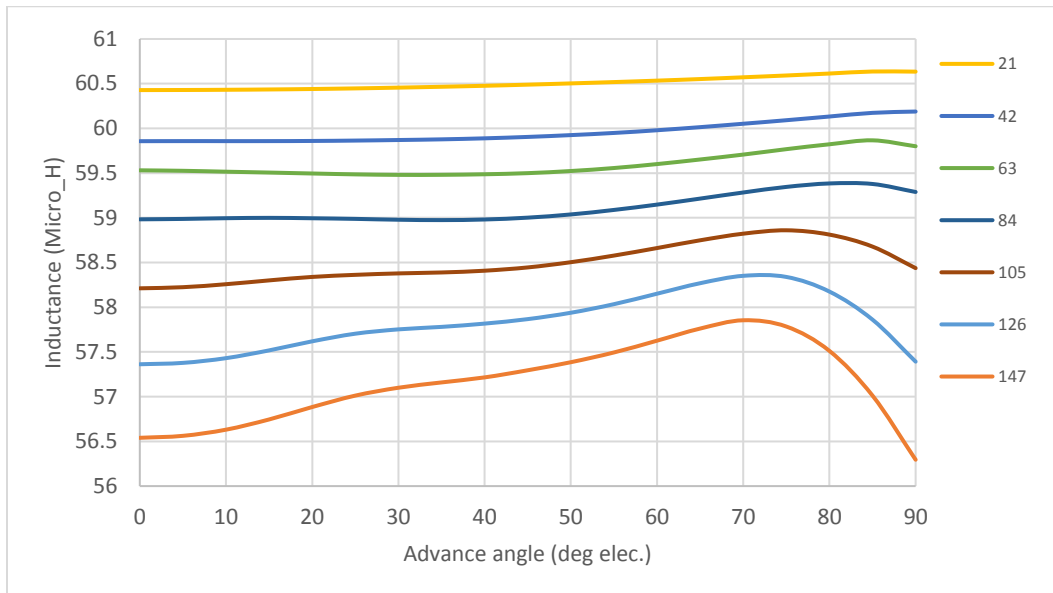


Figure 46: simulated s-axis inductance ( $L_{sd}$ ) vs current advance angle for different input phase current ( $I_s$ ).

### 2.2.4.2 Q-axis inductances:

To find the q-axis inductance, current was input in the q-axis.

#### Inductance vs rotor position

Consider first variation of q-axis inductance with rotor position as shown in Figure 47. As is to be expected, the mean value of the q-axis inductance falls with q-axis current due to saturation. As with the d-axis inductance the value varies by 1-2% according to position. This is likely to be due to the stator reluctance variation as the MMF moves from slot to tooth. Figure 48 shows the cross coupling between axes, as it illustrates the d-axis flux-linkage per unit current resulting from q axis current. The value is typically 2% of the main axes inductances and varies cyclically with rotor position. This effect is higher for high current inputs, but it is never large enough to have a major effect upon performance.

#### Inductance vs current phase advance angle:

Figure 49 shows how the q-axis inductance varies as the current angle is advanced from the q-axis towards the d-axis. Calculations were made every 5 degrees. At low currents there is almost no variation with current angle, but at high currents there is significant saturation when all the current is in the q-axis, dropping as the axis of current moves to the d-axis. The saturation occurs in the rotor bridges located between the magnet poles as in Figure 33. Figure 49 also shows that at rated current (126 amp) and when the current is on q-axis (at 0 electrical degrees), the q- axis inductance value is approximately lower by 3% compared to the inductance when the current is on d-axis (at 90 electrical degrees advance angle).

## Chapter 2: Winding arrangements and connection types

Apparently, q-axis inductance ( $L_q$ ) is bigger than d-axis inductance ( $L_d$ ) which is important in terms of rotor saliency. This produces an extra salient torque which is covered in section 2.2.3.2.

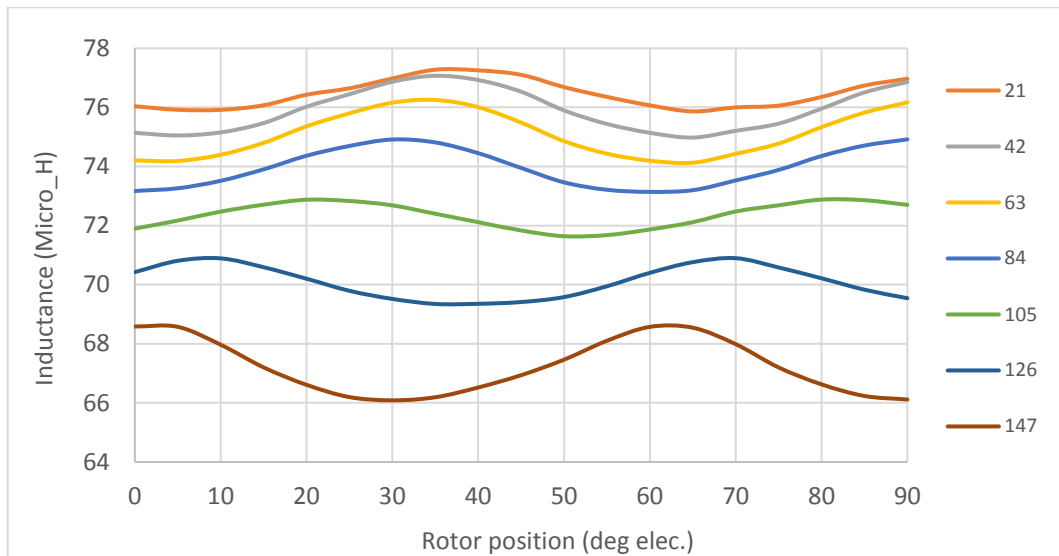


Figure 47: simulated q-axis self-inductance ( $L_{qq}$ ) vs rotor position for different input phase current ( $I_s$ )

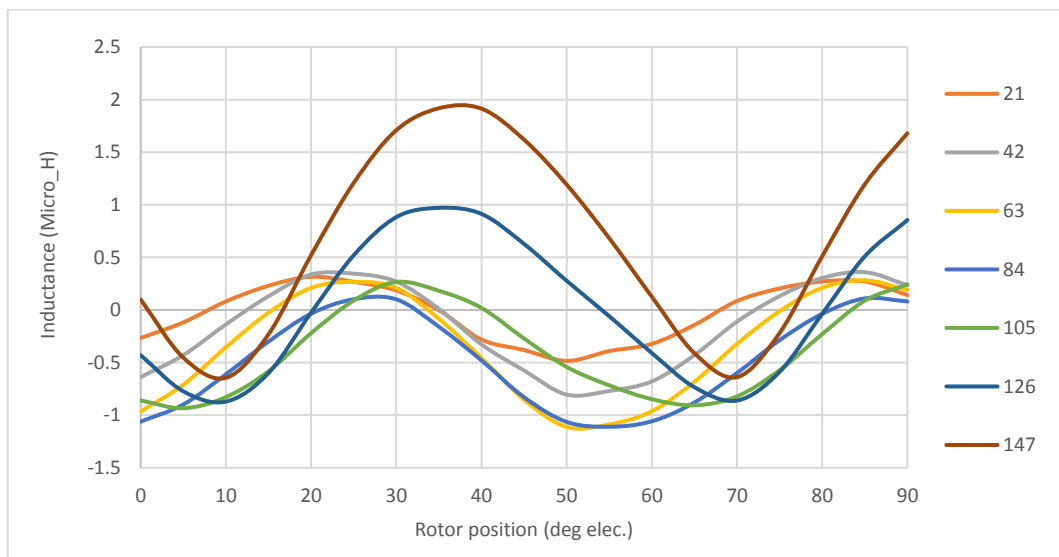


Figure 48: simulated q-axis inductance because of q-axis excitation ( $L_{\alpha q}$ ) vs rotor position for different input phase current ( $I_s$ )

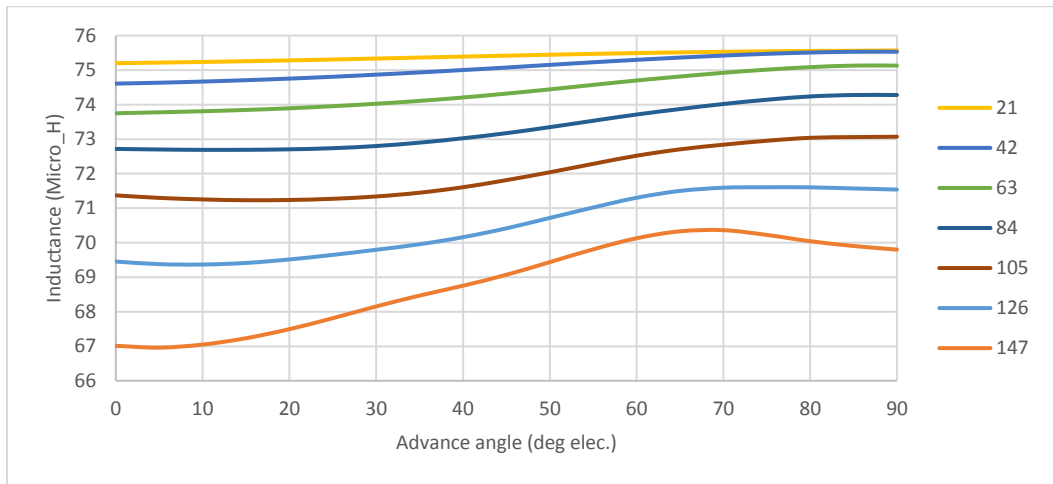


Figure 49: simulated q-axis inductance ( $L_{qq}$ ) vs current advance angle for different input phase current ( $I_s$ ).

### 2.2.4.3 Magnet Flux linkage:

To investigate the variation of magnet flux linkage with the coils, current was initially input in the negative d axis to represent what happens during flux weakening.

#### Flux-linkage vs rotor position

Here, the magnet flux linkage is directly proportional to the value of the current that is used before freezing the permeability of the core as it decreases the core saturation. The higher the d-axis current, the iron core desaturates more which leads to high magnet flux linking the stator windings as shown in Figure 50. However, the flux linking the coils in the q-axis due to d-axis fluxes is less than 0.5% (see Figure 51). This condition is only applicable at optimum advance angle, which is 90 electric degrees.

#### Flux-linkage versus current phase advance angle

In this section, the current is being advanced from the q-axis towards the negative d-axis which is a real-life example as the motor speeds up beyond the T-S curve knee point. As the current advances opposite to the magnets, the d-axis component of the flux linkage from the magnets increases (Figure 53). Additionally, the q-axis component of the magnet flux decreases towards neglecting values as the advance angle reaches 90 electric degrees (Figure 52).

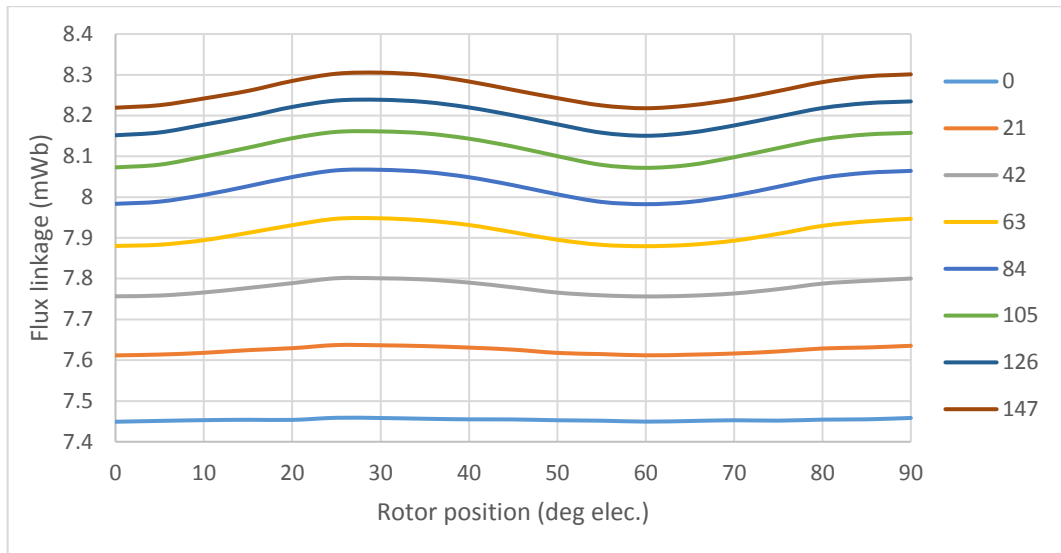


Figure 50: simulated d-axis magnet flux linkage ( $\psi_{Fd}$ ) vs rotor position for different current ( $I_s$ ).

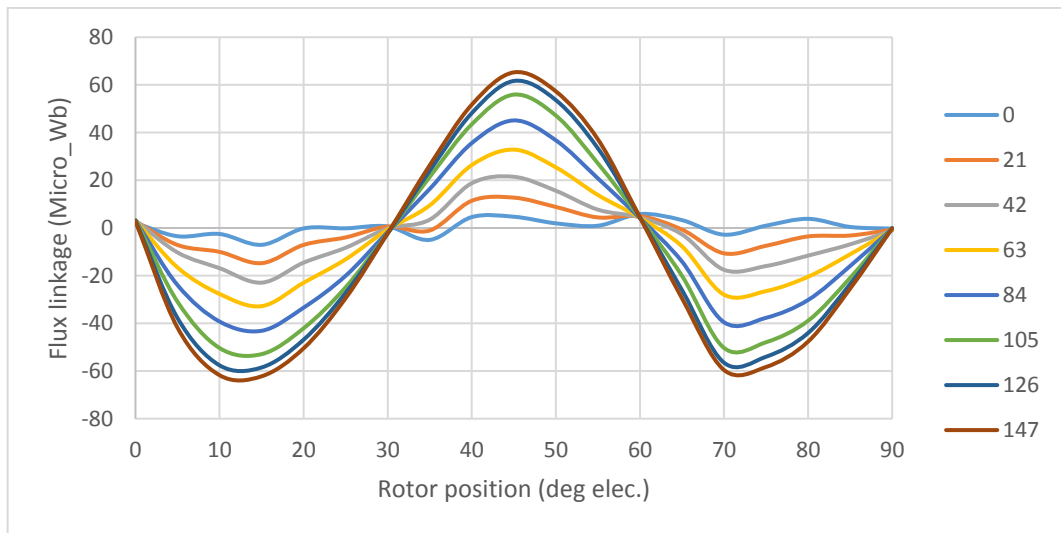


Figure 51: simulated q-axis magnet flux linkage ( $\psi_{Fq}$ ) vs rotor position for different current ( $I_s$ ).

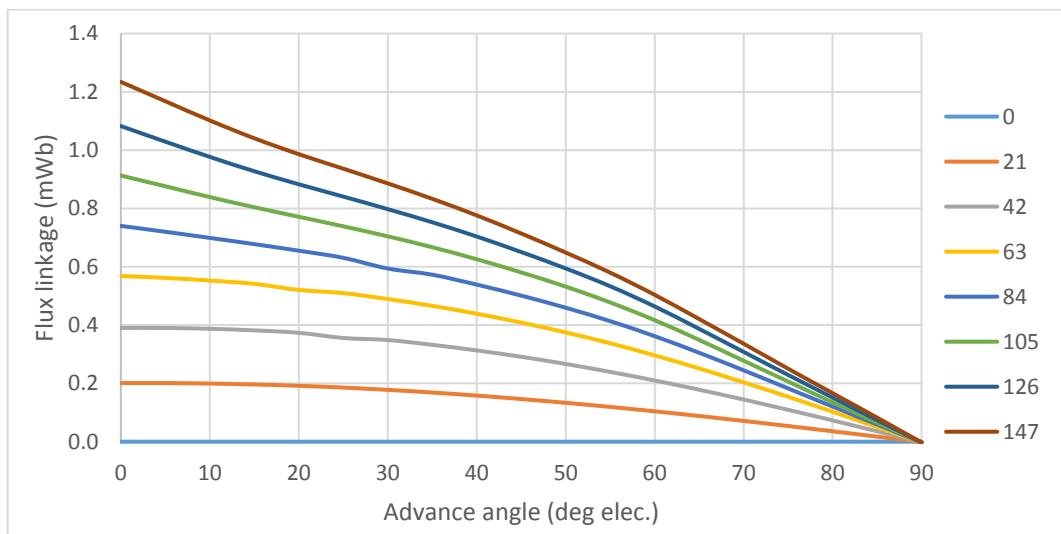


Figure 52: simulated q-axis flux linkage ( $\psi_{Fq}$ ) vs current phase advance angle for different input phase currents ( $I_s$ ).

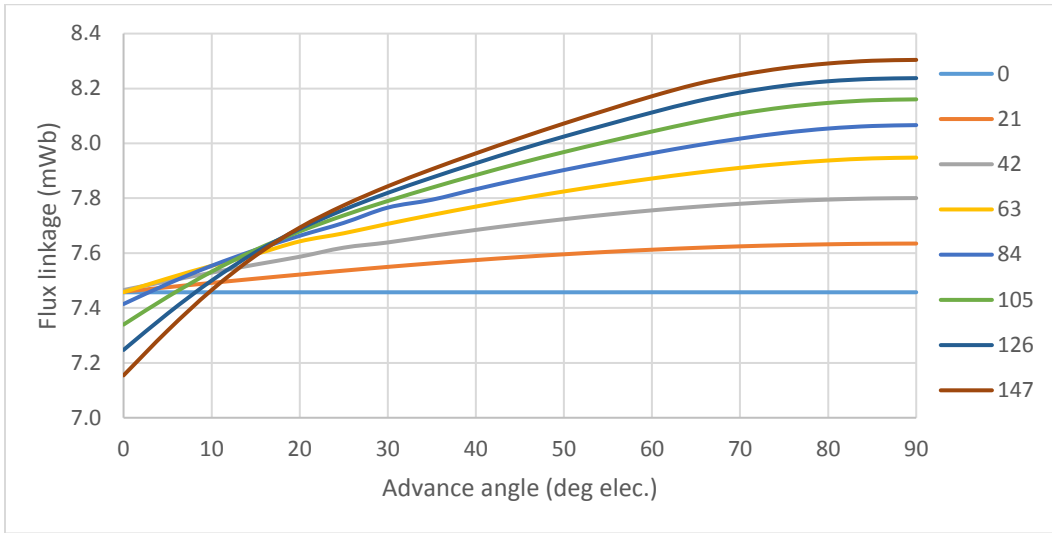


Figure 53: simulated d-axis flux linkage ( $\psi_{Fd}$ ) vs current phase advance angle for different input phase current ( $I_s$ ).

Interestingly, in Figure 53 the magnet flux linkage at loaded condition overlaps at a certain advance angle for different input currents (approximately 15 electrical degrees). The overlapping starts from half-load (63A) and higher currents when the saturation starts to occur. This might represent the maximum torque per ampere of the motor using frozen permeability based on the magnet flux linkage.

**2.2.5 Resistance calculation:**

The resistance was calculated based on the motor stack length, tooth width, wire diameter, end-winding wire length, slot-liner thickness, wire insulation thickness and the copper resistivity. To make the calculation more realistic, the proposed shape for calculating the end-winding length was assumed elliptical due to the nature of concentrated winding. With each turn, both radii of the ellipse were increased by radii of the wire and the insulator, considering that the tooth width and the distance of the end-winding from the stator stack specify both the ellipse radii.

$$R_{coil} = \rho \frac{l}{A} \quad \dots\dots (2-11)$$

Where  $R_{coil}$  is the coil resistance,  $\rho$  is the conductor resistivity,  $l$  is the active length of the conductor including all the coil turns and  $A$  is the active area of the conductor cross-section.

The active length ( $l$ ) is calculated using the equation below:

$$l = (S * 2 + p) * N \quad \dots\dots (2-12)$$

$$p \approx \pi(a + b) \left( 1 + \frac{3h}{10 + \sqrt{4 - 3h}} \right) \quad \dots\dots (2-13)$$

## Chapter 2: Winding arrangements and connection types

Where  $S$  is the stator stack length,  $N$  is coil number of turns,  $p$  is the ellipse circumference,  $a$  and  $b$  are both radii of the ellipse, and  $h = \frac{(a-b)^2}{(a+b)^2}$ . The above equation is only valid if it is assumed that the radii of the ellipse stay unchanged. To consider the exact end-winding circumference, each of the winding layers (shown in Figure 54) was calculated separately, then combined.

Table 2 summarises the calculations of the winding resistance, mass, volume and total length of the turn and turns. There are 12 coils wound around 12 teeth of the motor stator, and each phase contains 4 coils in parallel. This make the phase resistance divisible by 4 making the phase resistance approximately 11.18 mOhms.

Three identical motors were provided by ZF. The resistances were measured and shown in Table 3. For comparison purposes, the line-line resistances should be divided by two which makes the average measured resistance 10.7 mOhms that is approximately 4% different from the analytical calculations.

Total conductor Length /mm	2520.69	Average Length of Turn/mm	105.03	Total Winding Volume per coil/ mm <sup>3</sup>	2800
coil Resistance/ mohms	44.70	Average Body length of Turn/mm	72.00	All turns Conductor Area per coil / mm <sup>2</sup>	25.36
Overall Motor Length /mm	51.92	Average end turn Length /mm	33.03	Motor End-winding inductance /uH	15.47

Table 2: windings parameters calculations based on numerical equations for the baseline motor.

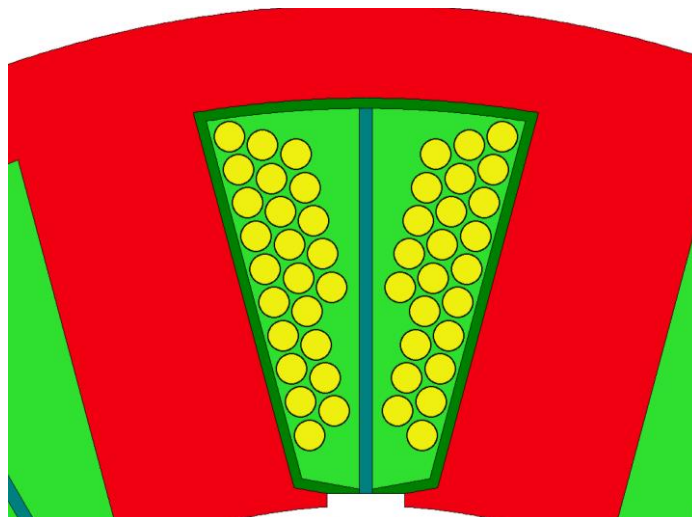


Figure 54: the winding layout of the baseline motor.

Motor #1		Motor #2		Motor #2	
Lines	Resistance (line-line) [m ohms]	Lines	Resistance (line-line) [m ohms]	Lines	Resistance (line-line) [m ohms]
AC	21.083	AC	21.479	AC	21.48
AB	21.134	AB	21.432	AB	21.476
BC	21.061	BC	21.332	BC	21.42

Table 3: measured winding resistance for three identical baseline motors.

### 2.3. Faulted condition:

Following a fault, a motor with a single drive comes to a halt and is no longer capable of producing torque. Despite that, when the rotor is rotated, the motor with shorted terminals produces a short circuit current due to rotor magnets flux linking the stator coils. The dissipated power in the coils' resistances can be seen from the driver in an EPS application as force which prevents the driver from spinning the steering. This negative force is called drag torque or damping torque.

The most credible faults that might occur within the motor drive are single FET failure and capacitor blow which leads to a three-phase balanced short if it becomes short circuit. Even when the windings are shorted the rotating magnet flux induces a back emf in each phase, the magnitude of which rises linearly with speed. The resulting current is limited by the impedance of the phase. At low speeds the winding resistance is larger than its reactance and so the current and torque rises linearly with speed. At high speeds the reactance dominates and the short-circuit current becomes independent of speed. Consequently, the winding loss is constant in this region and the drag torque is largely dependent of speed. The value of the short circuit current is mostly dependent on the back-emf, d-axis and q-axis inductances and the windings' resistances. The three-phase short circuit current and drag torque can be predicted based on the mentioned motor parameters using analytical equations. The analytical equations are derived based on the salient pole generator phasor diagram. The derivation is as follows:

$$-E = I_d X_d + I_q R \quad \dots\dots (2-14)$$

$$0 = I_q X_q + I_d R \quad \dots\dots (2-15)$$

Where  $E$  is the generated back-emf from the magnet flux,  $I_d$  direct-axis current component,  $I_q$  quadrature-axis current component,  $X_d$  direct-axis reactance,  $X_q$  quadrature-axis reactance and  $R$  is the winding resistance.

From the above equations,  $I_d$  and  $I_q$  are extracted:

$$I_d = \frac{-E}{\left(X_d + \frac{R^2}{X_q}\right)} \quad \dots\dots (2-16)$$

$$I_q = I_d \left(\frac{R}{X_q}\right) \quad \dots\dots (2-17)$$

The current components are then transformed back to the phase currents using the Park transformation shown in section 2.2.4.

To replicate the numerical analysis using finite element software, the baseline motor was simulated and investigated under faulted condition. The overall drag torque and short circuit current of the motor has been investigated by shorting all the terminals of the stator coils to each other in a symmetrical three phase short-circuit. For all the simulations, 150 steps per one electrical cycle were used as a compromise between simulation time and quality of the graphs. This gives confidence in the harmonic order calculations and the Nyquist numbers for each graph.

The overall effect is a drag torque – speed curve which is of the same form as an induction motor torque-slip curve and is illustrated in Figure 55. The difference between numerical and simulated results is due to not considering armature reactions and electromagnetic losses within the motor. Also, the saturation of the motor core is neglected which affects both the induced currents in the coils and the inductance values.

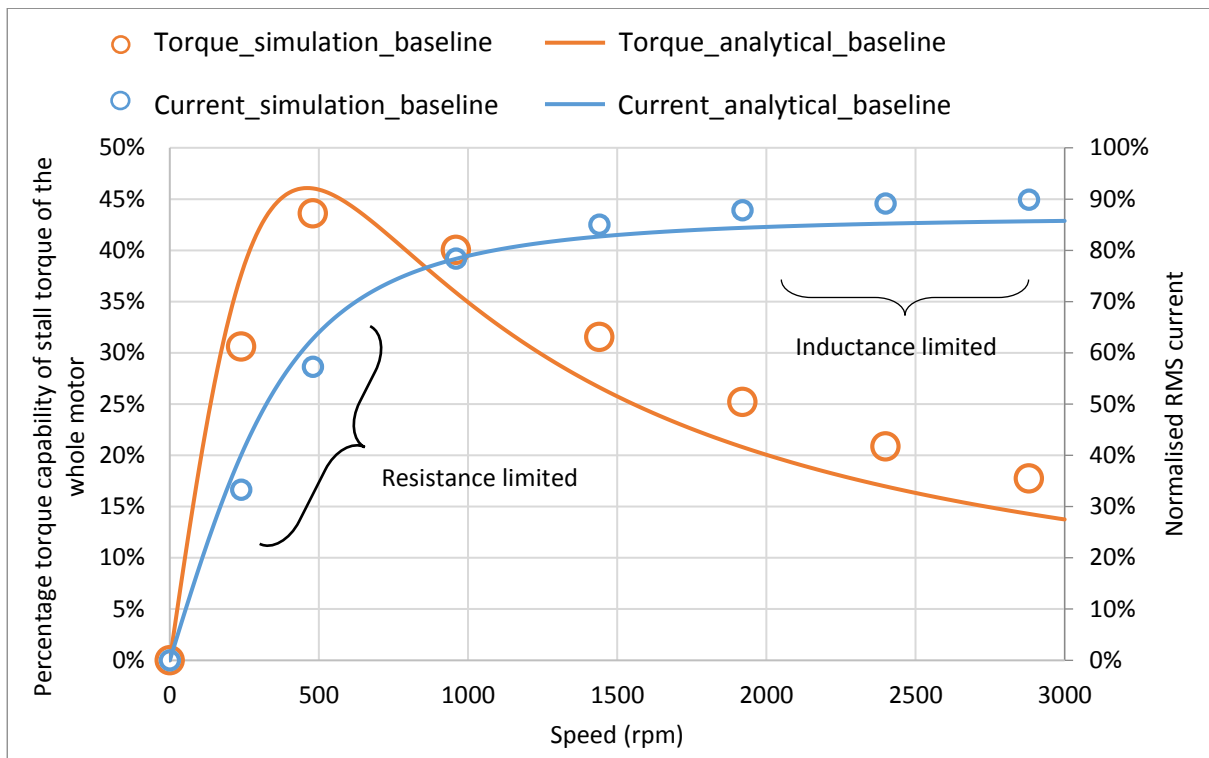


Figure 55: simulated drag torque and short circuit current against speed when all terminals of the machine is short circuited (2D FE).

If the motor’s per unit inductance is equal in magnitude to that of the per-unit back emf then the peak fault current is 1.0 per unit and it can be shown that the peak drag torque from a faulted lane is equal to one half of the rated torque [15].

The above reasoning suggests that the motor should be capable of providing 25% of the stall torque with one lane shorted and the other lane operating with rated current. However, these predictions assume that the three phases of any one lane are perfectly balanced. This does not happen with some connections and therefore needs investigation.

**2.3.1. Fault scenarios:**

To enhance the fault-tolerant capability of the baseline motor under different faults, a dual-lane system is proposed. In a dual lane system, the motor coils are divided into two lanes, each comprising six coils. Each lane then comprises a three-phase machine: it is assumed that each lane is then operated using two identical three-phase inverters from a single battery or two different battery supplies. To investigate the fault tolerant quality, different winding arrangements are proposed. As described in Chapter 1, the 12 slot 8 pole motor can be configured in different layouts in dual lane systems (alternating, half-split, and quarter-split) shown in Figure 56. Each layout impacts the

motor operation under fault conditions and one purpose of this work is to investigate the relative merits of each one. The possible motor layouts for the baseline motor are as follows:

**Interleaved (G1):**

This is termed interleaved because adjacent coils are from different lanes, as shown in Figure 56.a. it is the most complex implementation, as connections between windings of one lane must pass over those of the other lane, with twelve boundaries between lane1 and lane 2. With this winding connection, there is a manufacturing complexity and a harder physical segregation that creates safety issues as each coil end-winding from each lane should pass over the consequent coils end-winding.

**Half-half (G2):**

This category is effectively splitting the machine into two equal halves and connecting the windings accordingly as shown in Figure 56.b. It is the simplest implementation in which connections between windings do not pass over the other lane and it has fewest boundaries between lane1 and lane 2.

**Quarter (G3):**

In this scenario, the opposite consecutive three-phase coils are connected to each other as in Figure 56.c. It is a complex implementation in which connections between windings must pass over the other lane and there are four boundaries between lane1 and lane 2.

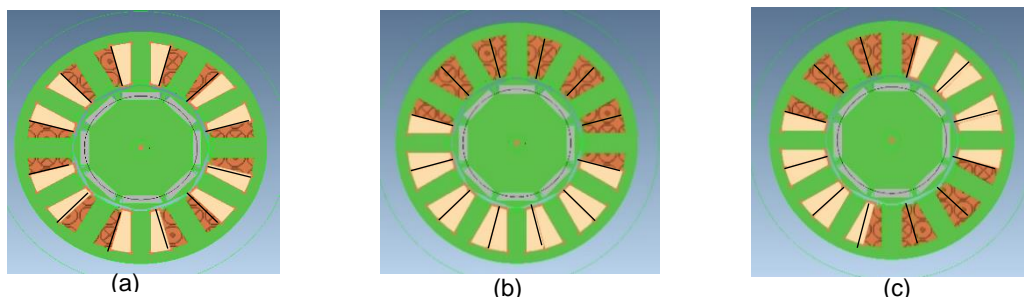


Figure 56: dual-lane different winding arrangement: (a) Interleaved (b) Half-half (c) Quarter.

The baseline motor is a three-phase star connected motor, in which each phase 4 coils in parallel (2 coils in parallel per lane for dual-lane systems). The star point is very crucial as it can be used to eliminate zero sequence and circulating currents.

The main comparative criteria between star and delta connections is the torque speed characteristics. The delta connection offers a broader speed range at a lower torque capability compared to star connection for the same power capability.

For the mentioned possible coil connections (Figure 57), the star connection is mostly preferred as it offers the star point preventing the current circulating between the phases. The circulating current might occur due to a possible fault either in the motor or the drive, or interaction between the different phases due to a fault that will be highlighted later.

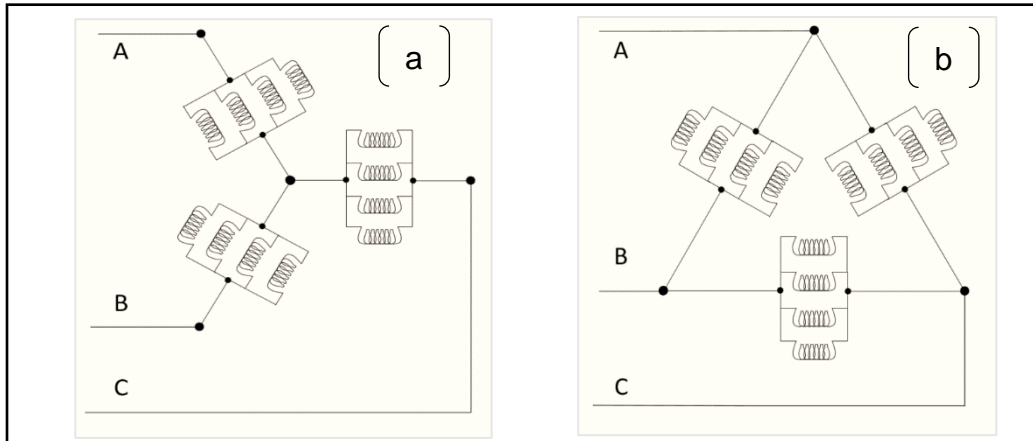


Figure 57: possible stator coils connections (a) star (b) delta.

### 2.3.2. Effect of a shorted lane upon the healthy lane back-emf:

In this section any magnetic coupling between lanes is investigated by observing the influence of the shorted lane upon the back emf of the healthy lane. In a double-layer configuration each slot contains two coil sides from different motor phases. Where the phases belong to different lanes then the transformer coupling between short-circuited and healthy lanes can be significant. The coupling varies with connection type, due to different numbers of slots carrying the coils of two lanes. The line-to-line back-emf under completely healthy conditions is used to compare with the back-emf after being affected by the faulty lane.

#### Three-phase short-circuit in one lane:

First consider the interleaved arrangement, where every slot contains the coils of both lanes (Figure 58) which is expected to have maximum coupling between lanes. Note, however, the interaction between the coils is symmetrical, as all phases are equally affected.

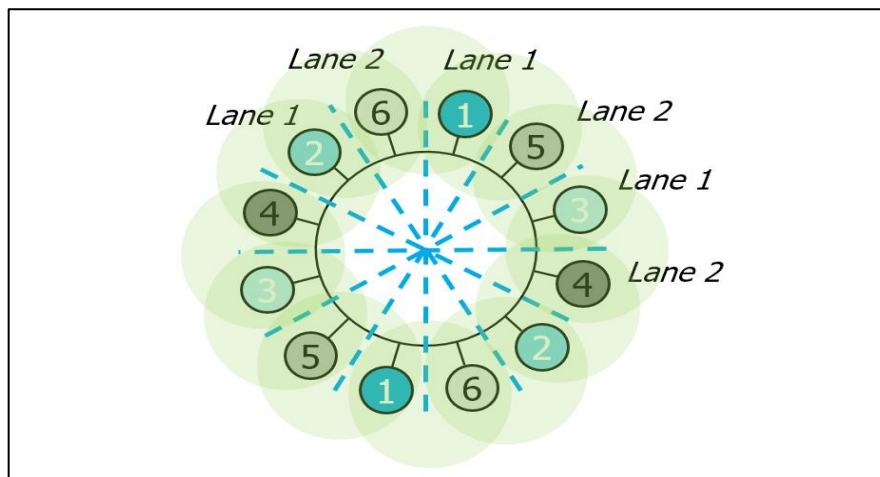


Figure 58: Interaction between motor lanes for Interleaved arrangement (green circles illustrate interactions).

Figure 59 graphically compares the back-emfs, with the dotted lines representing the back-emf when both lanes are open-circuit as a control. Solid lines are used to show the back emf in the healthy lane when the other one is shorted.

All the phases are affected symmetrically and there is a balanced reduction in the back-emf (approximately 16%) of all the healthy lane coils. This means that, in addition to the drag torque imposed by the faulty lane, the healthy lane can generate less torque due to the coupling between lanes. Figure 60 and Figure 61 give the harmonic breakdown of the back-emf waveforms. This illustrates how the drag torque ripple content is the lowest due to the symmetrical nature of the coupling between lanes. The green circles in (Figure 58) show the interaction between the consequent coils of the different lanes. This means that all the coils of lane 1 are equally affected by lane 2.

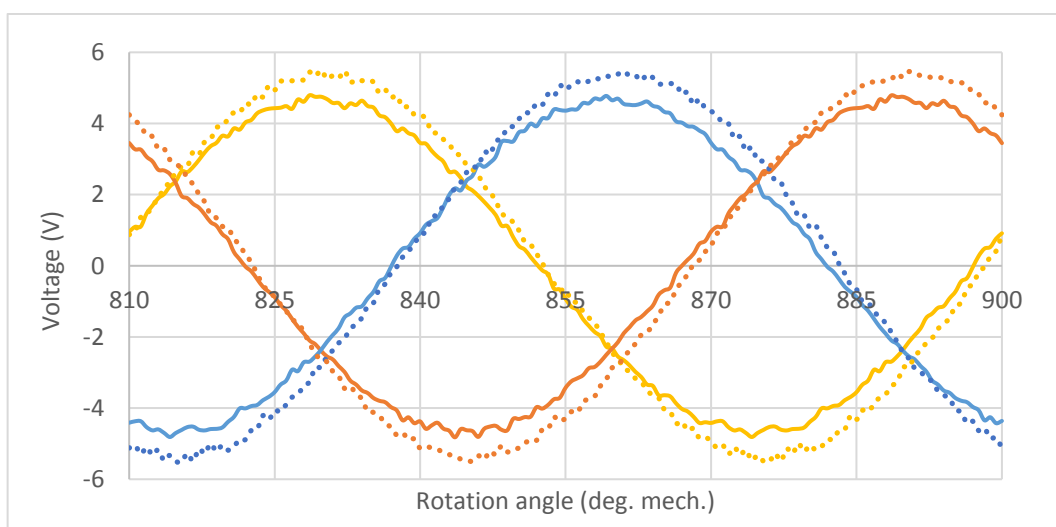


Figure 59: 2D FE back-emf comparison between faulted and healthy when a lane is short circuited (Interleaved).

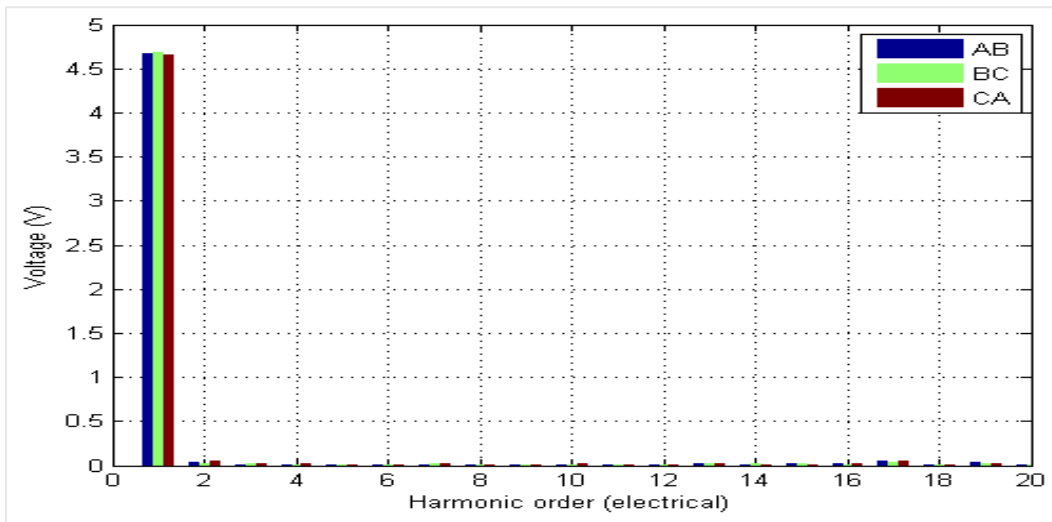


Figure 60: Harmonic components for the back-emf of the healthy lane affected by the faulty lane (Interleaved).

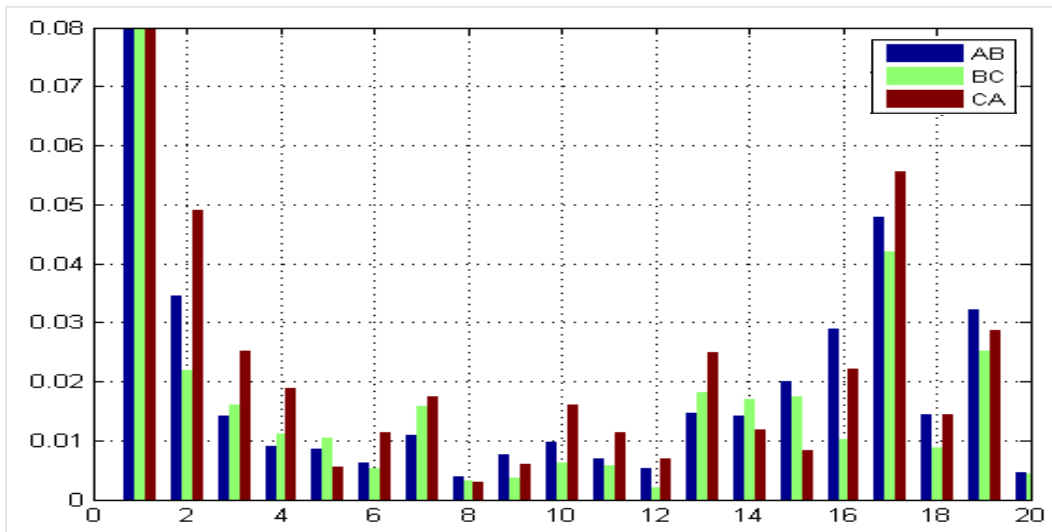


Figure 61: Harmonic components for back-emf of the healthy lane affected by the faulty lane (Interleaved) [scaled].

Consider now the half-half arrangement illustrated in Figure 62. Unlike the interleaved arrangement, the half-half arrangement has only two points of interaction, affecting two coils from each of the healthy and faulted lanes. Because of transformer coupling between the lanes at the interaction points (coil 2 and coil 3 in Figure 62), the line-to-line back-emf between those two coils is affected, but all the remaining are unaltered. This indicates that the effect upon the healthy lane is less than in the interleaved arrangement. On the other hand, there is now asymmetry between phases, which can lead to higher torque ripple. As shown in Figure 63, there is a considerable drop in the back-emf of one line voltage, of approximately 16% compared to normal conditions, whilst the other two phases remain almost unaffected. A third harmonic component results from the asymmetry due to the points of interaction and is evident in the

harmonic decomposition in Figure 63 and Figure 64. This might lead to circulating currents and significant torque ripple during loaded conditions.

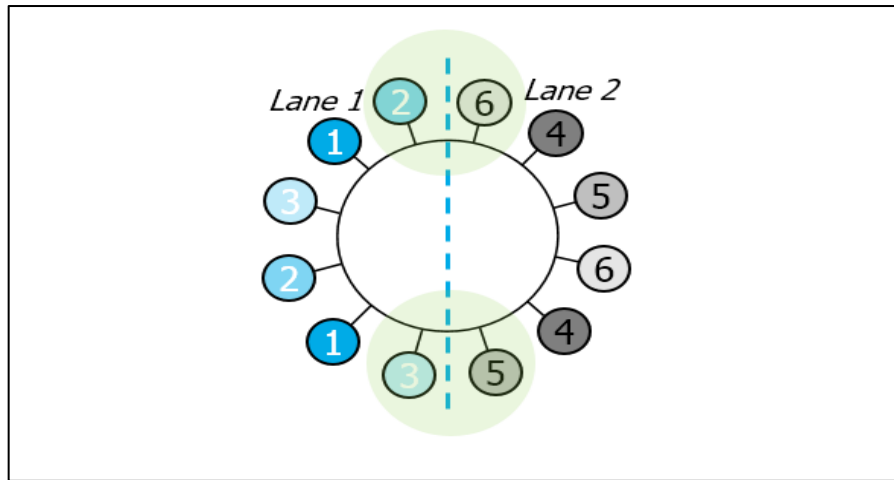


Figure 62: Interaction between motor lanes for Half-half arrangement.

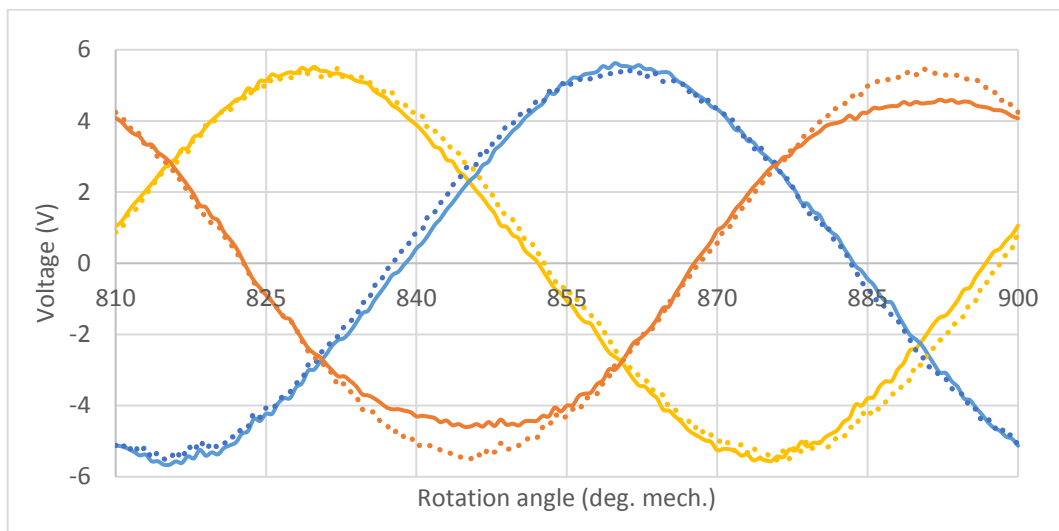


Figure 63: 2D FE back-emf comparison for faulted and healthy at no-load when a lane is short circuited (Half-half).

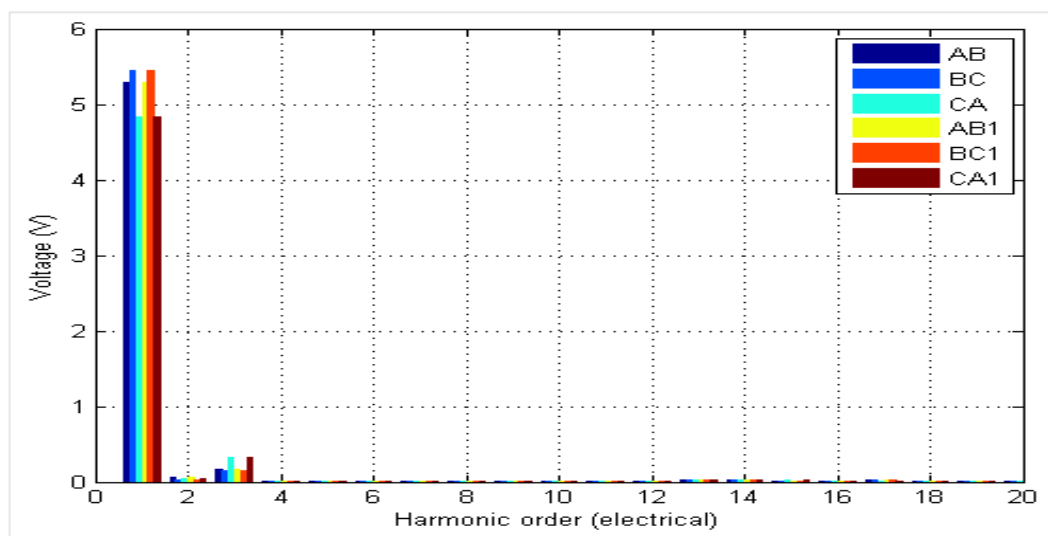


Figure 64: Harmonic components for the back-emf of the healthy lane affected by the faulty lane (Half-half).

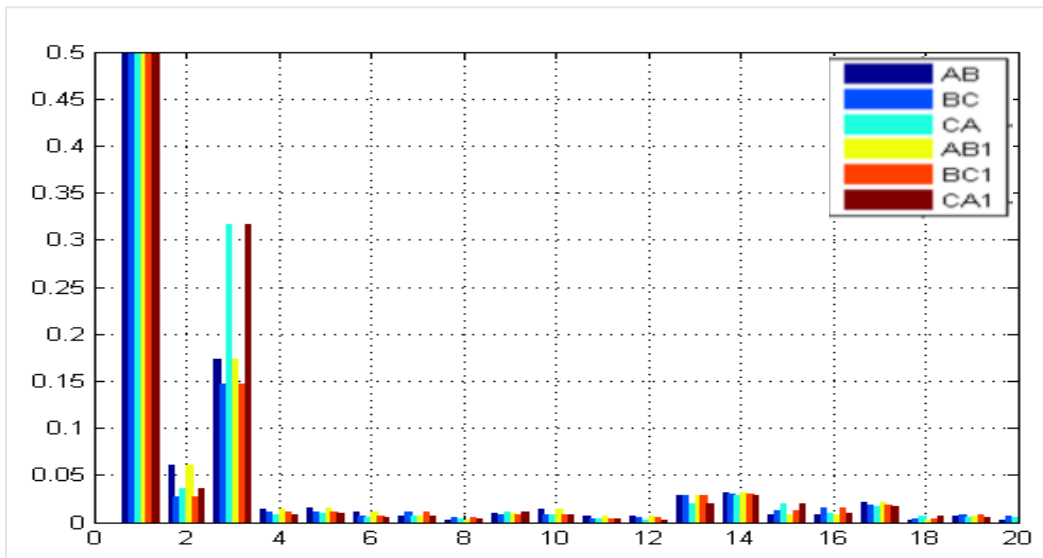


Figure 65: Harmonic components for the back-emf of the healthy lane affected by the faulty lane (Half-half) [scaled].

Finally, consider the Quarter arrangement. This has four points of interaction between the healthy and faulty lanes (Figure 66). This creates the highest asymmetry in the back-emf in the healthy lane. The third harmonic is significantly higher than in the half-half arrangement, due to having four points of interaction between the healthy and the faulty lane. Figure 67 to Figure 69 show approximately 25% drop in the back emf of one line voltage, whilst the others are not affected.

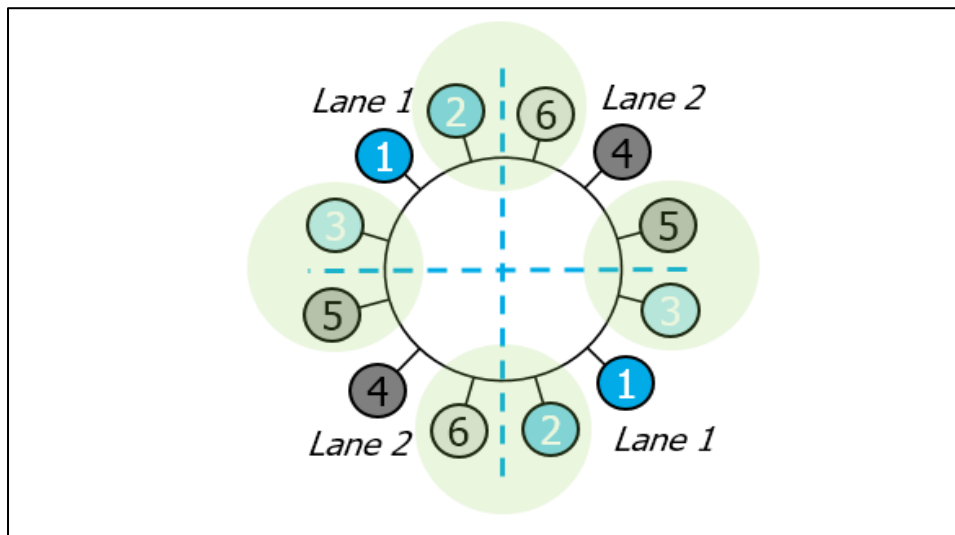


Figure 66: Interaction between motor lanes for Quarter arrangement.

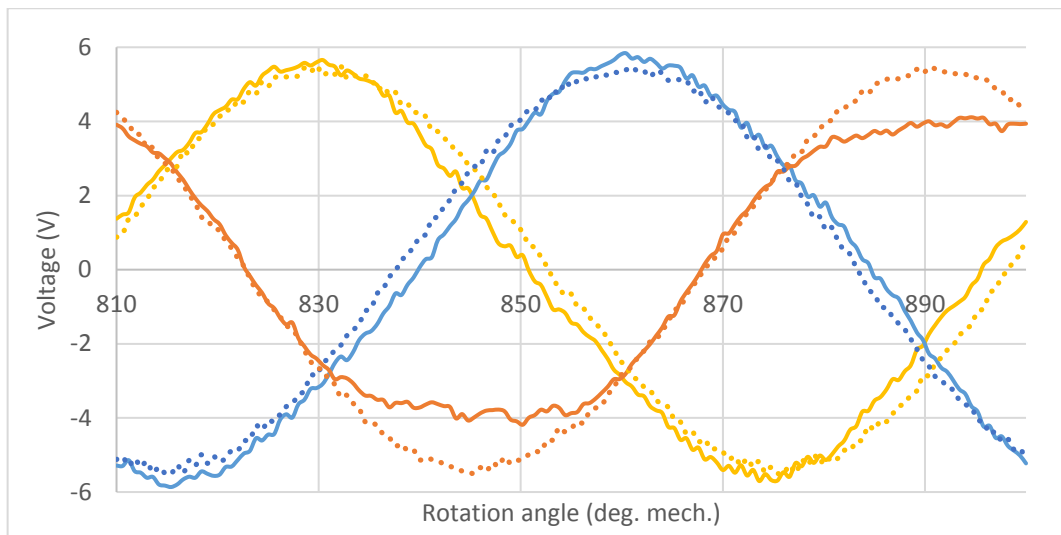


Figure 67: 2D FE back-emf comparison for faulted and healthy at no-load when a lane is short circuited (Quarter).

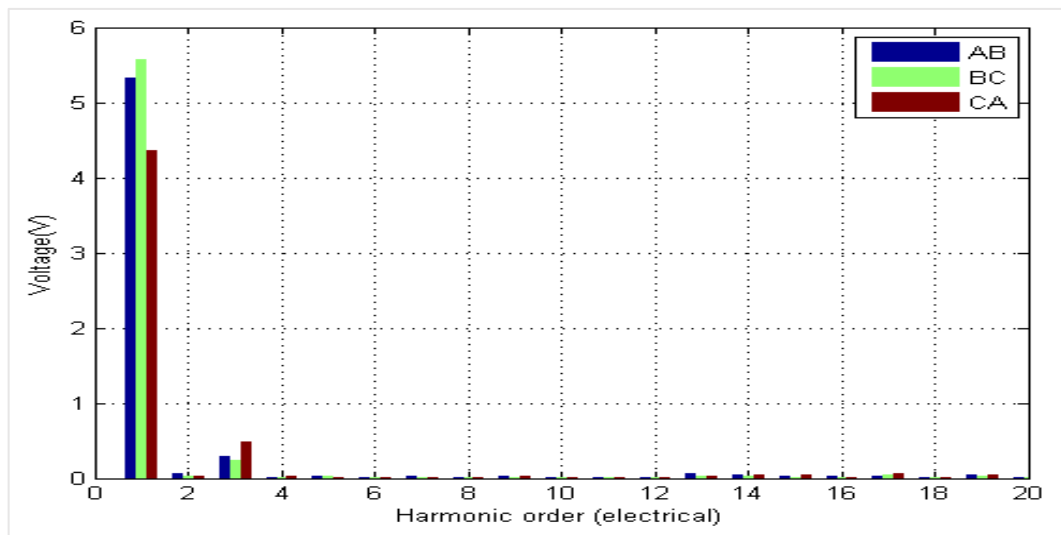


Figure 68: Harmonic components for the back-emf of the healthy lane affected by the faulty lane (Quarter).

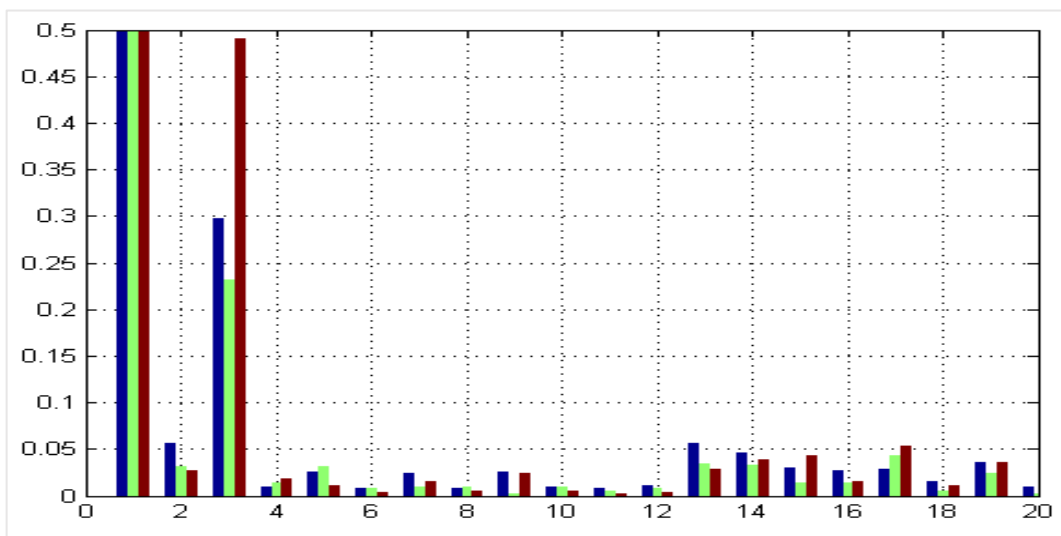


Figure 69: Harmonic components for the back-emf of the healthy lane affected by the faulty lane (Quarter) [scaled].

## Chapter 2: Winding arrangements and connection types

Based on 2D FE simulations and from a lane short analogy with one lane being symmetrically short circuited across all terminals and the other lane being passive (open-circuit), it is observed that the Half-Split arrangement is a compromise between Alternating and Quarter-Split arrangements (as shown in Table 4).

	Interleaved	Half-Half	Quarter
Drag torque Ripple	Green	Yellow	Red
Back-emf unbalance (healthy lane)	Green	Yellow	Red
S.C. current unbalance	Green	Yellow	Red
High S.C. current	Red	Green	Yellow
Zero Sequence	Green	Green	Green
Back-emf Reduction (healthy lane)	Red	Green	Yellow

Table 4: comparison between different arrangements when lane1 is shorted and lane2 is inactive.

To summarise, the half-half arrangement is the best compromise between all those investigated because it has the lowest points of interaction, the lowest back-emf reduction and medium asymmetry. The above comparison directly affects the drag torque ripple. Figure 70 shows the drag torque comparison between different connection types. This is no-load drag torque, in which one lane is short circuited across its terminals and the other is inactive.

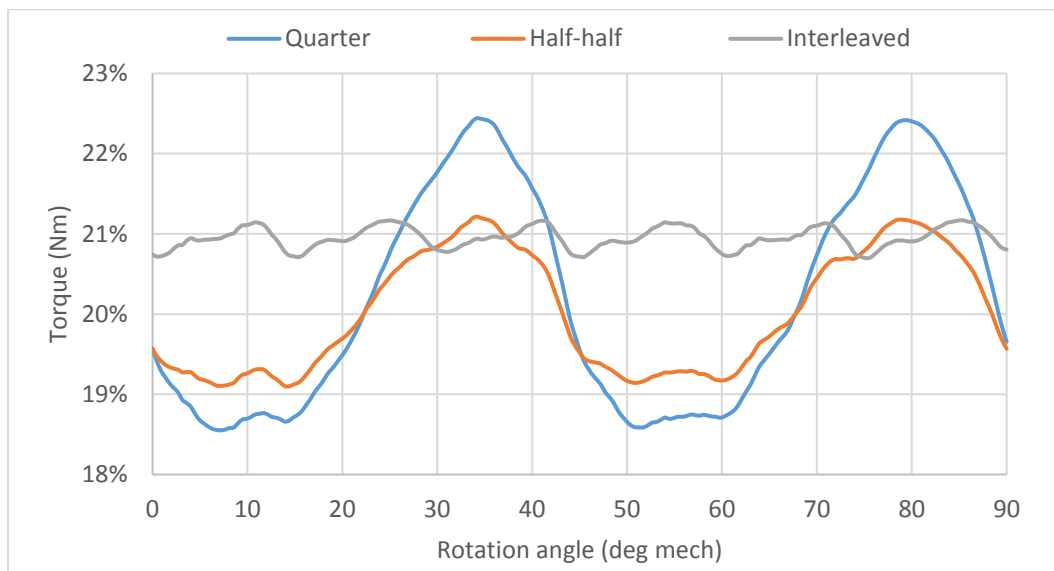


Figure 70: Drag torque for different arrangements when one lane short circuited and the other inactive.

To validate the work the simulation has been duplicated with measurement, in which one lane is short circuited. Figure 71 shows the comparison between simulated and practical results (the solid lines are practically measured values). The phase imbalance is clearly present in the measurements, with good comparisons at all positions and in all phases.

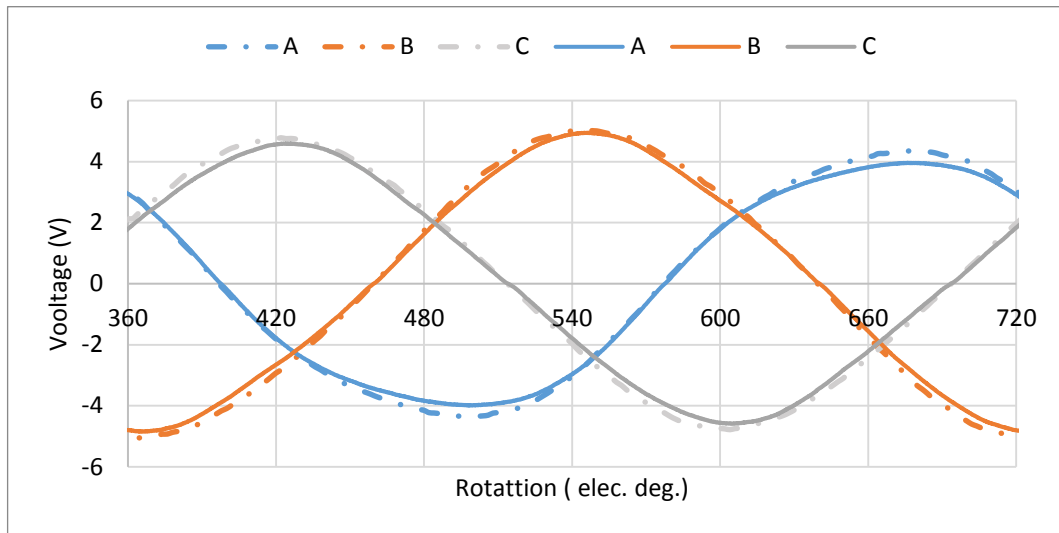


Figure 71: Practical and simulation comparison of the back-emf during one lane short-circuited (half-half connection).

It can be observed from the above graph that the Half-half offers the lowest drag torque and medium ripple. Based on the reached conclusion, one of the baseline motors was reconnected as Half-half arrangements for comparison purposes and to validate the simulation results.

The experimental results are compared to the 2D FE results after numerically calibrating the end-winding inductance and the nature of having shorter magnets per puck. The end-winding inductance is largely affecting the amplitude of the short-circuit current which shorter magnets in the rotor pucks affects the back-emf.

The drag torque which results from shorting one lane and leaving the other lane inactive, matched the simulation predictions (Figure 72). Likewise, the short circuit current in all the three lanes matches the simulation results (Figure 73). There is an unbalance between the phase current that mainly due to the transformer coupling between the adjacent coils. This will be further explained in the next section.

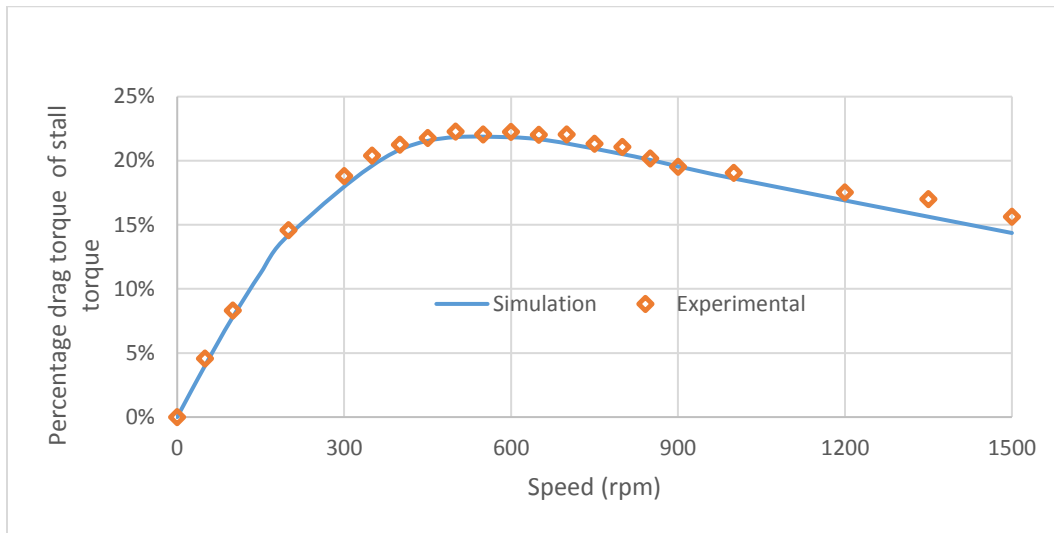


Figure 72: No-load drag torque comparison for Half-half arrangement.

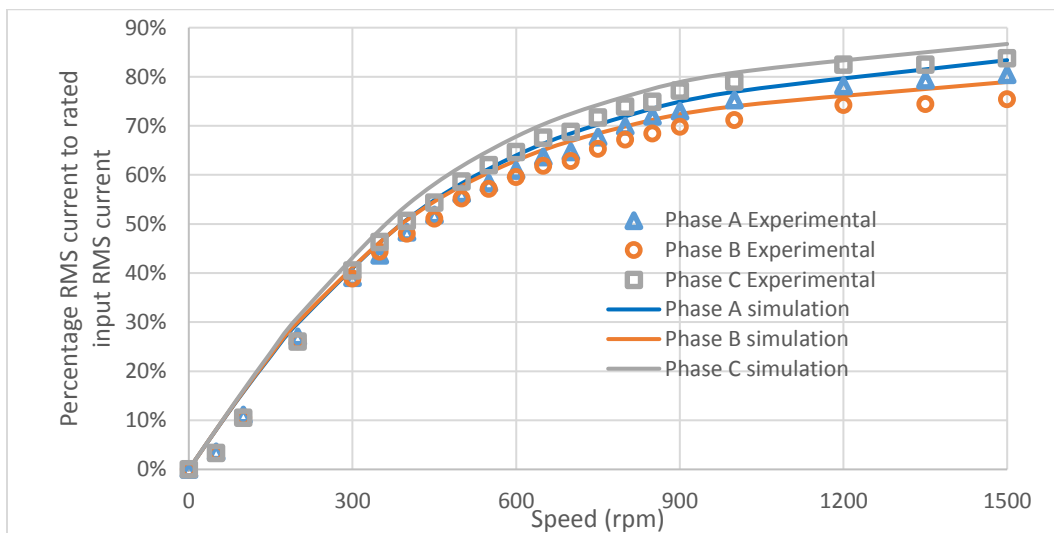


Figure 73: No-load short circuit current comparison for Half-Split arrangement

### 2.3.3. Torque, torque ripple and short circuit current:

In this section, the overall motor capability under fault conditions is investigated, taking the effect of different winding connections into account. As highlighted in the previous section, the half-half arrangement provides the highest capability compared to the Interleaved and quarter arrangements. This is due to the connection layout as there are only two points of interaction between the two separate lanes.

#### Three-phase short-circuit in one lane under loaded condition:

In this section, it is assumed that one lane is fully operated under healthy operation condition and the other is undergoing a three-phase balanced short circuit current. The input to the healthy lane is assumed to be a sinusoidal input current.

## Chapter 2: Winding arrangements and connection types

Based on 2D FE simulation results, Figure 74 shows that the worst case drag torque occurs at approximately 600 rpm at the motor is only capable of providing 26%, 25% and 21% of its normal stall torque for Half-half, Quarter and Interleaved arrangements respectively. Despite having the highest drag torque among all the winding arrangements, Interleaved can provide the smoothest torque as the all the coils are affecting their neighbours symmetrically (Figure 75 and Figure 76).

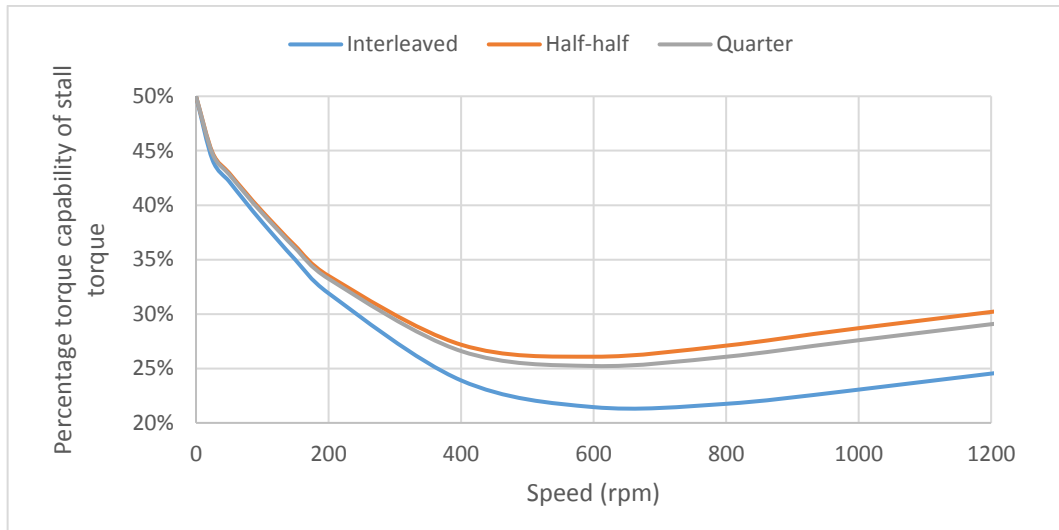


Figure 74: Motor torque capability under three-phase fault condition in one lane for different winding connections.

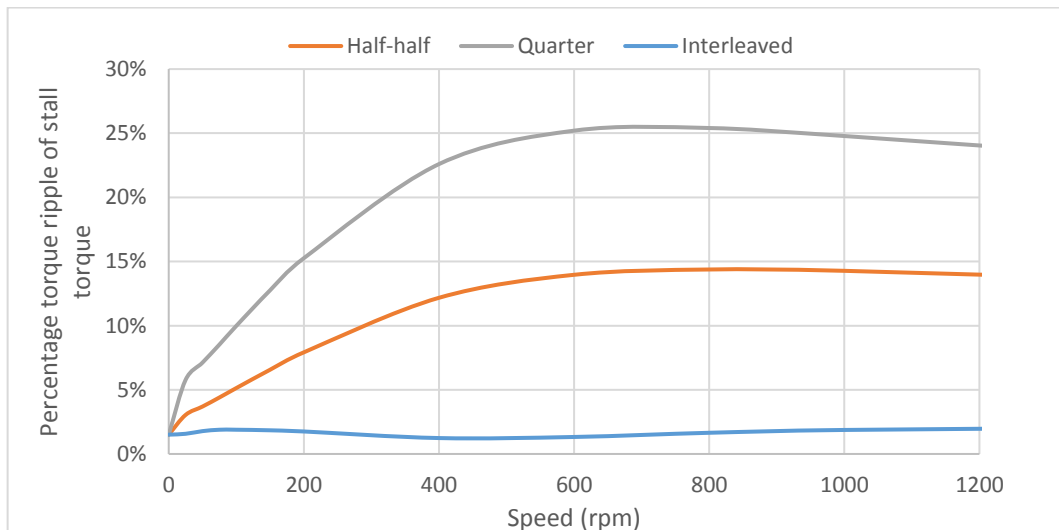


Figure 75: percentage torque ripple for different motor connection type under three-phase fault in one lane.

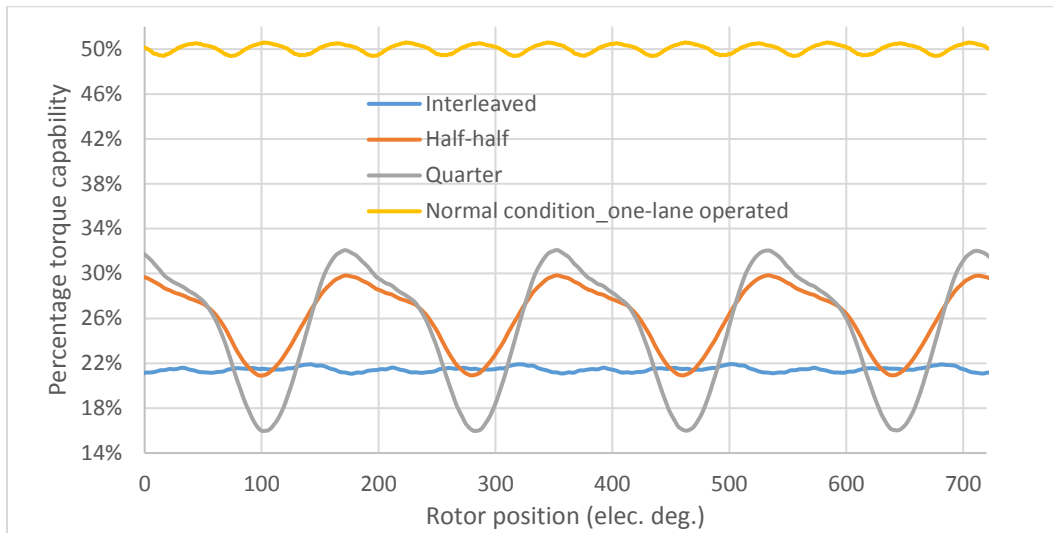


Figure 76: torque ripple amplitude for worst case drag torque for different winding connections at 600 rpm.

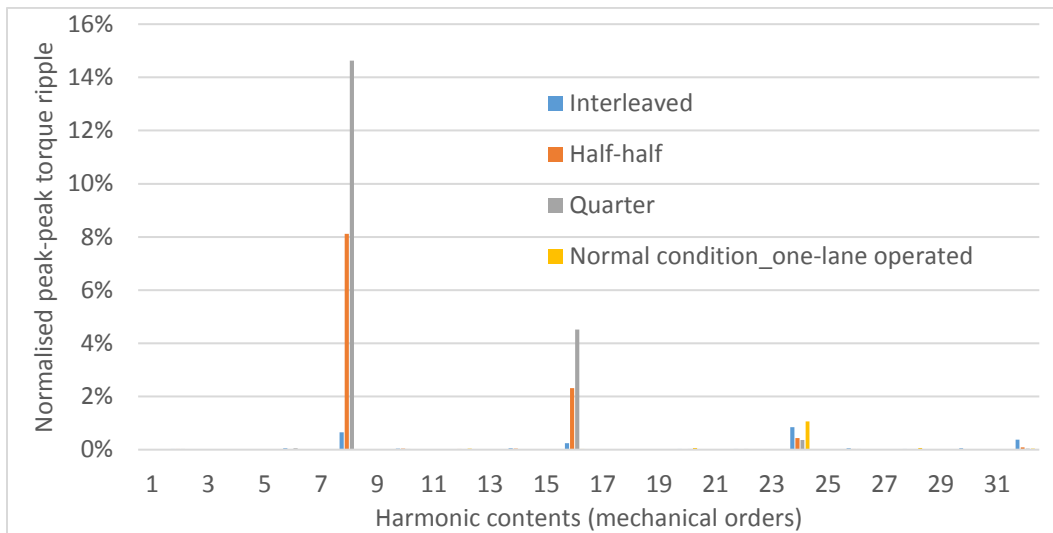


Figure 77: harmonic contents for worst case drag torque for different winding connections at 600 rpm.

From Figure 77, 8<sup>th</sup> and 16<sup>th</sup> orders from the harmonic contents of the torque ripple is due to the nature of the unbalanced current that would be discussed later. It also shows that the Interleaved have approximately 24<sup>th</sup> order harmonics to the normal condition as all the coils are affected equally.

Interestingly, the different winding connections result in different induced short-circuit phase currents in the shorted lane. This is due to variation of the transformer coupling between the coils that share the same slot. All the shorted coils of the faulted lane see different fluxes due to asymmetrical interaction between the coils, especially at the points of interaction for Half-half and Quarter arrangements. Figure 79, to Figure 81 show that the half-half arrangement has the lowest short-circuit current, which means less generated heat in the short-circuit path which includes motor and external paths.

However, the interleaved generated the highest loss as all the coils are affected by their neighbour. The losses are also reflected in the drag torque value (Figure 74).

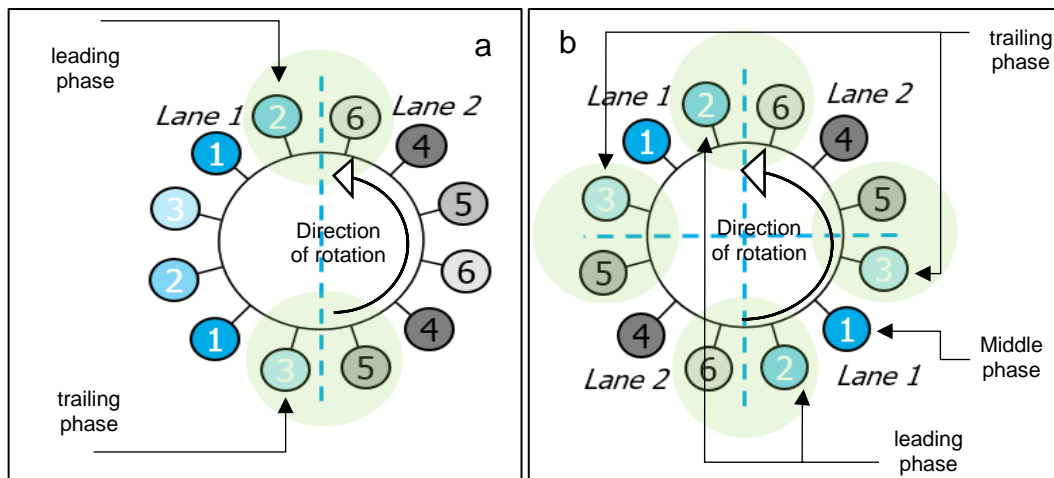


Figure 78: Half-half and quarter arrangement representation using coils' numbers and interaction points.

Based on the direction of the rotation, the leading and trailing phases swap places. As shown in Figure 78, if the direction of rotation is anti-clockwise, coil 2 becomes the leading phase while coil 3 becomes trailing phase. However, in Half-half connection as in Figure 78.a, the parallel coils from the phase 2 do not carry the same current amplitude due the integration for the coils with each other. Lastly, the middle phase (coil 1) always carry the lowest current as it has the lowest interaction with other lane.

Additionally, the short-circuit current under loaded condition is slightly lower than no-load condition due to the active interaction between the faulted and upfaulted phases which reduce the flux linking the coils.

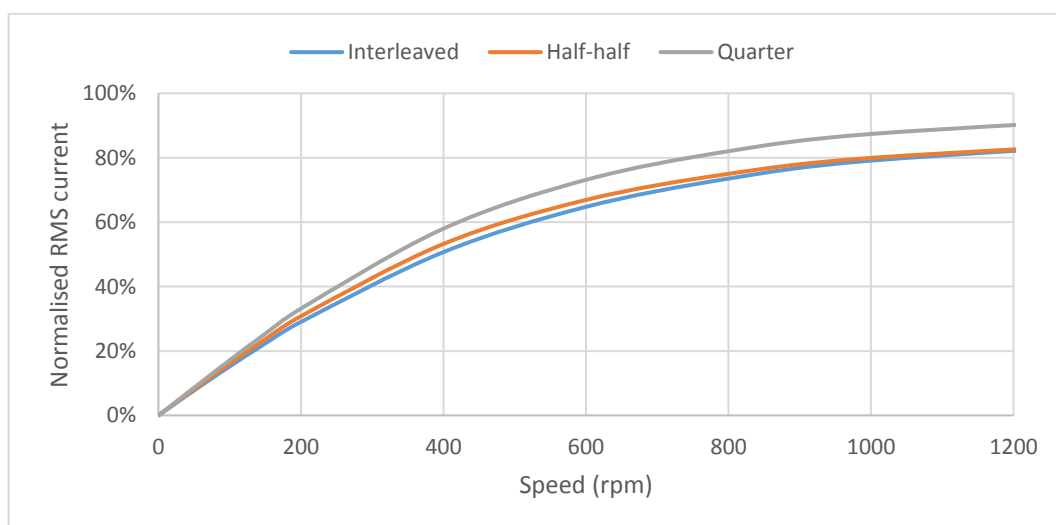


Figure 79: short-circuit current in the leading phase (phase 2 as in Figure 78).

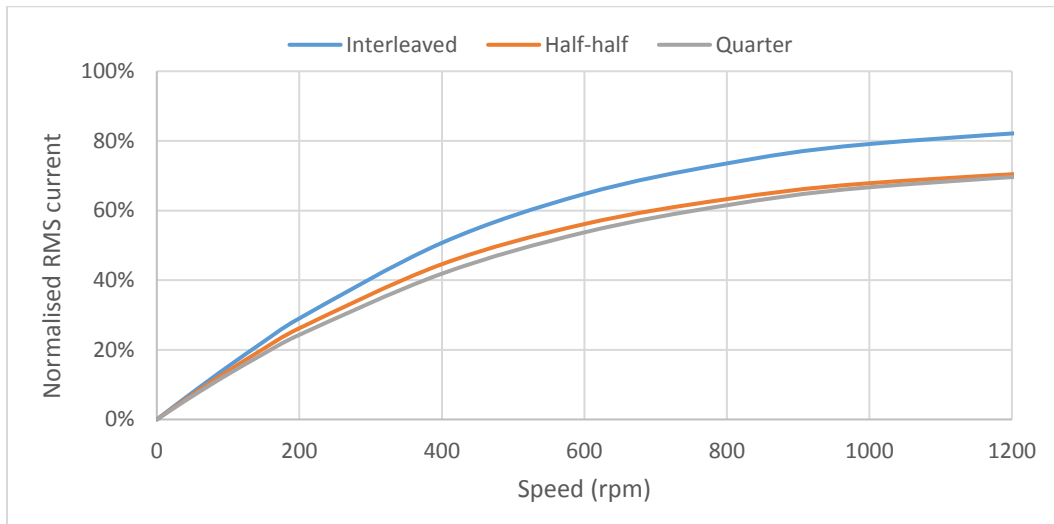


Figure 80: short-circuit current in the middle phase (phase 1 as in Figure 78).

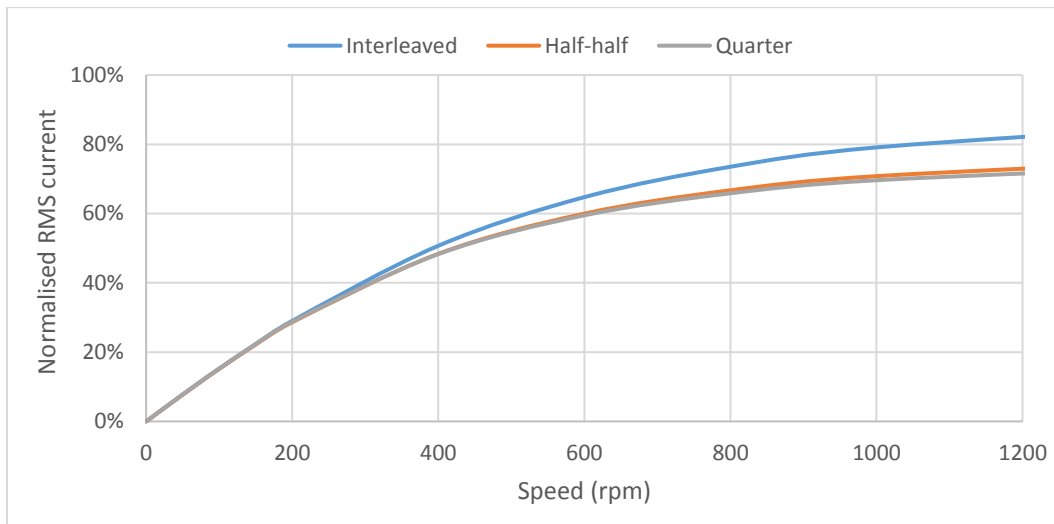


Figure 81: short-circuit current in the trailing phase (phase 3 as in Figure 78).

From the current versus speed graphs, there are significant differences between the phase currents in the different winding connection types. Due to all coils being affected in the interleaved connection, the induced current in all three-phase shorted coil are symmetrically distributed. This makes the short-circuit current amplitude the highest among the different connections (Figure 82). The leading phase in the Quarter arrangement (phase 2 in Figure 78) carries the highest induced short-circuit current as there are four points of interaction. Unlike the interleaved arrangement, the quarter arrangements' phase 1 and phase 3 carry lower induced current due to the asymmetry (Figure 83). Finally, the Half-half arrangement offers lower asymmetry between phases than the Quarter arrangement and the lowest induced current compared to the other two arrangements, as it has only two points of interaction (Figure 83).

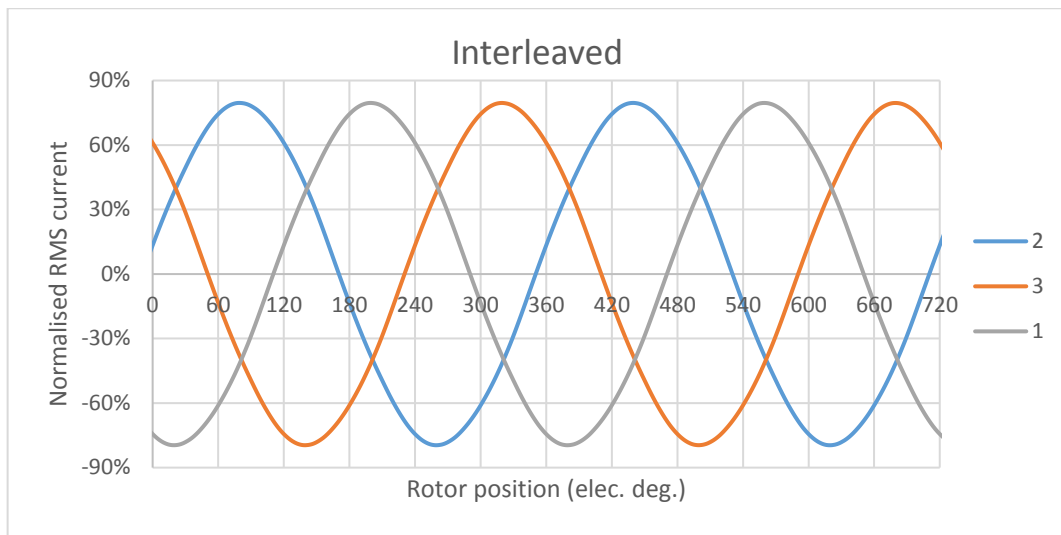


Figure 82: induced short-circuit current for all phases ( Interleaved arrangement).

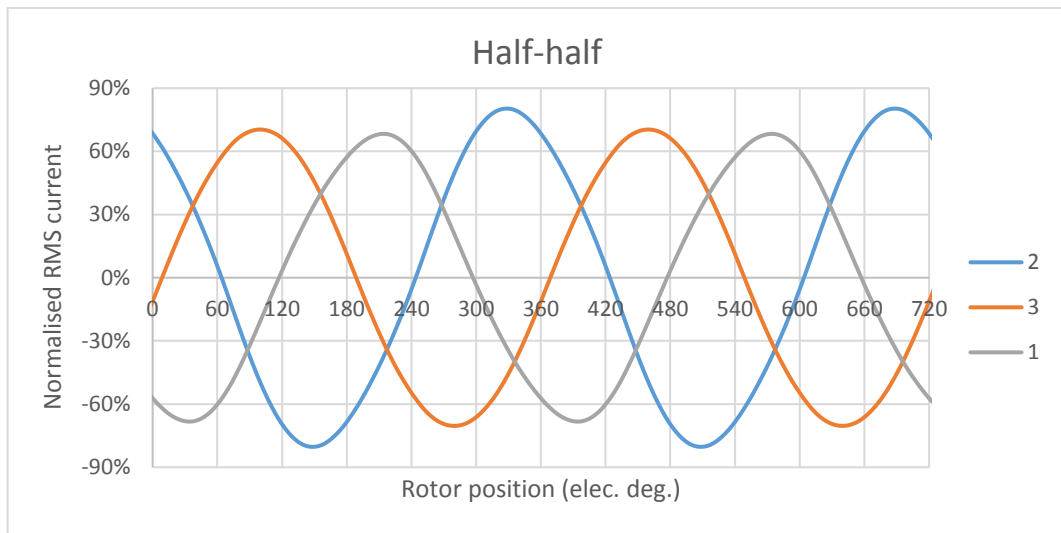


Figure 83: induced short-circuit current for all phases ( Half-half arrangement).

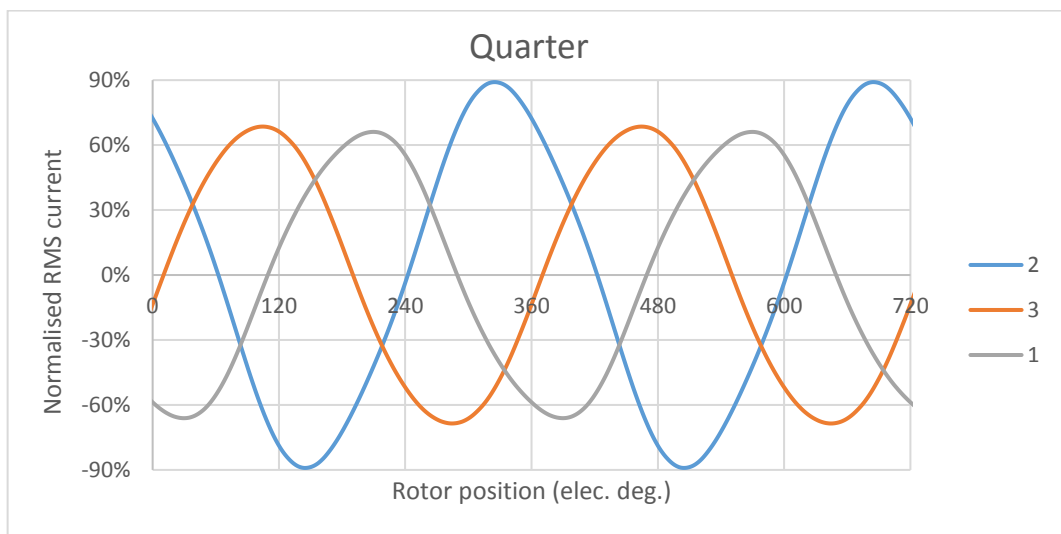


Figure 84: induced short-circuit current for all phases ( Quarter arrangement).

**Single MosFET short-circuit in one lane:**

In a three-phase motor drive, one of the theoretically possible faults which are most likely to occur is a MosFET short circuit leading to an unbalanced short-circuit current. The induced current flows through the shorted MosFET (red line T<sub>11</sub> in Figure 85) and returns through the free-wheeling diodes, parallel to the shorted MosFET (T<sub>13</sub> and T<sub>15</sub>). Like the three-phase short-circuit failure, speed, winding inductance and short-circuit resistance influence the amplitude of induced current.

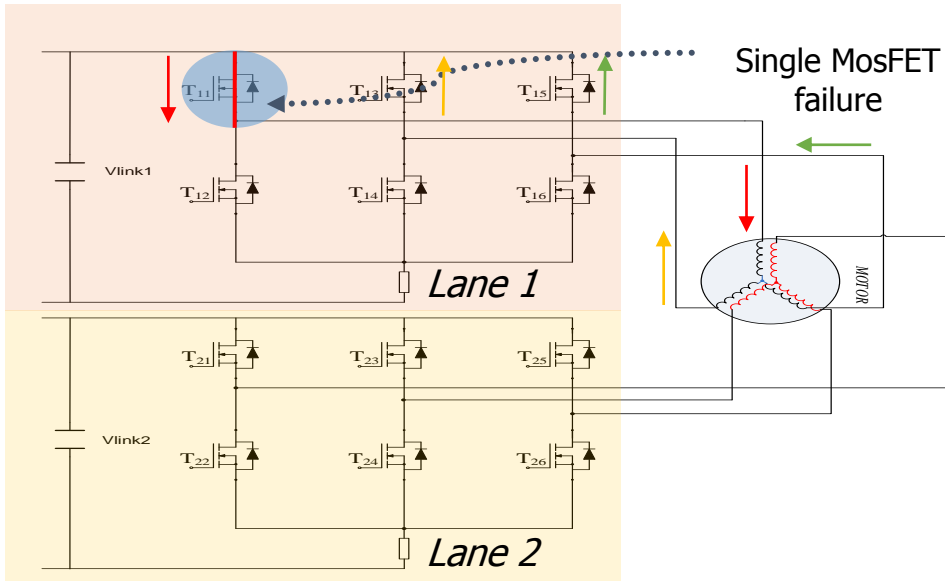


Figure 85: Single MosFET failure diagram for a dual-lane three-phase motor.

In the Interleaved arrangement, a failure in a MosFET connected to any phase winding results in the same drag torque and ripple content. However, asymmetry in the Half-half and quarter arrangements provides different responses according to which phase is connected to the shorted MosFET. They are categorised as edge-coil and middle-coil shorts. The edge coil can be either the leading or the trailing coil as denoted in three-phase balanced short-circuit analogy.

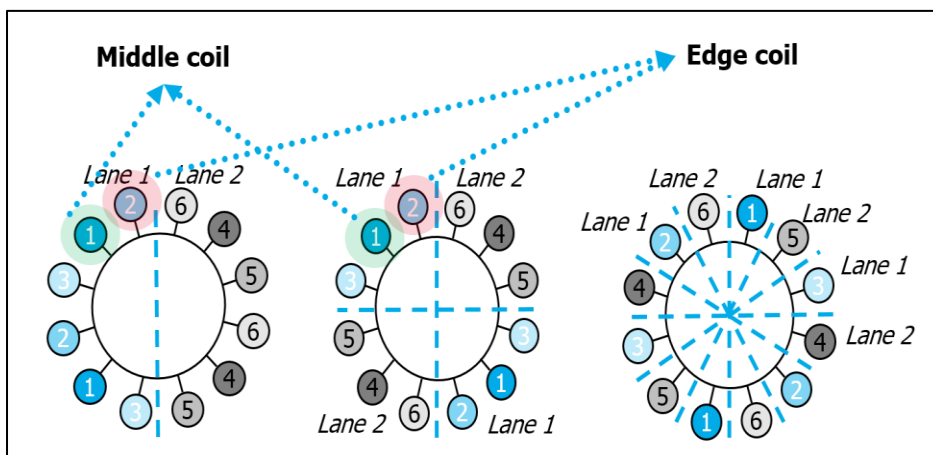


Figure 86: Winding connection layouts and coil highlight for MosFET failure.

An edge-coil short is one where the shorted coil is affected by transformer coupling from the healthy lane. This leads to higher induced short-circuit current and drag torque in the coil for both Half-half and Quarter arrangements. A mid-coil short circuit leads to a lower induced short circuit current and drag torque as the transformer coupling is less effective.

Figure 86 shows the different arrangement layouts and the places of mid-coils and edge-coils that affect the induced current and drag torque. Figure 87 compared the different coil connections' torque capability. Half-half is still the best compromise between all the arrangements for the torque capability.

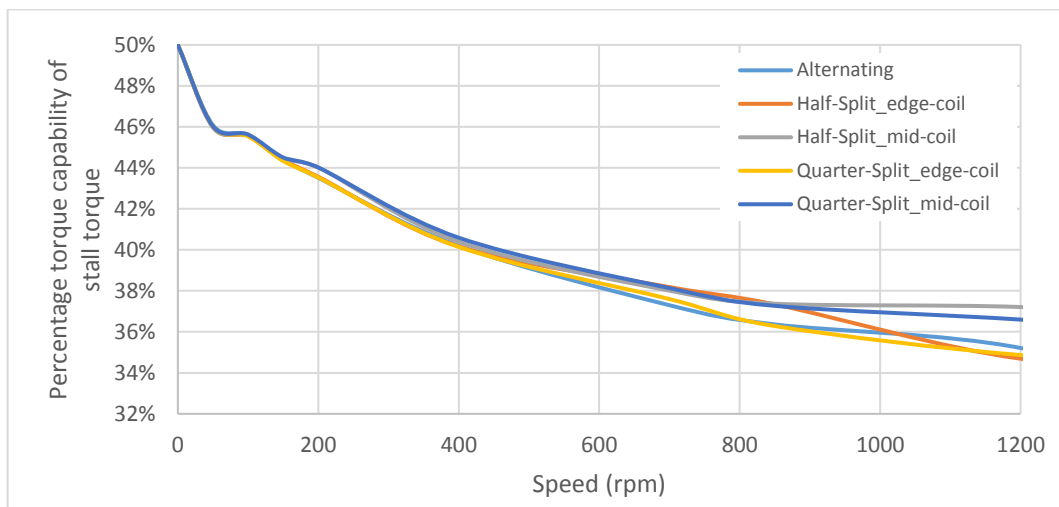


Figure 87: Drag torque for double layer winding and different winding connections.

However, Figure 88 illustrates that Quarter connection is still the worst in terms of percentage torque ripple which is approximately 5% and 10% higher than Interleaved and Half-half connections respectively. the normal condition torque ripple is not presented on the same graph due to its very low amplitude (approximately 1.5% of the stall torque).

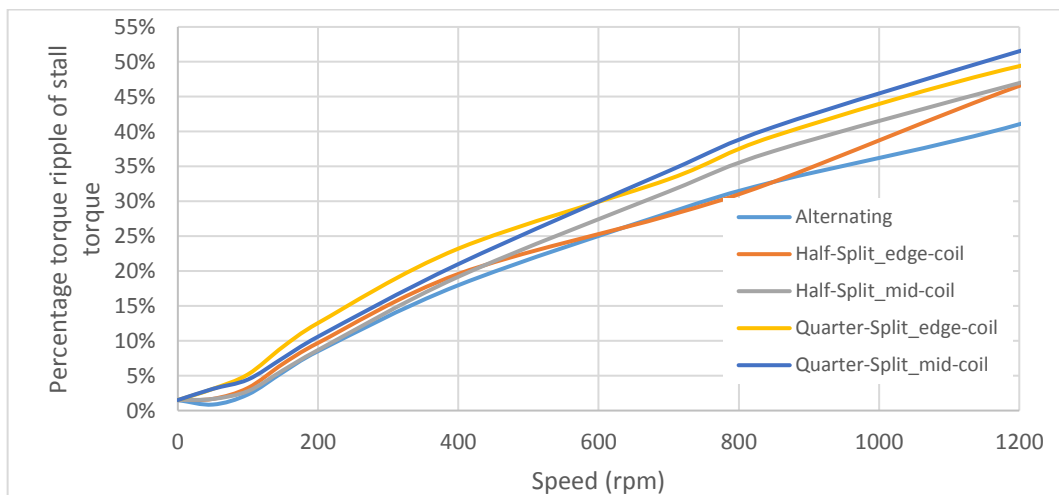


Figure 88: Torque ripple for double layer winding and different winding connections.

Finally, Figure 89 shows short circuit current for the different arrangements and different coil connections. Taking 1200 rpm as a highest speed sample, the edge coil option for both Half-half and Quarter connection leads to the highest induced current. However, the graph also shows that Half-half is the best connection for low induced short circuit current.

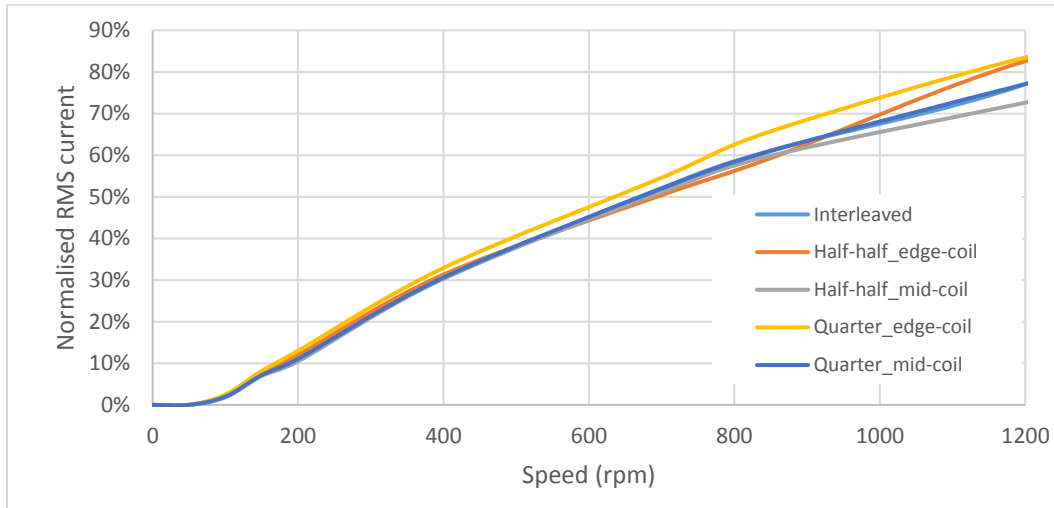


Figure 89: Induced short-circuit current for double layer winding and different winding connections.

### 2.4. Summary:

To summarise this chapter, the following key points have been investigated:

- A 12 slot 8 pole interior permanent magnet synchronous motor (IPMSM) has been studied. 2D and 3D results were compared to show the differences due to shorter magnets in the rotor pucks, end effects and fringing flux between the rotor pucks.
- The stator of the motor is a fractional slot concentrated winding in which each tooth is wound with a coil separate from the next tooth. This enables the coils to have a better physical and thermal isolation compared to distributed winding arrangements.
- This motor will be used as a baseline motor in the next chapters. In an electric power steering application, it is important that the motor's cogging torque and torque ripple are as low as possible. The motor is connected to the steering wheel through a mechanical gear which allows the torque ripple to be felt by the driver if it is too high. The baseline motor has a very low torque ripple and cogging torque.
- The inductance of the motor has been calculated using 2D FE simulation. The frozen permeability method was used for the investigation which enabled the

decomposition of the d-axis and q-axis inductances and the magnet flux under loaded conditions and for different advance angles. Also, the resistance has been calculated using analytic methods. For the end-winding resistance, an ellipse shape was considered to calculate the length of each turn considering the change in the radii when the turns overlap. Both calculated and measurements were compared, and they approximately match.

- e.) For fault investigation, the motor was simulated with all the winding terminals shorted together. Then, both the drag torque and short circuit current were calculated using 2D FE simulations and compared to analytical results.
- f.) To overcome a complete system halt and enable the motor to produce some torque, a dual-lane system was proposed. Three different winding connections were investigated:
  - 1.) Interleaved connection: this is the most difficult connection to route the interconnections between coils whilst maintaining physical isolation between the lanes. There is also significant magnetic and thermal coupling still between the lanes. However, it produces the smoothest torque under three-phase fault condition, yet it has lowest torque capability under faulted conditions compared to other arrangements.
  - 2.) Half-half connection: this arrangement was considered the best in terms of the physical and thermal isolation between the lanes. It was also considered the best compromise between the other two connections for producing highest torque under faulted conditions and medium torque ripple as there was only two points of integration between the motor lanes.
  - 3.) Quarter connection: this arrangement considered the worst as it has the highest torque ripple with four points of interaction. Physically, the end-winding connections of one lane should pass through the other lane as well. The torque capability under faulted condition also lies between the other two arrangements.

In conclusion, the half-half arrangement is the best compromise between the interleaved and quarter arrangements as it offers medium torque ripple and the lowest drag torque. It also has the lowest points of interaction between the lanes. This also means that the physical layout of the end-winding connections is preferred as they are not passing over other lanes.

- g.) The 2D FE fault results were numerically normalised to the measured values for the no-load drag torque and no-load short circuit current. The shorter magnet

axial length and end-winding inductance were the main parameters that were used to scale down the drag torque (which changes with the square of the length and inductance) and the short-circuit current (which changes linearly).

From the analysis in the previous sections, the investigated normal capabilities and faulted capability of the baseline motor will be used for comparison in the next chapters. This leads to further investigation on how to increase the torque and power density along with further enhancing fault tolerant capability of the existing motor.

## Chapter 3

### Modular winding arrangement and connections

This chapter investigates a modular winding arrangement which has been developed to fit within the baseline motor's cross-section. Modular winding is still fractional slot concentrated winding. However, the number of the coils wound for a 12 slot 8 pole motor is halved (only 6 coils wound instead of 12 coils). It considers the merits and drawbacks of the modular winding compared to the double layer winding used in the baseline design. The modular winding arrangement is proposed because it has lower mutual coupling between coils. The number of coils is halved as only every other tooth is wound. Figure 90 demonstrates a 2D cross section of the modular winding

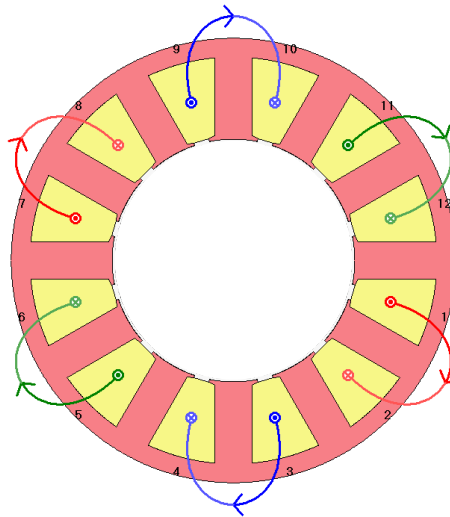


Figure 90: modular winding arrangement cross-section

The no-load characteristics of the modular design remain identical to that of a double layer winding. Cogging torque is due to interaction between the stator core and rotor permanent magnets, and so it is identical. The back-emf also remains identical as it is solely a function of the number of series turns, which are unchanged, the magnetic geometry and the speed. The modular winding has some drawbacks when operating on load – it creates more space harmonics (Figure 91) that can cause undesired effects such as acoustic noise and additional core saturation. Acoustic noise is not desired in EPS systems as it can be heard from the driver, especially in column drive systems where the motor is very close to the driver.

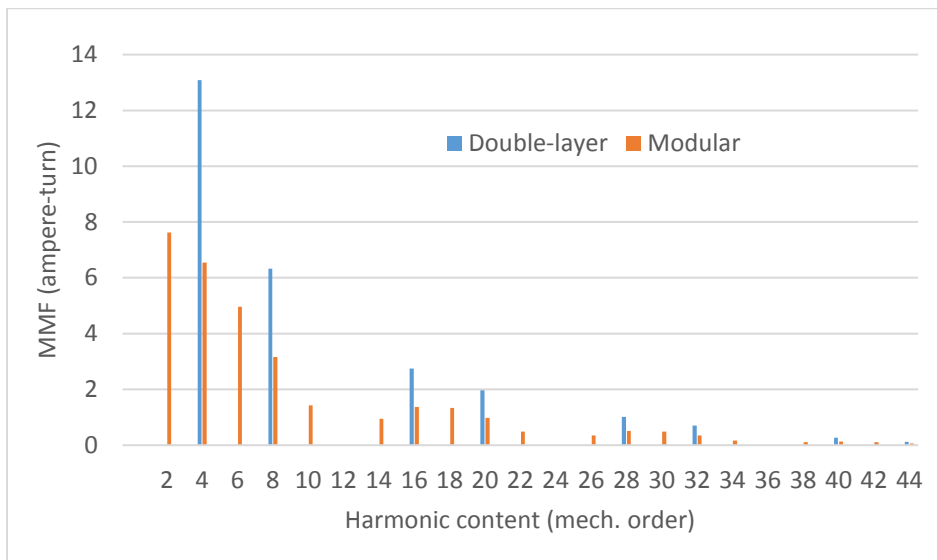


Figure 91: space harmonic comparison between different winding arrangements for similar stator cross-section.

### 3.1. Loaded Characteristic:

The only electromagnetic difference between the double layer winding and the modular winding is the MMF input. The MMF input round each wound tooth is doubled compared to the baseline motor. This leads to higher saturation in the core and rotor bridge between the magnets. It also leads to generating higher radial forces in the teeth (almost doubled), hence acoustic noise. Figure 92 and Figure 93 show the difference between the Double layer winding and modular winding magnetic fluxes. The saturated parts (highlighted by circles) in the simulation leads to a reduction in mean torque and increased torque ripple.

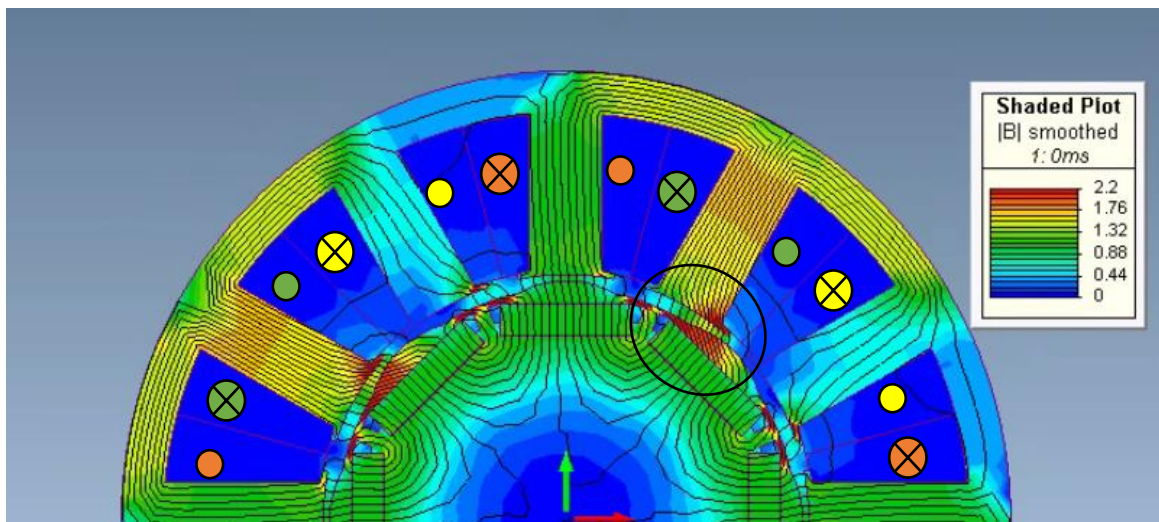


Figure 92: Baseline motor cross-section with double-layer winding (full-load).

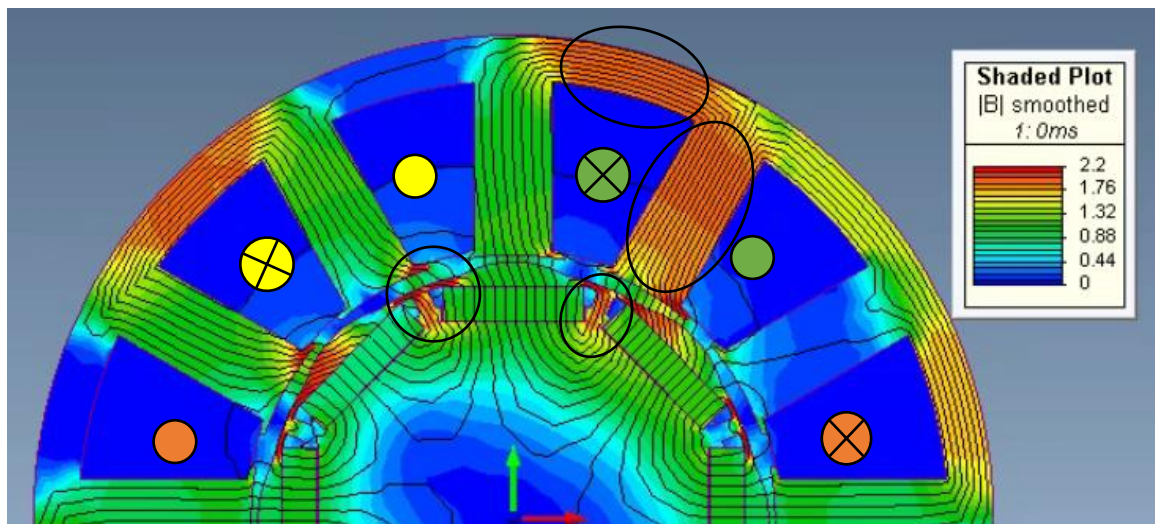


Figure 93: Baseline motor cross-section with modular winding (full-load).

The effect of saturation can be evaluated from examining the mean torque variation with current. From Figure 94, it can be seen that with the modular winding the motor's torque constant drops by 6% between half load and full load (43.65 mNm/amp and 40.95 mNm/amp for 63 amps and 126 amps respectively). For each design the current advance angle was adjusted to give the maximum torque. Compared to the double layer (baseline) windings arrangement, at rated current the full torque capability of the modular winding dropped by 8% due to saturation. The most serious problem associated with the modular winding is a significant increase in torque ripple due to saturation and space harmonics, as shown in Figure 95 and Figure 96. Overall the torque ripple has increased by a factor of 3.

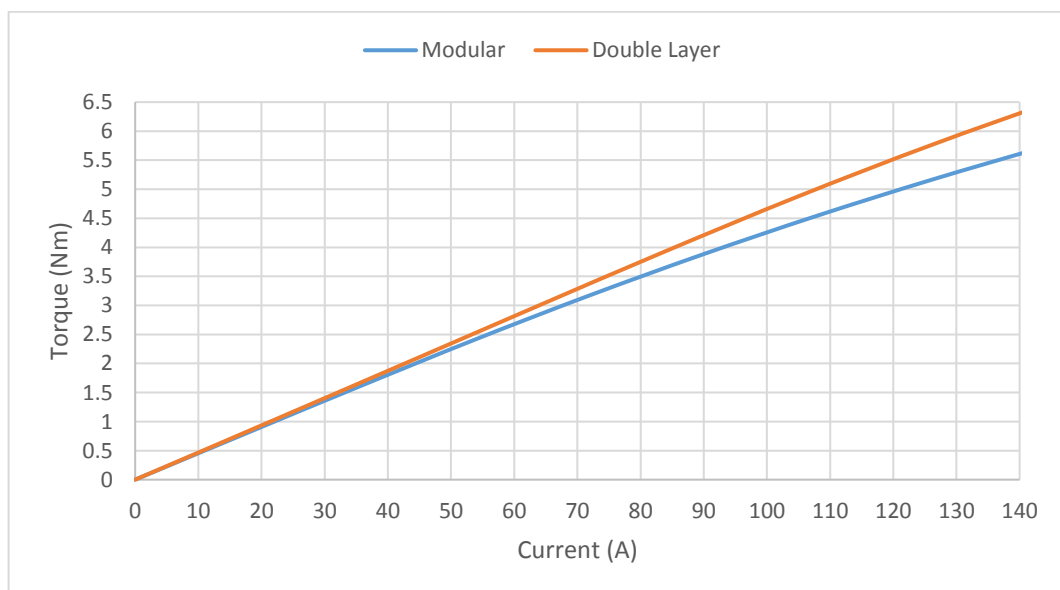


Figure 94: torque vs current comparison between double layer and modular winding at 1000 rpm.

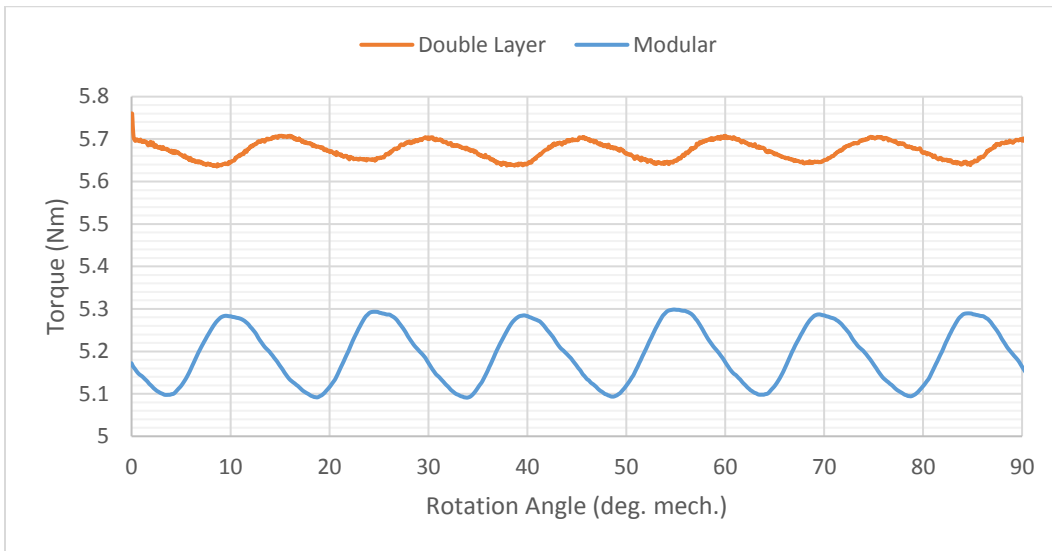


Figure 95: Torque ripple comparison between double layer and modular winding at full load and 10 elec. degrees current phase advance.

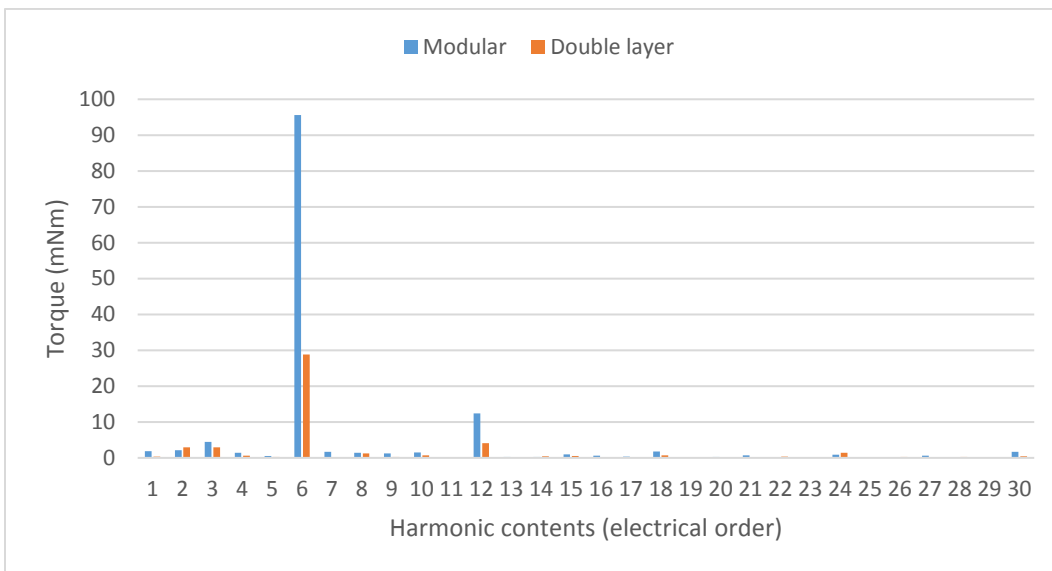


Figure 96: harmonic contents comparison between double layer and modular winding at full load and 10 elec. degrees current phase advance.

Figure 97 shows the effect of advance angle upon mean torque prediction in the modular design. Peak torque occurs at an advance angle of 10 degrees, though the increase over torque capability with current solely in the q-axis is only 2% similar to the double-layer winding. The only difference is that the maximum torque occurs at different advance angle which is solely due to saturation level.

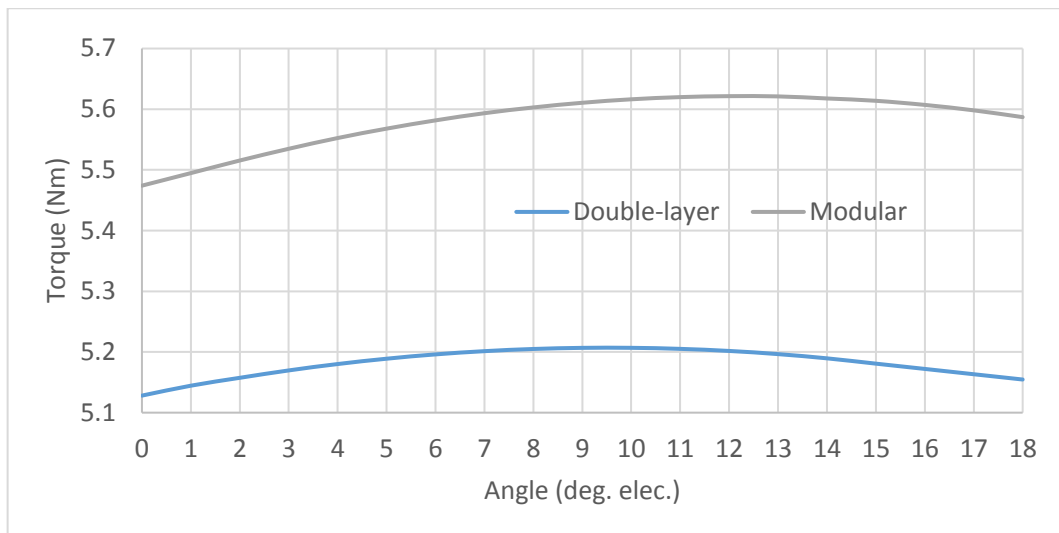


Figure 97: MTPA of the modular winding arrangement.

### 3.2. Inductance comparison:

Frozen permeability is used to calculate d-axis and q-axis inductances of the modular winding arrangement. The procedure for calculating the inductance is identical to the description given in section (2.2.4). Simplistic predictions suggest that the phase inductance of the modular winding should be twice that of the double-layer (DL) winding. This is due to having only two coils in parallel (parallel path) per phase as the number of coil turns kept unchanged. However, the inductance values are lower due to saturation in the stator core.

#### 3.2.1. D-axis inductances:

The d-axis inductance is central to the fault tolerant capability as it is the dominant component which limits any short circuit current induced at high speeds (equations 2-16 and 2-17). Additionally, it helps to increase extent of a constant power region during flux-weakening. Figure 98 shows that the modular winding d-axis inductance is approximately 70% greater than that of the double-layer winding. The fault-tolerant benefit of this will be highlighted in the next section. It is also clear how there is approximately 6% drop in the inductance as the current rises from half-load to full-load due to saturation in the stator teeth and the tooth-tips. Figure 99 shows how the modular winding has very little cross coupling between axes – typically about 1% of the main flux. Compared to the baseline motor, the cross coupling is approximately four times lower. As the current advance angle is increased from the q-axis towards the negative d-axis, Figure 100 shows how the inductance rises as the core comes out of saturation. This occurs as the current opposes the magnet flux and desaturates the core material.

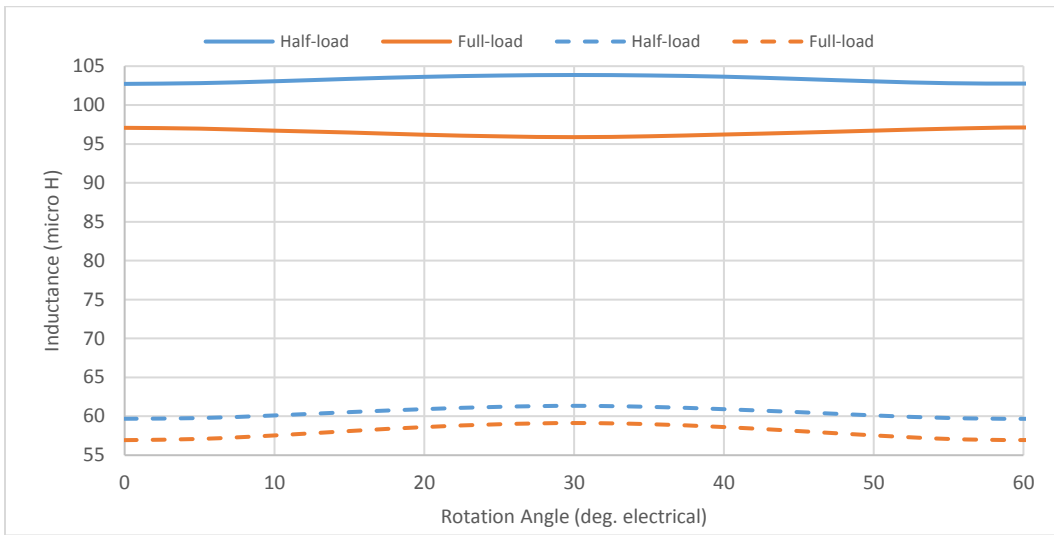


Figure 98: D-axis self-inductance ( $L_{dd}$ ) comparison for different input phase currents.

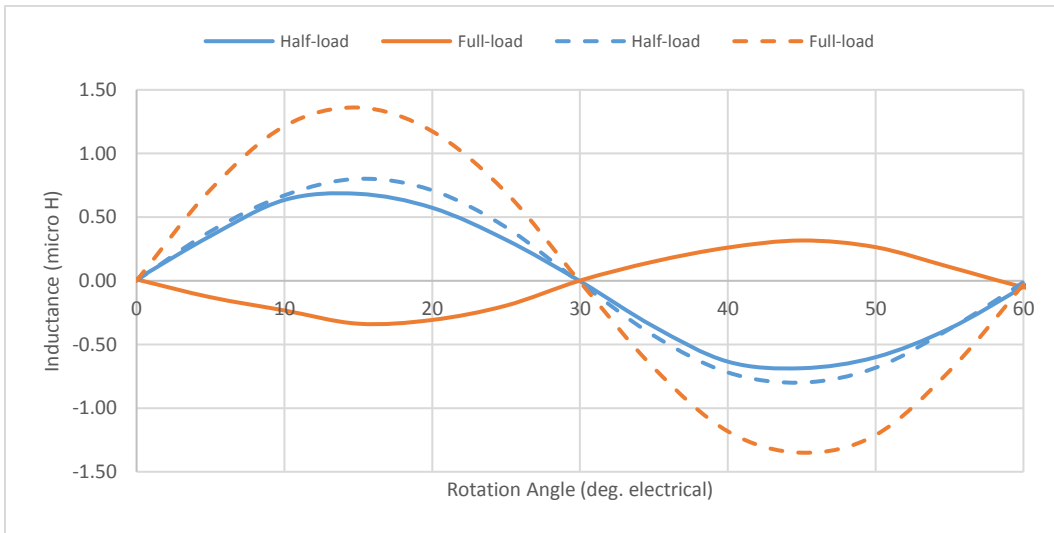


Figure 99: Q-axis inductance as a result of d-axis flux linkage ( $L_{qd}$ ) comparison for different input currents.

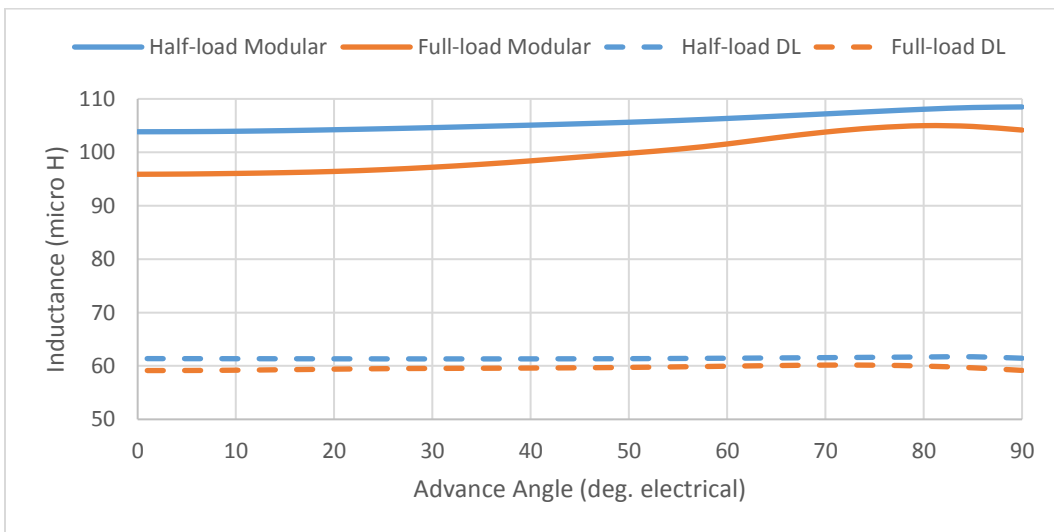


Figure 100: D-axis inductance ( $L_{dd}$ ) vs current advance angle for different input phase currents.

### 3.2.2. Q-axis inductances:

The Q-axis inductance has a much smaller role in reducing the induced short-circuit when a failure occurs; it also has a negative impact on the torque-speed curve knee point. This will be further explained in detail in Chapters 4 and 5.

Saturation in the q-axis inductance of the modular winding is significantly greater than that in the d-axis, amounting to approximately 20%, as shown in Figure 101. As highlighted in Figure 93 using circles, the q-axis flux path is highly saturated in the rotor. This also results in an increased cross-coupling inductance between d-axis and q-axis components when operating at rated current, as shown in Figure 102.

Figure 103 shows how the q-axis inductance varies markedly with advance angle: it increases rapidly as the current angle advances towards the negative d-axis. This is due to less current in the q-axis path; hence less saturation occurs

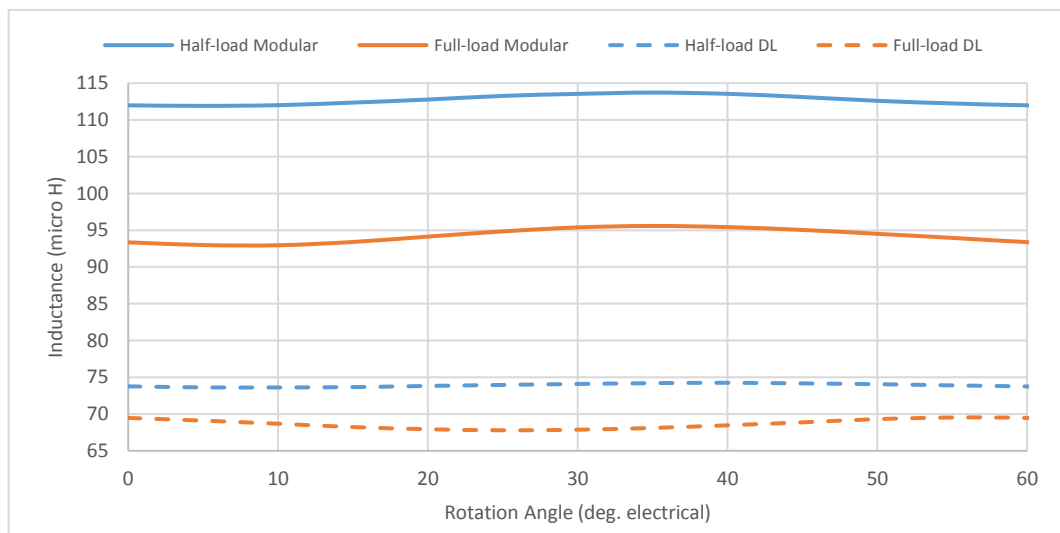


Figure 101: Q-axis self-inductance ( $L_{qq}$ ) comparison for different input phase currents.

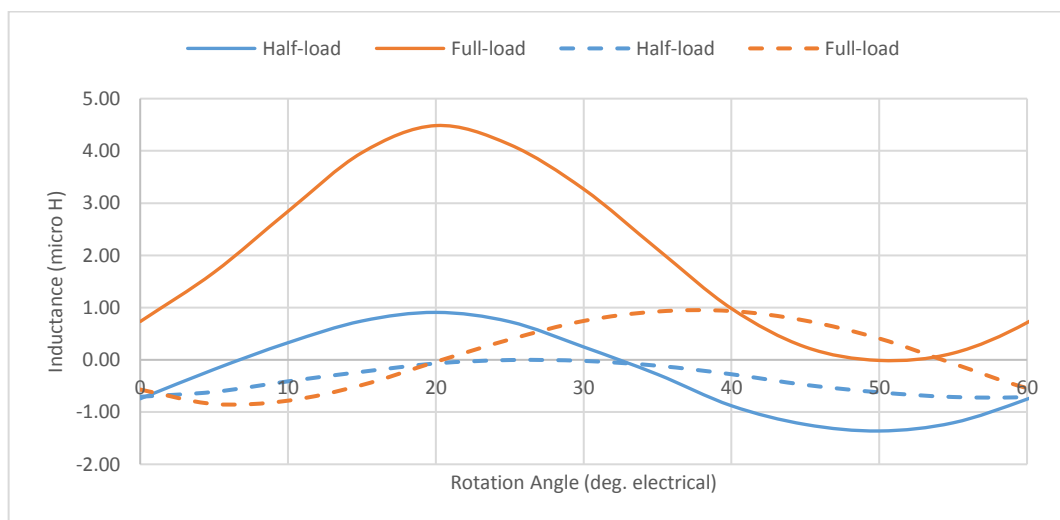


Figure 102: D-axis inductance as a result of q-axis flux linkage ( $L_{dq}$ ) comparison for different input currents.

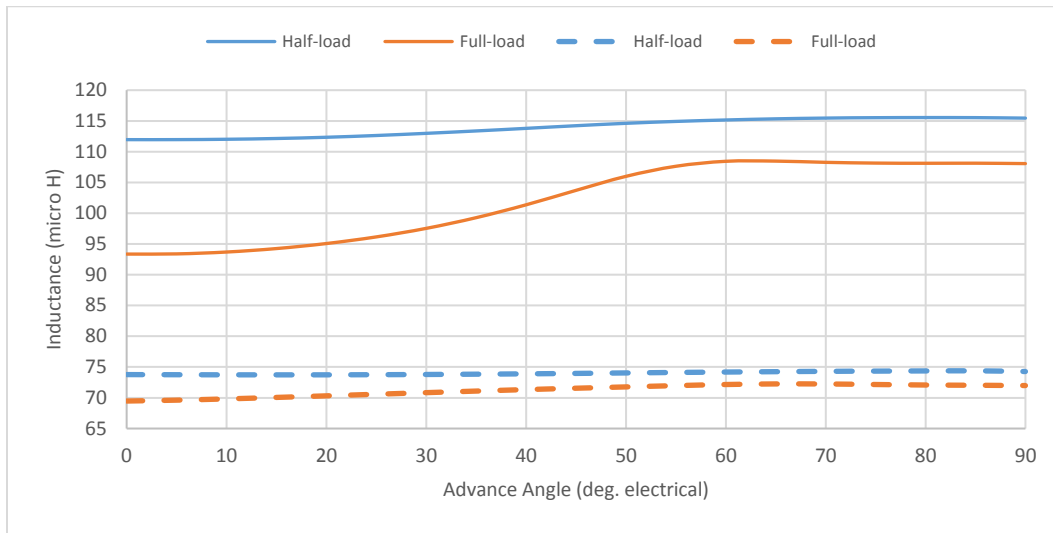


Figure 103: Q-axis inductance ( $L_{qq}$ ) vs current advance angle for different input phase currents.

### 3.2.3. Magnet Flux linkage:

The no-load magnet flux-linkage is identical in the modular winding and double layer winding machines: they have the same number of series turns and so their no-load back emf is identical. However, when current is placed in the negative d-axis the magnetic saturation changes. The modular winding has a greater inductance and so it reduces the d-axis flux more rapidly than in the baseline machine. Consequently, magnetic saturation in the stator reduces further and the back emf rises approximately by 4% and 5% for half-load and full-load respectively. This can be seen clearly in Figure 104. There is also a small amount of magnet flux which appears in the q-axis, even though all sources are in the d-axis. This is due to the slotted nature of the stator core and is shown in Figure 105: its overall effect is insignificant. However, the cross coupling becomes anti-phase compared to half load as the magnet flux from the stator is significantly large that changes the polarity of the flux over a cycle.

Figure 106 shows the effect of keeping the stator current of fixed magnitude and gradually advancing the current angle from the q-axis into the negative d-axis. As is to be expected, the machine d axis reduces in saturation and the magnet flux-linkage rises. The change is most marked in the modular winding machine because the armature reaction flux is larger.

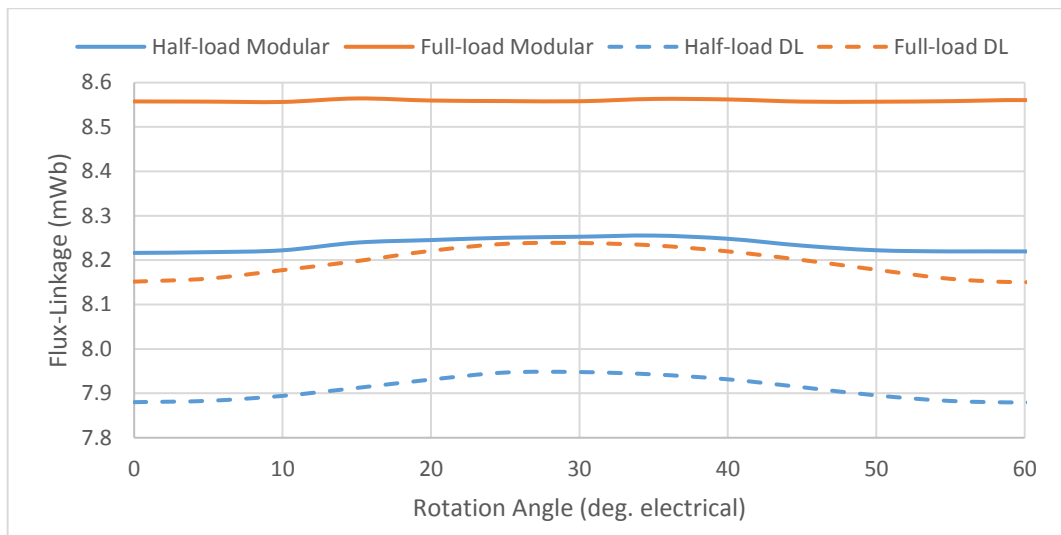


Figure 104: D-axis magnet flux linkage ( $\psi_{Fd}$ ) comparison for different input currents in the d-axis.

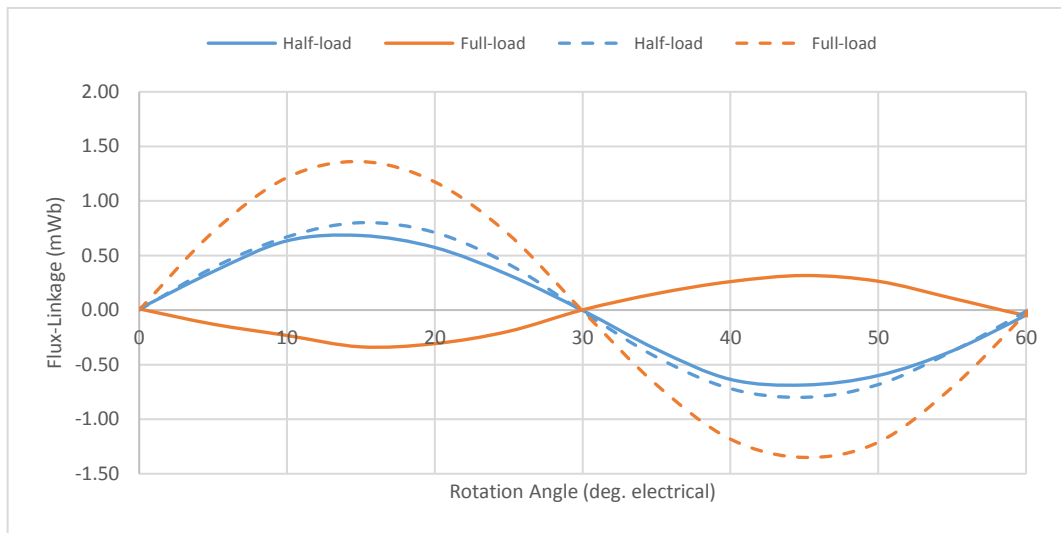


Figure 105: Q-axis magnet flux linkage ( $\psi_{Fq}$ ) comparison for different input currents.

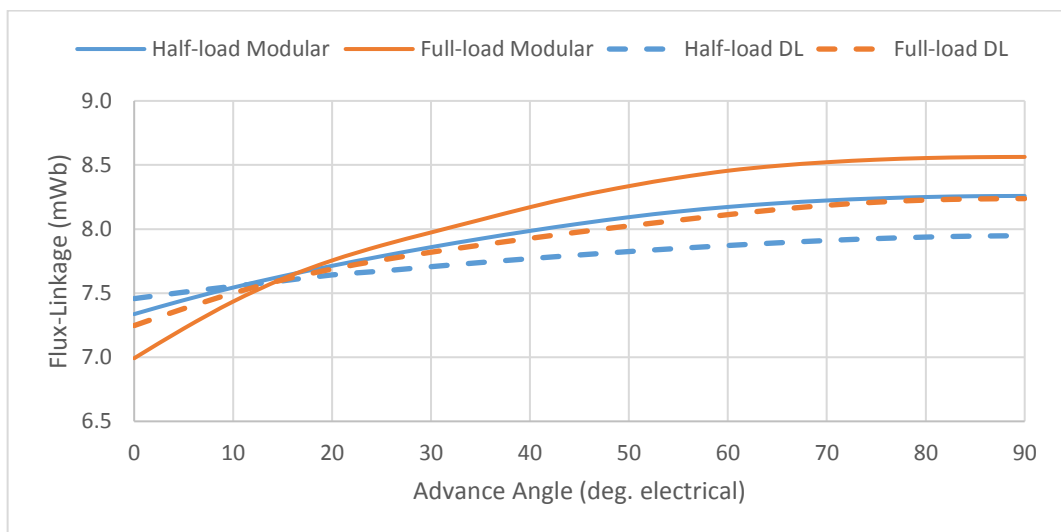


Figure 106: D-axis flux linkage ( $\psi_{Fd}$ ) vs current phase advance angle for different input phase currents.

**3.3. Fault scenarios:**

As there are only 6 coils wound on the 12 teeth, there are only two possible winding connections which can be considered for a dual-lane system in modular winding: the Interleaved and Half-half arrangements. The definition of these two arrangements is covered in section 2.3. This section will focus on the impact of a three-phase symmetrical short-circuit fault to emphasise the importance of the modular winding in reducing the mutual coupling between coils. A single MosFET short-circuit is not investigated at this point.

**3.3.1. No-load investigation:**

**All coils short:**

Similar to the double-layer winding investigation, all the coils of the motor are short-circuited, and the simulation is carried out at different speeds to investigate the drag torque and short-circuit current. The influence of having a high inductance can be seen in Figure 107 as the drag torque and short circuit current is approximately halved compared to the baseline machine. The inductance is the main component limiting the short-circuit current and hence the power dissipated in the winding resistance. It is this power which results in the drag torque.

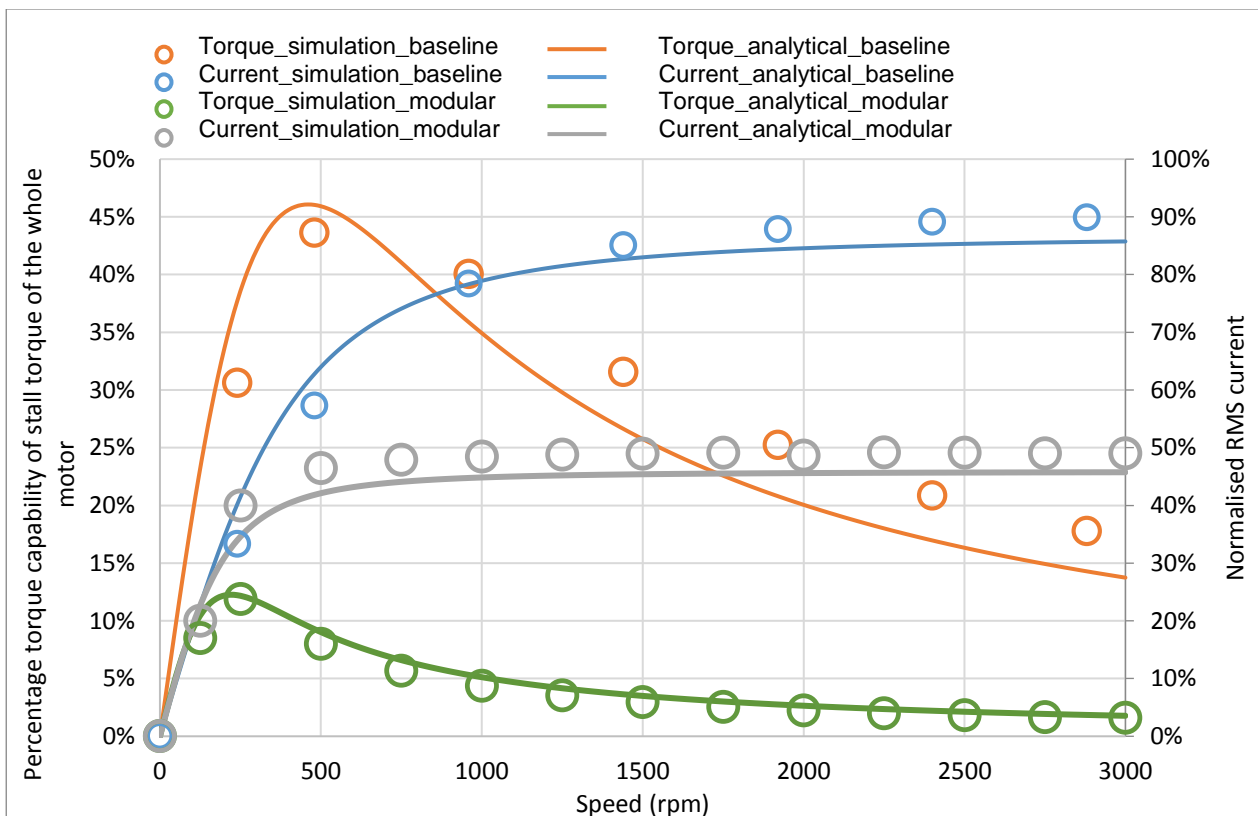


Figure 107: Drag torque and short-circuit current comparison between double layer and modular windings. The torque is normalised against the rated torque of the baseline motor.

As modular winding has higher inductances, the short-circuit current settles at a lower speed. This is also reflected on the peak of the drag torque shown in the above figure.

**Back-emf investigation in the healthy lane and no-load drag torque:**

In this section one of the dual lanes is left open-circuit, whilst the other one is shorted at the three phase terminals. The overall motor drag-torque and the mutual coupling between lanes is investigated and compared to that of the double layer winding. The induced voltage in the open-circuit lane is used as a measure of the coupling between the shorted lane and the healthy lane.

In Chapter 2 the same tests were carried out on the baseline motor. The open-circuit lane suffered from a reduction in back emf and, in some cases, an unbalanced emf due to mutual coupling between lanes. The magnitude of the effect depended upon the connection arrangement: Half-half, Interleaved or Quarter. The modular winding arrangement has been proposed in anticipation of it overcoming these issues.

Figure 108 to Figure 113 show the impact of the shorted lane upon the open-circuit lane with the modular winding machine. In Figure 108 - Figure 110 the interleaved arrangement is modelled. It is evident that the open-circuit lane is unaffected by the shorted lane. There is no reduction in the magnitude of the induced emf due to the short in the other lane and there are no significant harmonics introduced. Figure 111 - Figure 113 show the Half-half arrangement. Once more the effect of the faulted lane upon the open-circuit lane is virtually unmeasurable, though a small phase shift in the back emf can be observed in Figure 111, along with a very small reduction in magnitude.

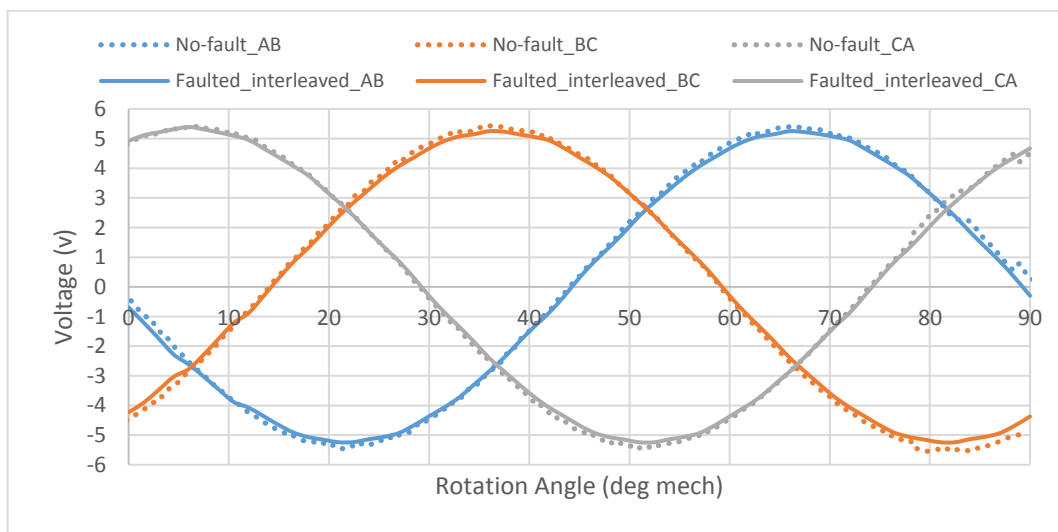


Figure 108: back-emf comparison between faulted and unfaulted situation (Interleaved).

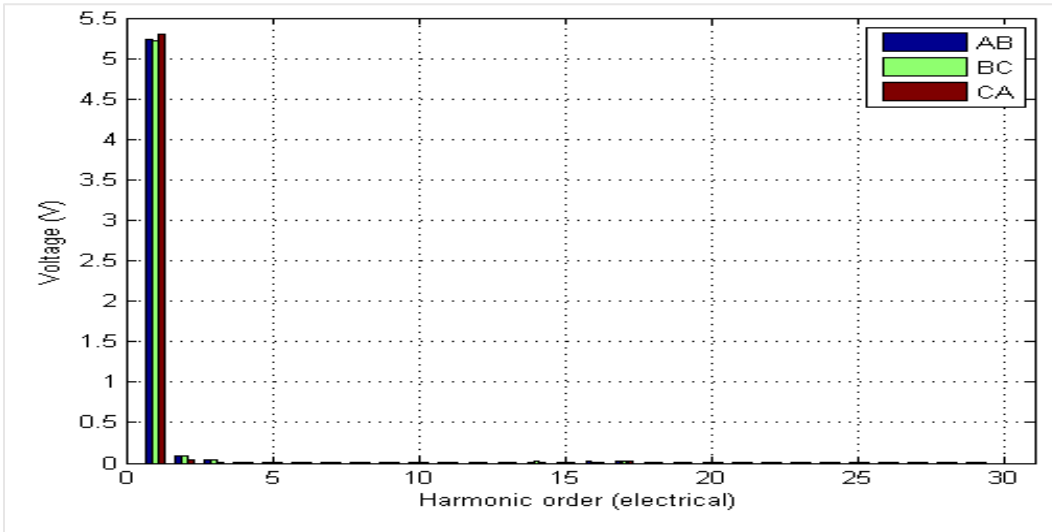


Figure 109: Harmonic content of the back-emf with Interleaved connection for modular arrangement.

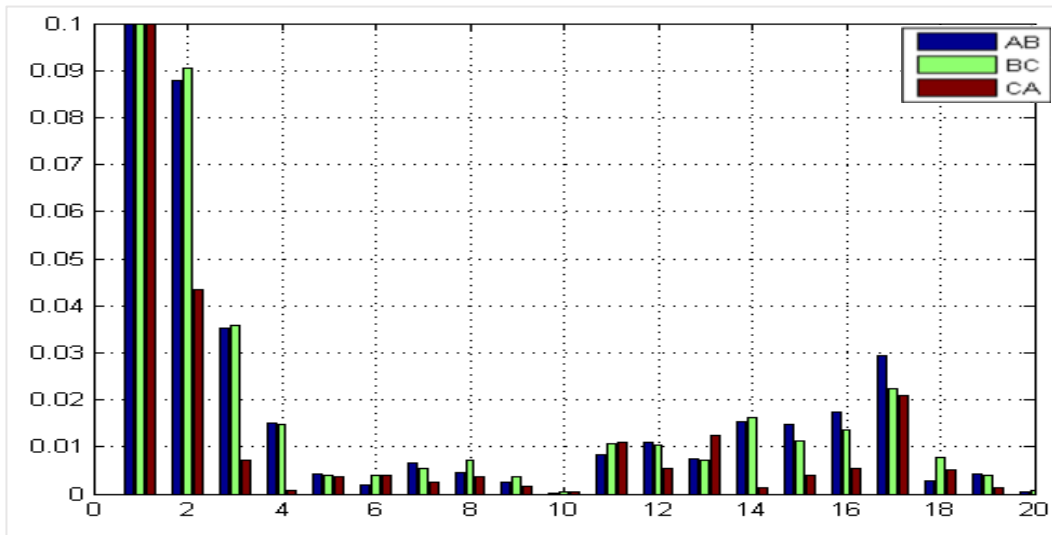


Figure 110: Harmonic content of the back-emf with Interleaved connection for modular arrangement [Scaled].

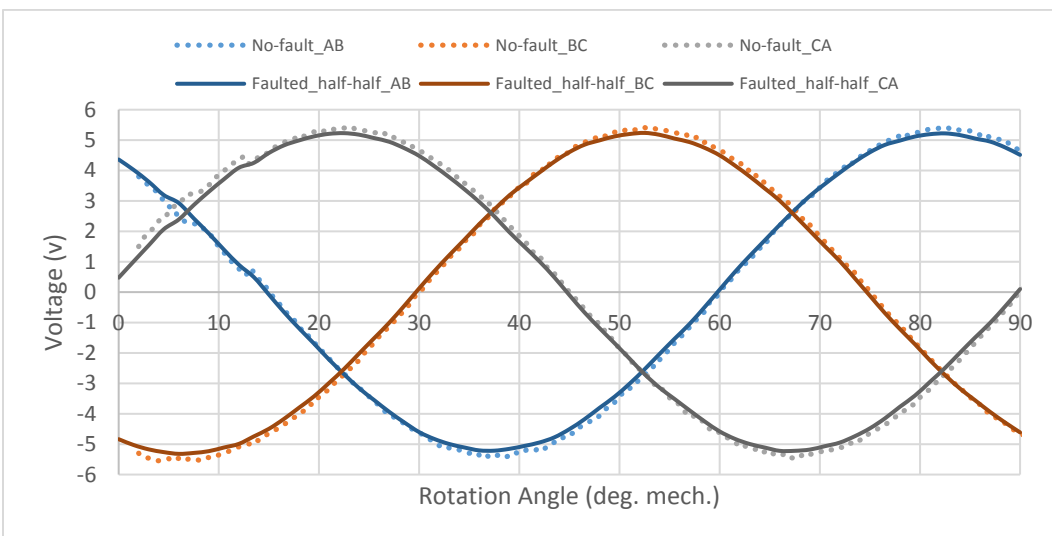


Figure 111: back-emf comparison between faulted and unfaulted situation (Half-half).

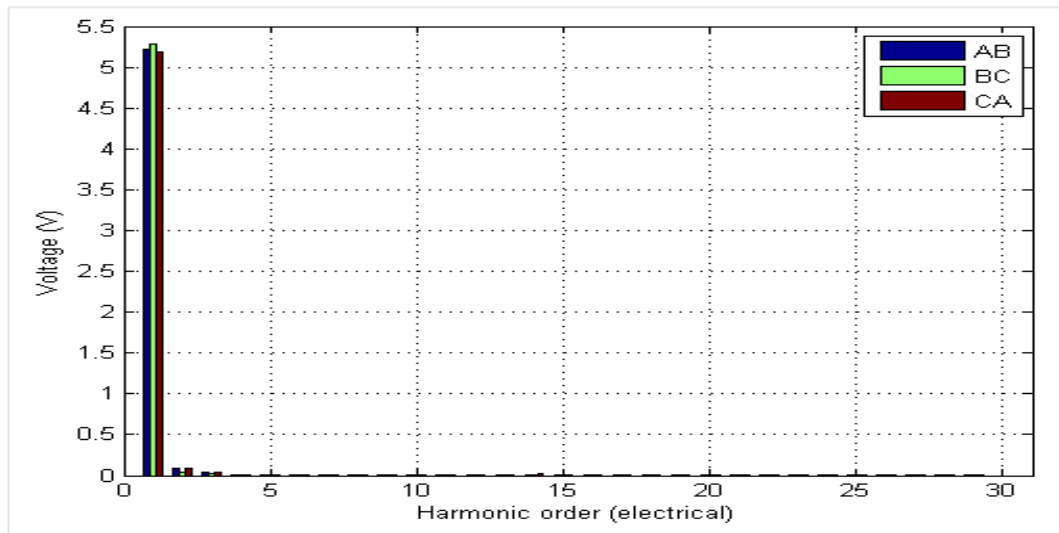


Figure 112: Harmonic contents of the back-emf with Half-half connection for modular arrangement.

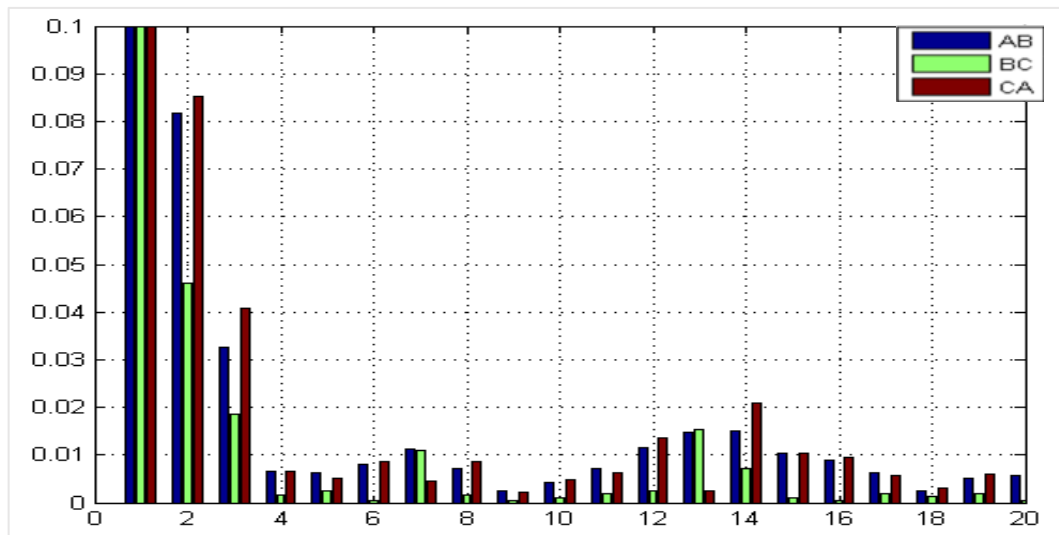


Figure 113: Harmonic contents of the back-emf with Half-half connection for modular arrangement [Scaled].

Comparing Figure 113 to Figure 65, modular winding reduced the interaction between the coils significantly as the unbalance between the line-line back-emfs is significantly reduced.

### 3.3.2. Loaded investigation:

This section investigates the motor's torque capability following a three-phase balanced short circuit across one lane, whilst forcing a sinusoidal current through the healthy lane. The main focus is on how the modular winding improves the fault tolerant capability and reduces torque ripple.

Figure 114 and Figure 115 show the net output torque from the modular machine at two conditions: high speed (1000 rpm) and at the speed corresponding to the maximum drag torque from the shorted lane (250 rpm). The torque is expressed as a percentage

of the torque capability when both lanes are healthy. Both Interleaved and Half-half arrangements are shown.

When operating at high speed the drag torque from the shorted lane is low and so the torque capability should approach 50% of un-faulted condition. The detailed simulations indicate that the torque capability is close to this at 45% of the healthy case. Even at high speed there is a small drag torque from the shorted lane and this is the cause of the 5% shortfall. At the maximum drag torque position, which occurs at low speed, the torque capability reduces to approximately 35%, due to there being approximately 13% drag torque from the faulted lane.

It can be seen that the performance of the modular winding is significantly better than that of the double layer winding due to the elimination of mutual coupling between lanes (comparing Figure 76 and Figure 114). The Interleaved and Half-half arrangements' performances are similar because both have very little mutual coupling between lanes. However, the Half-half arrangement is marginally better with 2% higher torque during the worst-case condition. The Half-half arrangement is also preferable because the connections between coils have no overlap with the other lane. Despite the merits of modular windings, the extra length of the coils' end-windings is considered to be a major challenge as it leads to extra motor length that affects the packaging and the system size. Although, the coils need to be wound with thicker wire which affects the slot fill factor, however, there is no need to have a clearance space between the coils, unlike double layer windings due to practical considerations.

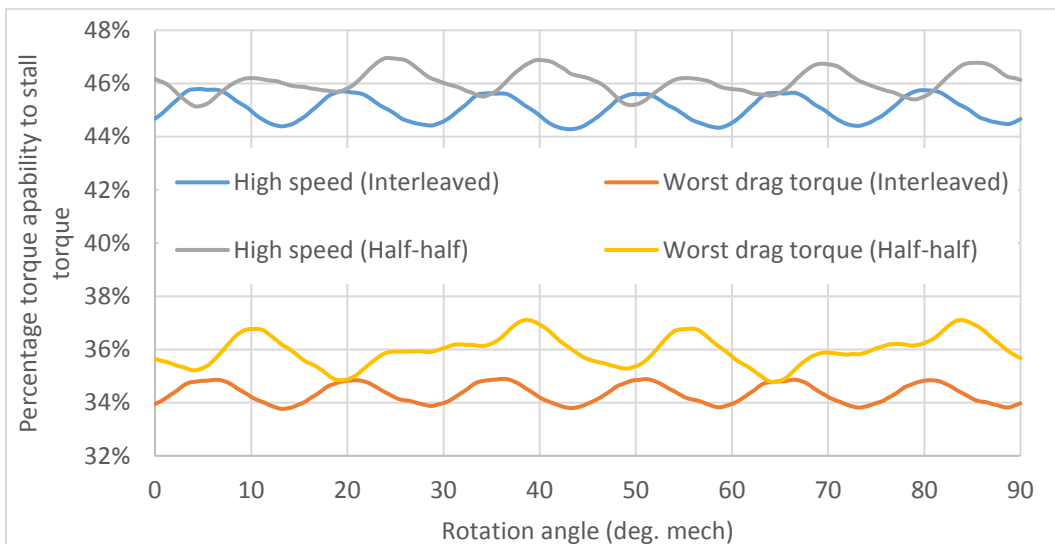


Figure 114: torque comparison between Interleaved and Half-half arrangements of the modular windings.

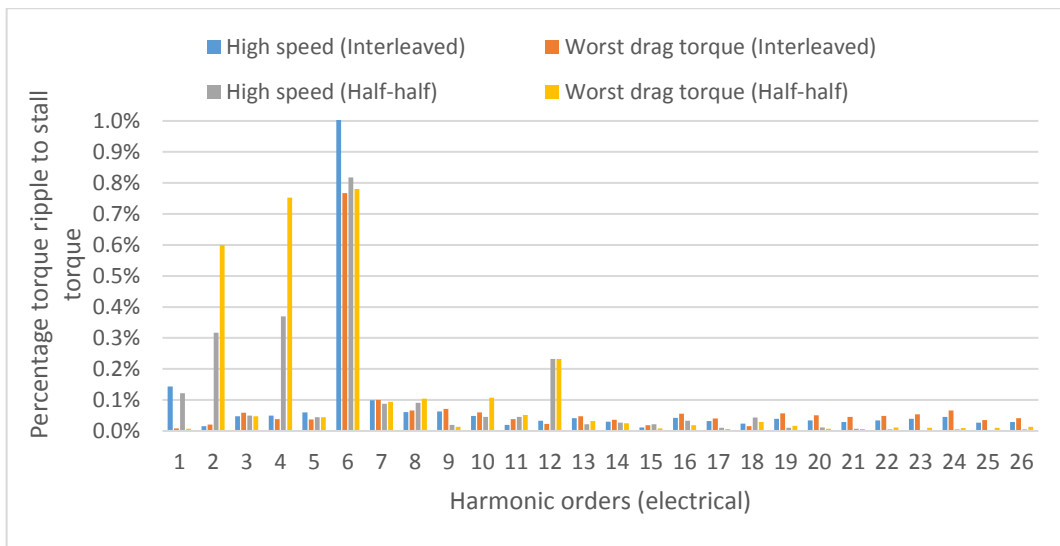


Figure 115: torque ripple comparison between Interleaved and Half-half arrangements of the modular windings.

### 3.3.3. Short circuit current:

The short-circuit current is used to investigate any unbalance within a lane and transformer coupling between the coils. Figure 116 shows the shorted currents in which either one lane or both lanes of any one arrangement are shorted. Transformer coupling is negligible, with the phase current of all different connections (all short, Interleaved and Half-half) almost identical. The solid lines show phase current when all the motor coils are shorted at a certain speed, whilst the dotted and dashed lines are the phase current taken from a shorted lane, while the other lane is normally excited at the same speed. This shows that the short-circuit current in the faulted lane is independent of whether the healthy lane is loaded or unloaded.

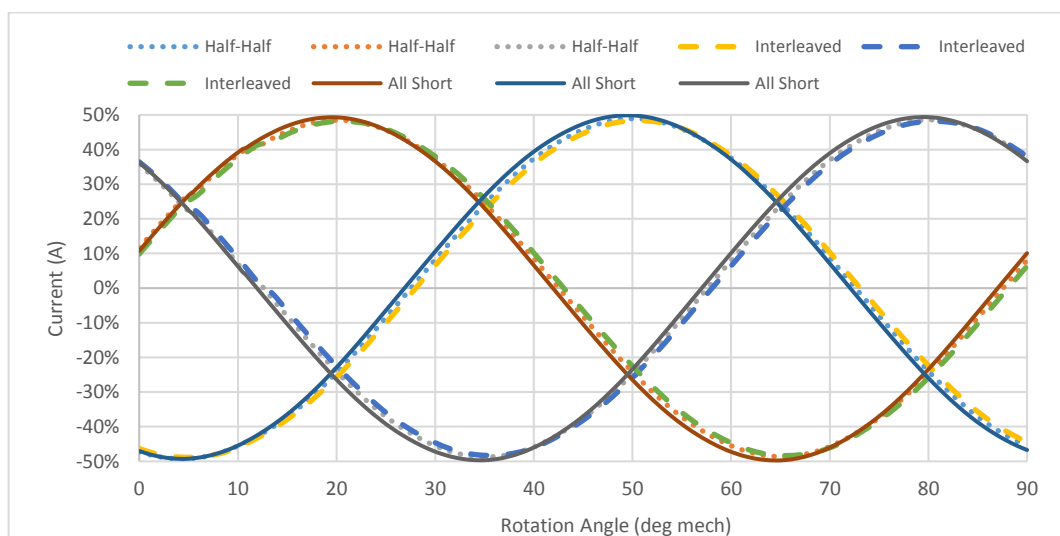


Figure 116: Short-circuit current comparison for different winding arrangements of the modular winding.

### **3.4. Summary:**

The modular winding arrangement offers better fault-tolerant capability than the double layer winding arrangement. By winding alternate teeth there is virtual elimination of mutual coupling between lanes in a dual-lane system. However, the increased armature reaction flux of the modular arrangement results in a reduction in torque at high currents, amounting to 8% and approximately doubles torque ripple which is undesired. However, both drag torque and torque ripple are significantly lower than baseline motor.

The modular winding arrangement leads to a higher end-winding length in which the overall motor's axial length increases. The coils need to be wound with thicker wire. This leads to a lower slot fill factor. The thicker wire required is also likely to be more difficult to wind.

Additionally, both d-axis and q-axis inductances are significantly higher than the baseline motor due to having half of the number of the coils in parallel per phase. Notably, the magnet flux linkage under loaded condition, approximately 5% higher than that of the baseline design when the current is on the d-axis. This was due to the d-axis current reducing the core saturation.

In this chapter, there are not any practical results as this design wasn't built: the magnetic geometry required redesigning for the modular arrangement. The next chapter will develop a new design aiming for higher torque and better fault tolerance through modification of the stator only.

## Chapter 4

---

### A new modular design

This chapter presents a new design, created to overcome magnetic saturation in the stator of the baseline magnetic geometry when a modular winding is employed. Two-dimensional finite element simulations are used to develop the machine. It is shown how changing the teeth profiles for the wound and unwound teeth can offer higher torque capability, as the motor winding factor can be substantially increased. The chapter also highlights the impact of a high per-unit inductance upon the constant power and constant torque operating regions, along with its effect upon faulted performance. The new stator is constructed and combined with the baseline rotor to validate the predictions.

#### **4.1. Design development process:**

Starting with the baseline design, a new stator was developed in several steps (Figure 117) aiming to deliver more torque, whilst emphasising fault-tolerant capability. Figure 117 A is the baseline motor that is investigated in detail in chapter 2.

Moving first to the modular winding (Figure 117 B), it is shown in Chapter 3 that the teeth and yoke of the baseline motor become more magnetically saturated due to additional armature flux-linkage, caused by the space harmonics of the modular winding. The saturation in the stator resulted in torque degradation, torque ripple and higher torque harmonic content.

To eliminate saturation in the wound teeth and the yoke, the stator saturated parts were then widened, as shown in Figure 117 C. The aim was to reduce the flux density in the excessively saturated stator sections to similar levels of those within the baseline motor of Figure 117 A.

Finally, the design was optimized, with the objectives of eliminating the torque drop, matching or improving the torque ripple, and keeping the slot area, all without changing the outside diameter or stack length. The first observation made in attempting to accomplish this was that saturation in the unwound teeth was considerably lower than in the wound teeth and that they did not need to have equal dimensions. The arc of the wound tooth tips can be increased towards 180 electrical degrees, whilst simultaneously reducing the arc of the unwound teeth towards 60 electrical degrees. The width of the main body of two sets of teeth, along with the depth of the core back

were then adjusted to give appropriate levels of flux density under load. This results in the profile of Figure 117 D.

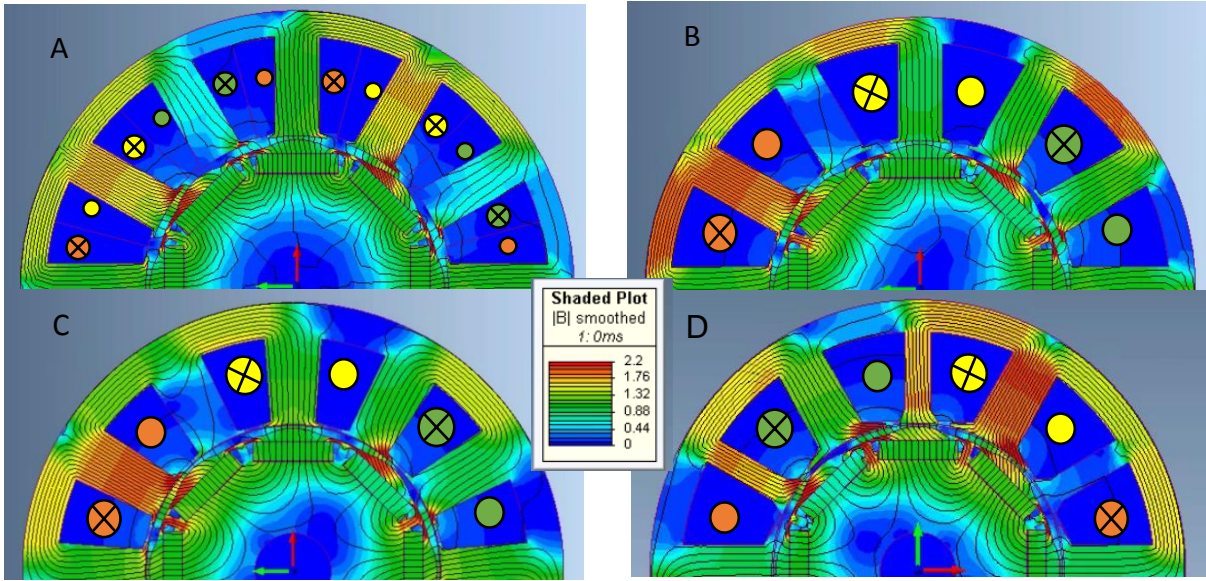


Figure 117: stator development to restore torque capability and reduce torque ripple: A. Baseline motor (Double Layer), B. Baseline motor (Modular), C. Modified equal tooth design, and D. New design (dissimilar teeth) [full-load].

Figure 118 shows the torque profile of all four designs when operating with rated current on-load and 10 degrees electrical phase advance angle, at 1000 rpm. It can be observed that the new stator design both overcomes the loss of torque with the original modular winding – it actually increases torque capability over the baseline motor by approximately 5%, whilst having the same number of the coil turns and motor volume.

Equation (4-1) relates the torque density of an electrical machine to its winding factor, magnetic loading and electric loading.

$$TRV = \frac{T}{V_r} = \frac{\pi}{\sqrt{2}} k_{w1} AB \frac{Nm}{m^3} \quad (4-1)$$

Where  $TRV$  is torque per rotor volume,  $V_r$  is the rotor volume,  $A$  is electric loading,  $B$  is magnetic loading and  $k_{w1}$  is the first harmonic of the winding factor.

Compared to the baseline motor, there has been no increase in the electric loadings as the MMF input and current density kept the same, and so it must be the winding factor which is responsible for the increase in torque. The number of coil turns are kept the same, however, the parallel paths are halved for achieving modular winding. However, the input current to be doubled average electric loading similar to the baseline design. With the wider wound teeth each tooth now spans a whole magnet

pole, thereby increasing the flux-linkage and resulting in a higher back-emf and thus higher torque [24].

Comparing to the baseline design, the new stator design has slightly higher resistance due to longer end-windings considering similar current density. This also affects the motor overall length; hence affecting the motor packaging size.

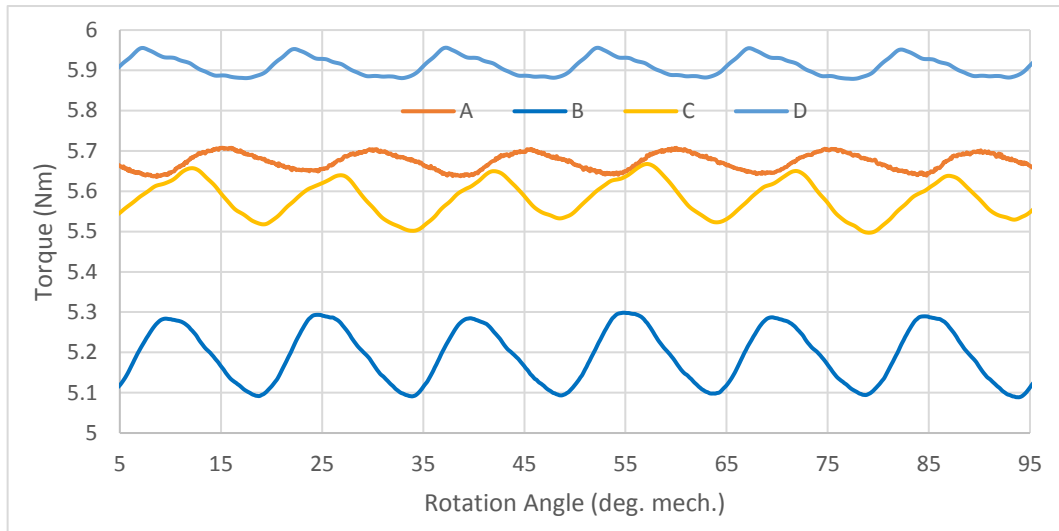


Figure 118: torque comparison between the developed stator designs for the same rotor with rated current and 10 degrees electrical phase advance angle.

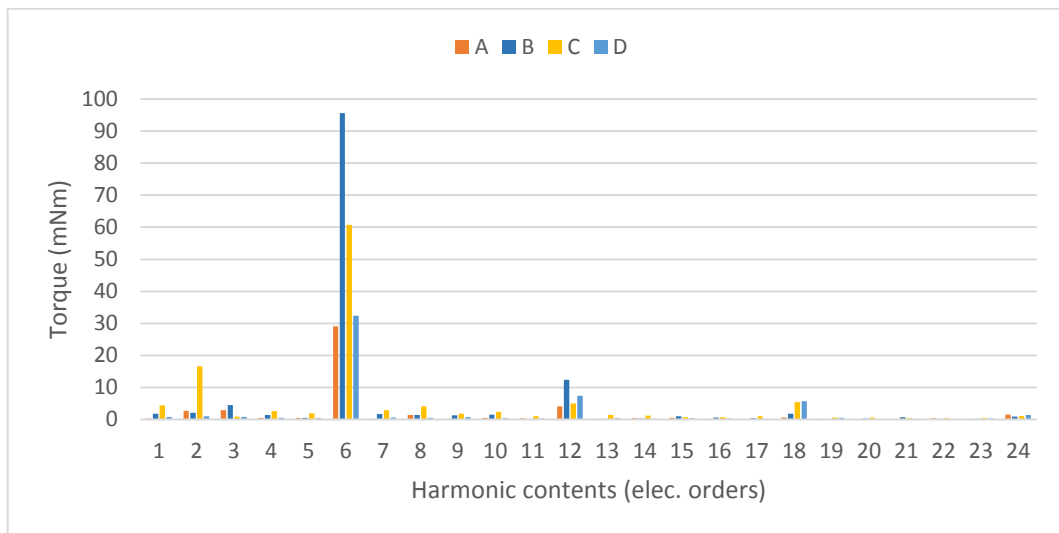


Figure 119: torque harmonic contents of the developed stator designs with rated current and 10 degrees electrical phase advance angle.

The baseline motor's winding factor is calculated from equations (4-2) to (4-4) considering that the rotor is skewed as well.

$$K_{pn} = \cos\left(\frac{n\beta}{2}\right) \quad (4-2)$$

Where  $K_{pn}$  is pitch factor in winding degrees,  $n$  is harmonic order, and  $\beta$  is ratio of the coil pitch to the pole pitch.

The difference between the coil pitch of the two different designs can be seen in Figure 120. This leads to a higher pitch factor (and hence higher winding factor) as the angle of the sine term approaches  $(\pi/2)$ .

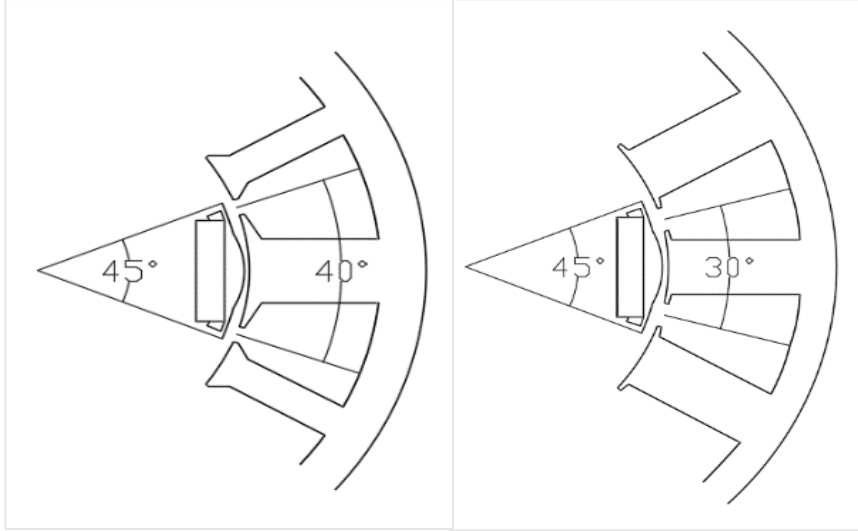


Figure 120: Cross-section comparison between baseline motor and new designed stator.

The distribution factor  $K_{dn}$  of the two designs remains unity as the coil or coils of any one phase are at the same electrical angle. The winding factor  $K_{wn}$  is the product of pitch factor and distribution factor.

$$K_{wn} = K_{pn} * K_{dn} * \text{skewing factor} \quad (4-3)$$

The rotor for all the motors at this stage is identical that is skewed across three rotor packs by 16.2 mechanical degrees. This makes the skewing factor identical for all the designs as shown below.

$$\text{skewing factor} = \frac{\sin(n\alpha/2)}{(n\alpha/2)} \quad (4-4)$$

$$\text{skewing factor} = \frac{\sin(n\alpha/2)}{(n\alpha/2)} = \frac{\sin(20/2)}{\left(20 * \left(\frac{\pi}{180}\right) / 2\right)} = 0.936$$

Although, the baseline pitch factor is different from the new-design's pitch factor. For the baseline, the pitch factor  $K_{pn} = \cos\left(\frac{n\beta}{2}\right) = \cos\left(\frac{60}{2}\right) = 0.866$ , and for the new-design, the pitch factor  $K_{pn} = \cos\left(\frac{20}{2}\right) = 0.985$ .

Considering the distribution factor for concentrated winding to unity, the baseline motor winding factor  $K_{w-baseline} = 0.866 * 0.936 = 0.81$ , and the new-designs winding factor  $K_{w-new-design} = 0.985 * 0.936 = 0.92$ .

The new stator's winding factor is improved by approximately 13.5% upon the baseline design's winding factor (0.92 and 0.81 respectively). However, this cannot be seen in the torque comparison as in Figure 118, due to the motor saturation which will be discussed later.

### **4.2. Stator construction and winding:**

The stator laminations were constructed by an external company. The stack length of the new-designed stator is similar to the baseline motor (36 mm). The stator laminations are stacked together and then wire eroded to achieve high accuracy. Due to small slot openings and thicker wires to wind the coils, the power of this motor is compromised, especially the knee point of the torque-speed curve due to higher winding resistance. Unlike production motors (can be seen in the Test rig:), slot-liners were used instead of endcaps.

Finally, the end-windings are bulkier because of using thicker wires for winding and the wound tooth is wider which makes the wires bending even more difficult. At the beginning, two strands in hand were as used to wind the stator aiming for a high slot fill factor (Figure 121). However, only 22 turns out of 24 was achievable due to lack of area and the nature of unitary stator. Finally, the stator is winded using a single thick wire of 1.7 mm by accepting the power compromise as in Figure 122.

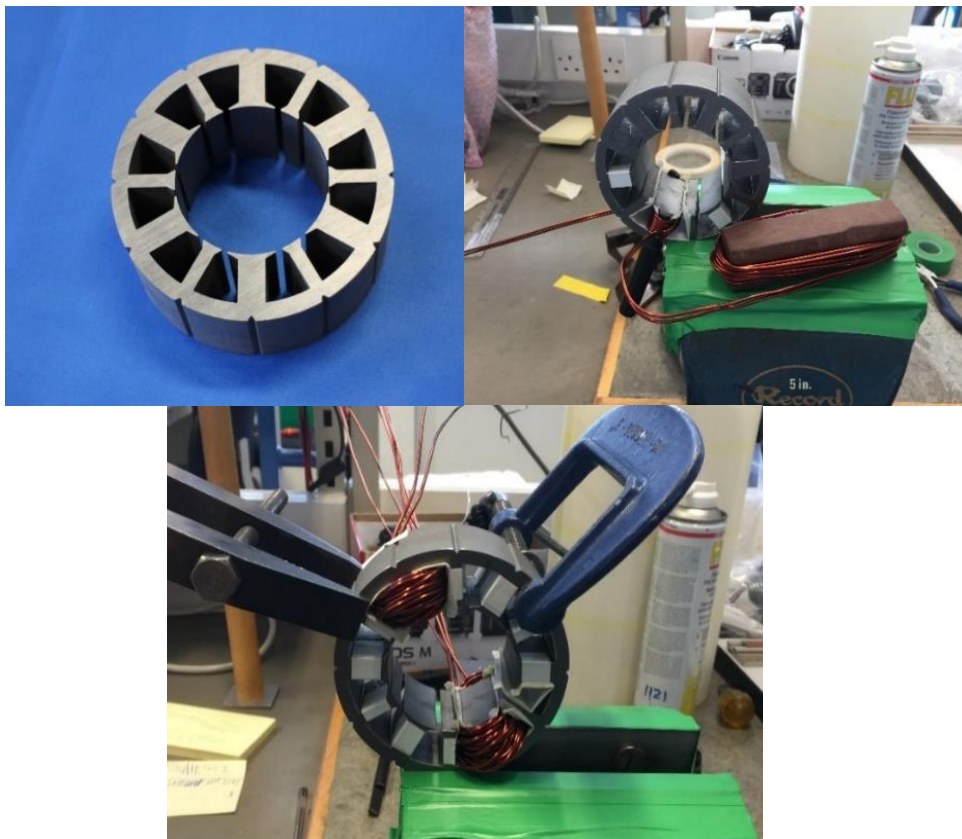


Figure 121: Dissimilar teeth stator as an intermediate design to be combined with baseline motor's rotor

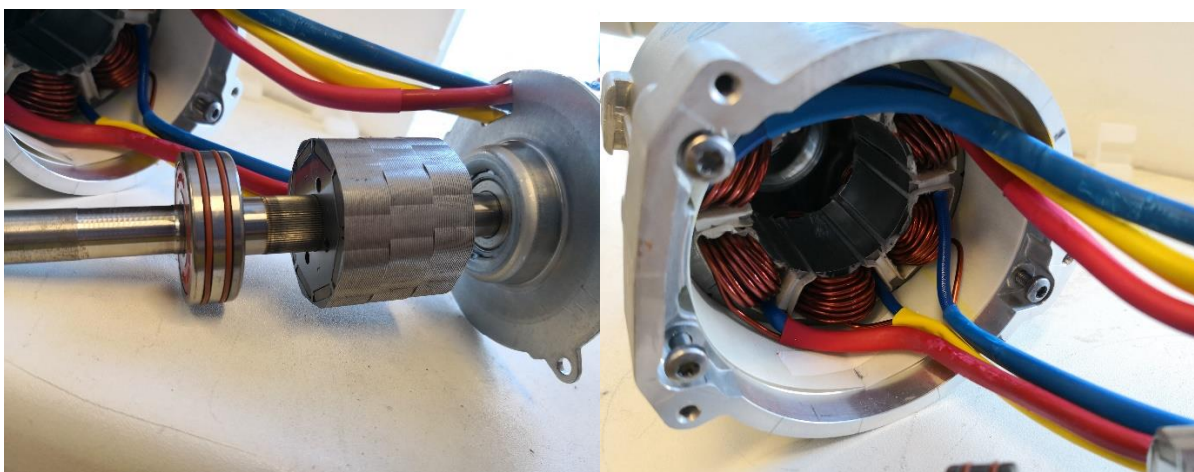


Figure 122: Rotor from the baseline motor and wound stator assembled in to the housing.

Lane 1		Lane 2	
Lines	Resistance (line-line) [m ohms]	Lines	Resistance (line-line) [m ohms]
AB	55.7	AB	58.0
BC	56.6	BC	55.8
CA	56.0	CA	59.4

Table 5: measured winding resistance for the new-stator design with modular windings.

Total conductor Length /mm	3320	Average Length of Turn/mm	138.3	Total Winding Volume per coil / mm <sup>3</sup>	7900
coil Resistance/ mohms	27.4	Average Body length of Turn/mm	72.00	All turns Conductor Area per coil / mm <sup>2</sup>	54.48
Overall Motor Length /mm	58.4	Average end turn Length /mm	66.3	Motor End-winding inductance /uH	18.32

Table 6: windings parameters calculations based on numerical equations for the new-stator design with modular windings.

Table 5 and Table 6 show that the measured winding resistance numerical values are within 5% difference. However, the new-stator designs phase resistance is approximately higher by 20% which significantly affects the power drop across the windings; hence, the knee point of the torque-speed curve will be highly affected.

### 4.3. No-load investigations and comparisons:

This section compares the new-design's no-load performance with that of the baseline motor using two dimensional and three-dimensional finite element analysis. It then compares these results with measurements on the built prototype.

#### 4.3.1. Cogging torque:

As shown in Figure 123 and Figure 124, based on 2D FE analysis, the new design's un-skewed cogging torque is reduced by a factor of five over the baseline motor. This is due to the arrangement of the dissimilar teeth. The different tooth widths have an effect upon cogging which is similar to that which has been encountered with cases where the rotor magnets have varying pole arcs. Bianchi and Bolognani [28] used the varying rotor pole arc approach to minimize the cogging torque. However, changing the magnet pole arcs leads to unbalanced back-emf in the coils. With the design proposed in this paper this issue can be overcome as the back emf only induces a voltage in the single layer winding, wound on the wide tooth.

Both designs are the skewed to minimise the 6<sup>th</sup> electrical harmonic of cogging torque, which is the dominant contributor. Figure 125 and Figure 126 show the result for the skewed machine. The 6<sup>th</sup> electrical harmonic is reduced by two orders of magnitude. However, it is clear that the torque ripple benefit of the new design no longer occurs: both the new design and the baseline design have similar levels of torque. But, the spread of harmonics is different, although overall peak to peak magnitude is similar.

## Chapter 4: A new modular design

Clearly the new design has not attenuated the higher harmonics to as large an extent. The 18<sup>th</sup> electrical harmonic is higher in the new-design by approximately 17% for both skewed and un-skewed rotor. This is due to the three step skewing which does not affect that particular harmonic, as explained in [59].

However, it does raise the question: can the new design be used without the need for skew?

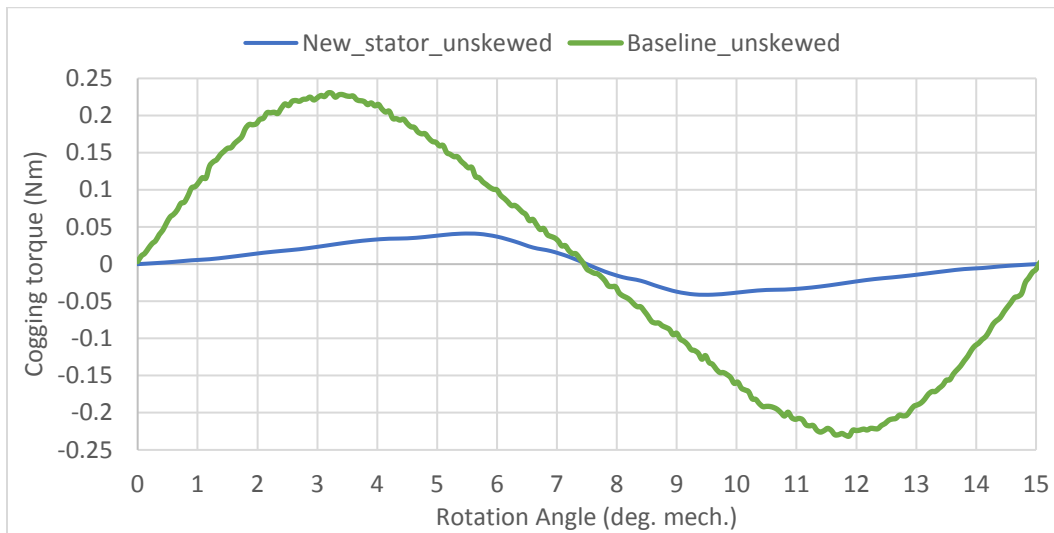


Figure 123: Cogging torque comparison between the baseline motor and new-stator design (2D FE simulations and un-skewed rotor).

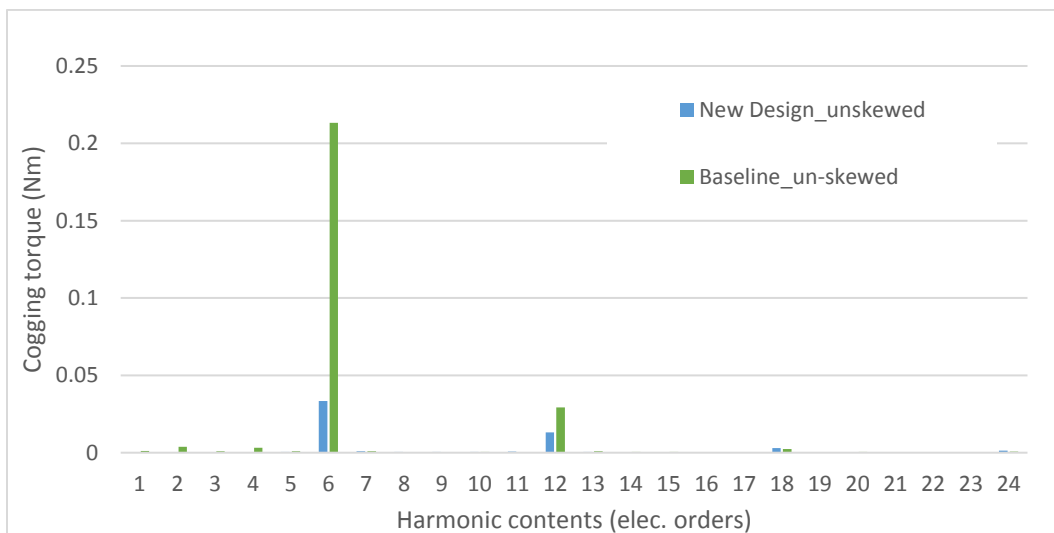


Figure 124: Harmonic content of Figure 123 (2D FE simulations and un-skewed rotor).

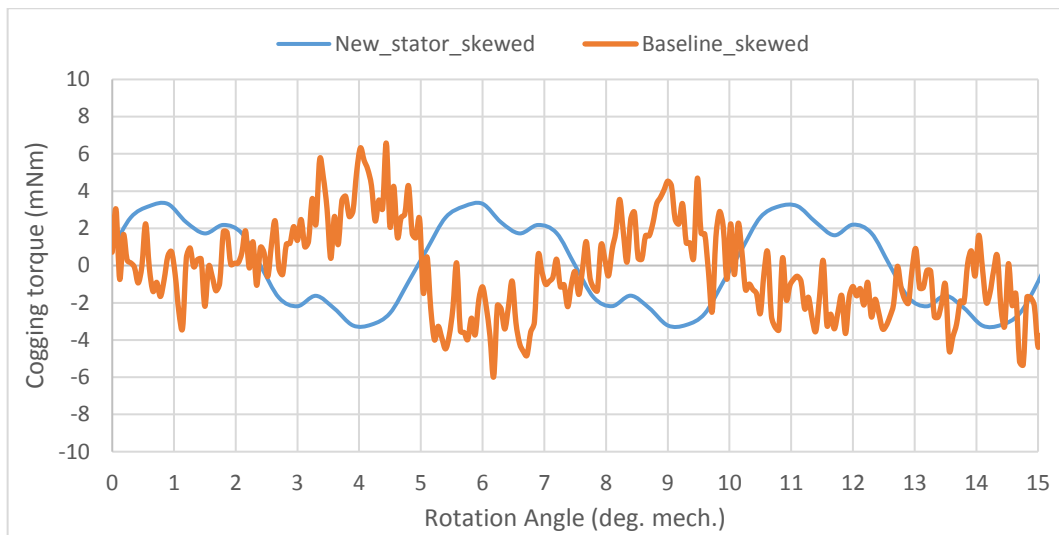


Figure 125: Cogging torque comparison between the baseline motor and new-stator design (2D FE simulations and skewed rotor).

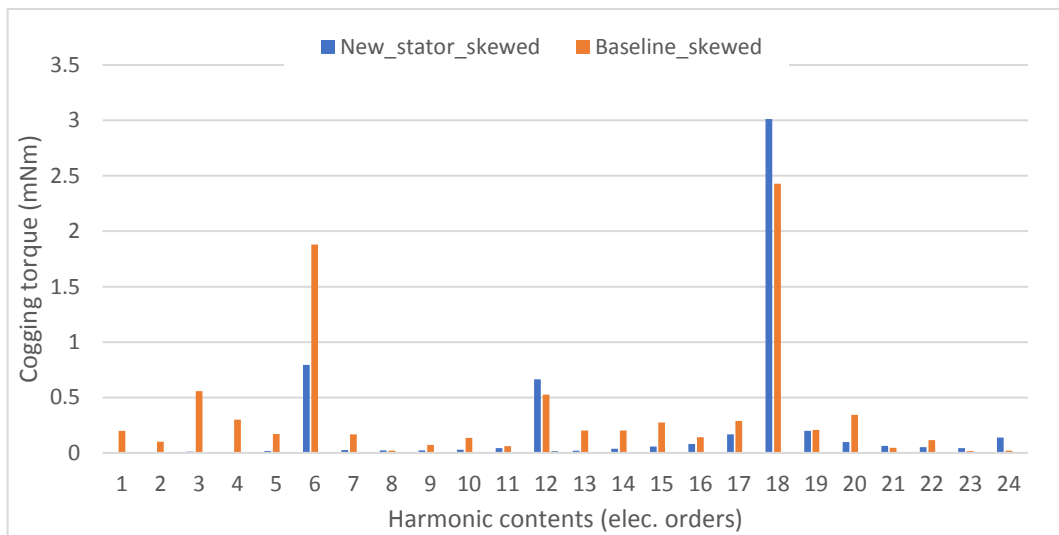


Figure 126: Harmonic content of Figure 125 (2D FE simulations and skewed rotor).

### 3D results vs practical:

Two-dimensional modelling predicts cogging torque of approximately 4mNm in an electrical machine capable of delivering over 5Nm; hence cogging torque is around 0.1% out the output torque – an exceptionally low value. At the ends of the machine there are fringing flux elements travelling across the axial ends of the air-gap and axial fluxes between the step skewed rotor pucks. These fluxes can produce a small cogging element and so they also need to be modelled using a 3D finite element model. This has been done and harmonic analysis of the overall cogging torque undertaken. The prototype motor has also been experimentally tested to produce experimental results for cogging torque (setup and test rig is described in **Test rig**).

Figure 127 shows both 3D finite element model results and experimental results for both the new design and for the baseline motor. The new design’s cogging torque is low but is still approximately double that of the baseline motor. This is not surprising, as the rotor and stator have not been designed together to minimise cogging torque.

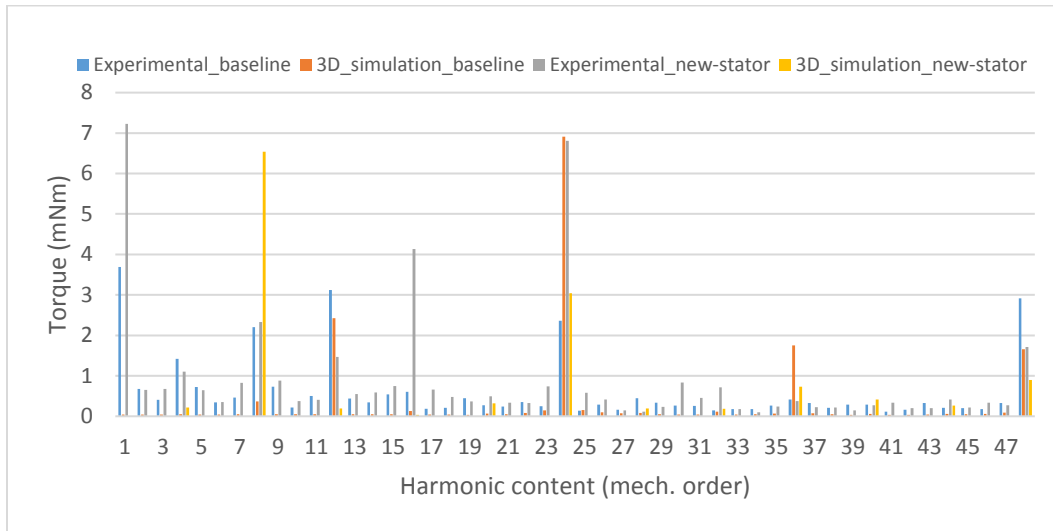


Figure 127: Harmonic content comparison of the cogging torque for both baseline and new-stator designs

	Baseline Experimental	Baseline 3D Simulations	New-stator Experimental	New-stator 3D Simulations
4 <sup>th</sup> order	1.42	0.05	1.1	0.21
8 <sup>th</sup> order	2.2	0.37	2.33	6.54
12 <sup>th</sup> order	3.12	2.43	1.46	0.2
16 <sup>th</sup> order	0.61	0.13	4.13	0.04
24 <sup>th</sup> order	2.36	6.9	6.8	3.04
36 <sup>th</sup> order	0.42	1.75	0.52	0.73
48 <sup>th</sup> order	2.92	1.65	1.71	0.89

Table 7: Comparison of certain harmonic contents of Figure 126 which are cogging torque in mNm.

### 4.3.2. Back-emf:

As mentioned earlier, two-dimensional finite element simulations predict that the back-emf of the new design will be approximately 13.6% greater than that of the baseline motor, due to an increase in winding factor. This is confirmed in Figure 128 and Figure 129. The increased back emf should also result in a corresponding increase in torque per Ampere.

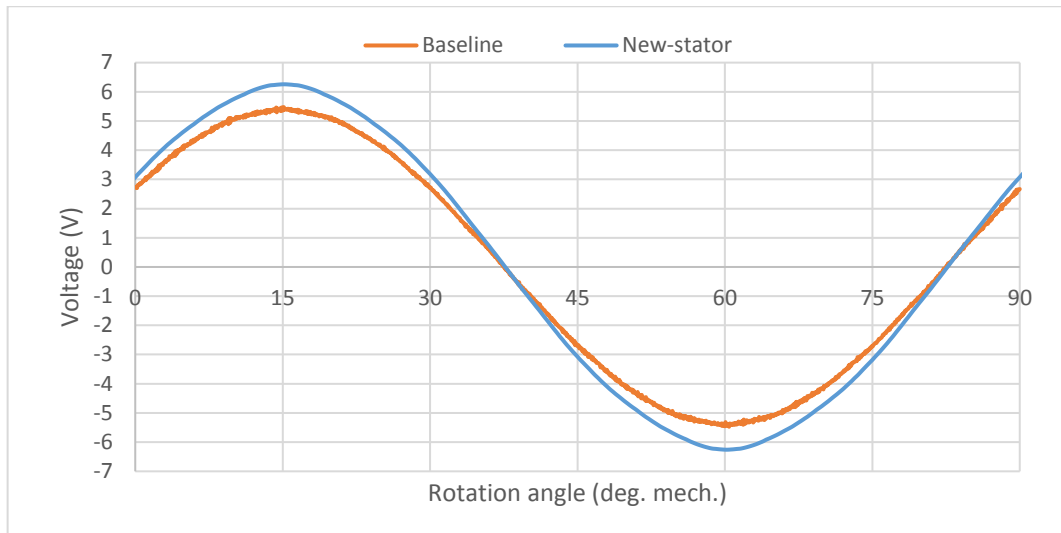


Figure 128: 2D FE back-emf comparison between baseline and new-stator designs for skewed rotor.

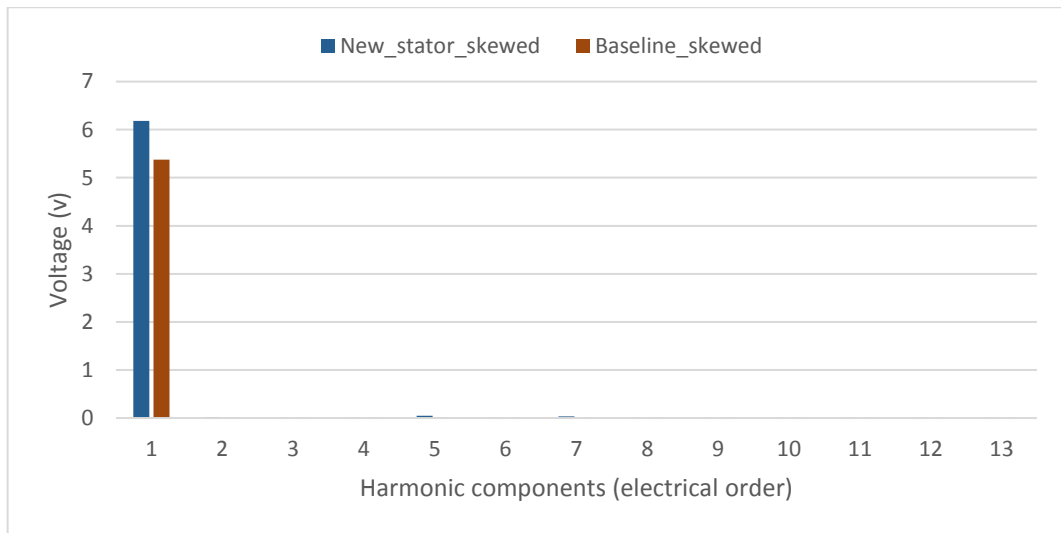


Figure 129: Harmonic content of back-emf comparison (Figure 128).

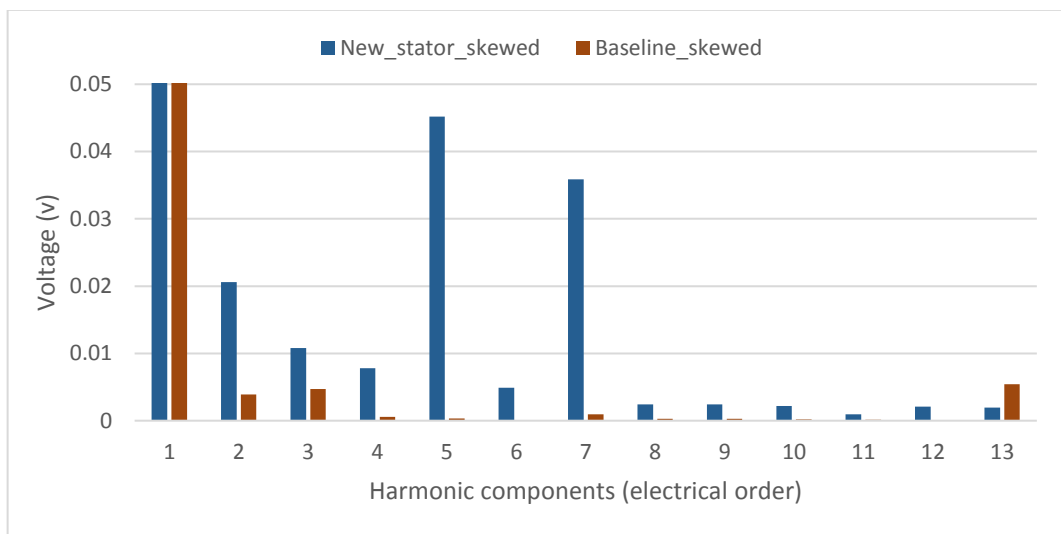


Figure 130: Harmonic content of back-emf comparison (Figure 128) [scaled].

Figure 130 shows the harmonic content of the back emf waveform in some detail. 5<sup>th</sup> and 7<sup>th</sup> harmonic orders in the new-stator design are around 1% of the fundamental, which is much higher than in the baseline design. These harmonic components lead to torque ripple at loaded conditions.

### 3D results vs practical:

Just as with cogging torque, three-dimensional simulations are needed to include end effects and axial fluxes between rotor pucks and their impact upon the back emf. As predicted in the simulated back-emf results, the new-stator design offers higher back-emf over the baseline design. Figure 131, shows both measured and simulated results for the new design and the baseline motor.

Simulated 3D results of the fundamental back emf are within 3% of the measurements for both machines. The differences were postulated to be down to manufacturing tolerances and variations in material characteristics.

It is notable that, unlike two-dimensional simulation results, both simulations and measurements of the new design have lower harmonic content in the back emf than that in the baseline motor.

Figure 132 shows that there are differences between 2D and 3D FE results for both motors which might be due the fringing fluxes, magnet self-linking fluxes at edges and axial fluxes between the magnets of the different pucks.

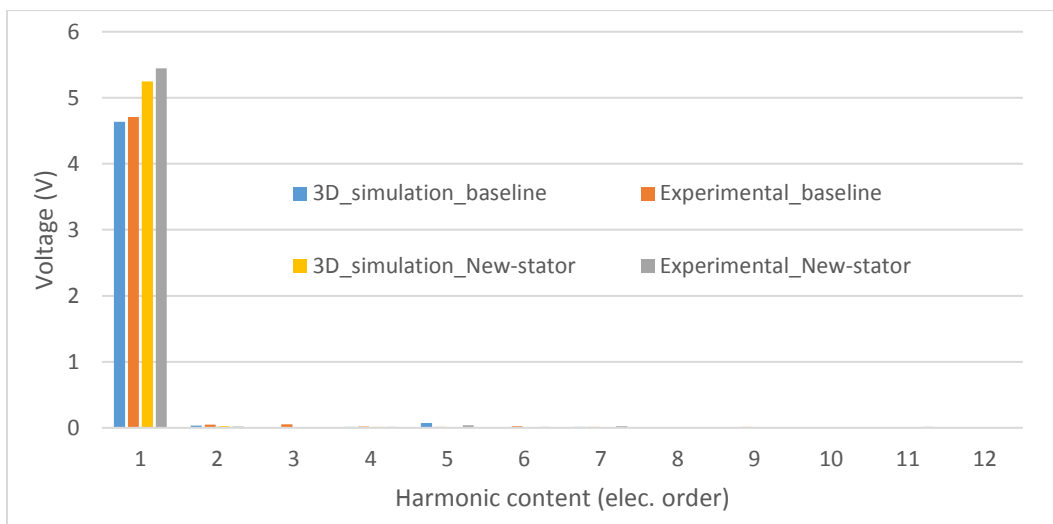


Figure 131 : Back-emf comparison of the both the motor designs (practical vs simulation).

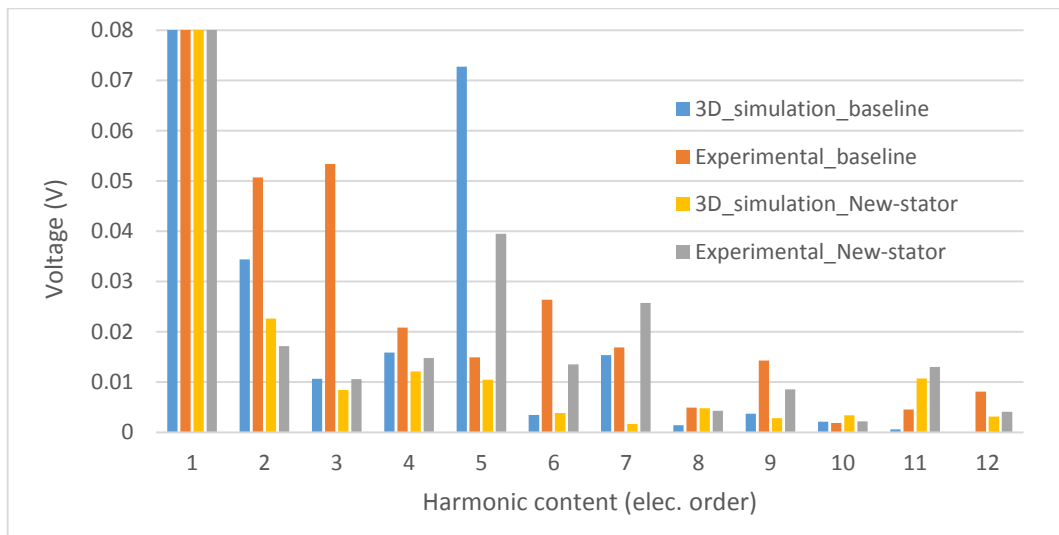


Figure 132: Back-emf comparison of the both the motor designs (practical vs simulation) [scaled].

#### 4.4. Loaded comparisons:

This section investigates the new-stator design’s loaded characteristics and compares them to those of the baseline design.

##### 4.4.1. Torque vs input current:

Figure 133 compares the torque of the two designs as a function of current. The new design gives greater torque than the baseline design at all currents. However, 2D analysis suggests that the torque constant drops by 4% when moving to half load and by 8% when moving from light load to full load. In contrast the torque of the baseline motor drops by only 2% between light load and full load. This effect is a direct result of the increased armature reaction flux, causing increased stator saturation. as the back-emf increased by 13.6%, saturation in the stator prevents that increase to reflect on the motor torque at full-load.

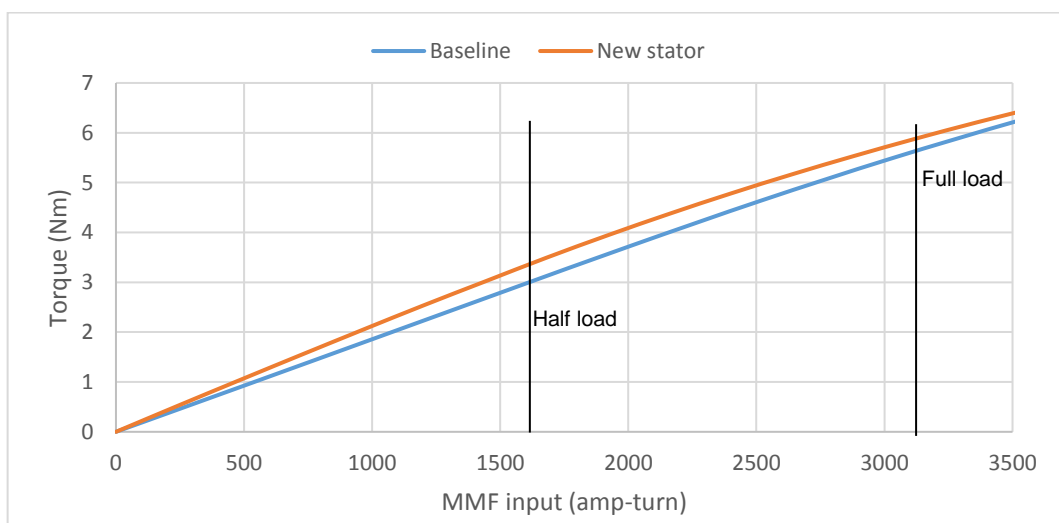


Figure 133: 2D FE torque-MMF comparison between the new designed stator and baseline motor.

Figure 134 and Figure 135 show magnetic flux plots on load for the baseline and new designs in order to give more insight into the areas of magnetic saturation. Saturation in the new-stator design mostly occurs in the wound teeth and the yoke (highlighted by circles). This can be improved further by widening the wound tooth and the yoke, however it affects the slot area and slot fill factor which may lead to higher current density and hence more heat generated in the winding.

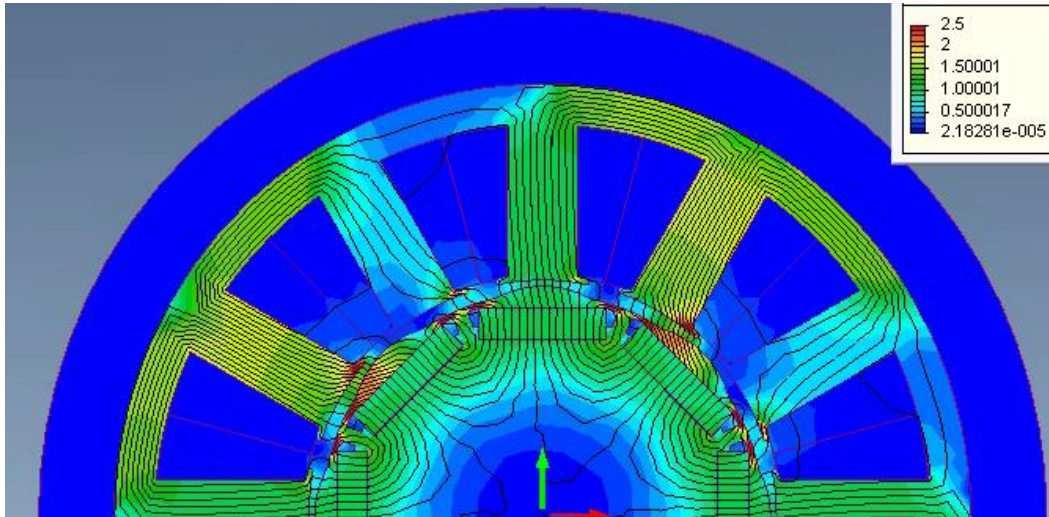


Figure 134: 2D FE magnetic flux density in the baseline motor (double-layer) for 10 degrees electrical current phase advance and at rated current (full-load).

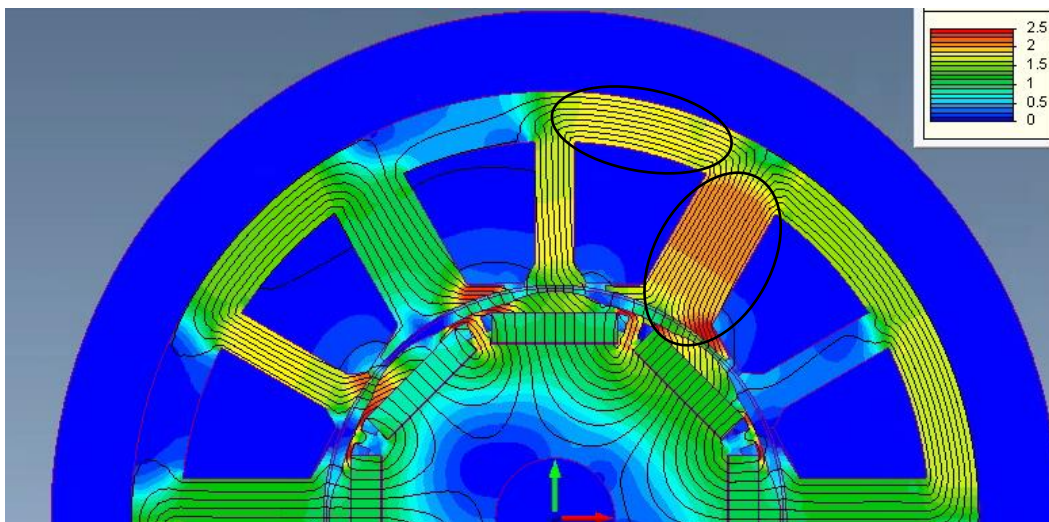


Figure 135: 2D FE magnetic flux density in the new-stator design for 10 degrees electrical current phase advance and at rated current (full-load).

#### 4.4.2. Torque vs Advance angle:

The extra torque that results from advancing the current angle towards the d-axis is due to saliency. Both motors have a degree of saliency that leads to maximum torque

per ampere at a certain advance angle as in Figure 136. The new-stator design has approximately 2% of saliency torque, whilst that of the baseline motor is 2.5%.

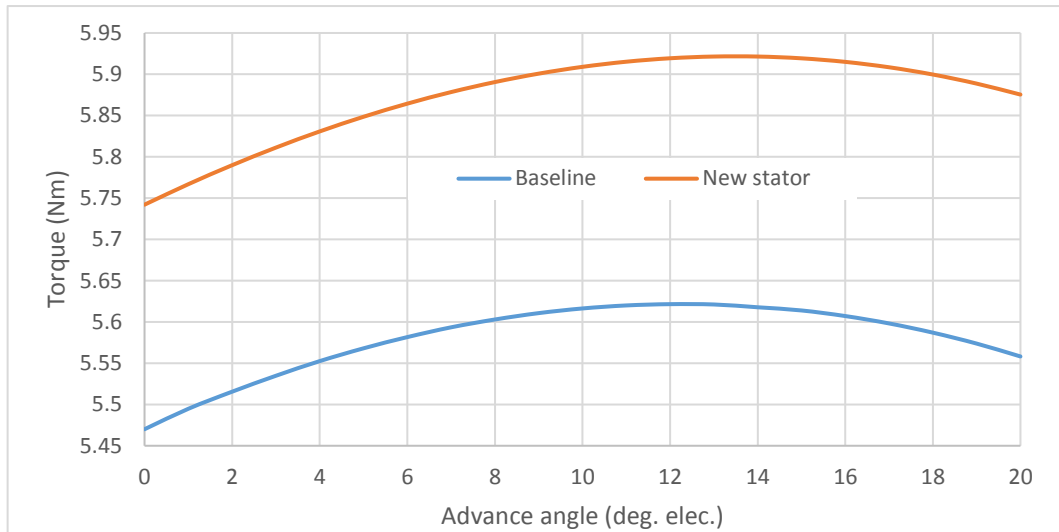


Figure 136: Comparison between MTPA of both baseline and new-stator designs based on 2D FE analysis.

#### 4.4.3. Torque ripple:

Figure 137 illustrates how the new design's torque ripple is higher than that of the baseline design. This is understandable as the design has not been optimised for minimum torque ripple. (This will be covered later in this chapter). The modular winding produces a rich set of space harmonics travelling asynchronously with the rotor (presented earlier in Figure 91). Some of these interact with harmonics of rotor saliency and produce another component of torque ripple which is current dependent.

Based on 2D FE analysis, the major harmonics of the new stator's torque ripple are approximately twice the magnitude of the baseline design.

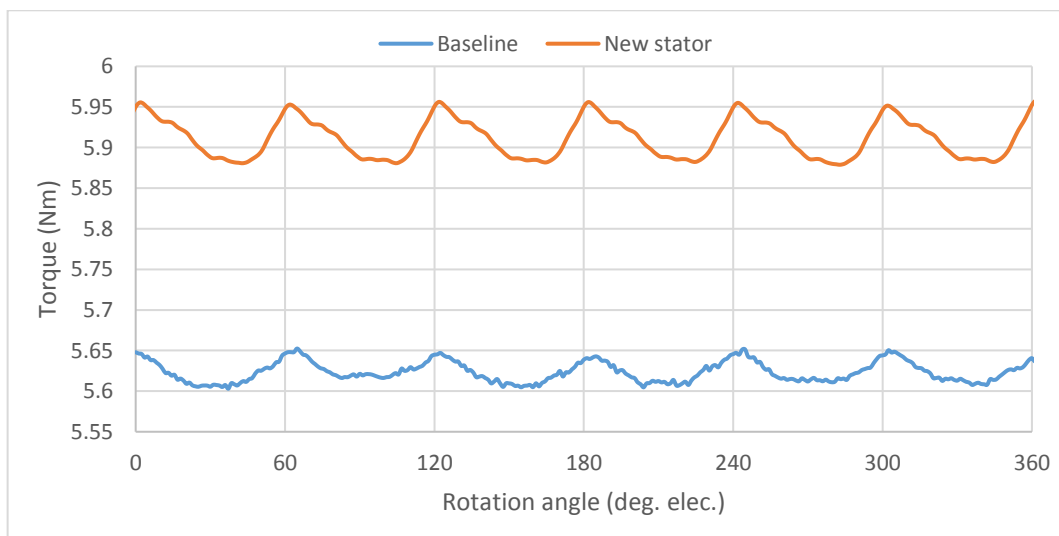


Figure 137: 2D FE torque and torque ripple comparison for both designs.

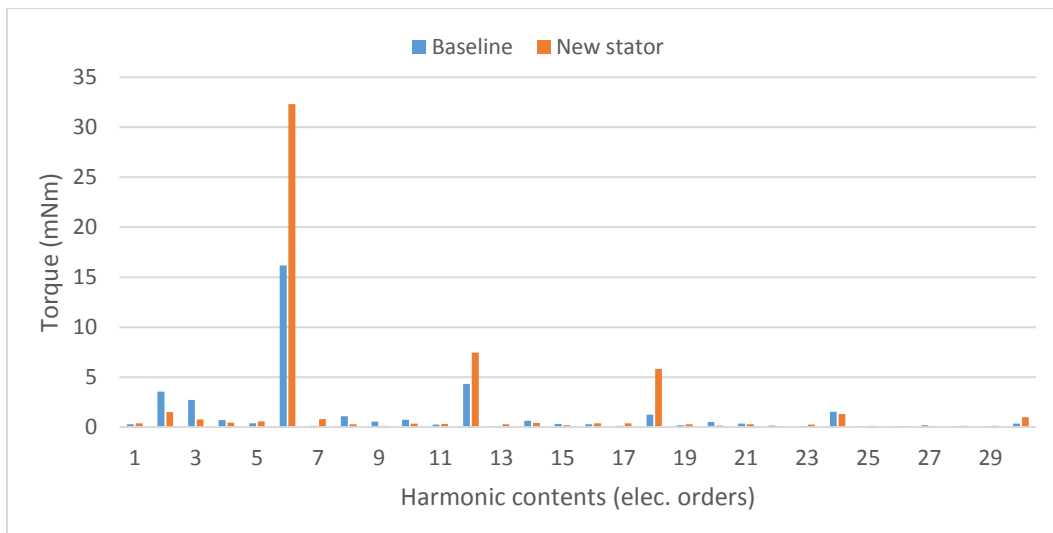


Figure 138: Harmonic content of 2D FE torque ripple comparison.

### 3D results vs experimental:

Figures 124 and 125 show how the torque capability of both designs is lower in 3D FE simulations and in experimental results than that predicted by 2D FE simulations. This is due to a number of effects, including:

- End-effects in which a component of the magnet flux axially leaks through the air, rather than link the stator.
- An effect due to the stepped nature of the skew, achieved by having a number of rotor pucks. This is not adequately represented in 2D simulations: there is an element of magnet flux which travels straight from puck to puck at the point of interface and from one puck through another to a different angular position in the stator, thereby reducing the flux linking the winding.
- The magnets are shorter by 7% in each rotor puck due to manufacturing tolerances which leads to a lower back-emf hence lower torque capability.

As explained in Chapter 2, 3D simulation of the baseline machine overestimates the measured mean torque value by 4%., thought to be due to variations in magnet properties and manufacturing tolerances.

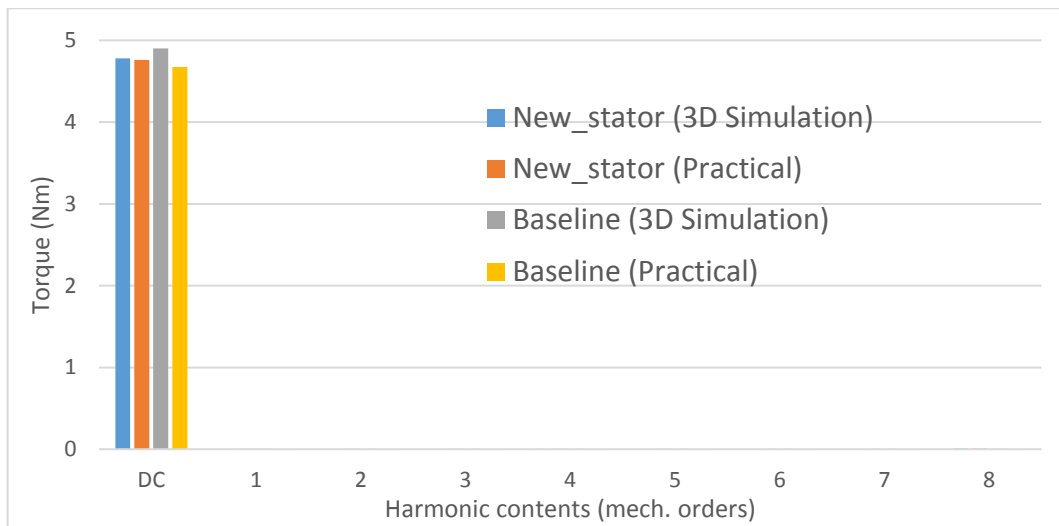


Figure 139: Torque (3D simulation and practical) comparison between baseline design and new-stator design.

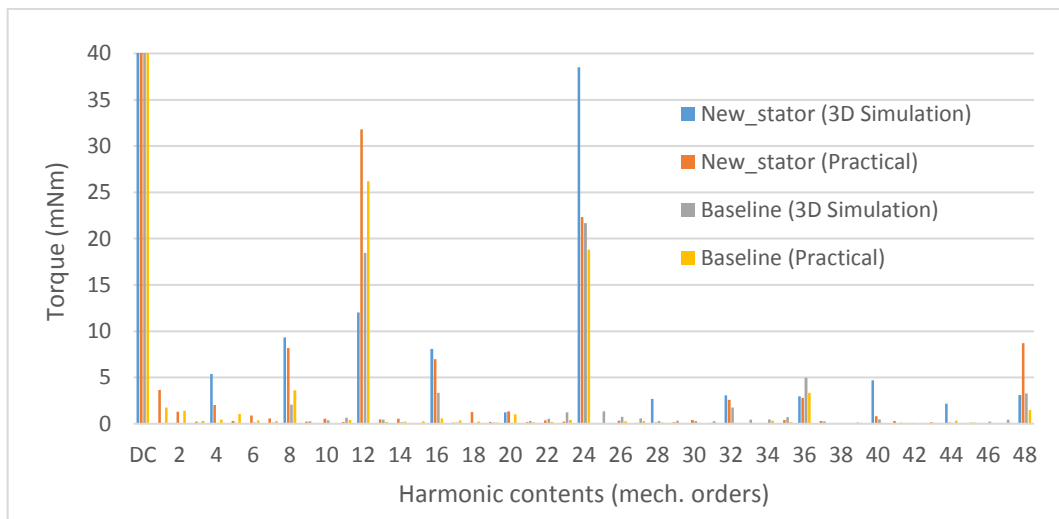


Figure 140: Torque ripple (3D simulation and practical) comparison between baseline design and new-stator design.

	Baseline 3D Simulations	Baseline Experimental	New-stator 3D Simulations	New-stator Experimental
Average torque (Nm)	4.9	4.67	4.78	4.76
4 <sup>th</sup> order (mNm)	0.08	0.43	5.4	2
8 <sup>th</sup> order (mNm)	2	3.62	9.3	8.2
12 <sup>th</sup> order (mNm)	18.45	26.2	12	31
16 <sup>th</sup> order (mNm)	3.34	0.56	8.06	6.97
24 <sup>th</sup> order (mNm)	21.66	18.8	38.5	22.3
36 <sup>th</sup> order (mNm)	4.96	3.34	2.98	2.8
48 <sup>th</sup> order (mNm)	3.26	1.47	3.1	8.7

Table 8: comparison of certain harmonic contents of torque ripple as in Figure 140.

From the above table, the harmonic components with noticeable values are 12<sup>th</sup> and 24<sup>th</sup> orders. In the experimental values, the 12<sup>th</sup> order is always higher than that of simulation values. This might be due to manufacturing tolerances. The amount of the rise in 12<sup>th</sup> order can clearly be seen from the 24<sup>th</sup> order drop.

#### 4.4.4. DC torque comparison (3D FE vs experimental):

In this test a constant dc current is fed into one phase and out a second phase. The rotor is then rotated at 10 rpm, and the torque measured. The main purpose of evaluating the DC torque is to highlight saturation effects when moving from half load to full load. Also, it is a cross-check between average torque with sinusoidal current and peak of the ripple on top.

The DC torque is a combination of both alignment torque and reluctance torque, with the reluctance torque varying at twice the spatial frequency of the alignment torque. These two effects can be easily be seen in this test. By taking the Fast Fourier transform (FFT) of a complete DC torque cycle, the 4<sup>th</sup> mechanical order shows the alignment torque while the 8<sup>th</sup> order shows the salient torque. Figure 141 and Figure 142 show that both measurements and 3D FE simulation results are very similar. They also show that the proportion of saliency torque is higher at high load: this is to be expected as, saliency is proportional to permeance variation in which saturation plays a big role. Also, in the absence of saturation of the rotor bridges between the magnets, saliency torque is proportional to the square of current.

Finally, the measured results in Figure 143 demonstrate that the new-stator design outperforms the baseline design by approximately 4% and 12% at full load and half load respectively. Here, it can clearly be seen that the DC torque at half-load is approximately higher by the increase of the winding factor (which is same as the increase of the back-emf).

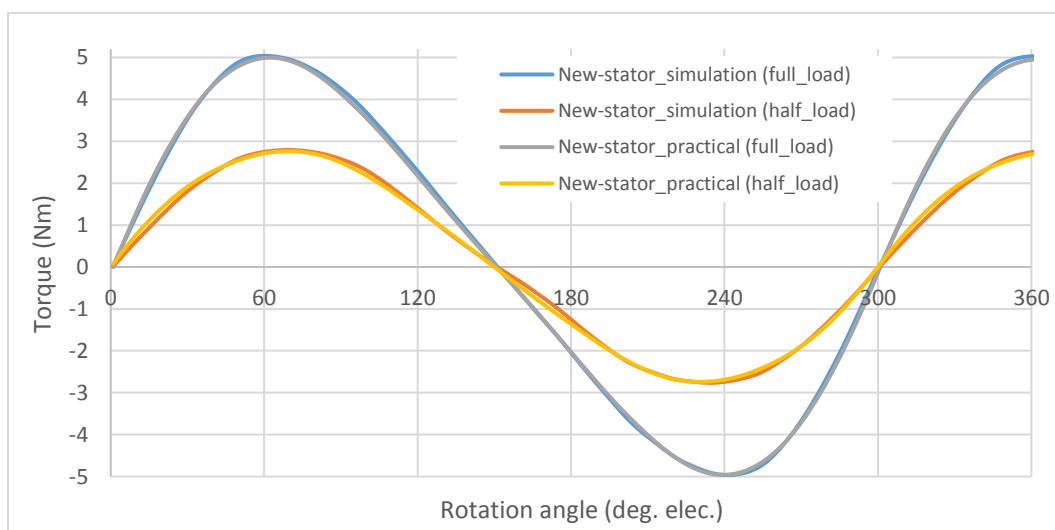


Figure 141: New-stator DC torque comparison between half load and full load.

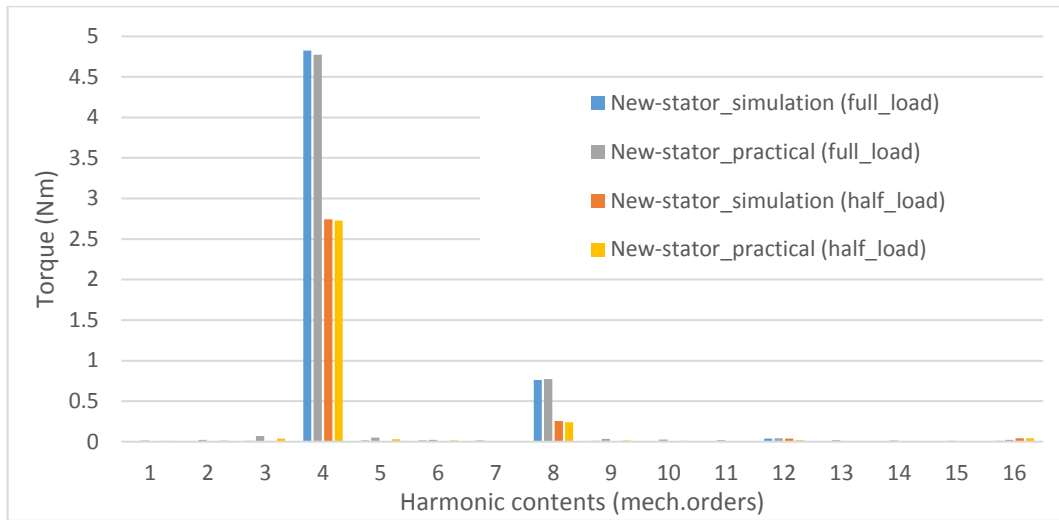


Figure 142: New-stator DC torque harmonic content comparison between half load and full load.

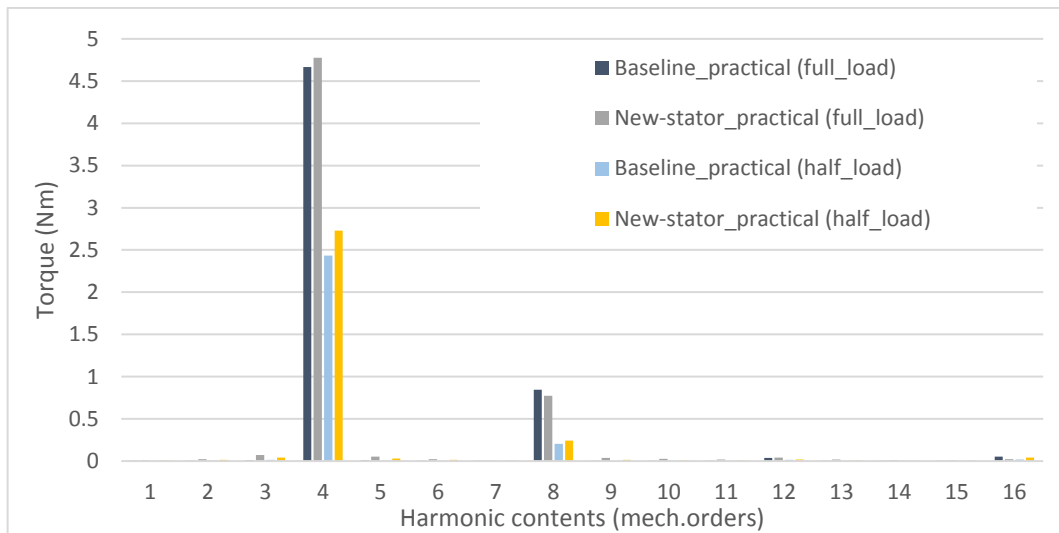


Figure 143: Harmonic content comparison of both baseline and New-stator designs.

	Baseline full-load	Baseline half-load	New-stator full-load	New-stator half-load
4 <sup>th</sup> order (Nm)	4.66	2.43	4.78	2.73
8 <sup>th</sup> order (Nm)	0.84	0.21	0.77	0.24

Table 9: comparison of main harmonic contents of DC torque as in Figure 143.

#### 4.5. Inductance comparison:

As in previous chapters, the frozen permeability method is used to calculate the direct axis and quadrature axis inductances. From the comparisons, the new-stator design offers approximately twice the phase inductance of the baseline design. This is due to the higher winding factor and the nature of modular windings.

**4.5.1. D-axis inductances:**

As mentioned earlier, the d-axis inductance is important for increasing the fault tolerant capability as it is the dominant component which limits the induced short circuit current at high speed. Figure 144 shows how the new stator design has more than double the inductance of the baseline motor. This is due to having half of the number of coils in parallel per phase. However, the inductance is higher than modular windings of chapter 3, as the stator tooth absorbs higher flux. Saturation in the core gives a 10% reduction in d-axis inductance in the new design when operating at full load.

The cross-coupling inductances, shown in Figure 145, are trivially small and can be neglected.

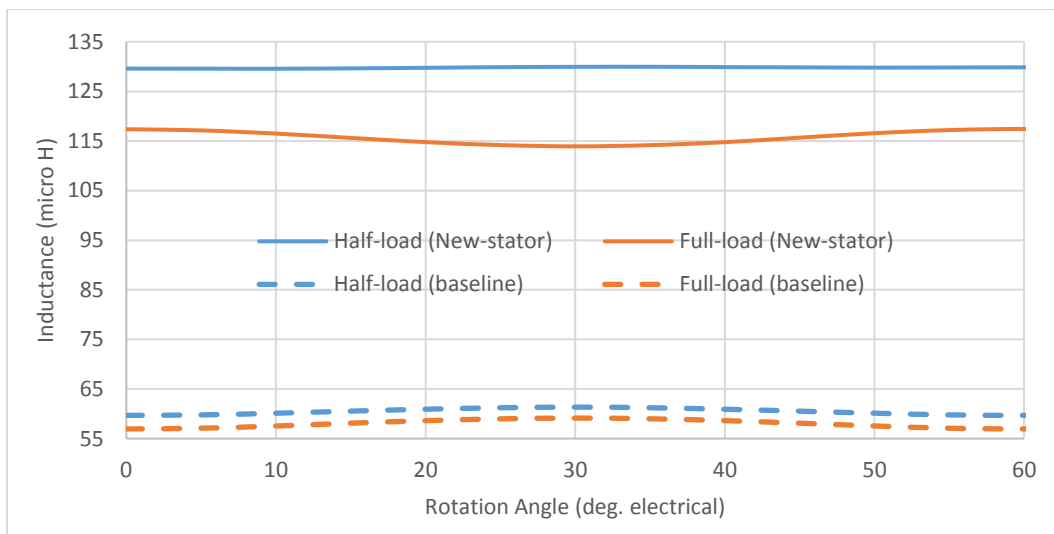


Figure 144: 2D FE d-axis self-inductance ( $L_{dd}$ ) comparison for different input phase currents.

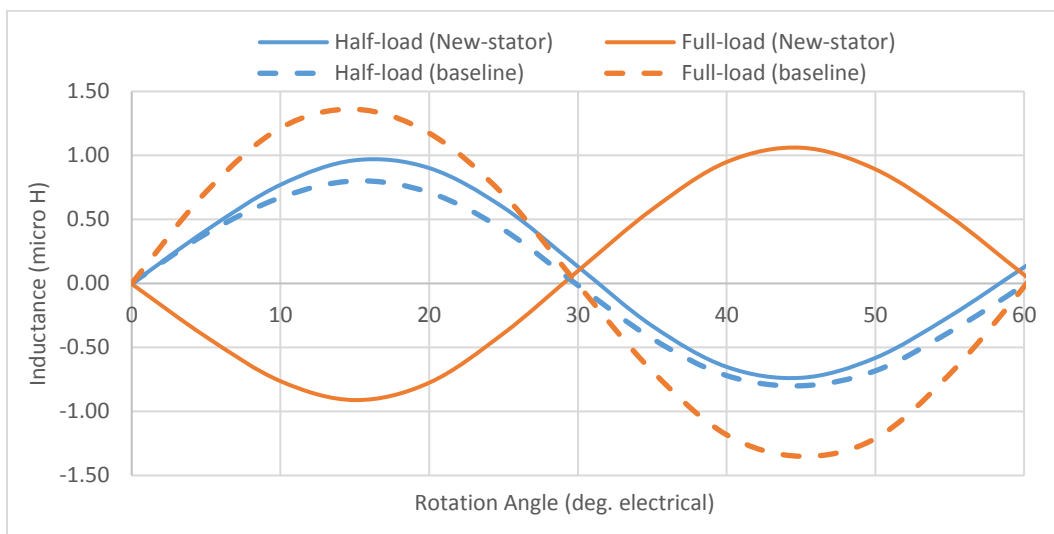


Figure 145: 2D FE q-axis inductance as a result of d-axis flux linkage ( $L_{qd}$ ) comparison for different input currents.

Figure 146 shows the case where the current is held at constant magnitude and moved from the q-axis to the negative d-axis. This shows how the d axis inductance rises as the current reaches the d-axis, reducing the flux and reducing magnetic saturation.

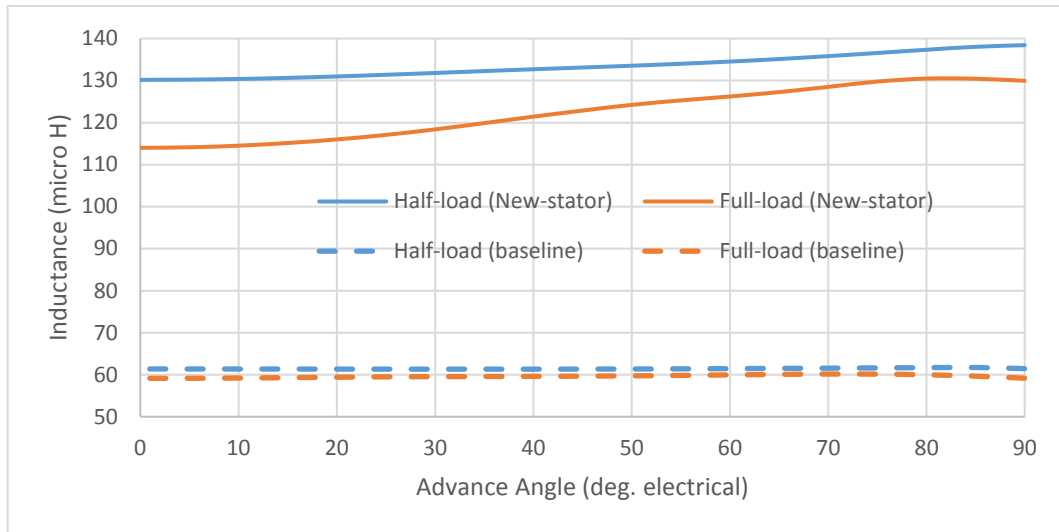


Figure 146: 2D FE d-axis inductance ( $L_{dd}$ ) vs current advance angle for different input phase currents.

#### 4.5.2. Q-axis inductances:

Figure 147 and Figure 149 show that in the new design the q-axis inductance is once more approximately doubled in the new stator design. It also drops markedly with current. This is due to saturation of the thin rotor bridges between the rotor poles. In all cases of current advance angle, the rotor is stationary while the current is being advanced from q-axis (0 electrical degrees) towards d-axis (90 electrical degrees).

Figure 148 shows how, once more, the cross-coupling inductance is negligible.

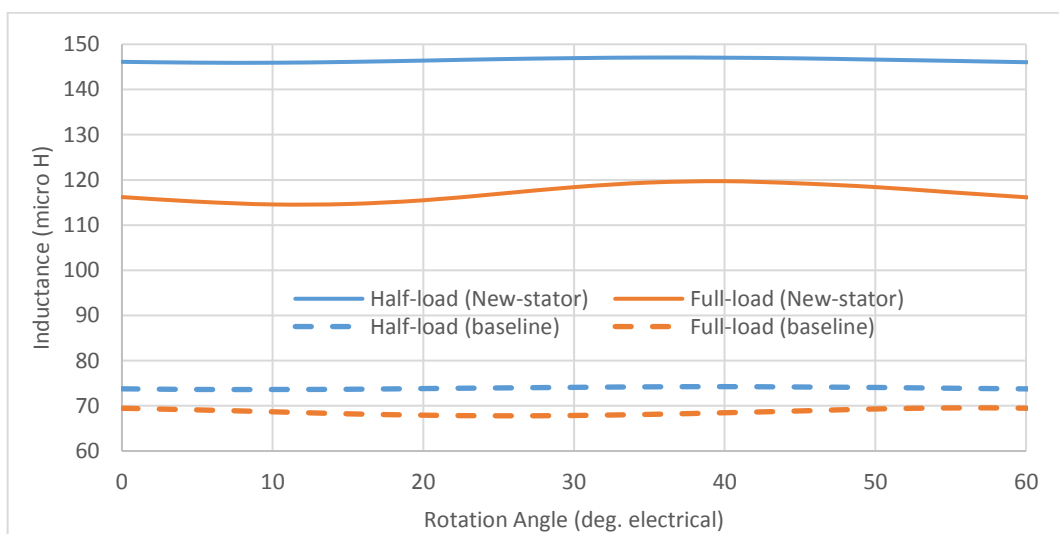


Figure 147: 2D FE q-axis self-inductance ( $L_{qq}$ ) comparison for different input phase currents.

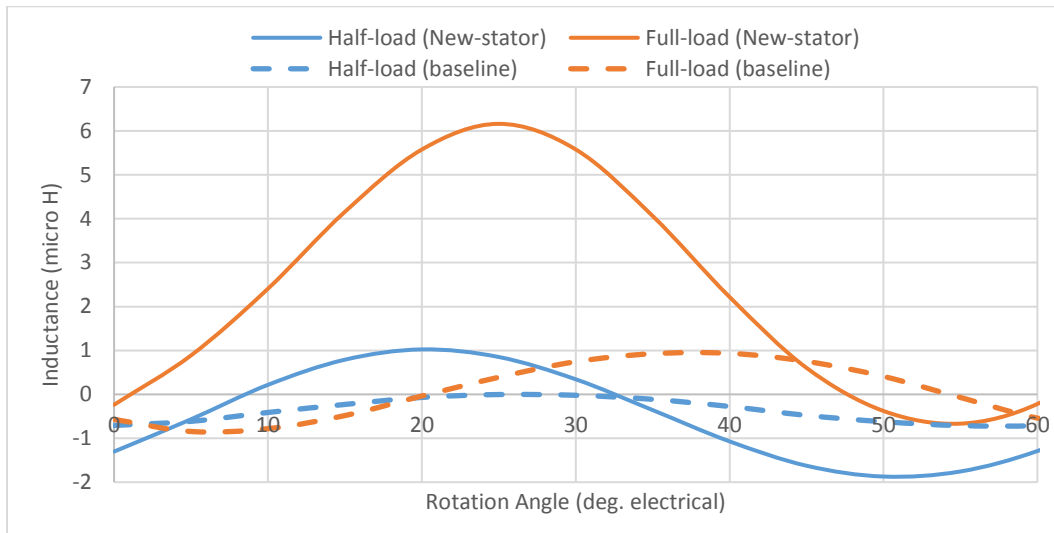


Figure 148: 2D FE d-axis inductance as a result of q-axis flux linkage ( $L_{dq}$ ) comparison for different input currents.

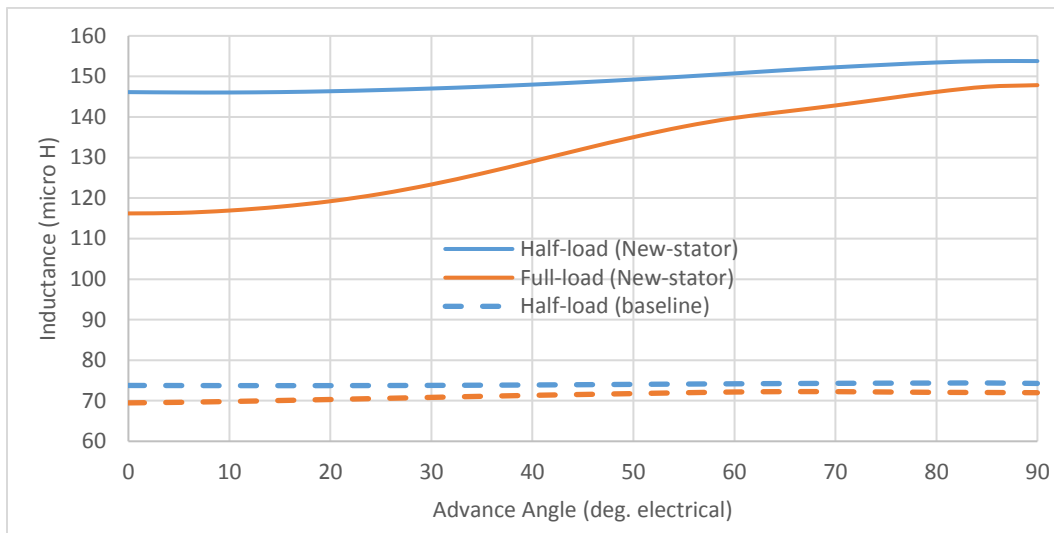


Figure 149: 2D FE q-axis inductance ( $L_{qq}$ ) vs current advance angle for different input phase currents.

### 4.5.3. Magnet flux linkage:

The magnet flux has to share its magnetic circuit with the armature reaction flux. As the load conditions vary then saturation in the core changes and, in turn, the magnet flux is altered. Similar to Chapters 2 and 3, the magnet flux is calculated under loaded condition when the current is fully imposed on d-axis (maximum advance angle). The magnet flux becomes higher under full-load compared to half-load as the core desaturated due to high input current (similar to the baseline motor) as shown in Figure 150. For both designs and at full advance angle, the magnet flux linkage is higher by approximately 3% due to core desaturation by the d-axis input current

Figure 151 shows the magnet flux linking the q-axis component due to cross coupling is approximately 10%, and at full-load the polarity of the flux linkage becomes opposite due to doubling the current per tooth.

However, when the current is on the q-axis (as in normal operating conditions), the magnet flux as expected is lower at full-load than half-load. However, when the current towards the d-axis (as in the flux weakening conditions), the current component on the d-axis increases hence the core desaturates. As the current reaches a certain point (where saliency torque is at maximum), the magnet fluxes at both half-load and full-load conditions become equal. Finally, when the current component is fully inserted in d-axis, the full-load magnet flux for both machines are clearly higher than half-load conditions as in Figure 152.

While the New-stator design is modular winding and possesses higher winding factor, the magnet flux is nearly 18% higher. Also, the current input per tooth is doubled which desaturates the core more that is why the percentage is slightly higher the winding factor.

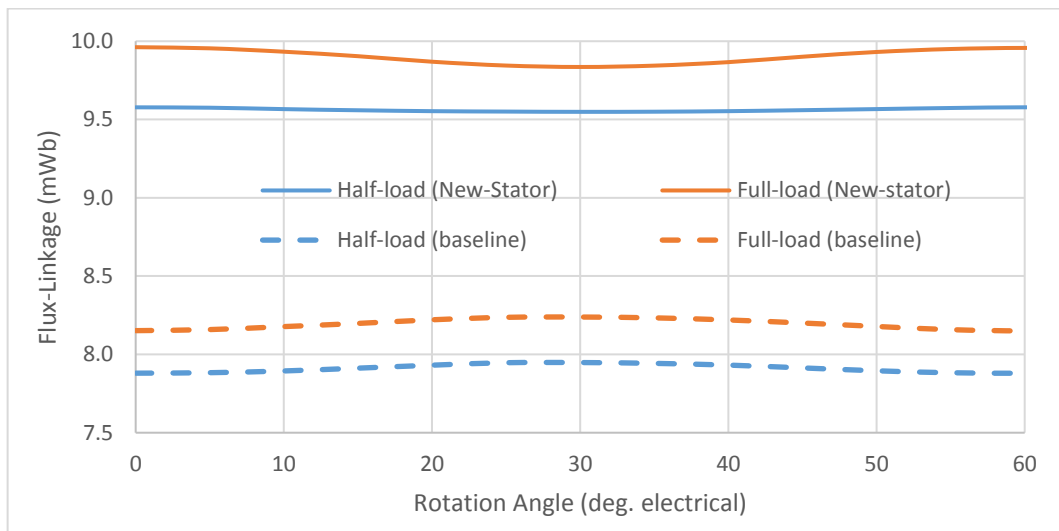


Figure 150: 2D FE d-axis magnet flux linkage ( $\psi_{Fd}$ ) comparison for different input currents.

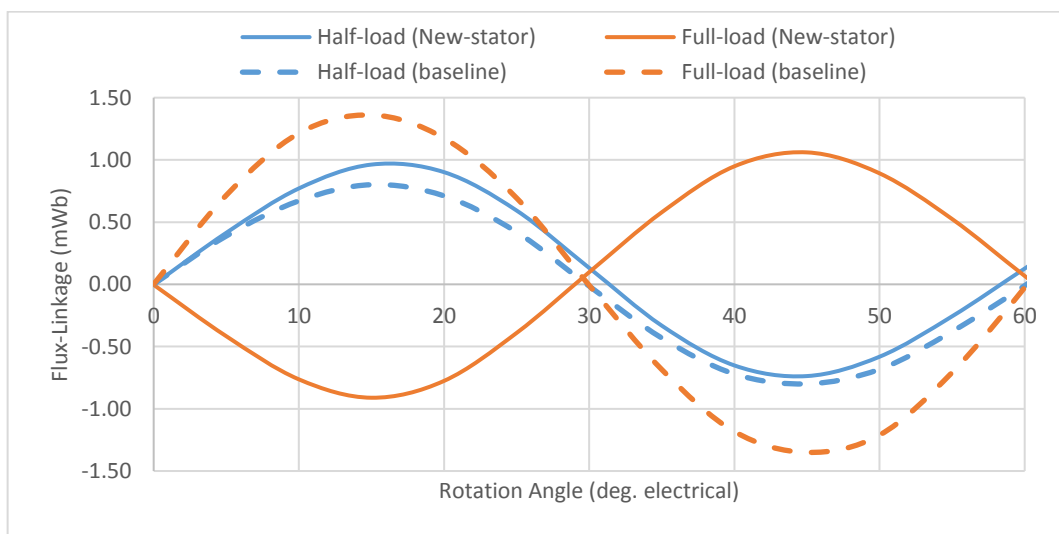


Figure 151: 2D FE q-axis magnet flux linkage ( $\psi_{Fq}$ ) comparison for different input currents.

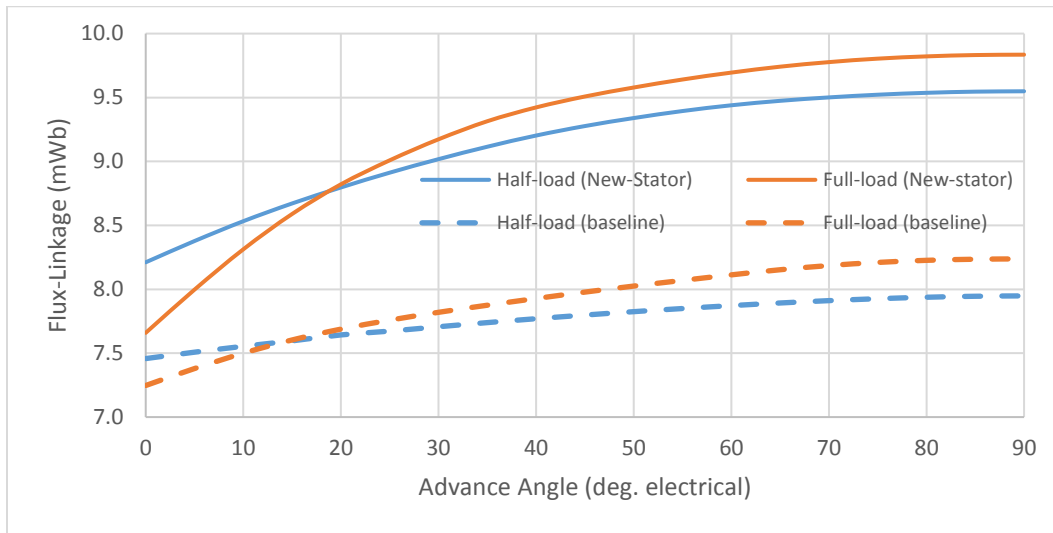


Figure 152: 2D FE d-axis flux linkage ( $\psi_{Fd}$ ) vs current phase advance angle for different input phase currents.

#### 4.6. Torque capability under fault conditions:

The new stator design offers higher fault-tolerant capability as predicted, due to its higher inductance. As the overall torque capability is increased and the short circuit current decreased due to the inductance, the new stator outperforms the baseline motor in the constant torque region. From all coils short analysis (Figure 153), it can be seen that the drag torque of the new-stator design is significantly lower, and the peak drag torque occurs at half of the speed compared to the baseline due to having approximately double of the inductance and similar resistances. Unlike the baseline motor, the drag torque and the short-circuit current of the new-stator design significantly matched the numerical values due no transformer coupling between the coils. The un-wound narrow tooth helps in decoupling the motor phases and almost eliminates any unbalance in the back-emf, hence there is lower torque ripple whilst operating under faulted conditions (which will be shown in later sections). This section will focus on any improvements that the new-stator design provides under faulted conditions.

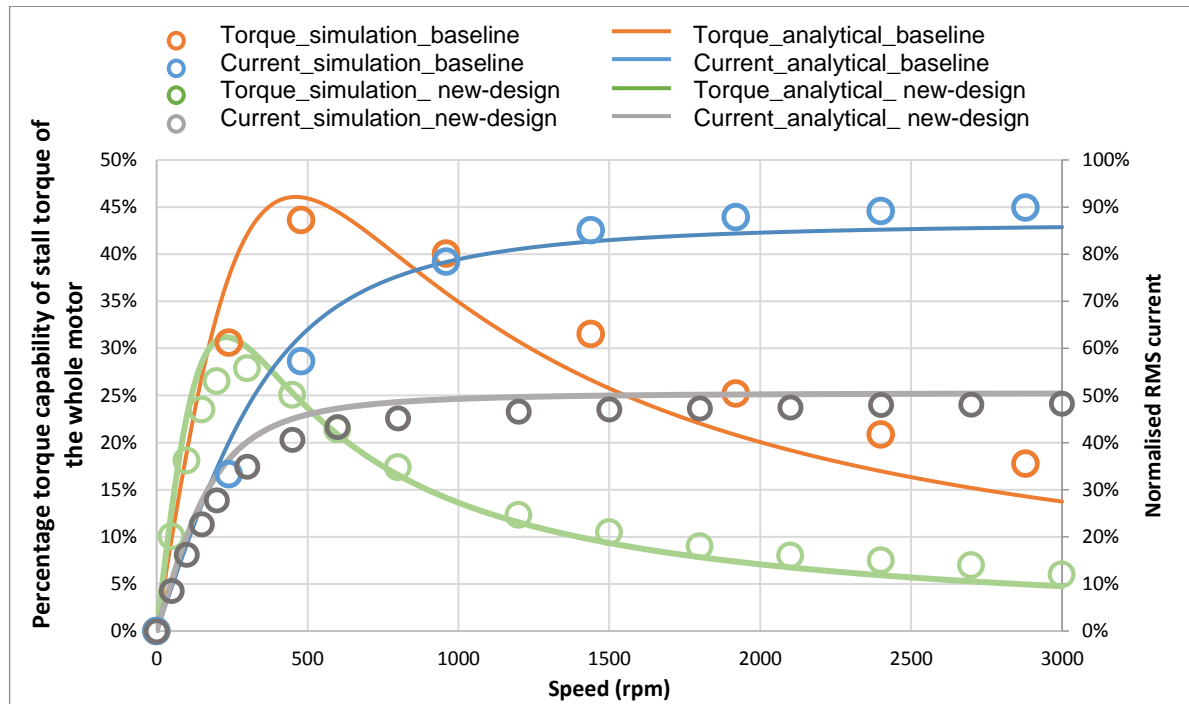


Figure 153: Drag torque and short-circuit current comparison between baseline and new-design. The torque is normalised against the rated torque of the baseline motor.

#### 4.6.1. No-load investigation:

As investigated in Chapter 3, the modular winding arrangement magnetically and physically isolates the phase windings. This improves the motor performance under faulted condition as the impact of the faulty lane on the healthy lane is significantly reduced.

During no-load investigations, the healthy-lane of the motor is inactive, whilst the faulted lane is short-circuited across its terminals. The points of interaction which are explained in Chapter 2 and their effects are significantly reduced. The back-emf of the inactive lane shows that the effect of the short-circuit current of the shorted lane upon the healthy is virtually negligible. Figure 154 demonstrates that the back-emfs are not affected. The dotted lines are the no-load back-emf when the motor is operated under healthy conditions, whilst the solid and dashed lines represent the back-emfs of the interleaved and half-half arrangements of the inactive lanes when a lane of the motor is short-circuited.

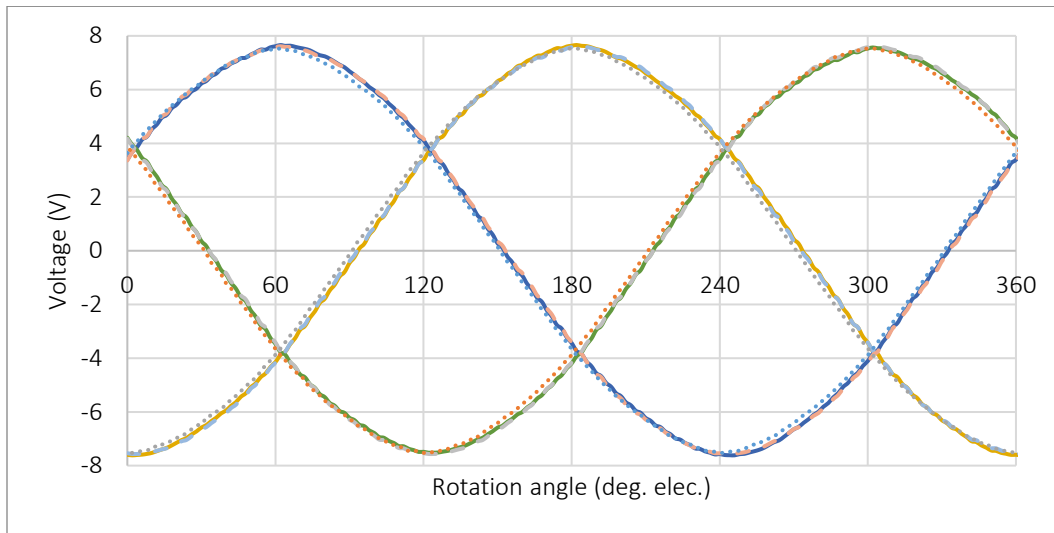


Figure 154: 2D FE back-emf comparison of different winding arrangements of the New-stator design under healthy and faulty conditions (solid lines: no-load back-emf, dotted lines: interleaved arrangement and dashed lines: half-half arrangement). This is a lane inactive and a lane 3-phase balanced short.

A comparison between measured and predicted back-emfs can be seen in Figure 155. It shows that both simulations and practical match very closely.

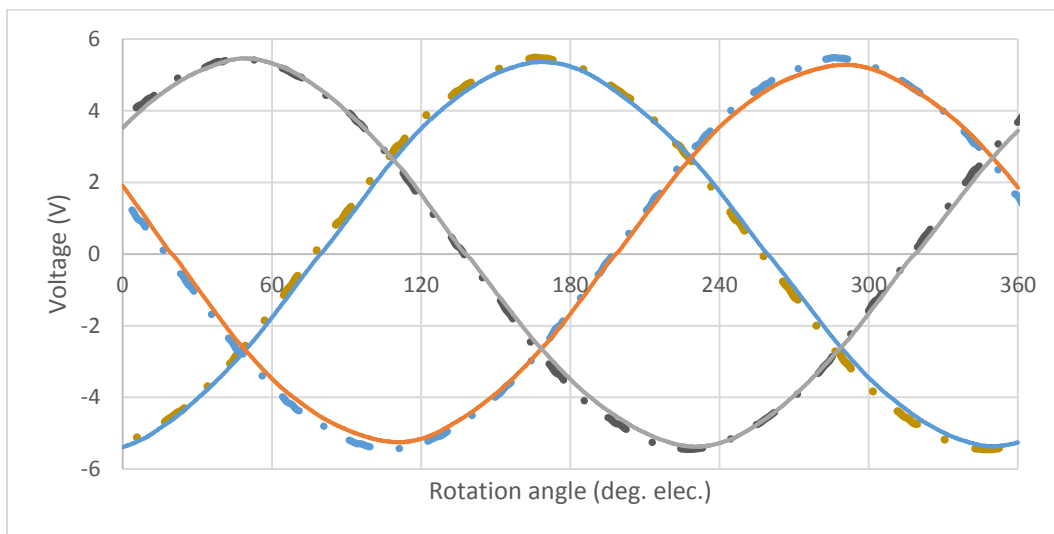


Figure 155: back-emf comparison between practical and simulation of the New-stator design (Half-half arrangement).

Because of the new-stator's high inductance, the short circuit current is significantly reduced and so is the short-circuit drag torque a short-circuit condition. Figure 156 and Figure 157 show how the peak no-load drag torque is reduced by approximately 40% and the short-circuit current at very high speeds is reduced by almost 45%. Measurements agree very closely with predictions. By combining the motor capability under both healthy and faulted conditions, the new-stator design is expected to outperform the baseline design in the constant torque region.

## Chapter 4: A new modular design

In the following graphs, both the short-circuit currents and the drag torques are measured leaving a lane of the motor inactive and shorting all the coils of the other lane together. Two identical motors were connected back to back, one of the motors was spun at different speeds and the average drag torque and RMS short-circuit current were calculated for each speed.

For the simulation results, the average torque and RMS short-circuit current were calculated then scaled to be compared to the measured results. The scaling was carried out taking both the end-winding inductance and shorter magnets per puck into considerations. They were both translated into a single percentage as the percentage value is directly proportional to the short-circuit current while the drag torque changes quadratically with the number.

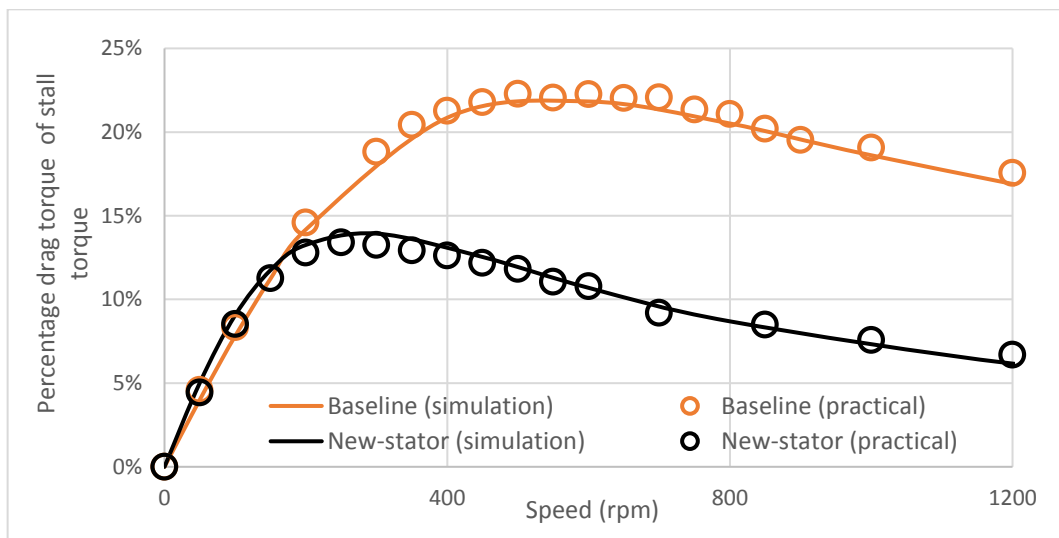


Figure 156: no-load drag torque comparison between baseline motor and new-stator design.

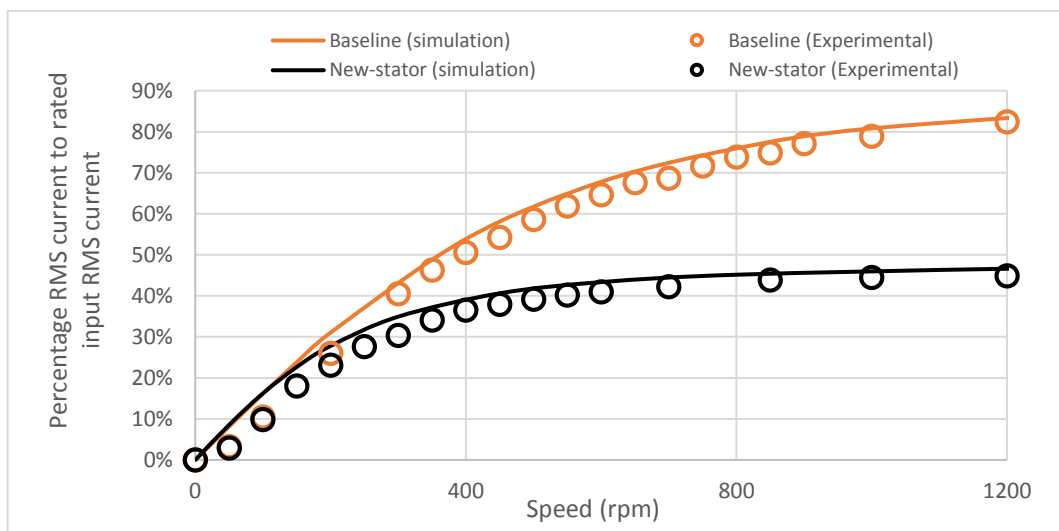


Figure 157: no-load short circuit current comparison between baseline motor and new-stator design.

**4.6.2. Loaded investigation:**

Because the short-circuit drag torque is significantly reduced, the overall motor performance is enhanced. Figure 158 shows how this design is capable of delivering almost 36% of the motor full torque capability during the three-phase short-circuit fault condition. Compared to the baseline motor, the new-stator design delivers an average torque increase of 12% across all speeds. The difference between half-half and interleaved arrangements in terms of torque capability is below 1% (Figure 158). This means that the stator coils are significantly decoupled (physically and magnetically). Therefore, the torque ripple resulting from lane to lane interaction is significantly lower in which in the new-stator design. It is reduced by approximately 10% (from 14% to almost 4%) (Figure 159 and Figure 75). However, the Half-half arrangement torque ripple is still higher than the interleaved arrangement in the new-stator design but is not as large as in the baseline design.

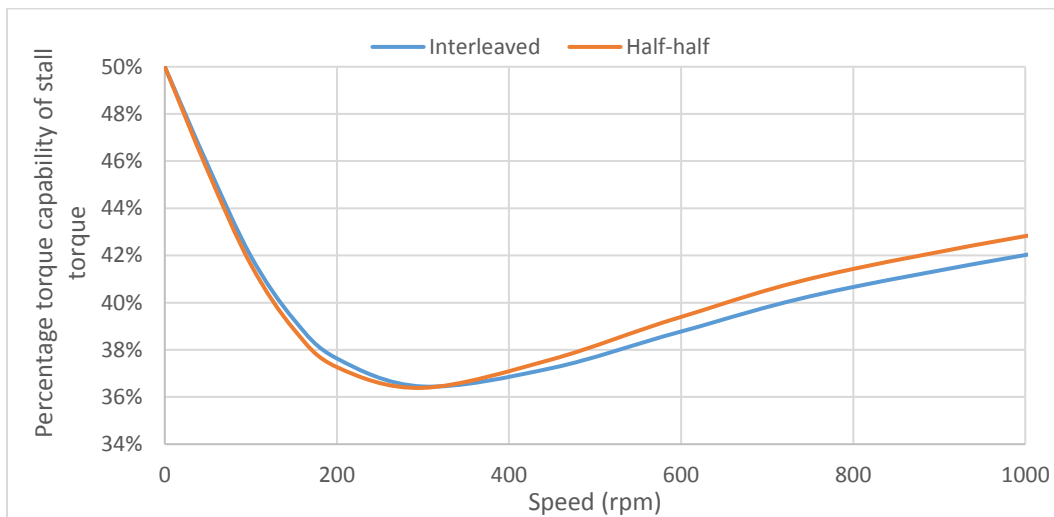


Figure 158: 2D FE torque capability under three-phase fault condition in one lane for different winding connections.

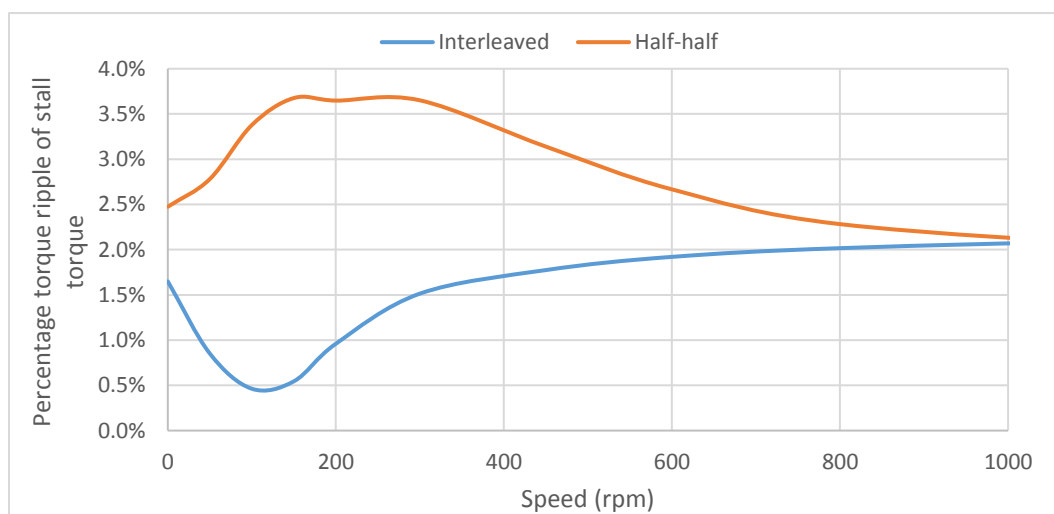


Figure 159: percentage torque ripple for different motor connection type under three-phase fault in one lane (2D FE).

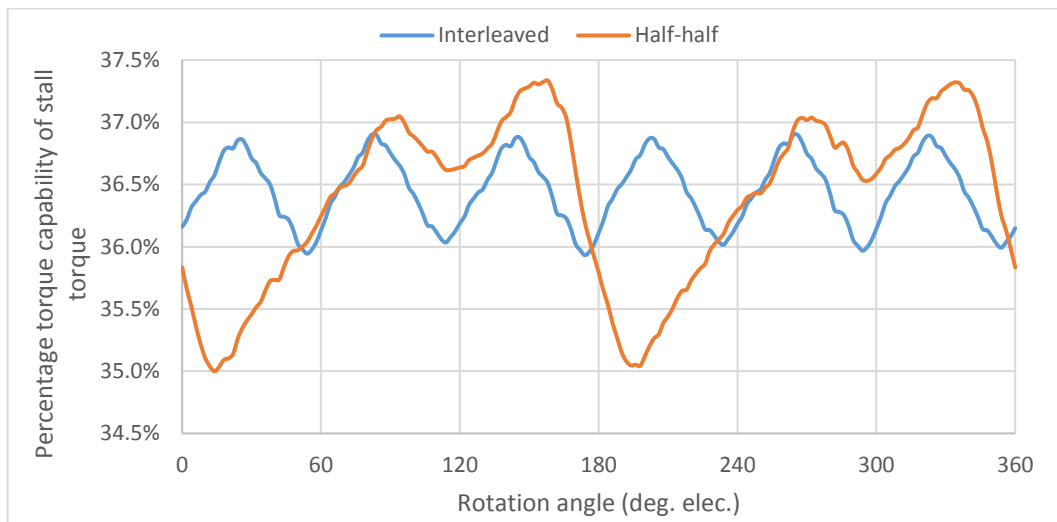


Figure 160: torque ripple amplitude for worst case drag torque (at 300 rpm) for different winding connections. The healthy lane is operated with full current at 10 degrees electric advance angle.

The induced short-circuit current of the New-stator design is approximately 30% lower than the baseline design and it reaches up 50% of the rated input current. This is due to both modular winding configuration that has high inductance and almost eliminating the transformer coupling effect between the shorted coils and healthy coils. The unbalance between the short-circuit current values of the shorted coils is significantly reduced. Compared to the baseline design (half-half arrangement), the highest unbalance difference between the coil currents is nearly 3-4% in which it was up to 18% in the baseline design. Figure 162, Figure 163, and Figure 164 shows that only the edges coils are slightly affect, which mean coils 4 and 6 as in Figure 161. All the results are scaled 2D FE analysis with skewed rotor.

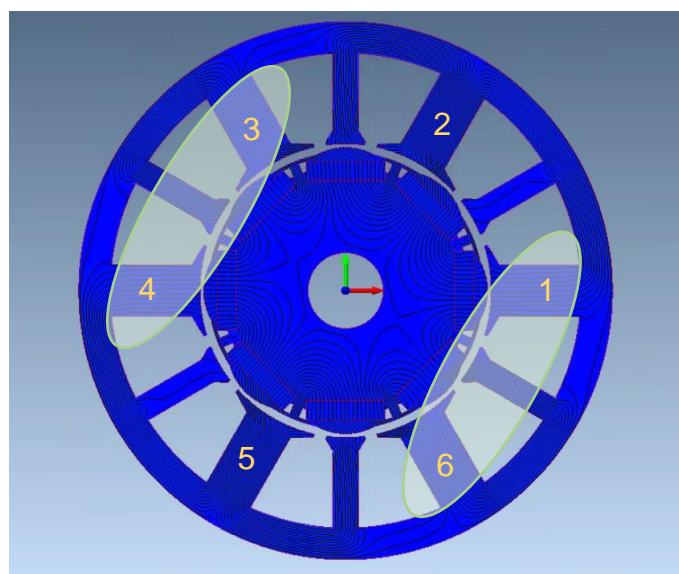


Figure 161: Interaction between motor lanes for Half-half arrangement (new-stator design layout).

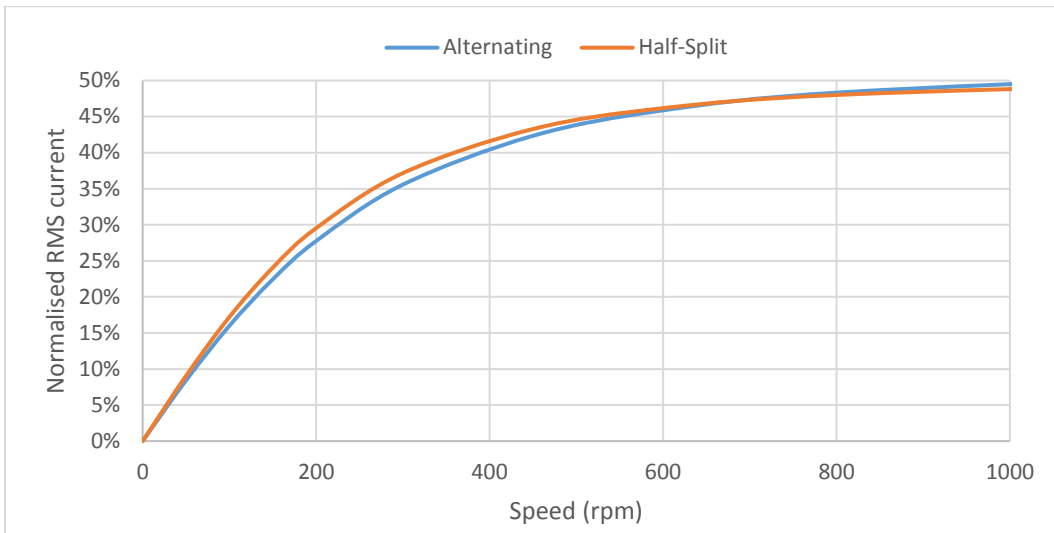


Figure 162: short-circuit current in the edge phase as in Figure 161 (coil 4: leading coil in shorted lane)

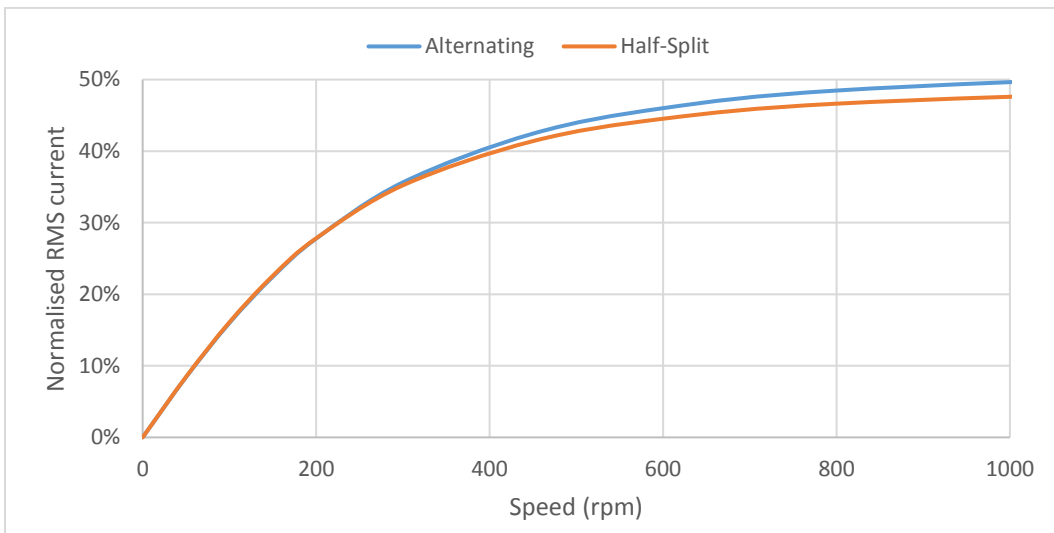


Figure 163: short-circuit current in the edge phase as in Figure 161 (coil 6: trailing coil in shorted lane)

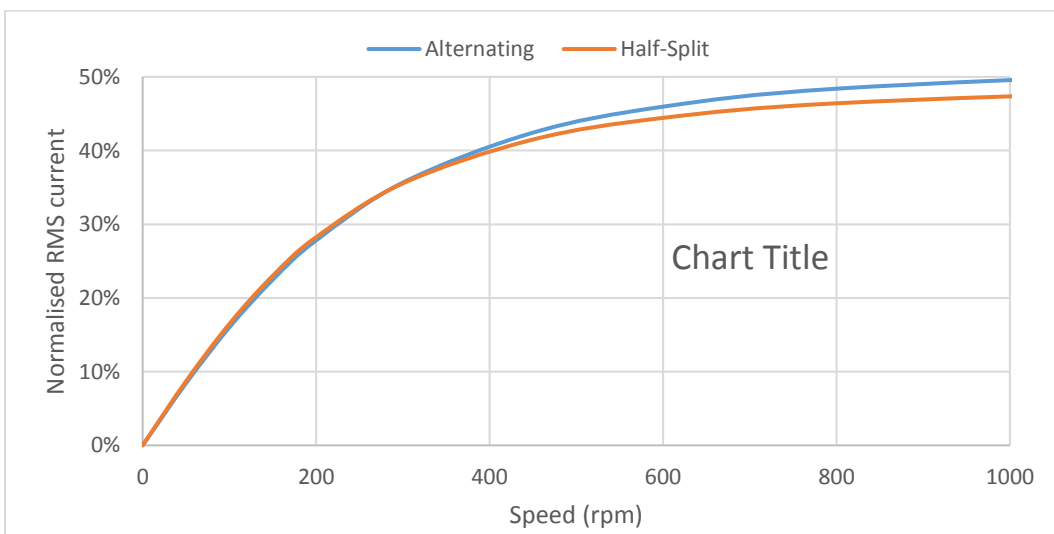


Figure 164: short-circuit current in the edge phase as in Figure 161 (coil 5: middle coil in shorted lane)

#### **4.7. Torque-speed characteristics and phasor diagram at normal conditions:**

As previously discussed, it is generally suggested that it is better to have a high inductance to achieve better torque capability under faulted conditions and a broader constant power region.

Phasor diagrams for both the baseline motor and the new-stator design motor are shown in Figure 165 and Figure 166 for operation in the constant torque region with rated current at an angle corresponding to maximum output torque. The phasor diagrams include the cross-coupling term for the magnet flux, in which it is effectively skewed partly into the q-axis by magnetic saturation. The resultant flux of new-stator design is approximately 25% larger, so it runs out of voltage at a lower speed, affecting the knee point of the torque-speed curve in Figure 167. This is mainly due to the high inductance, especially, the q-axis inductance as the d-axis component is actually reducing the flux level. As expected from the phasor diagrams' resultant fluxes, the speed at the knee point is also reduced by 25% in the new design.

The 2D analysis does not account for end effects, including end-winding leakage inductance, which affect the back-emf, optimum advance angle and torque. Of course, all these effects are present in the measured torque-speed curves of Figure 168. The measured torque capability is lower than predicted because of reduced open-circuit flux, as discussed earlier.

The 2D FE torque-speed comparison is obtained by assuming a fixed DC voltage of 12 Volts. The fundamental first harmonic was taken for each speed and compared to the DC voltage. When it was similar or slightly lower the DC input, the average torque was taken and then plotted. It is assumed that the motor is operated at room temperature, no SVM input with no modulating index. It is assumed that the power is constant beyond the knee point when the voltage reaches 12 Volts. Then the input current is advanced towards the d-axis to push the magnet flux and reduce the back-emf, correspondent to the speed.

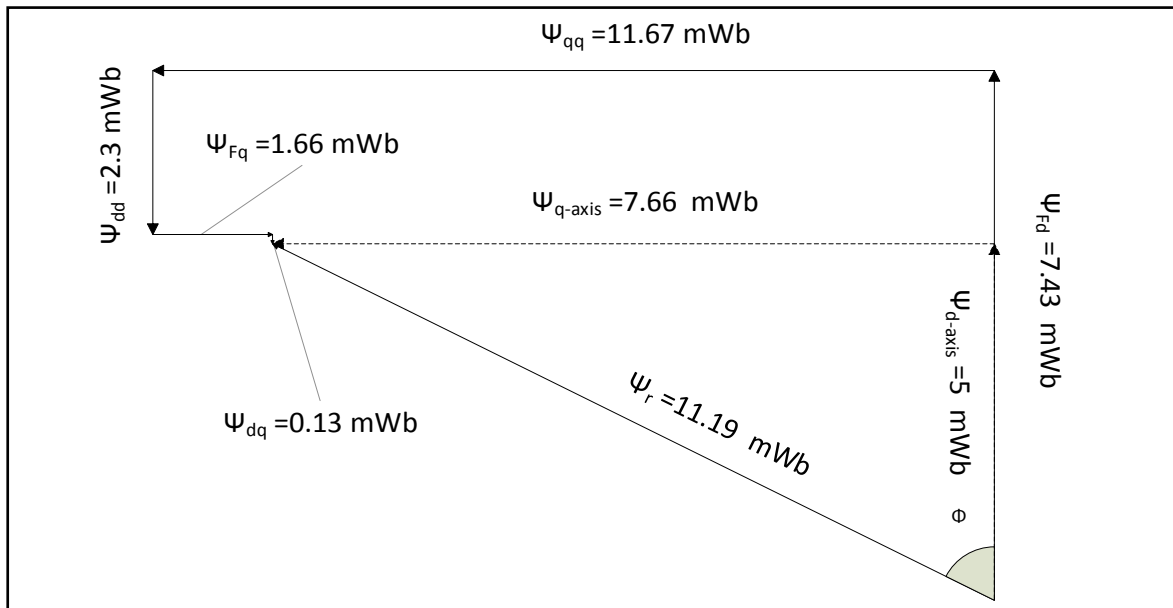


Figure 165: New-stator design's phasor diagram for constant torque region at MTPA (based on 2D FE).

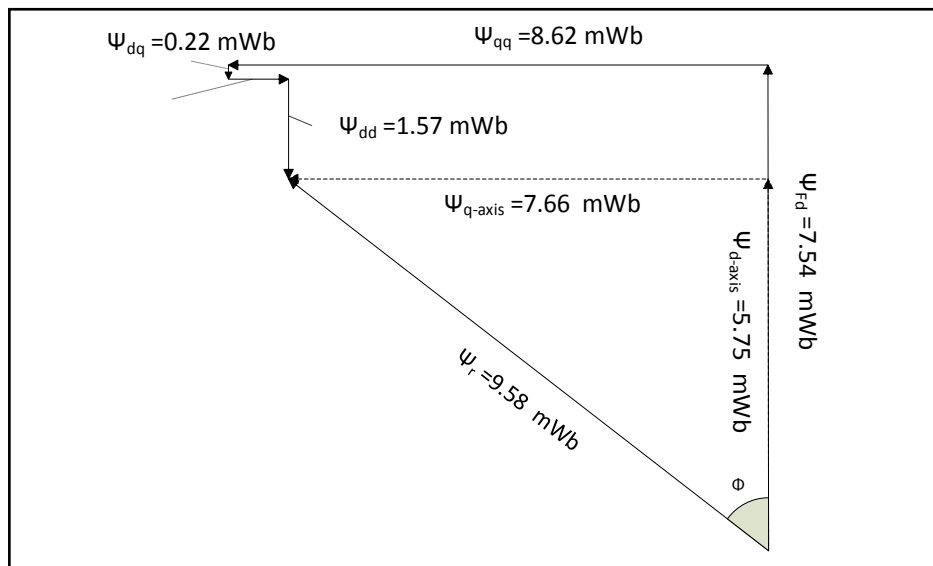


Figure 166: Baseline motor's phasor diagram for constant torque region at MTPA (based on 2D FE).

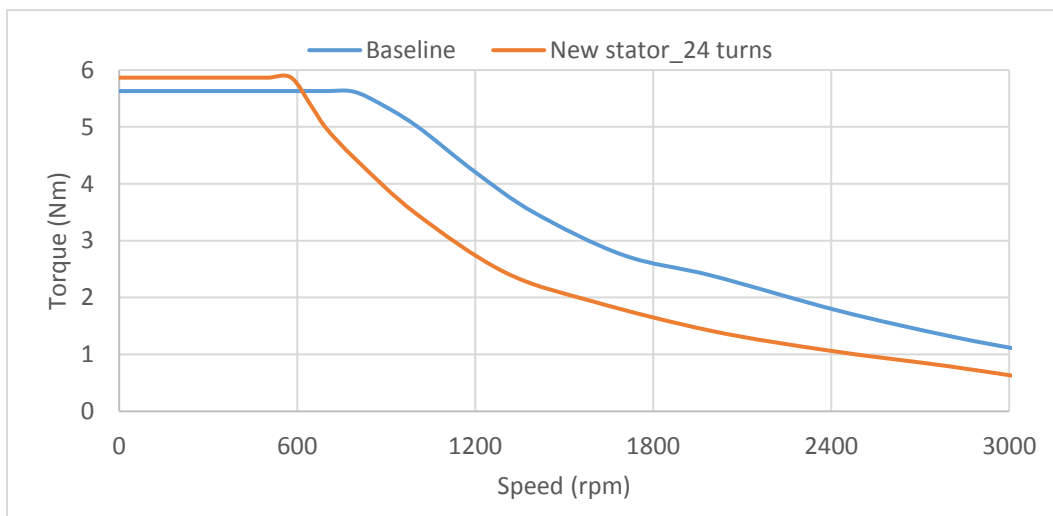


Figure 167: 2D FE torque-speed curve comparison between baseline design and New-stator design.

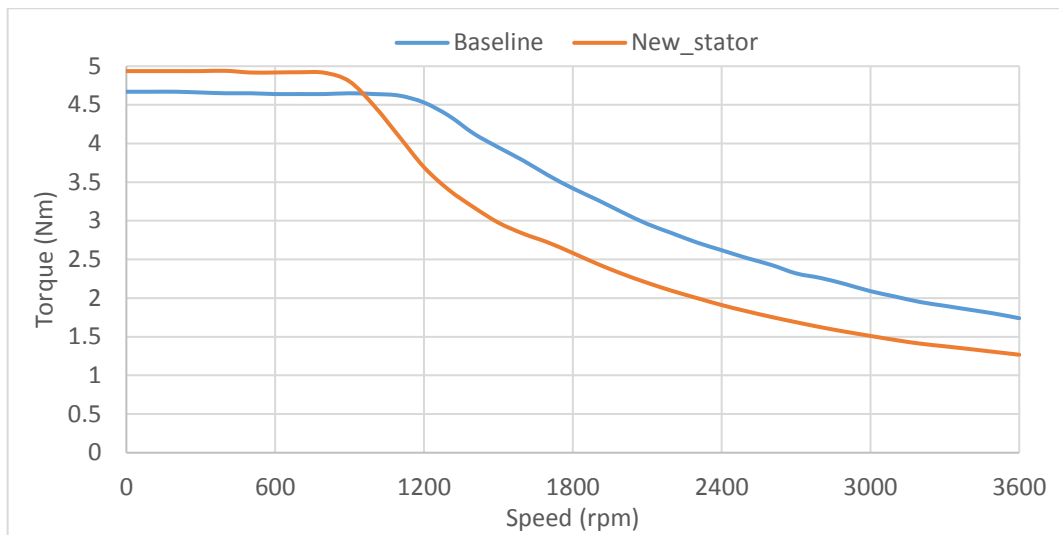


Figure 168: practically tested torque-speed curve comparison between baseline design and New-stator design.

The measured torque-speed curves confirm that the peak power capability of the new design is compromised. The effect is particularly prominent at high speeds where there is a large advance angle. Figure 169 and Figure 170 show that, for an electrical advance angle of 60 electrical degrees, the resultant flux is nearly twice that of the baseline resultant flux.

The resistance of the new-designed stator is approximately 13% higher than the baseline motor. After reconfiguring the baseline motor and extending the wires, the line to line resistance per phase per lane became 48 mOhms. This also affects the knee point of the torque speed-curve combined with the inductance. As in Figure 168, the difference between the knee point speeds is approximately 33% (800 rpm to 1200rpm), in which justifies the combined effect of resistance and inductance on the torque-speed characteristics. The practical setup for measuring the torque-speed characteristics is explained in Appendix A.

Additionally, the flux linkage components which are used in representing the phasor diagrams are taken from the inductance graphs at certain advance angles. The resultant flux from the phasor diagrams was compared to the resultant flux at loaded condition to double check the values and the accuracy of the method, it was within 1% difference.

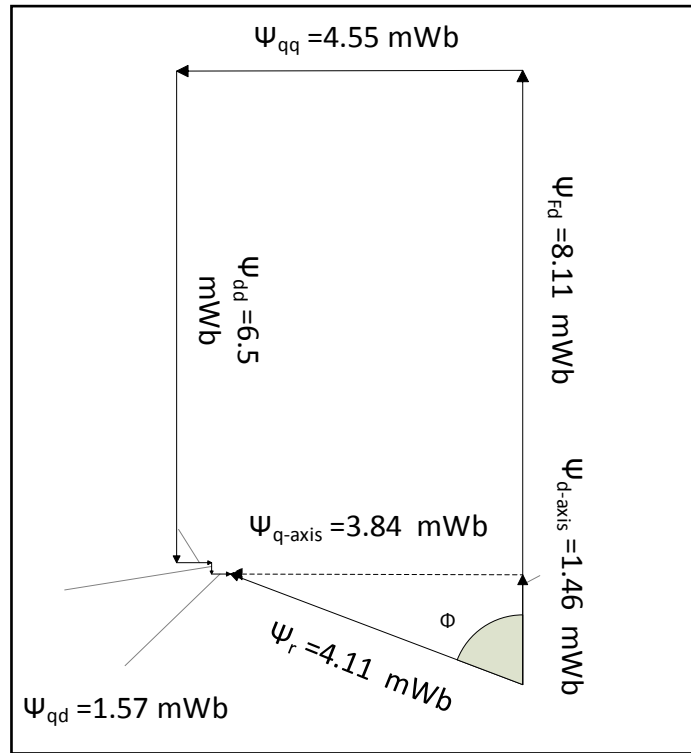


Figure 169: baseline design's phasor diagram at 60° electrical advance angle.

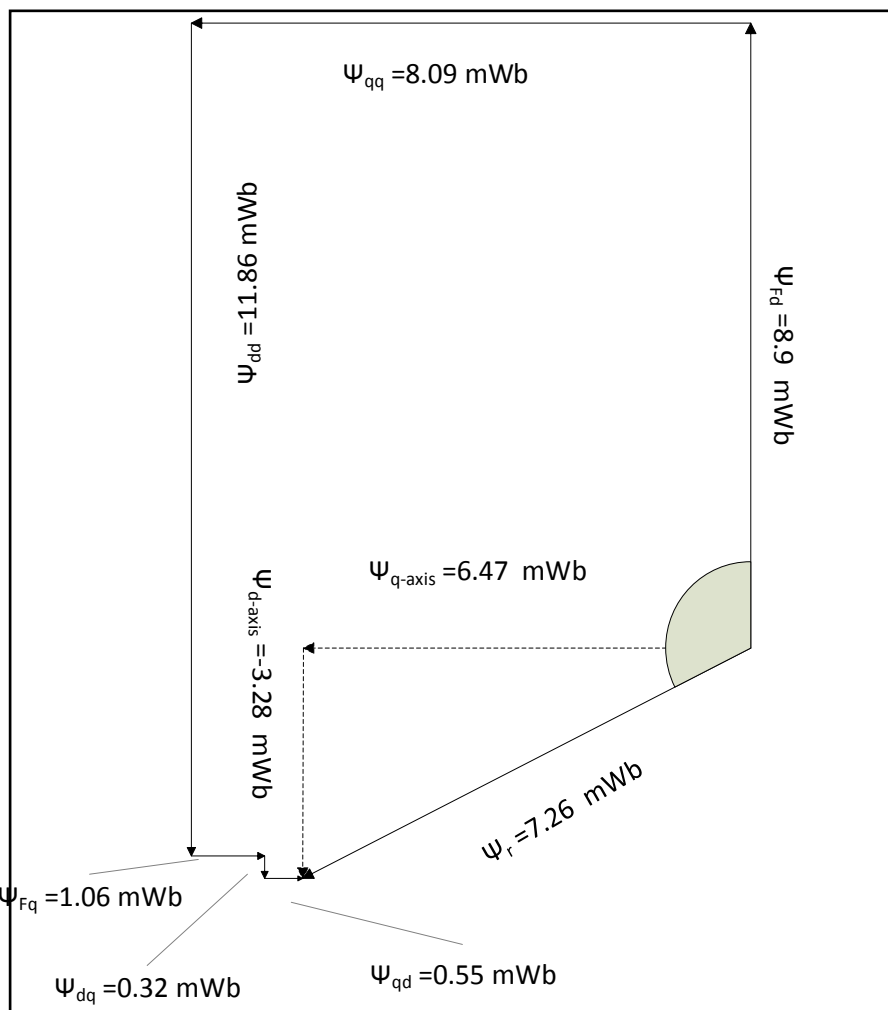


Figure 170: New-stator design's phasor diagram at 60° electrical advance angle.

The loss of power capability in the constant power region can be partially regained through changing the number of turns in the winding or redesigning the rotor, though this will compromise the fault-tolerant capability. If the winding turns is reduced by the same ratio of the knee point speed drop and the input current increased by the same amount, the torque-speed characteristics can be regained (explained in the next chapter in detail). As the inductance changes with the square of the number of turns, the fault-tolerant will be compromised due to higher short-circuit current, hence higher drag torque. According to Bianchi *et al.* [45], by increasing the d-axis inductance and reducing the q-axis inductance through creating a bridge and air barriers in the rotor, the constant power region can be enhanced, and extra torque can be achieved through inverse saliency. These solutions will be further investigated, and a solution will be proposed in the next chapter (Chapter 5).

### **4.8. Summary:**

In this chapter, a new-stator design was proposed as a solution to overcome the challenges associated with the baseline design, such as a high short-circuit current, high drag torque, and high torque ripple during faulted operation.

Firstly, the process of developing the stator was explained and how saturation affected the torque drop if the baseline motor's stator used with a modular winding. Using the dissimilar teeth stator was beneficial for recovering the torque drop and increasing the winding factor by keeping the coils magnetically and physically separate. The winding factor was increased through having wider wound teeth that almost covers the rotor magnets.

The stator was constructed and wound using thicker wires to keep the winding phase resistance similar to the baseline motor. However, due to having a unitary stator, it was difficult to wind the coils with very thick wires to achieve similar resistance hence the power of the motor was compromised.

The motor drag torque under faulted conditions is largely reduced due to having a significantly higher inductance. It is shown that the motor is capable of delivering 36% of its stall torque at its worst case, under 3-phase short circuit in one lane. This comes with very low torque ripple compared to the baseline design. However, the motor power capability is compromised due to having very high q-axis inductance which is shown using phasor diagrams that matches both simulation and practical results.

This design offers a higher winding factor, hence higher torque capability in the constant torque region. It provides approximately 7% more torque at full load compared to the baseline motor. This percentage is higher at half-load as the stator core (especially the tooth tips) saturates heavily at rated current. The torque capability under faulted conditions is greatly improved along with reduced torque ripple by decreasing the mutual coupling between the stator coils.

However, the new-stator design suffers from having high q-axis inductance so that it runs out of voltage at high speed and the knee point of the torque-speed curve is reduced by approximately 25%.

## Chapter 5

---

### Novel SPM design and development

As discussed in Chapter 4, the new stator design with a modular winding, combined with the baseline motor's rotor, provides higher fault tolerance by significantly reducing the mutual coupling between the phase coils. It also reduces the short circuit current and drag torque by increasing the inductance. However, achieving high inductance also affects the constant power region of the motor's capability. The constant power capability is poorer than the original motor, with a lower knee point in the torque-speed characteristic curve.

This chapter investigates different approaches that help to restore the loss of power at high speeds arising from the high inductance. It also proposes a novel motor design with higher torque and power density, yet with sufficient inductance to reduce the low speed drag torque and torque ripple during three-phase and single MosFET failure.

#### **5.1. Enhancing constant power region capability:**

A high Q-axis inductance is not desirable when operating in the constant power region as it increases the overall resultant flux linkage [45]. From the phasor diagram in Figure 171a, a baseline resultant flux can be set for comparison to the new-design's flux values under flux weakening operation. Based on Figure 171b, it is observed that the new-stator design with the baseline motor's rotor, needs to be operated at a lower current to reduce the overall resultant flux for the same advance angle. The resultant flux is almost twice that of the baseline design. Hence, the input current for the new-design needed to be reduced by half to achieve the same resultant flux and enable the supply voltage to overcome the back-emf, as shown in Figure 171c. This leads to a considerable power drop in the constant power region.

As can be seen from the highlighted axis ( $\psi_{qq}$ ), the new-stator design needs to be operated at half load (Figure 171c) to achieve a similar q-axis flux component to the baseline design (Figure 171a). In this analysis, the resistive voltage drop element is neglected as, at high speed, it is very small compared to inductive voltage drops.

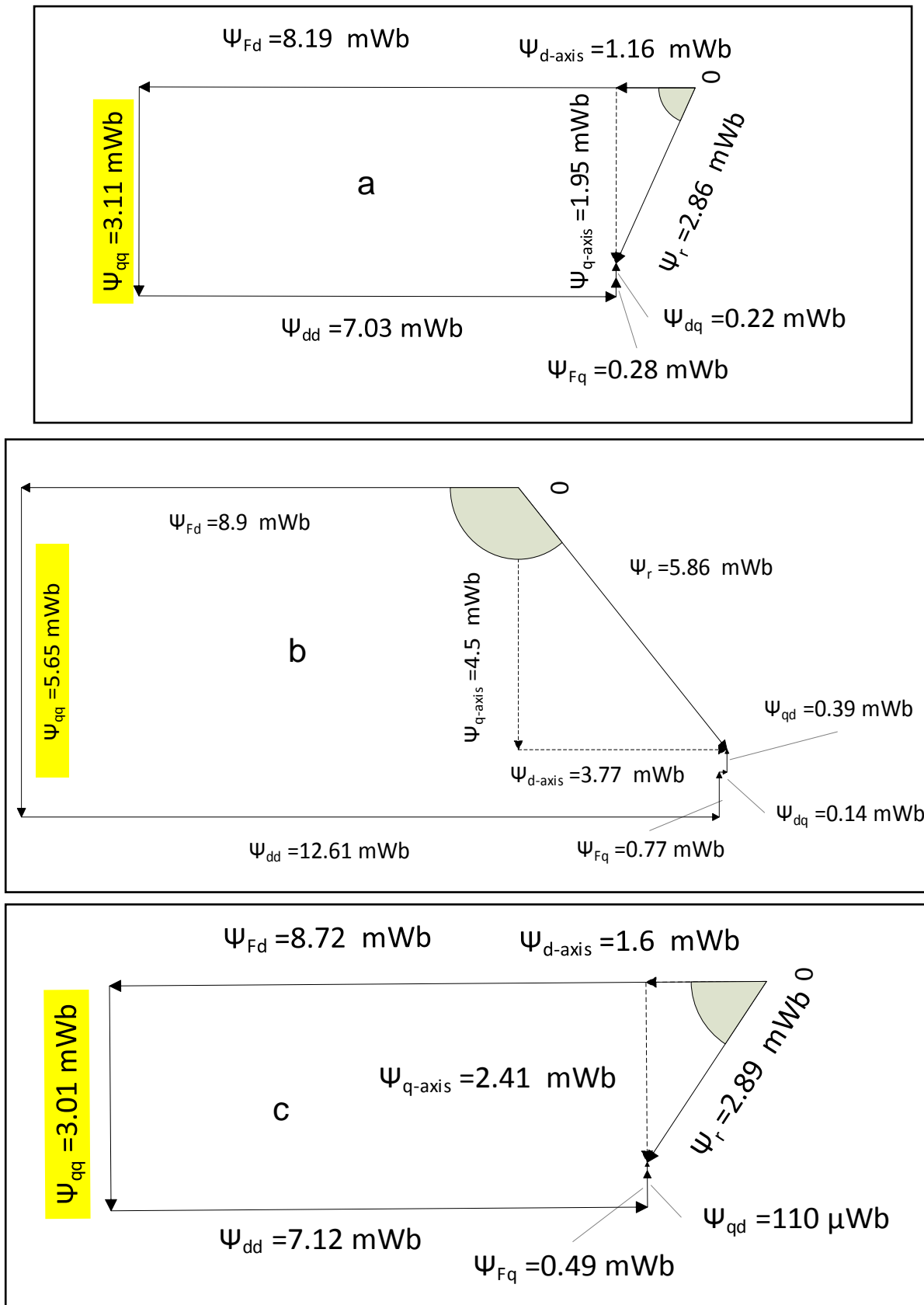


Figure 171: phasor diagram of the motor's operating point at 70 elec. deg. advance angle for (a) Baseline motor at full load \_24 turns, and (b) New-stator with Baseline motor's rotor at full load \_23 turns and (c) New-stator with baseline motor's rotor at half load \_23\_turns.

Where

$\psi_{Fd}$  is the magnet flux component that results in the back-emf,

$\psi_{qq}$  is the q-axis flux component from the input current on the q-axis,

$\psi_{dd}$  is the d-axis flux component from the input current component on the d-axis,

$\psi_{Fq}$  is the magnet flux component on the q-axis due to cross-coupling,

$\psi_{dq}$  is the q-axis flux component from the input current on the d-axis due to cross-coupling,

$\psi_{qd}$  is the d-axis flux component from the input current on the q-axis due to cross-coupling,

$\psi_{q-axis}$  is the total flux on the q-axis,

$\psi_{d-axis}$  is the total flux on the d-axis,

$\psi_r$  is the resultant flux.

Based on 2D FE analysis the phasor diagrams demonstrate that, after reducing the number of coil turns by one, and reducing the input current to half of its value, similar resultant flux is achievable. This means that the torque will drop for same current advance angle, compared to the baseline design.

There are different proposed solutions to minimise the q-axis inductance, and there are always trade-offs associated with any solution. The following sections show the different approaches that lead to partially or fully recovering the power.

### 5.1.1. Changing the number of turns:

This approach aims to keep the output torque in the constant torque region, by keeping the armature MMF similar. It seeks to recover the loss in power in the constant power region through changing the number of turns. The inductance value changes with the square of the winding number of turns as in Equation (5-1).

$$L \propto \frac{\mu_r \mu_0 N^2 A}{l} \quad (5-1)$$

Where L is inductance,  $l$  is airgap length,  $N$  in number of turns,  $A$  is area and  $\mu_r$  is relative permeability and  $\mu_0$  permeability of free space.

Therefore, by reducing the number of turns and increasing the input current (to keep the same MMF input), the position of the knee point can be recovered, whilst maintaining the same torque capability. The speed at which the knee point occurs is inversely proportional to the number of turns and so, as the knee point is at 580 revs/min, rather than the desired 780 revs/min, equation 5-2 can be used to determine the new number of turns.

$$\frac{N_1}{N_2} = \frac{Speed_1}{Speed_2} \quad (5-2)$$

$$\frac{24}{N_2} = \frac{780}{580} \Rightarrow N_2 = 17.84 \sim 18 \text{ turns}$$

And to keep the MMF input unchanged, the input current should be increased by 33% as shown below:

$$I_2 = I_1 \frac{N_1}{N_2} = I_1 \frac{24}{18} = 1.33 I_1 \rightarrow I_2 = 1.33 I_1 = 126 * 1.33 = 168 \text{ Amp}$$

Figure 172 shows that a similar torque speed curve can be achieved, with slightly higher torque capability in the constant torque region. For the same current density, the drawbacks of this approach are:

- higher motor phase current, increasing the inverter losses
- increased winding conductor diameter, making the machine harder to wind.

If the above drawbacks can be tolerated then this approach is the easiest way to recover the power at high speed, whilst maintaining the fault tolerant benefits.

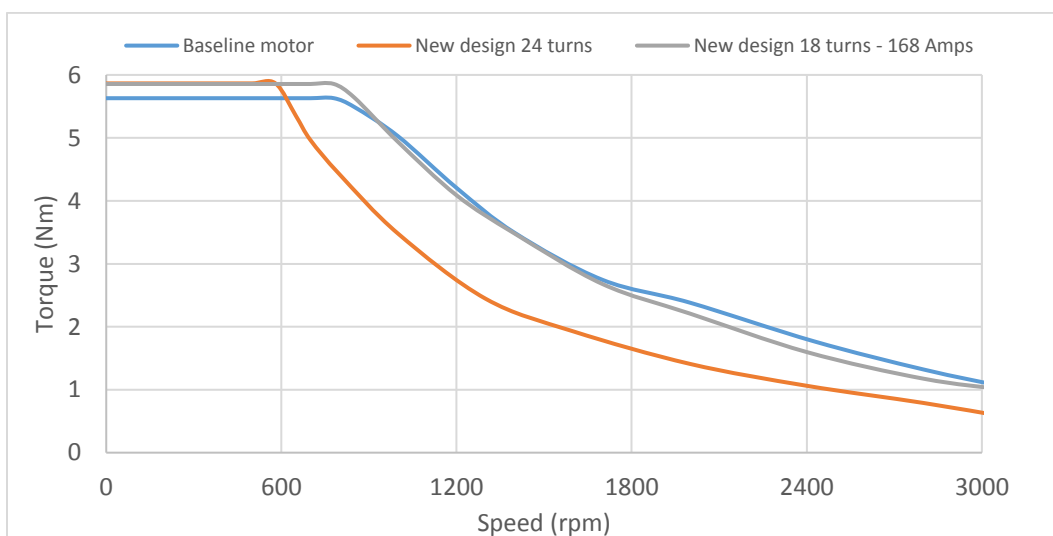


Figure 172: 2D FE torque-speed curve comparison between baseline design and New-stator design (with different number of turns and different input current).

### 5.1.2. Shaping the baseline rotor:

Bianchi *et al.* [61], propose flux barriers in the rotor to change the rotor negative saliency to positive saliency by blocking the q-axis flux path. Positive saliency occurs when  $L_d$  is larger than  $L_q$ . Their study investigated both surface mounted and spoke type interior permanent magnet motors.

Using 2D FE simulations and the frozen permeability method, the q-axis flux path of the armature current is shown in Figure 173. The circled areas indicate the flux paths that need to be blocked to increase the reluctance and hence reduce the q-axis inductance.

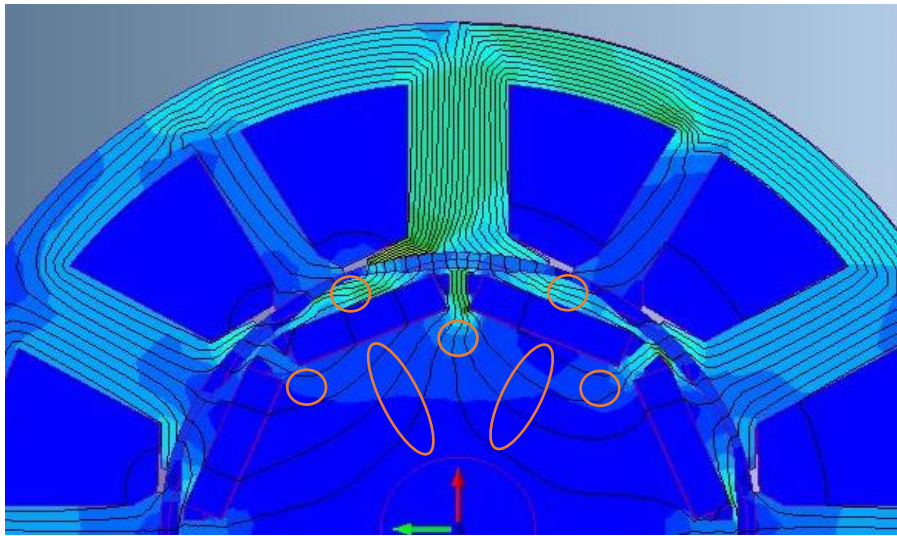


Figure 173: q-axis flux path using frozen permeability method (full load).

Various flux barriers and rotor designs were investigated to achieve the aim of restoring the power drop, as shown in Figure 174. The consequence of having flux barriers is significant increase in torque ripple, which is undesirable in an in EPS application. The flux barriers in the pole cap affect the harmonic content of the back emf and introduce torque ripple. As the torque of the motor is amplified through a gearbox, high torque ripple in the motor can become apparent to the driver.

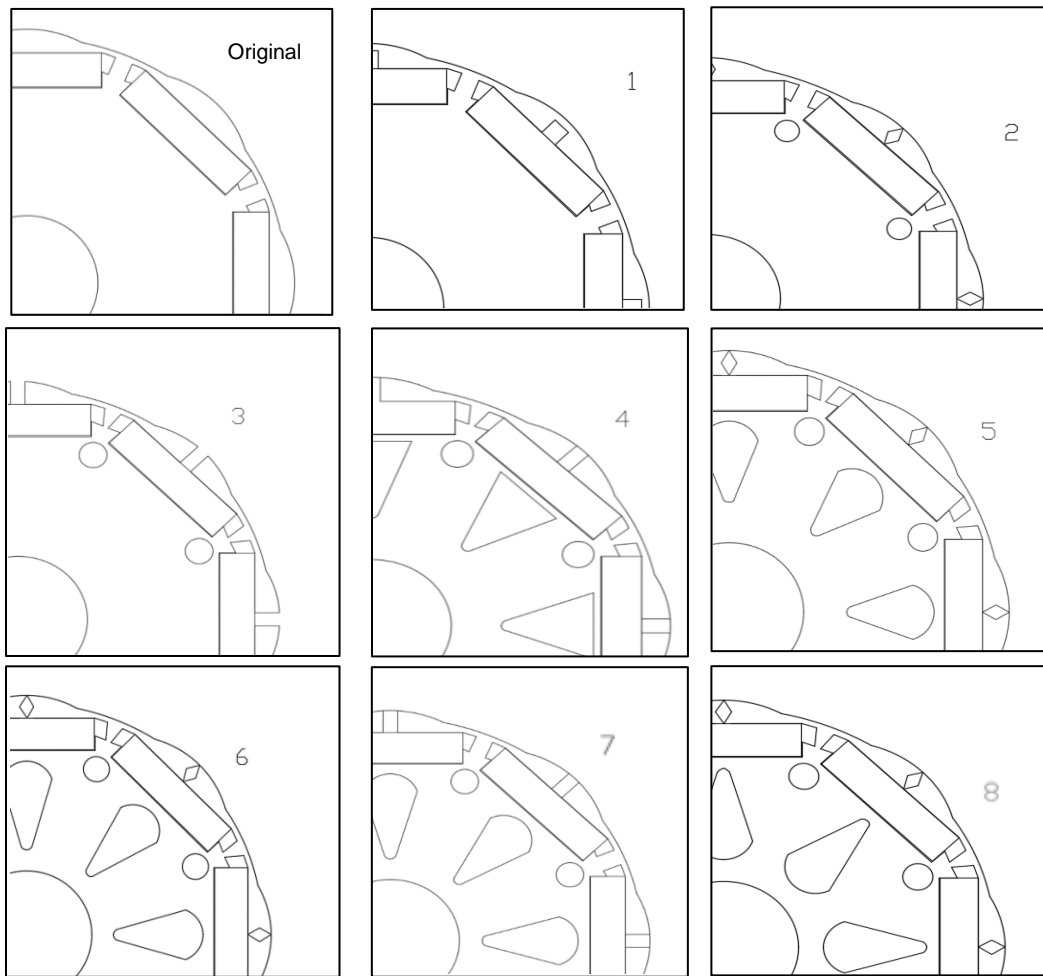


Figure 174: introducing flux barriers to the baseline motor's rotor.

Figure 174.1 to Figure 174.3 are focused on blocking the q-axis flux path in the pole caps and saturating the rotor core between the magnet poles. This led to high torque ripple without affecting the q-axis flux significantly. In Figure 174.4 to Figure 174.7, triangular shapes were introduced beneath the magnet poles to block the Q axis flux. Figure 174.8 was found to offer the best compromise between the different shapes to recover average torque at the expense of increasing torque ripple. However, the torque remains below the desired torque and torque ripple requirements in both constant torque and constant power regions. Figure 175 illustrates the predicted torque speed envelope of various options. Clearly the rotor shaping has only had a minor impact.

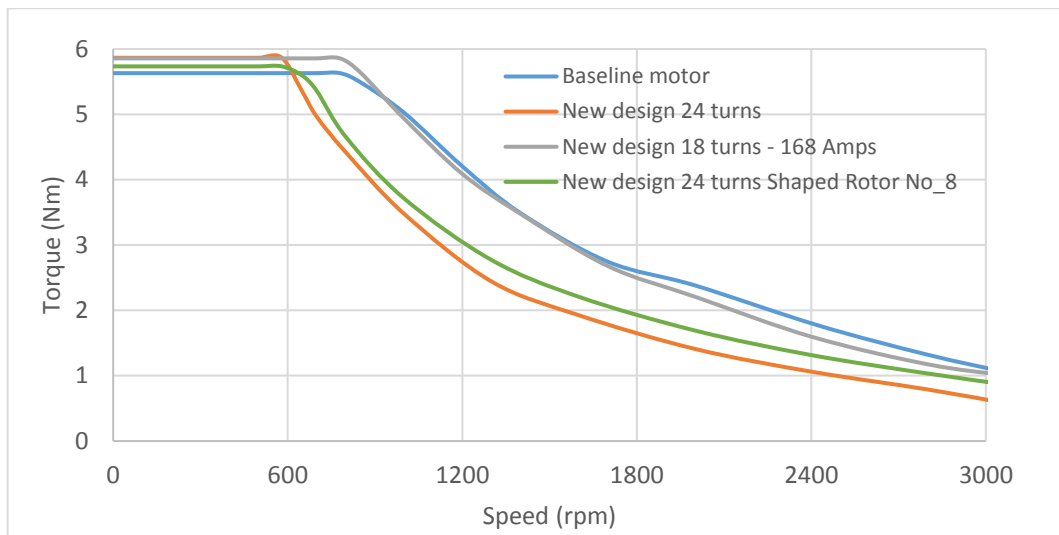


Figure 175: 2D FE torque-speed curve comparison between baseline design and New-stator design (with different number of turns and different input current, and rotor shaping).

### 5.1.3. A surface mounted magnet alternative and associated demagnetisation issues:

Following on from the above, further investigations were carried out, aiming to block the q-axis flux whilst taking account of the rotor inertia and mass, without increasing torque ripple. A surface mounted PM (SPM) rotor was investigated as a solution which reduces the inductance, as all armature reaction flux must pass through the high reluctance of the magnet. There are challenges associated with SPM rotors, such as the need for a containment sleeve, which increases the effective air-gap. Moreover, shaping the magnet to minimise torque ripple and cogging torque creates a non cylindrical outer surface, which adds difficulty to introducing the sleeve. Another challenge occurs with surface mounted magnets: the magnets are subject to all the armature reaction flux and hence more prone to demagnetisation. This may require a higher, and more expensive, grade of magnet.

For the first SPM design of Figure 176, the q-axis armature reaction field is the main demagnetisation source during normal operation. As there is no iron bridge to protect the magnet, the magnet edge is directly exposed to the armature reaction flux. Figure 176 shows the q-axis flux for a surface mounted magnet design loaded at rated torque. Rotor material has been removed to minimise inertia. It can be seen that a lot of q-axis flux passes through the thin passage between the magnet holder and the shaft. This tends to demagnetise the magnet corner, as shown in Figure 177. The flux density is scaled to highlight the minimum flux density at the magnet corner and set it as a base for later stages to observe how much it can be increased.

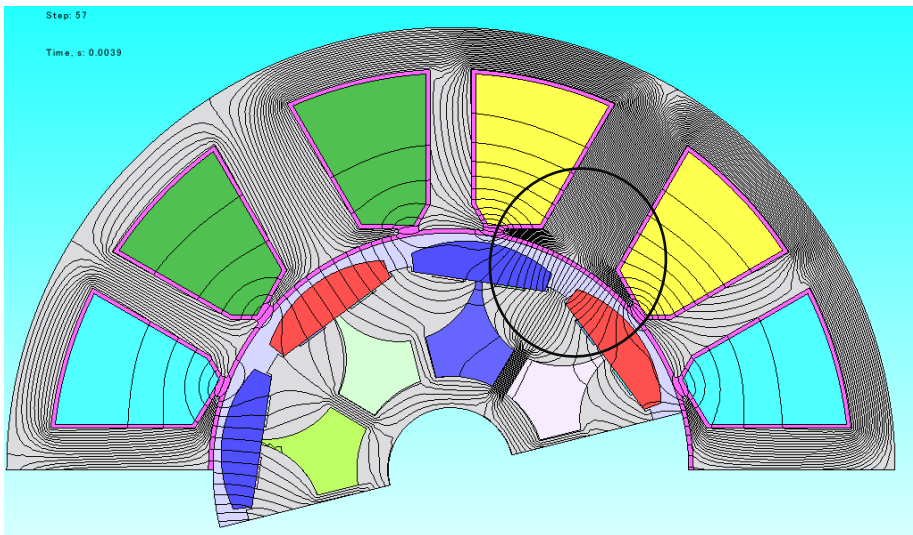


Figure 176: q-axis flux path in SPM motor design with the magnets disabled.

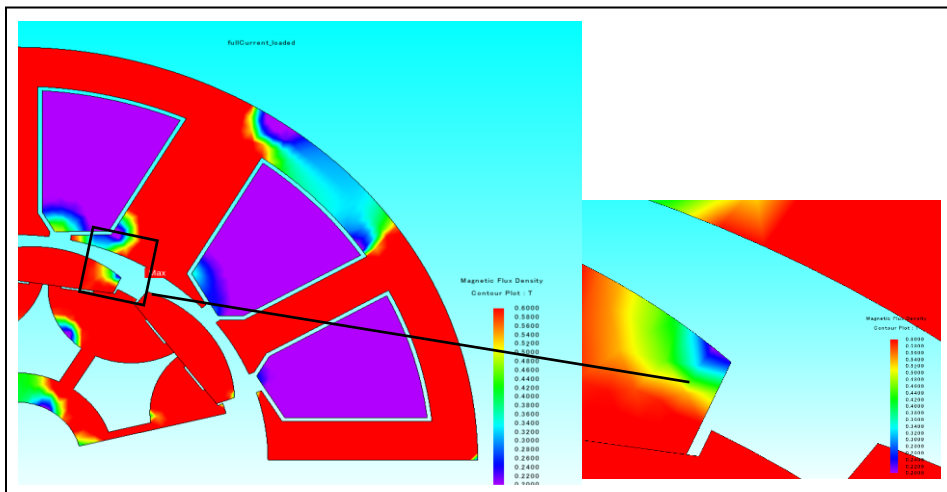


Figure 177: Demagnetisation check of the SPM magnet under q-axis current (full-load).

However, by decreasing the magnet arcs and forming a “bread loaf” shape, as in Figure 178, magnet demagnetisation is reduced.

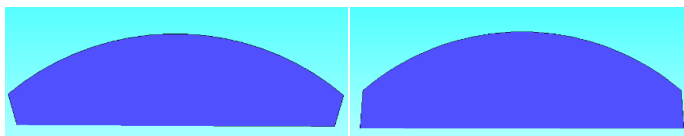


Figure 178: Magnet shapes used to achieve very low torque ripple and cogging torque and lower demagnetisation at the edge of the magnet.

Figure 179 shows a sequence of designs introduced to decrease the q axis inductance and the inertia.

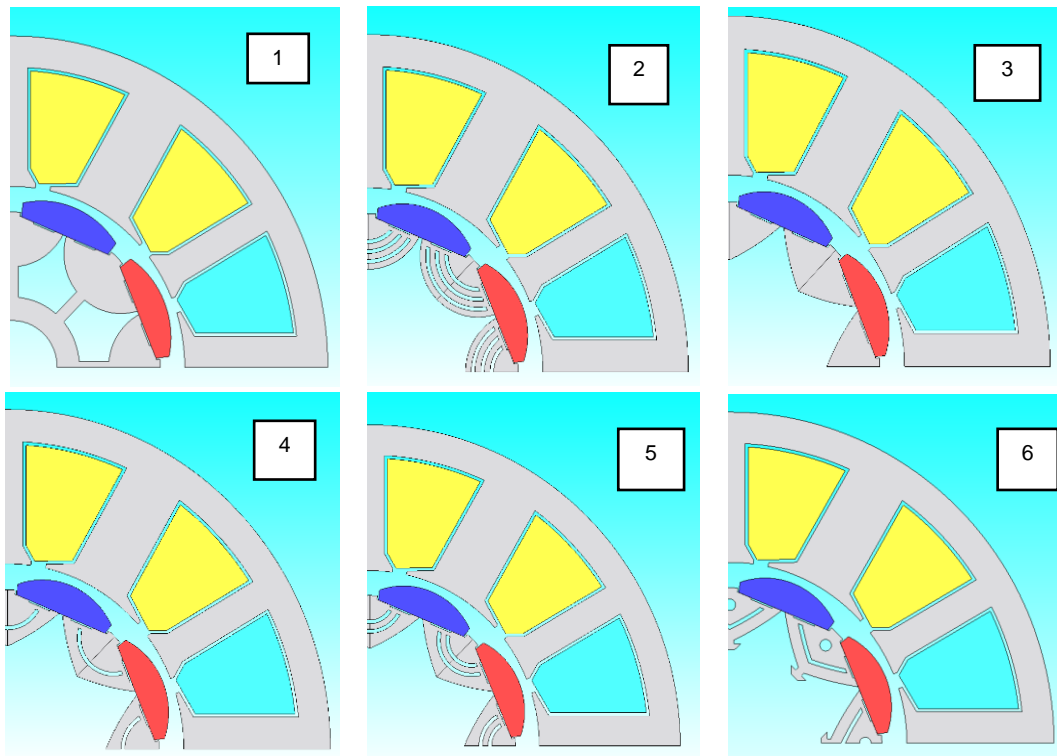


Figure 179: introducing flux barriers into the rotor core-back to block the q-axis flux and develop the design.

The six designs progress as follows:

1. Design 1 has removed material from the rotor, leaving semi-circular flux paths for the flux to flow from magnet to magnet. Lamination ligatures are kept to hold the flux paths to the rotor shaft.
2. Design 2 takes design 1, removes the lamination ligatures and also introduces three flux barriers in the semi-circles to further increase the q axis reluctance. The ligatures are removed because they were found to significantly increase the inductance. However, no structure is shown to mechanically hold the rotor segments in place. The magnet edges are protected from demagnetisation (see later), however this design doesn't look realistic due to very thin bridges, making it difficult to manufacture.
3. Aiming to achieve similar results to those of Design 2, Design 3 simplifies the rotor lamination segments by reducing them to a more triangular shape. This makes it harder for flux to skip from segment to segment. However, due to the solid segment structure, the magnet edge demagnetisation was unacceptable.
4. Designs 4 and 5 reintroduce flux barriers into design 3 to further reduce the q-axis flux.
5. Of all the above designs, Design 6 came closest to achieving the specification. Design 6 adds a small dovetail feature to provide location for the segment, along

with a mechanical alignment feature. A hole is added to each segment to add an additional q axis flux barrier.

Figure 180 shows the q-axis flux path for designs 1 and 2, where it is observed that the flux travels through the air between the magnet holders. Note how the flux barriers are shaped to direct the magnetic flux between the permanent magnets. Interestingly, these designs seem to offer very low cogging torque and so they were developed without any skew. This makes assembly easier: furthermore, 2D and 3D models show similar performance as there are only small end effects to take into consideration.

Different magnet shapes were investigated. The magnet on the right side in Figure 178 offers a higher robustness against the magnet edge demagnetization. By comparing the designs shown in Figure 180, the segmented rotor with flux barriers reduced the q-axis flux, as can be seen from the flux lines and the shaded plots. The magnetic flux density at the magnet edge had recovered from 0.1 Tesla to 0.5 Tesla, after simulating both designs (Figure 180.1. and Figure 180.2.) with full current on the q-axis in 2D as in Figure 181. Note that the SPM magnet cross-sectional area is approximately %15 higher than the original motor's magnet cross-section area.

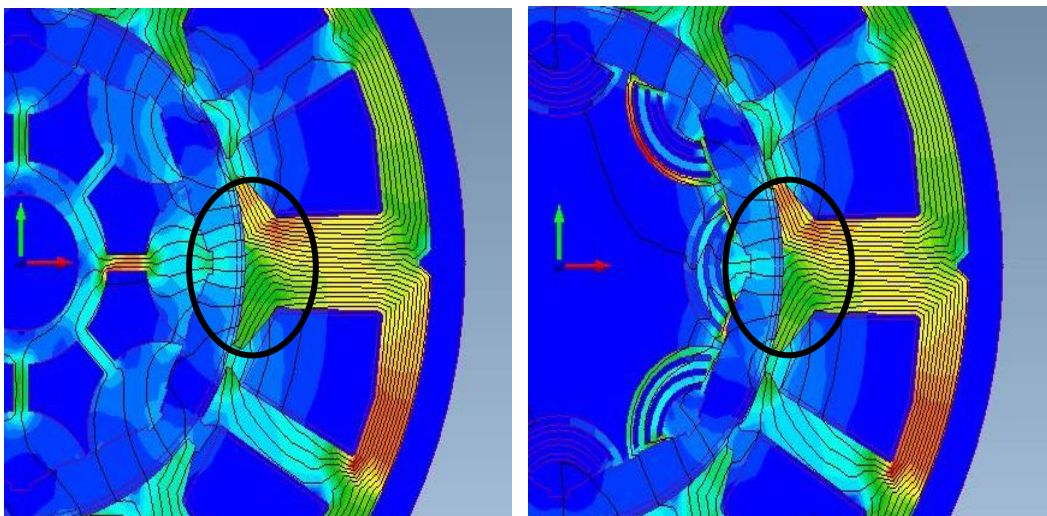


Figure 180: q-axis flux path in different designs after introducing flux barriers (full-load).

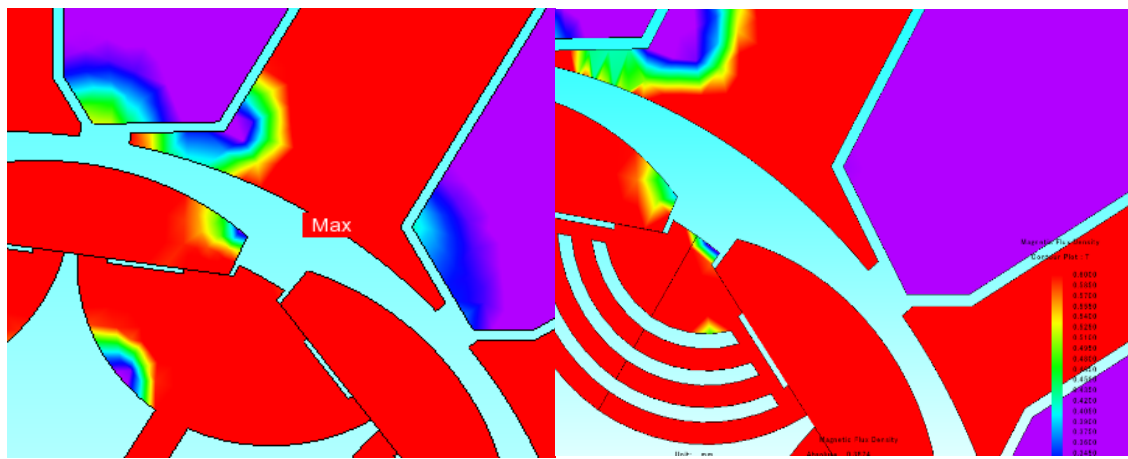


Figure 181: Magnetic flux density at full-load and demagnetisation area within the magnet (full-load).

The new design offers significantly higher torque capability in both constant power and constant torque regions as the SPM has a higher airgap flux density than the baseline motor. It can therefore be shortened to match the baseline motor's capability. This makes the overall volume of the magnet close to the baseline design. From the above investigations, the torque -speed curve, is significantly improved and the 2D FE results show that the SPM design outperforms the baseline design significantly (Figure 182). To further enhance the SPM design, the stator is also modified to reduce the saturation in the teeth, tooth-tips and yoke.

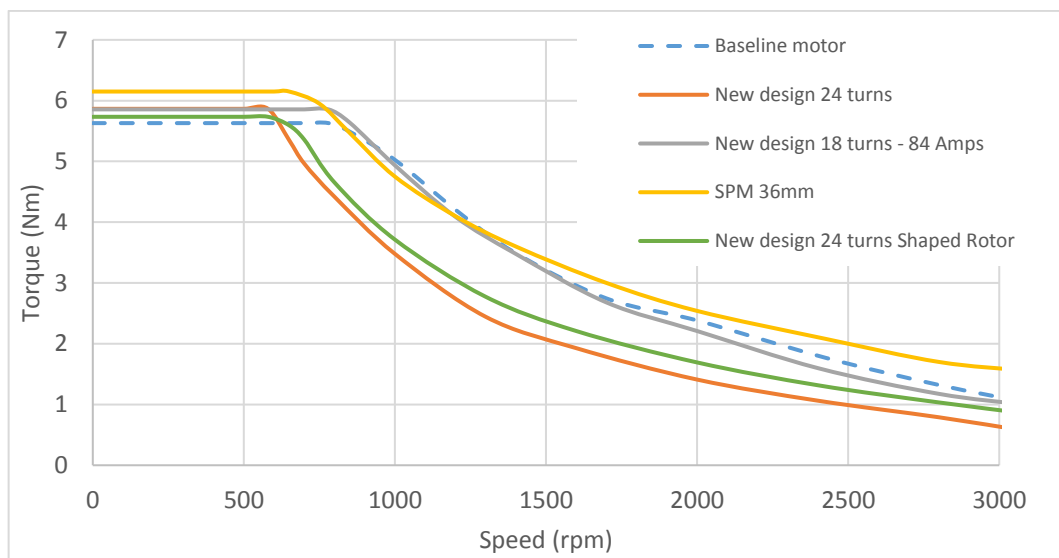


Figure 182: Torque-speed characteristic of three different stator design with different rotors.

## 5.2. The impact of tolerance in the stator construction:

As discussed in chapter 4, the stator with a modular winding and dissimilar wound and unwound teeth was developed with the aim of achieving both high fault tolerance capability and high torque density. In a double layer winding arrangements, the coils of different phases share a slot and there needs to be separation between coils, which

reduces the slot fill factor. With a single layer winding arrangement there is only one coil side per slot, which allows the winding area to be fully used. As the MMF input per tooth for the same number of turns is doubled, achieving same current density will be through increasing the wire diameter. Therefore, it is harder to wind the stator.

To simplify the winding challenge it is proposed to use separate lamination stacks for the unwound teeth. The wound teeth are integral with the core back and are wound to achieve a high fill factor. The unwound teeth are inserted on the stator back iron as in Figure 183. Both “jigsaw” like interfaces and dove tailed joints are considered as alternative solutions, shown in Figure 183. The winding resistance is expected to be lower than the baseline motor, as the stator would be wound with 22 coil turns, compared to 24 turns in the original design. Furthermore, because the torque density is increased, the proposed stack length is 11% shorter.

When the separate teeth are inserted the joint between laminated components will not be perfect: it is estimated that a mean gap of approximately 100 micro-metres exists in the worst-case condition. This influences the local distribution of flux and causes a small reduction in the overall flux flowing. Mean torque, torque ripple and cogging torque are all affected. As shown in Figure 184 and Figure 185, there is 4% drop in the mean torque, however the torque ripple also drops by approximately 40% in the 2D simulations of the SPM motor.

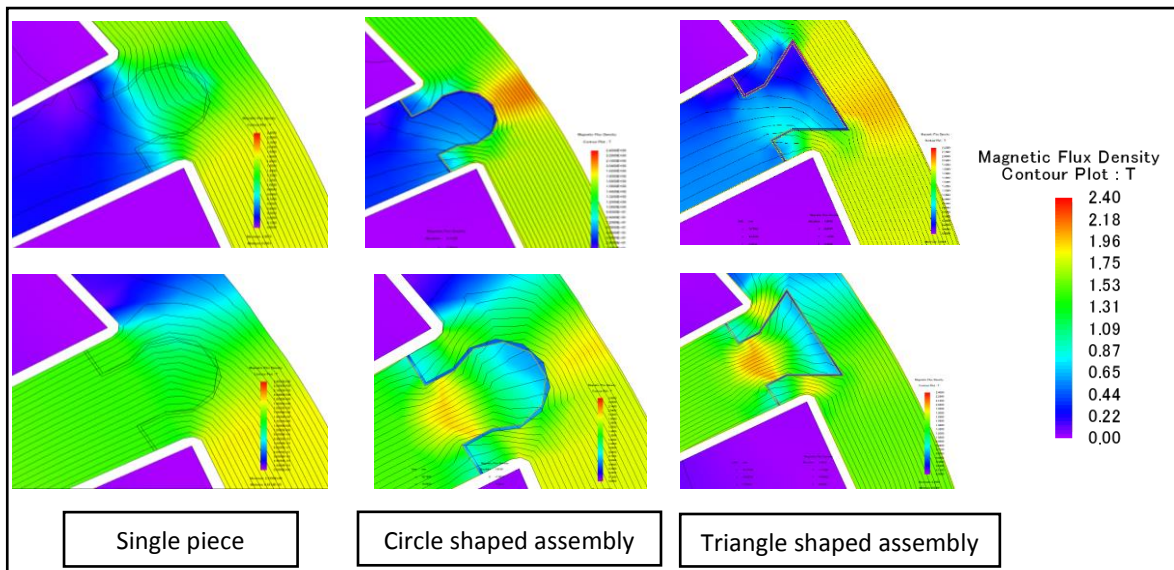


Figure 183: thin tooth assembly methods including mechanical tolerances (full-load).

The above flux plots were captured for two rotor positions. One for the thin tooth to become the return path for the main flux, and the other for the flux to travel only through the yoke.

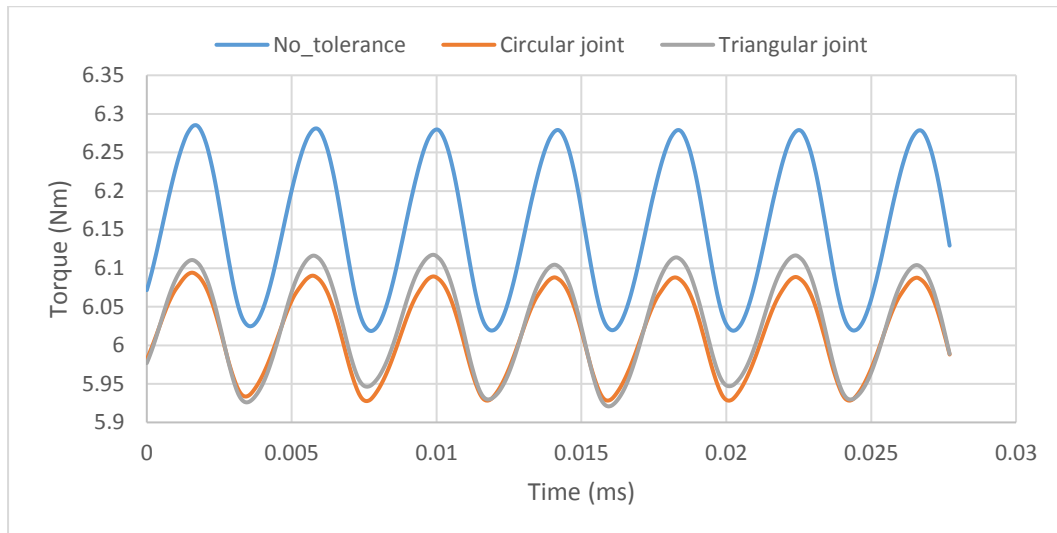


Figure 184: 2D FE torque capability for the SPM motor with tolerances for 36 mm stack length.

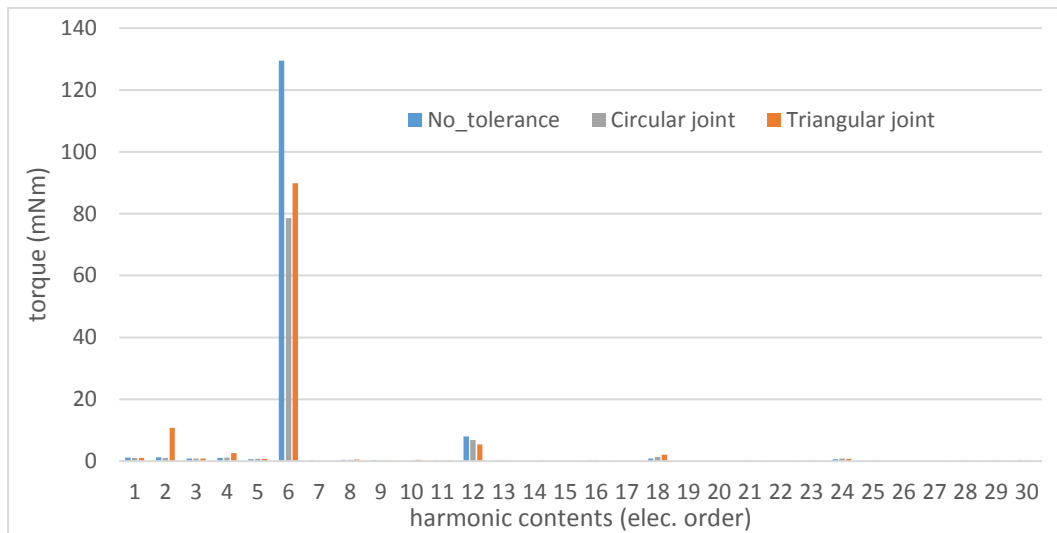


Figure 185: 2D FE harmonic content of the SPM motor torque capability.

The gaps also affect the no-load characteristics of the motor. As the flux in the thin teeth reduces, this affects both back-emf and cogging torque, as shown in Figure 186, Figure 187, Figure 188, and Figure 189.

In the arrangements simulated, the different joint shapes introduce different harmonic orders: Figure 184 shows how the circular joint introduces 2<sup>nd</sup> harmonics of torque when loaded. However, Figure 187 shows how the triangular joint introduces this in the cogging torque. Note that this assumes the worst-case scenario in which there is no physical contact between the tooth and stator yoke.

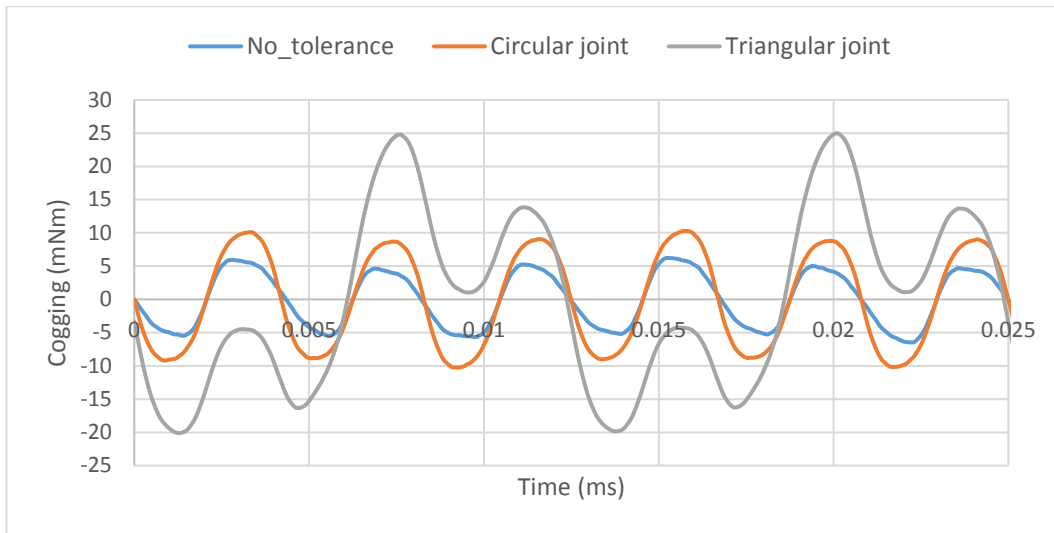


Figure 186: 2D FE cogging torque for the SPM motor with tolerances for 36 mm stack length.

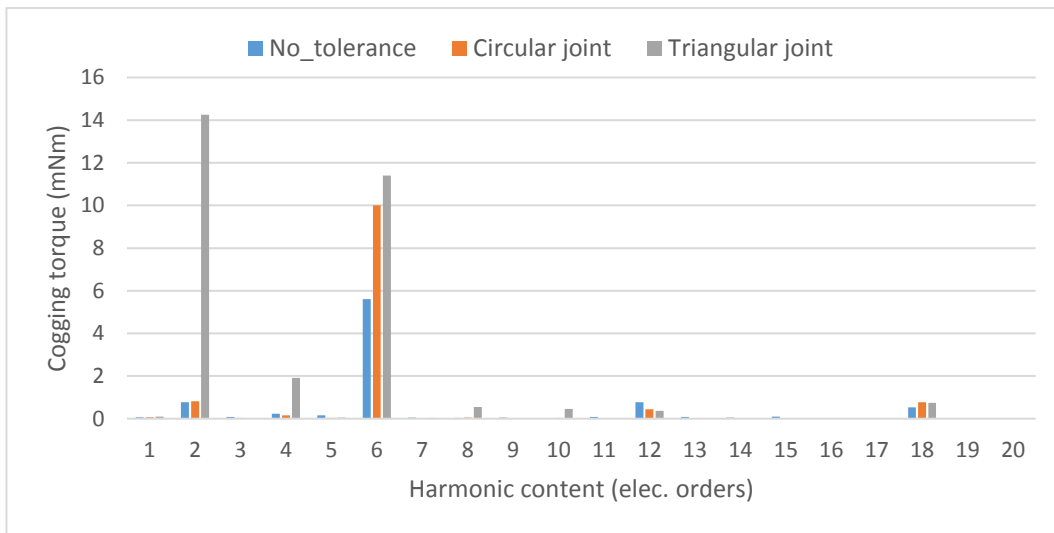


Figure 187: 2D FE harmonic content of the SPM motor cogging torque.

Furthermore, Figure 188 and Figure 189 show how the back-emf harmonic content is also affected. In addition to a small reduction in the fundamental back emf, the joints increase the 5<sup>th</sup> harmonic, decrease the 7<sup>th</sup> order and introduce an 11<sup>th</sup> harmonic in the arrangement simulated.

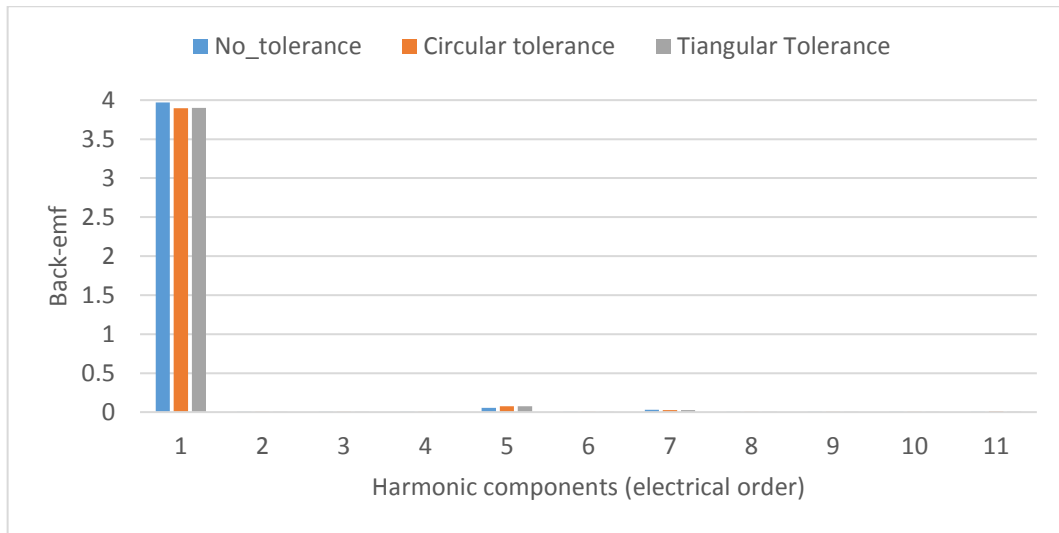


Figure 188: 2D FE back-emf harmonic content of the SPM motor for different this tooth tolerance shape.

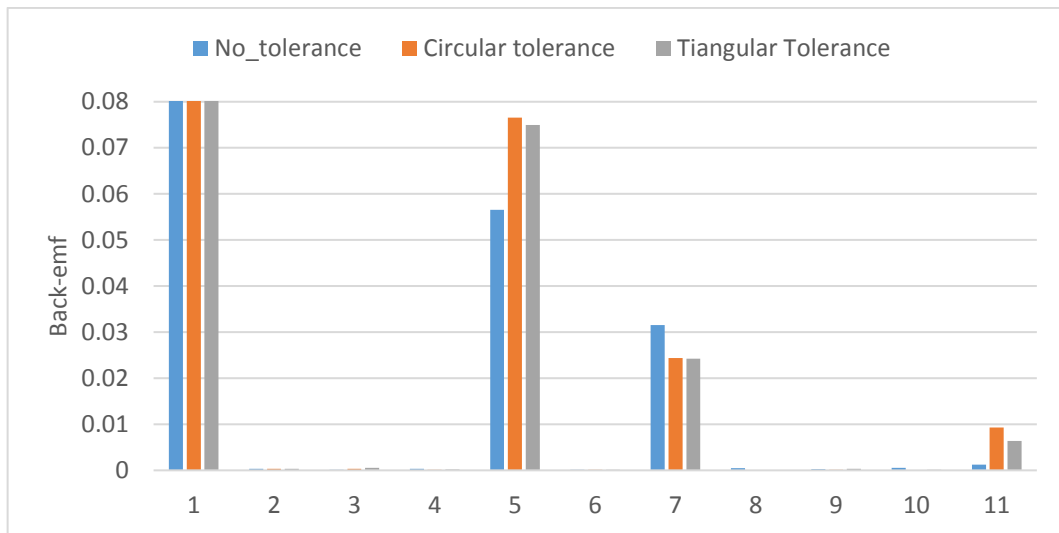


Figure 189: 2D FE back-emf harmonic content of the SPM motor for different this tooth tolerance shape [scaled].

Clearly the joint between laminations is important: there was therefore consultation with the mechanical engineering team within the ZF group. A new joint design was produced, aiming to enhance the mechanical integrity of the stator, and keeping maximum contact between the thin teeth and the stator yoke. The resulting design is shown in Figure 190. The circular portion of the joint is to keep the tooth attached to the yoke, whilst small “arms” are introduced to minimise circular movement. Two stators were constructed for comparison purposes: one has a unitary stator and one with the new design of inserted teeth.

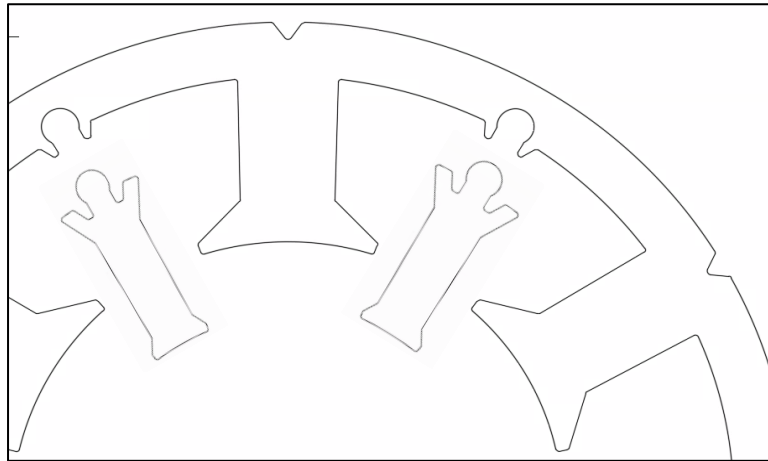


Figure 190: Last stator design for the SPM motor.

Achieving tight tolerances is one of the major challenges in mass production motor construction. The tooth pieces were constructed separately and then inserted after winding the stator. Theoretically, a tighter fit of the thin tooth can be achieved by preheating the stator before sliding in the tooth. Figure 191 and Figure 192 show both the stator with push in teeth and the unitary stator.

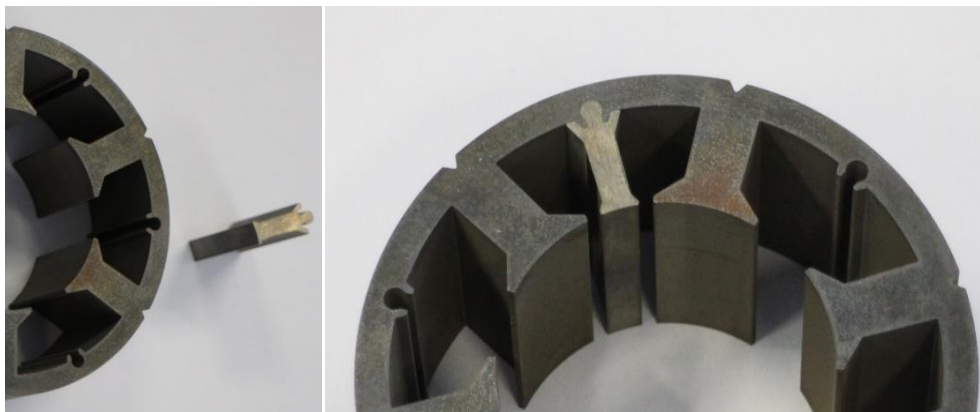


Figure 191: stator construction with push in teeth and ready to be wound.



Figure 192: unitary stator constructed and ready to be wound.

The motor winding resistance shows that the stator with the push-in teeth has significantly lower resistance, as it is wound with 1.9 mm wire diameter. Compared to the unitary stator, the resistance is approximately 30% lower because higher wire diameter (1.9 mm compared to 1.6mm wire diameter that could be wound). The resistance is also 34% lower than that of the stator design in chapter 4 due to a shorter stack length (32 mm compared to 36mm stack length), lower number of turns (21 turns instead of 24 turns), and higher wire diameter (1.9mm instead of 1.7 mm). Table 10 and Table 11 show the comparison between both SPM stators and compare both experimental and numerical values. The difference between the estimated and measured values are with 2% for the stator with the push-in teeth and with 4% for the unitary stator.

Lane 1		Lane 2	
Unitary Stator			
Lines	Resistance (line-line) [m ohms]	Lines	Resistance (line-line) [m ohms]
AB	54.1	AB	52.4
BC	52.3	BC	53.0
CA	54.1	CA	53.0
Stator with push-in teeth			
Lines	Resistance (line-line) [m ohms]	Lines	Resistance (line-line) [m ohms]
AB	36.8	AB	37.0
BC	36.9	BC	37.0
CA	37.0	CA	37.0

Table 10: measured winding resistance for the new-stator design with modular windings.

Unitary stator					
Total conductor Length /mm	3047	Average Length of Turn/mm	145	Total Winding Volume per coil / mm <sup>3</sup>	6430
coil Resistance/ mohms	25.5	Average Body length of Turn/mm	64	All turns Conductor Area per coil / mm <sup>2</sup>	42.22
Overall Motor Length /mm	58.3	Average end turn Length /mm	81.13	Motor End-winding inductance /uH	16.34

Stator with push-in teeth					
Total conductor Length /mm	3170	Average Length of Turn/mm	151.9	Total Winding Volume per coil / mm <sup>3</sup>	9440
coil Resistance/ mohms	18.78	Average Body length of Turn/mm	64	All turns Conductor Area per coil / mm <sup>2</sup>	59.54
Overall Motor Length /mm	61.9	Average end turn Length /mm	86.95	Motor End-winding inductance /uH	16.93

Table 11: windings parameters calculations based on numerical equations for the SPM stator with modular windings.

**5.3. Construction of the SPM rotor:**

As described earlier, the process of blocking the q-axis flux path leads to a segmented rotor design with surface mounted permanent magnets. The rotor design used to investigate tolerance effects on the motor characteristics is shown in Figure 193. The rotor segments were carefully designed, accounting for clearances between the magnets and the rotor segment edges as well as allowing a slot beneath the magnets for glue to retain the magnets. Additionally, extra material is added at the inner point of the segments to hold the rotor segments onto the shaft.

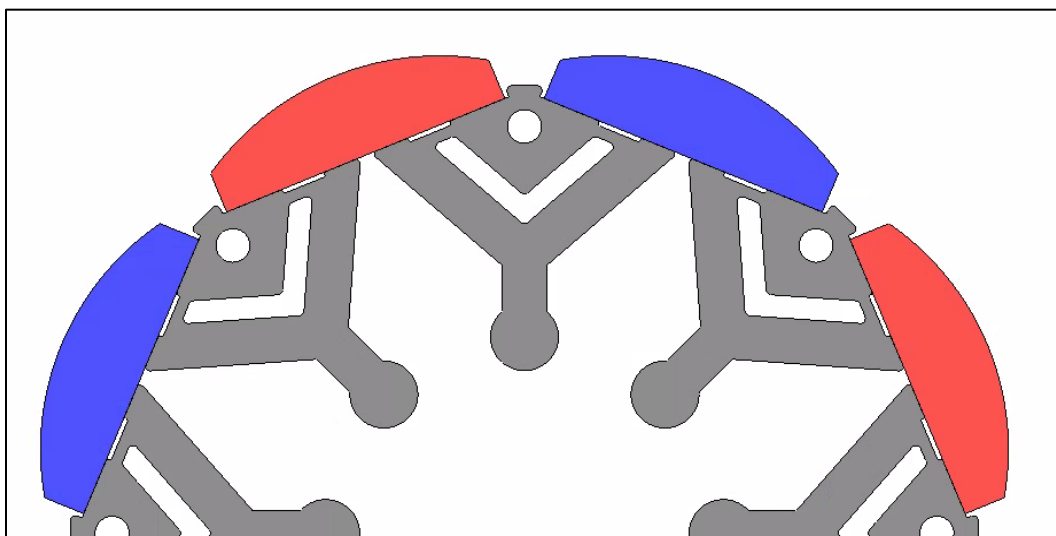


Figure 193: last proposed rotor design.

However, when considering prototype manufacture, problems were encountered. Wire erosion of the rotor segments proved difficult and so the design was simplified, coalescing the circular hole and the barrier into one, as shown in Figure 194.

In addition, the rotor pieces used to locate the segments onto the shaft were shortened to allow use of a baseline motor’s shaft, reducing the number of new components needed. The modified design was modelled and found to have virtually identical

electromagnetic behaviour to the design of Figure 193. The final version of the rotor which is constructed is shown in Figure 194.

For precise construction of the rotor, it was constructed in a series of steps. Firstly, the inner surfaces of the rotor lamination segments were wire eroded, as shown in Figure 195 along with the shaft and assembly jig.

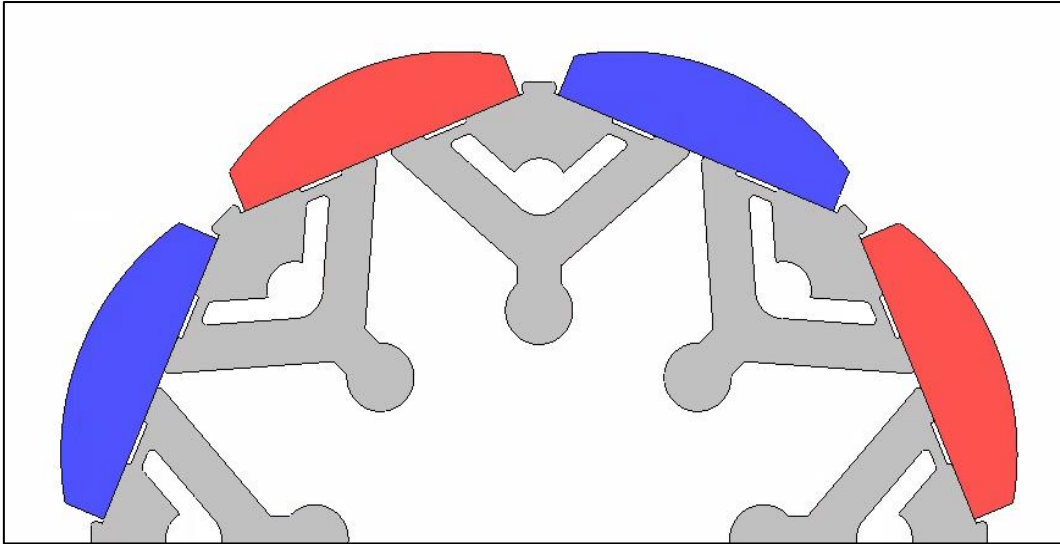


Figure 194: last constructed rotor shape.

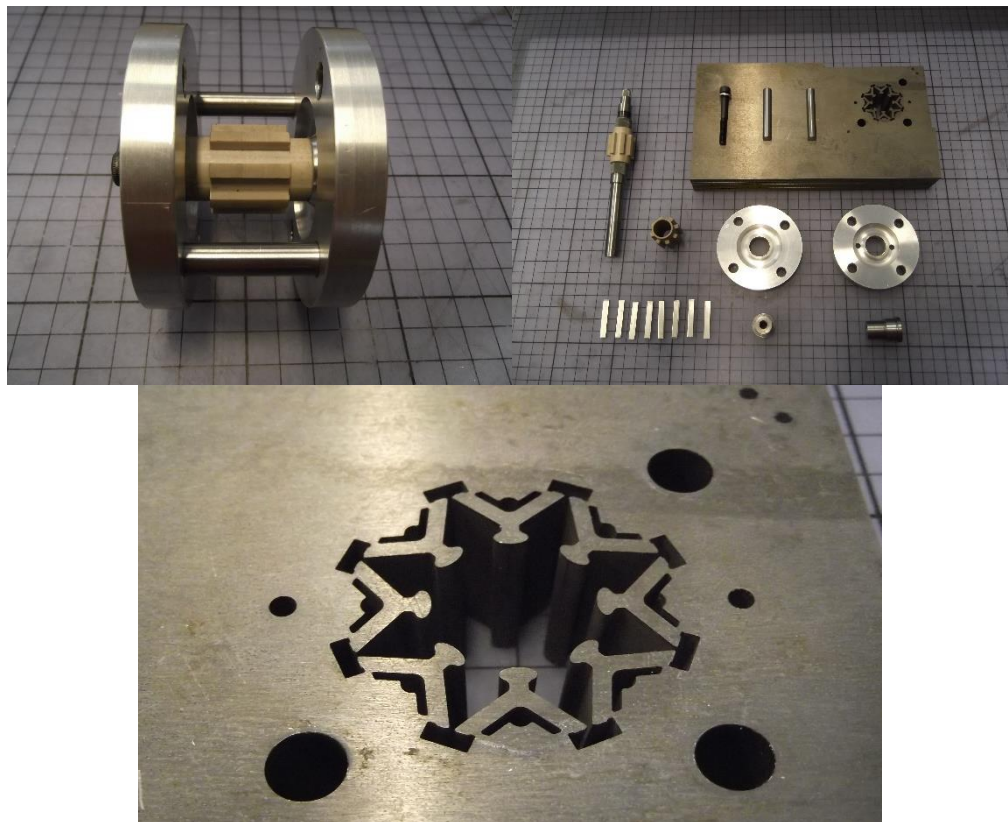


Figure 195: laminations, toolings and assembly for the rotor.

The lamination stack of Figure 195 had locating holes used to ensure alignment when the segments were placed into the assembly jig. Once assembled onto the shaft using the jig, the structure above was filled with epoxy resin and allowed to set.

The segments were now rigidly connected together via the epoxy and so the outside surface of the rotor was subsequently wire eroded. Magnets were glued to the surface. The outer radius of each magnet was validated using a mechanical clock-gauge, with variations found to be less than 50 micro-metres. A 0.3mm thick aluminium sleeve was then placed over the outside of the magnets for protection top to give additional structural integrity. The entire process is illustrated in Figure 196.

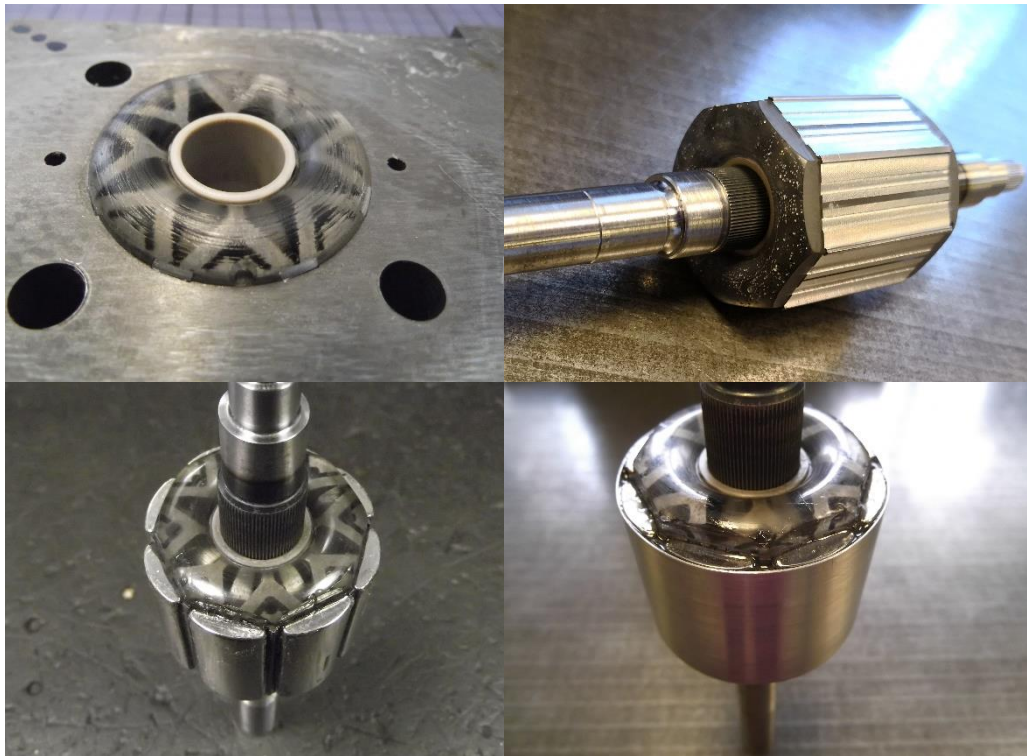


Figure 196: manufacturing process of the SPM rotor.

#### 5.4. Inductance comparison:

As mentioned earlier, high inductance leads to lower short-circuit current following a short-circuit fault, and hence improves the fault-tolerance capability of the system. However, high q-axis inductance results in power loss in the constant power region. The new-stator design offers a very high fault tolerant capability when compared to the baseline design due to high inductance but poor torque capability in the constant power region. The SPM offers higher d-axis inductance and a lower q-axis compared to the baseline motor which solves these issues. The frozen permeability method in 2D FE simulations are used to obtain the results shown in Figure 197 and Figure 198. There

is a large drop in inductance between half load and full load due to saturation in the new-stator design. However, both the SPM and the baseline designs are less prone to saturation.

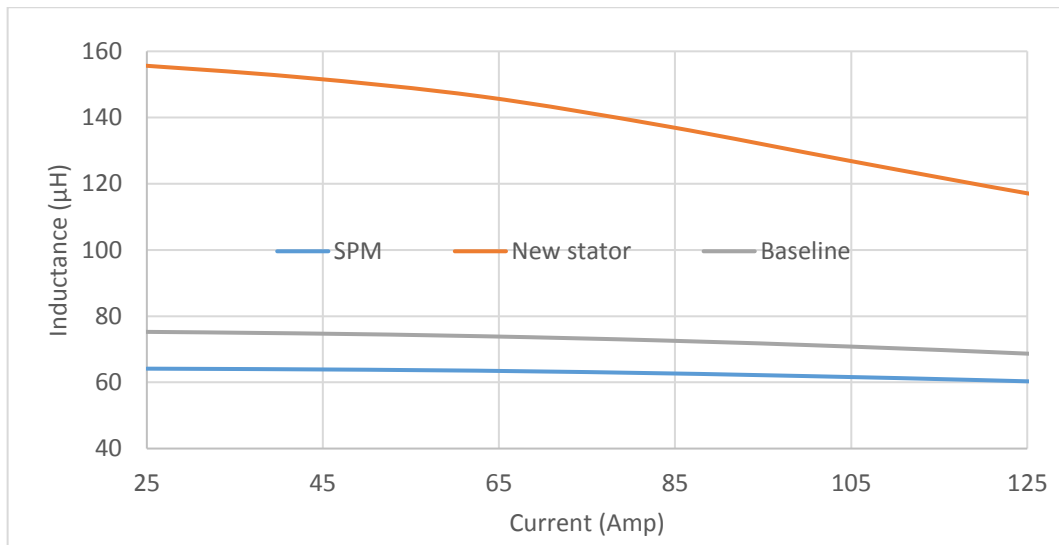


Figure 197: comparison between q-axis inductance vs input current for all the motor designs.

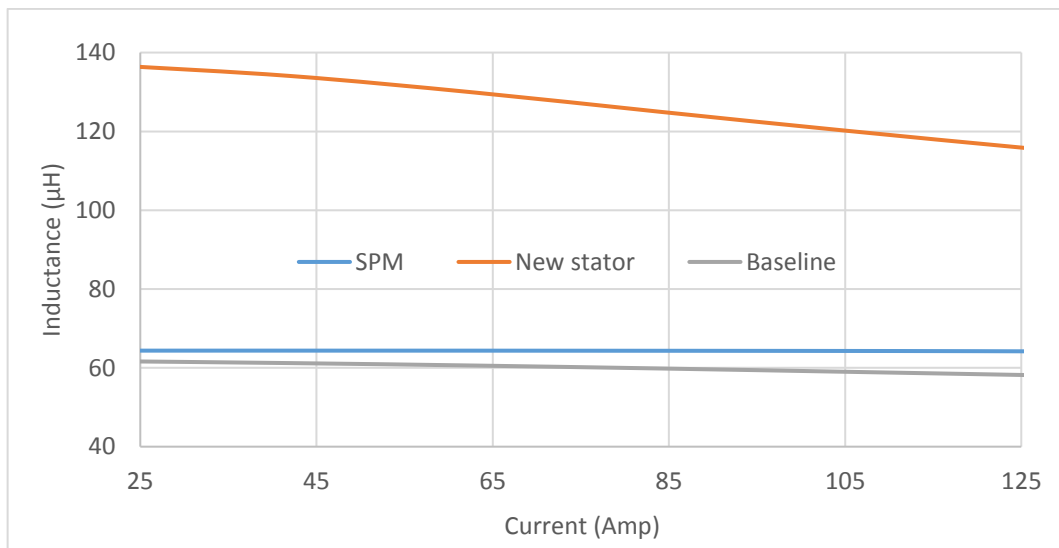


Figure 198: comparison between d-axis inductance vs input current for all the motor designs.

### 5.5. Choosing an appropriate motor stack for manufacture:

Figure 199 and Figure 200 show predicted performance for three different stack lengths. Both 2D and 3D simulation results are shown for a 36mm stack. The 3D results show a small reduction in mean torque, amounting to less than 1% less than 2D simulations, and a similar torque ripple. The other two designs are for shorter stacks, with the stator 1mm longer than the rotor. Torque ripple remains similar in all cases and so the choice was made based upon mean torque capability. The design with a 32 mm stator and 31 mm rotor stack lengths was chosen for manufacture. This is predicted to have 6% greater mean torque capability than the specification, leaving

some margin for torque drop in the event of having to shape the current to mitigate a higher than desired low speed torque ripple.

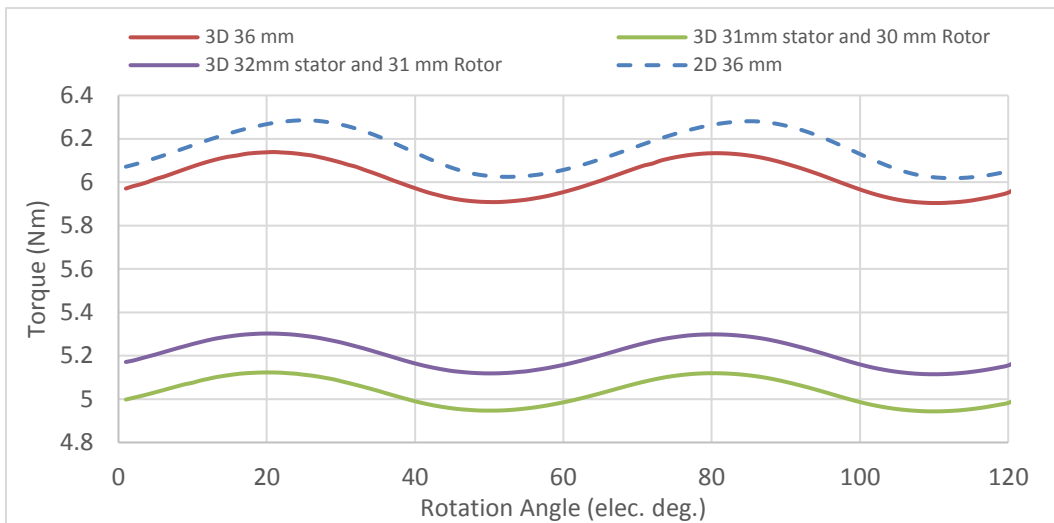


Figure 199: 2D FE and 3D FE comparison of the SPM torque capability for different stack lengths.

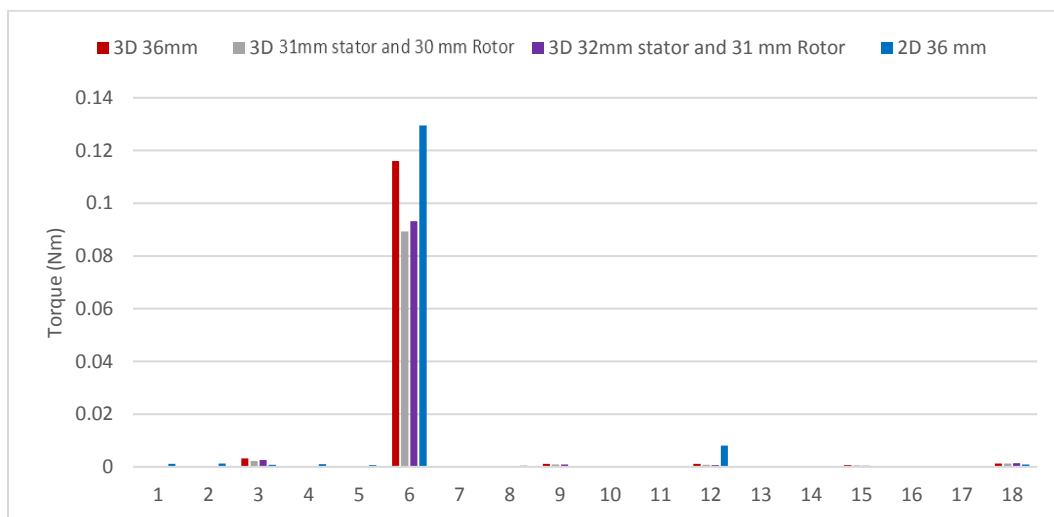


Figure 200: Harmonic contents of the SPM torque capability.

### 5.6. Measured capability comparison between designs:

Simulation has shown earlier how the SPM outperforms the baseline motor and all other designs under consideration due to its high torque density, no need for skewing, and higher airgap flux density. In order to keep the same output torque, the SPM motor is constructed with a shorter stack length. The motor is designed to have a very low cogging torque; however, it is predicted that on load the torque ripple is higher than that of the baseline motor. This can be tackled by shaping the input current, at the cost of a slight drop of the average torque and an increase in control complexity. The three designs (baseline, new-stator with baseline rotor and SPM) are compared in the coming section.

### 5.6.1. No-load characteristics:

This section compares both measured cogging torque and back-emfs for all the three motor designs. As explained earlier, the wound stator teeth of the SPM design have their arc increased to 41 mechanical degrees, corresponding to 164 electrical degrees. This combined with the un-skewed rotor brings the winding factor to almost unity ( $K_w = 0.993$ ).

The difference between the 2D and 3D FE simulations of the SPM motor are expected to be due to the stacking factor and material specification of the stator which is constructed. The design has been checked in the FE software packages (JMAG, Ansys, and MotorCAD), and all provided very low cogging torque with similar harmonic content.

The measured cogging torque of the SPM is higher than the baseline motor. This may be due to the manufacturing tolerances. Figure 201 shows the cogging torque comparison between all the motor designs. From Table 12, the SPM motor's cogging torque is significantly higher than the simulation results. There are unexpected harmonic components such as 6<sup>th</sup> and 18<sup>th</sup> orders which are significantly high. The peak to peak cogging torque of the SPM design is approximately 1.5% of the motor's torque capability.

The unitary stator's 8<sup>th</sup> order cogging component is approximately half compared to the stator with push-in teeth. This is shown in Figure 187 in which the triangular joint produces a very high 8<sup>th</sup> order harmonic.

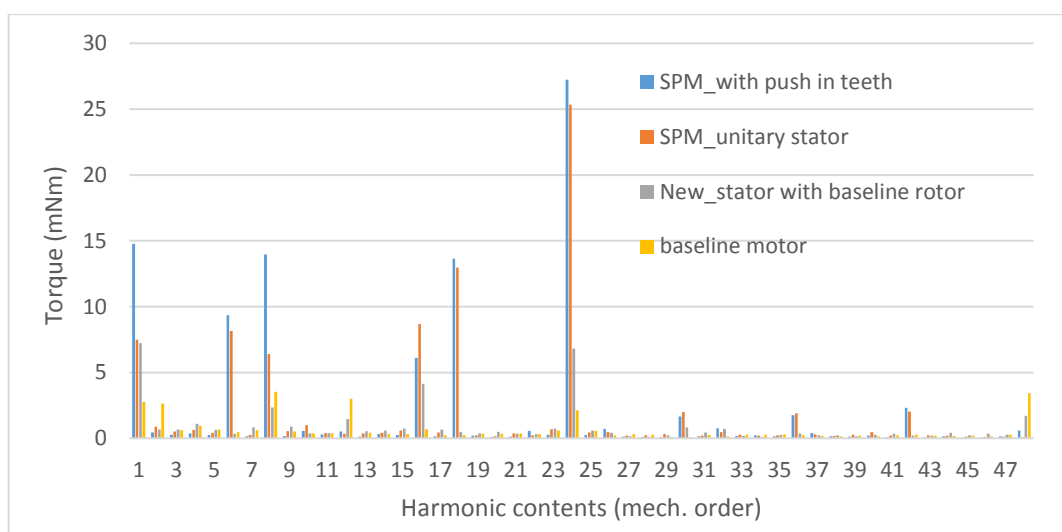


Figure 201: harmonic content comparison of the cogging torque for all the motor designs (measured values).

## Chapter 5: Novel SPM design and development

	SPM with push-in teeth	SPM unitary stator	New-stator with baseline rotor	Baseline motor
2 <sup>nd</sup> order	0.44	0.88	0.65	2.64
4 <sup>th</sup> order	0.383	0.65	1.10	0.96
6 <sup>th</sup> order	9.35	8.16	0.35	0.47
8 <sup>th</sup> order	13.958	6.39	2.33	3.54
12 <sup>th</sup> order	0.513	0.34	1.46	3.01
16 <sup>th</sup> order	6.117	8.69	4.13	0.68
18 <sup>th</sup> order	13.645	12.98	0.48	0.24
24 <sup>th</sup> order	27.245	25.35	6.81	2.13
30 <sup>th</sup> order	1.649	2	0.83	0.075
36 <sup>th</sup> order	1.756	1.91	0.37	0.22
42 <sup>nd</sup> order	2.307	2.01	0.20	0.27
48 <sup>th</sup> order	0.598	0.08	1.71	3.43

Table 12: comparison between cogging torque certain harmonic contents.

The back-emf of the different designs shows how the SPM outperforms the other designs due to a higher airgap flux density and un-skewed rotor. The SPM motor is wound with 21 coil turns and a 13% shorter rotor, unlike the other two designs which are wound with 24 coil turns. The SPM motor is purposely designed to have very low cogging torque, with less attention paid to torque ripple; hence, the 5<sup>th</sup> and 7<sup>th</sup> harmonic contents of the back-emf are higher (as shown in Figure 203). These harmonic components lead to higher torque ripple during loaded conditions.

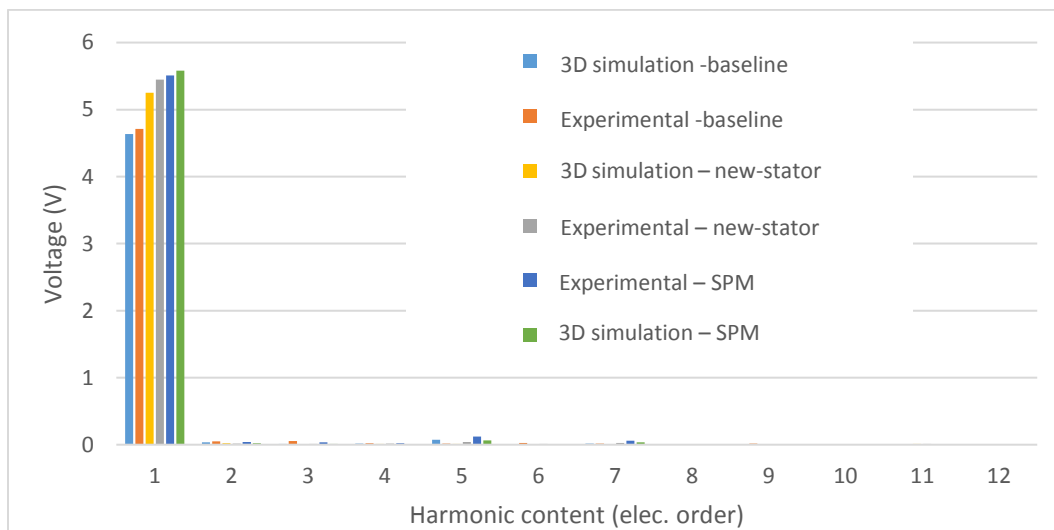


Figure 202: Harmonic content comparison of the back-emf for all the motor designs.

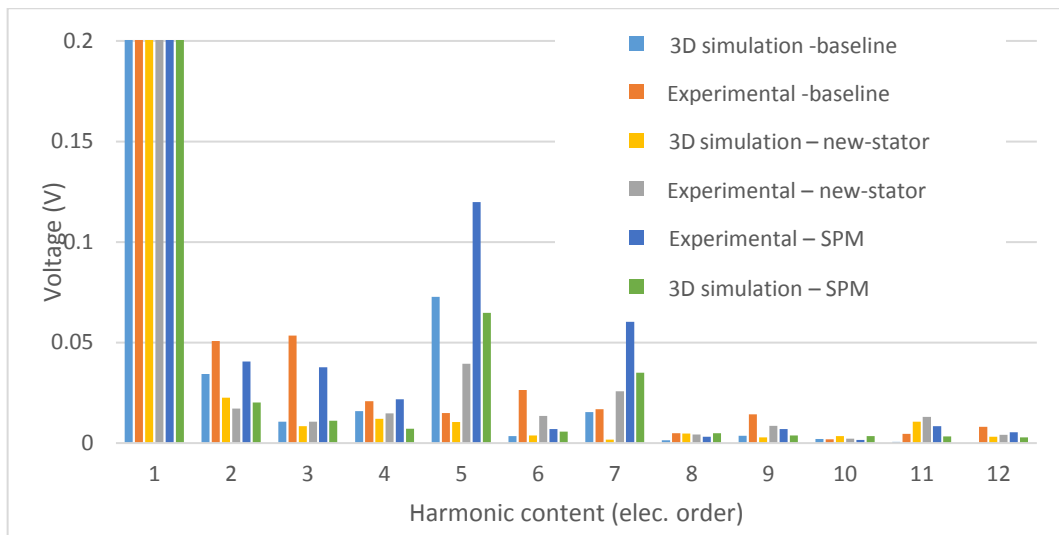


Figure 203: Harmonic content comparison of the back-emf for all the motor designs [scaled].

**5.6.2. Loaded characteristics:**

3D FE simulations were conducted to analyse the SPM design’s performance. DC torque evaluation involves placing a dc current into the machine and then rotating the rotor. There is an extra element of saturation due to the stacking factor that affects both the fundamental component (4<sup>th</sup> order), which is alignment torque, and 8<sup>th</sup> order which is reluctance torque (Figure 204).

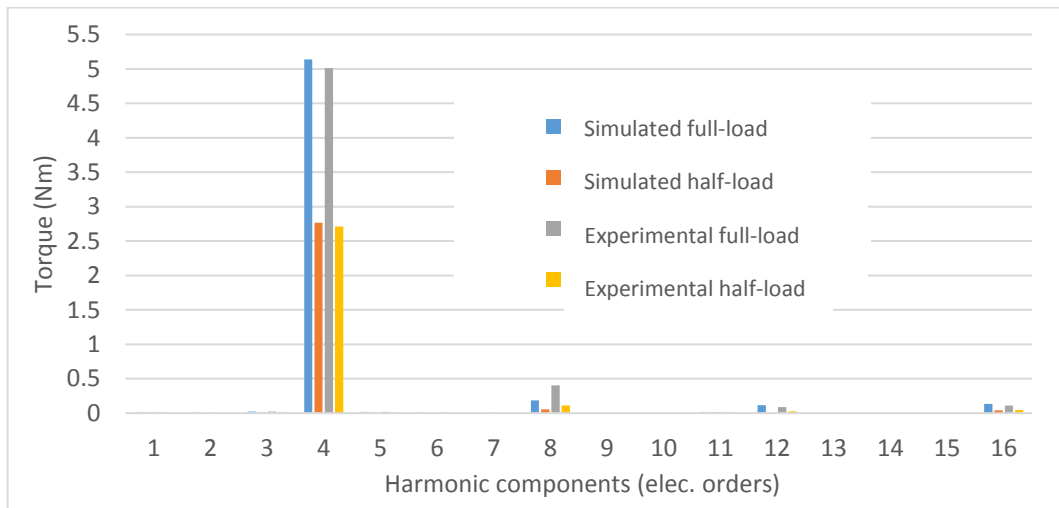


Figure 204: DC torque comparison between simulation and practical results of the SPM design.

Based on measured results, the SPM design outperforms the previous designs in terms of mean torque. Despite the 13% shorter stack and 5% less input current, the SPM is capable of delivering approximately 6% and 10% more torque at full load and half load, respectively (Figure 205). This means that the motor stack can be further reduced, leading to a yet smaller size and providing no current shaping.

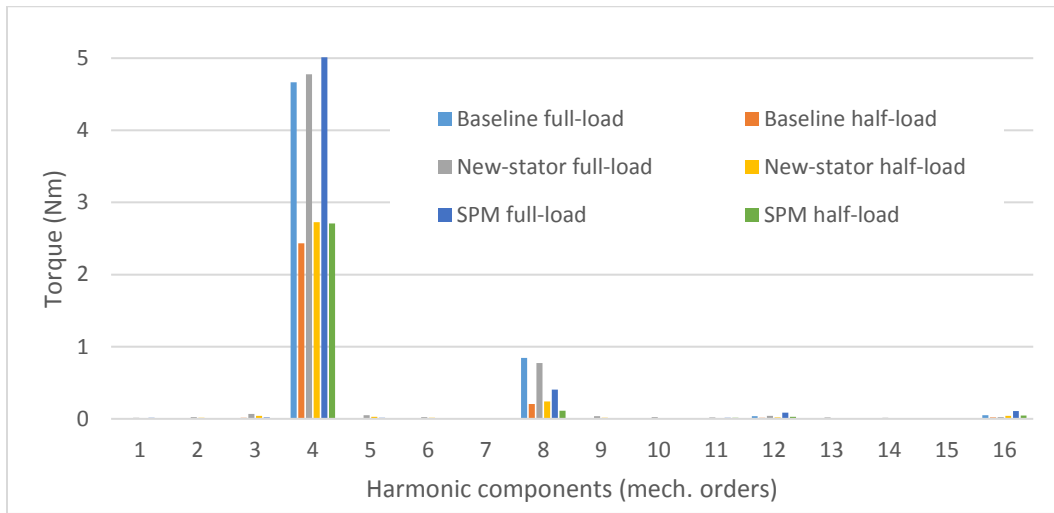


Figure 205: experimental DC torque comparison for all the motor designs.

The SPM torque ripple prediction using 3D FE analysis is differs slightly from the measured values. This may be due to manufacturing tolerances and the failure to model the stacking factor accurately in the 3D model. The 24<sup>th</sup> harmonic order is higher in the 3D FE simulation with negligible other orders. However, the experimental results show considerably higher amplitude low order harmonics including the 6<sup>th</sup>, 8<sup>th</sup>, 12<sup>th</sup>, 16<sup>th</sup> and 18<sup>th</sup> orders (Figure 206). This may be due to time harmonics in the current generated from the electrical power supply and mechanical tolerances in the motor assembly.

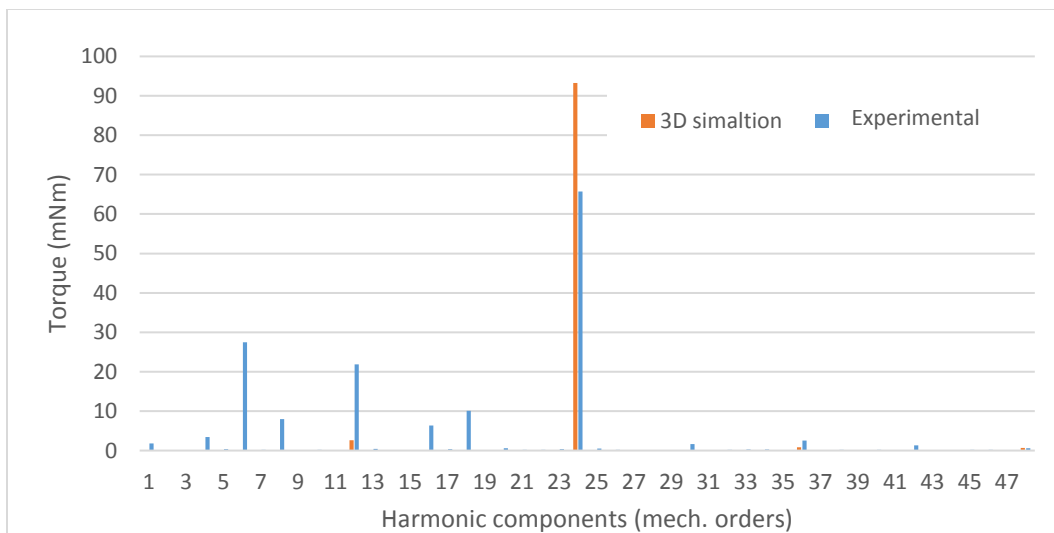


Figure 206: SPM's torque ripple comparison between practical and simulation results.

However, the SPM motor's torque ripple remains higher than the baseline motor. The motor was designed to meet the objectives of fault tolerance and low cogging torque, which compromised the torque ripple (Figure 207).

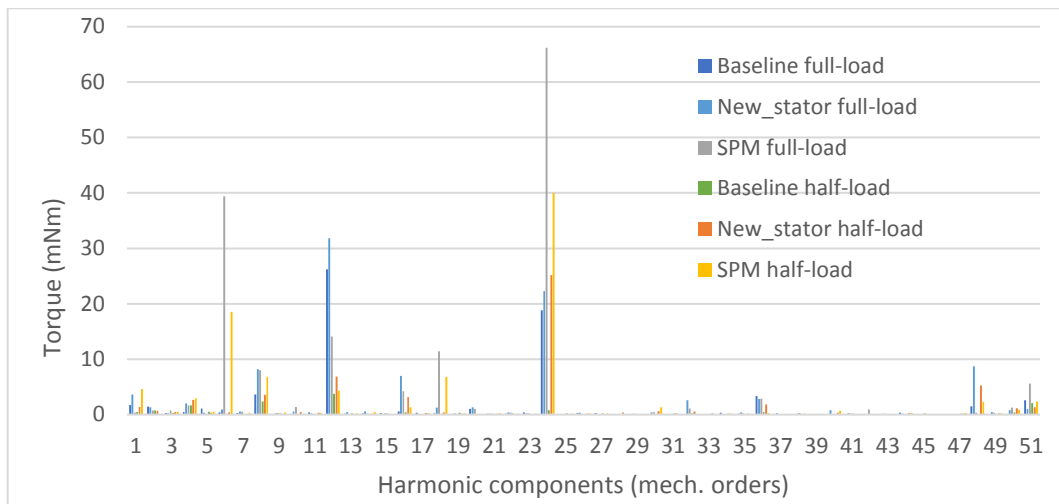


Figure 207: Torque ripple comparison between all the motor designs based on harmonic contents.

### 5.6.3. Performance under faulted conditions:

This section will consider each design and compare the torque-speed capability under faulted conditions for both loaded and un-loaded operation. As shown in the previous chapters, modular windings using dissimilar teeth stators offer higher torque capability under fault conditions through reducing the mutual coupling between the coils and higher torque capability through the winding factor.

#### 5.6.3.1. No-load comparison (Simulation vs Experimental):

The motor's no-load drag torque shows that there is a trade-off between the peak drag torque that occurs at low speeds and its value at high speeds. Clearly, both the baseline motor and the SPM motor designs offer poorer fault tolerance compared to the intermediate motor design (Figure 208). However, the SPM design has lower drag torque at high speed due to the resistance to inductance ratio and a higher d-axis inductance.

Additionally, the induced short-circuit current in the SPM winding is lower than that in the baseline motor by approximately 8% and is approximately 20% below the rated current but is almost 30% higher than the intermediate design (Figure 209). As expected, the SPM no-load drag torque is very similar to the baseline motor as it has a similar phase resistance and inductance. However, the main advantage of this design is better segregation between the coils for the half-half winding arrangement and lower torque ripple under faulted conditions compared to the baseline motor. The drag torque is 1% lower (Figure 208) at high speeds for an SPM which has a significantly higher back-emf constant than the IPM motors. Although the no-load drag torque is similar for the SPM and baseline design, the torque capability of the SPM motor is expected to be higher as the transformer coupling becomes lower.

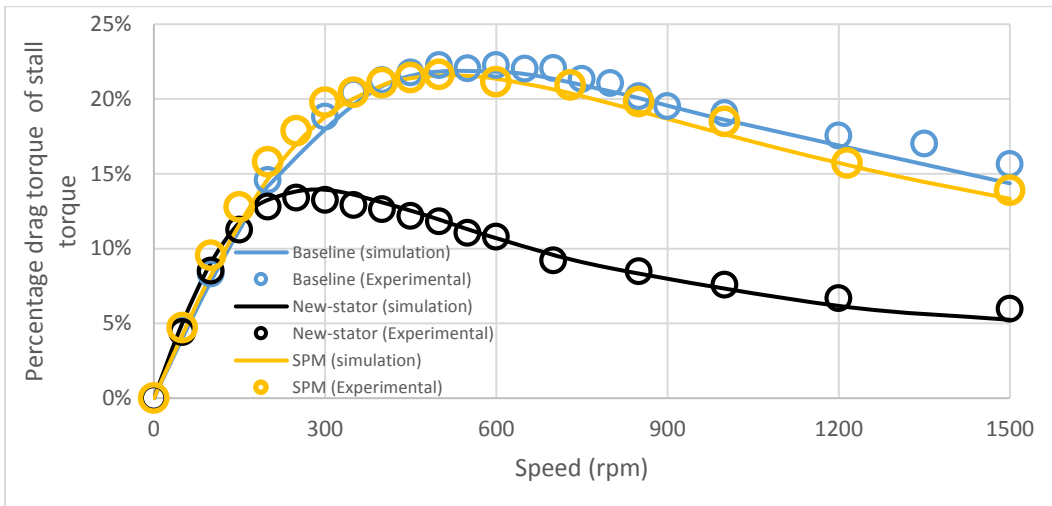


Figure 208: Comparison between all the motors for no-load drag torque.

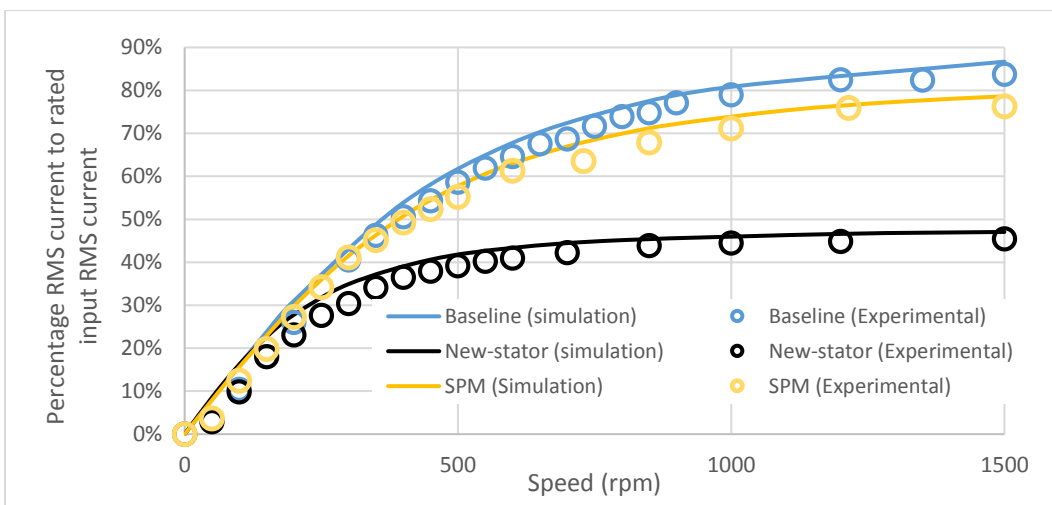


Figure 209: Comparison between all the motors for no-load induced short-circuit current.

**5.6.3.2. Loaded comparison:**

Based on the no-load drag torque prediction, the SPM motor design is capable of delivering approximately 30% of its stall torque following a three-phase short circuit, which is approximately 4% higher than the baseline motor, however, it is approximately 8% lower than the new-stator motor (Figure 210).

The SPM half-half winding arrangement gives the largest mean torque. The torque ripple is higher due to transformer (mutual) coupling between the edge coils (as in Figure 211 and Figure 212). As the SPM’s torque ripple under normal conditions is 3.5%, transformer coupling only contributes to 3-4% of the torque ripple under faulted conditions. Compared to the baseline design, the SPM transformer coupling is 10% lower. Additionally, the SPM motor’s torque capability is normalised across the speed range to its stall torque in Figure 210. The stall torque of the SPM design is higher than

the baseline design by 6% and 10% at full-load and half-load, respectively. This means that the SPM produces an extra 4-5% higher torque compared to the baseline motor.

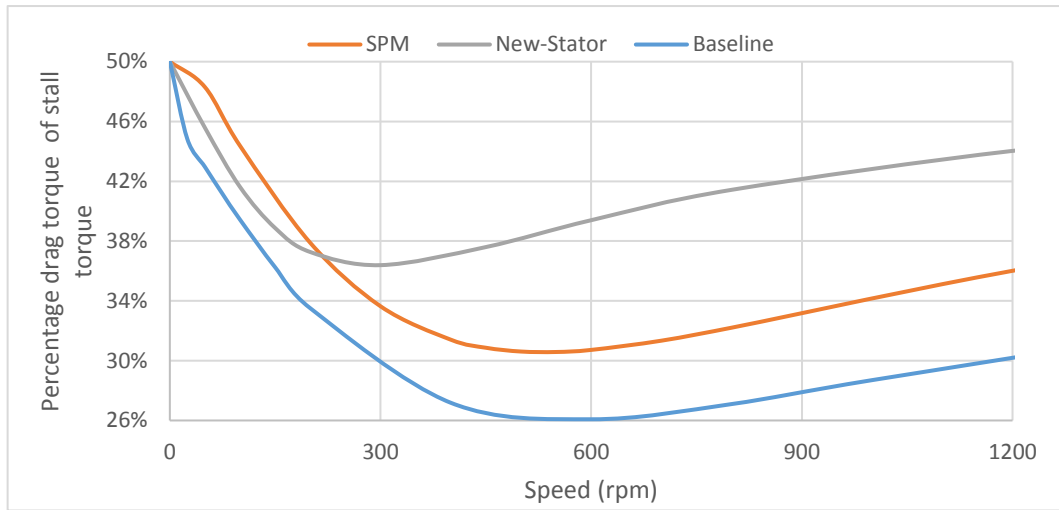


Figure 210: comparison between all motor design torque capability under three-phase short circuit fault for half-half arrangement.

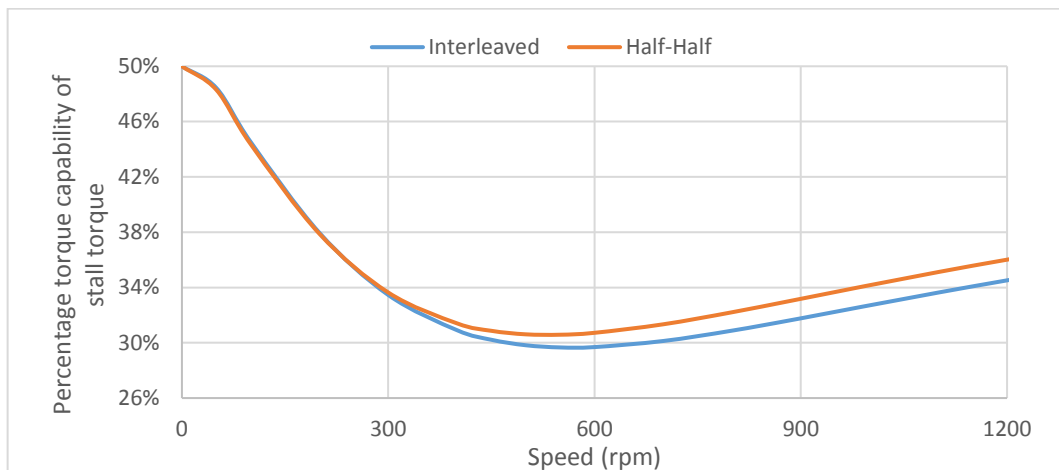


Figure 211: comparison between torque capability of the SPM for different winding arrangement under three-phase short circuit fault.

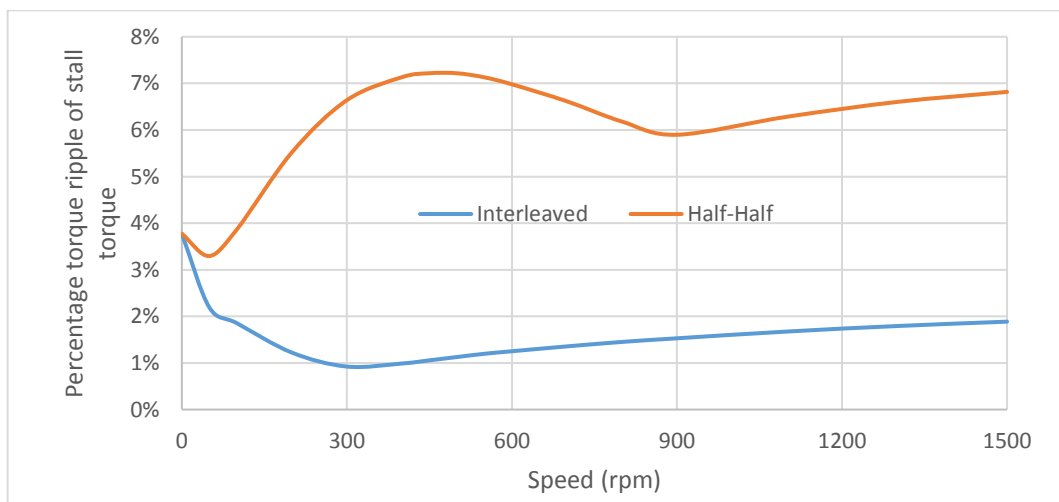


Figure 212: torque ripple comparison between SPM's different winding arrangement under three-phase short circuit fault.

### **Experimental results:**

The motors were tested using ZF test facilities. A dyno and an external ECU with an external encoder (described in Test rig: and Appendix A:) were used to investigate the motors' capability under various conditions.

Before testing each motor, the external encoder was aligned with the d-axis of the rotor by energising the motor at no-load. This process helps in indicating the rotor mechanical position relative to the input voltage in which the encoder can be used as position feedback.

Additionally, the motors were tuned to obtain maximum power. The tuning process is carried out by testing the motor at different advance angles using a ramp test across the speed range. By using a MATLAB based software, all the torque-speed curves for the different advance angles were loaded to obtain the optimum torque across the speed range. The results out of the tuning process are input current value and advance angle for the speed range.

To obtain maximum power under faulted conditions, the drag torque should be at its minimum. One of the main approaches to get 50% of the motor's capability under faulted conditions is to disconnect the faulted lane from the drive, creating an open circuit. This solution brings the drag torque to zero and lowers the risk of fault propagation due to the short-circuit current.

The baseline design suffers from low order harmonics due to transformer coupling between the coils (fully covered in Chapter 2). The open lane influences the healthy lane, so parallel paths of the same phase are not sharing similar current. This means that the MMF input across two teeth of the same phase are not equal. The highest MMF carrying tooth imposes 8<sup>th</sup> order mechanical harmonics and both the teeth impose 16<sup>th</sup> order harmonics. These are be shown in the next section.

#### **5.6.3.3. Comparison using colour map graphs:**

The colour map shows the spread of harmonics across the speed range. It has frequency on the x axis and speed on the y axis, displaying the amplitude of harmonic content through intensifying the colour. A MATLAB developed GUI software makes a Fast Fourier Transform of the torque for each speed and creates a grid of data by collating individual signals on top of each other. A vertical line in the graph means that there is a constant frequency in the signal for at the speeds, such as that produced by

mechanical resonance. However, a horizontal line means that there is a large amount of harmonic at a given speed.

Figure 213 shows an example of the torque ripple colour map in which harmonic content of the main harmonics are diagonally starting from the origin. The amplitude of the specific harmonic order is based on the intensity of the colour of the diagonal line. At the top and right corners of the colour plot, the harmonic orders are labelled in coordination with the diagonal lines.

In Figure 213, there are harmonic orders that can be clearly identified such as 8<sup>th</sup>, 12<sup>th</sup>, and 24<sup>th</sup>. There is also a mechanical resonance at 450Hz which can be due to rig resonance.

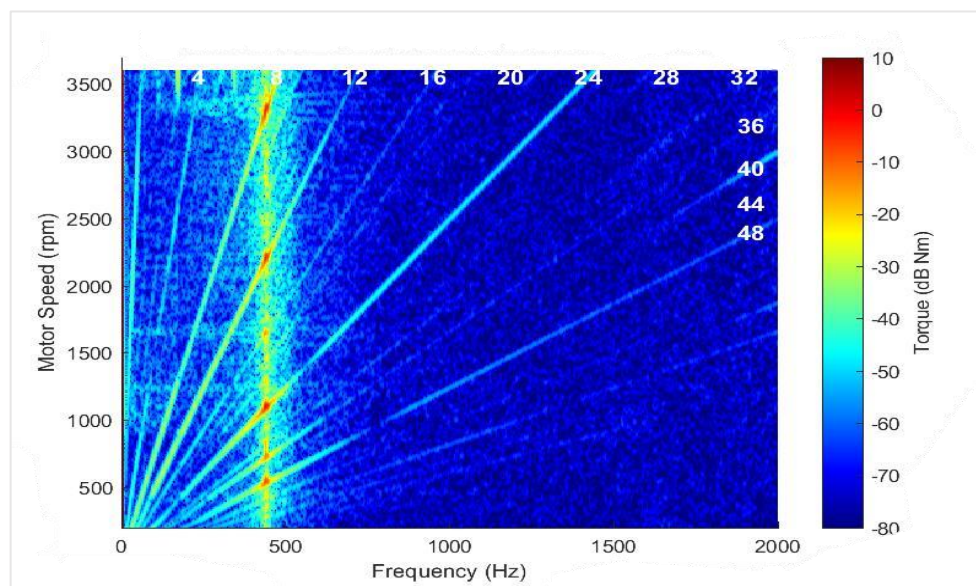


Figure 213: example of the colour map graphs for torque ripple content of a torque speed characteristic.

The next section will compare the torque capability and torque ripple harmonic content using colour map graphs, comparing the three designed motors (baseline, intermediate design and SPM with the push-in stator inter-poles). The comparison is between the three designs under different operating conditions (such as normal operation with both lanes operating, one lane operating and the other inactive, one lane operating and the other experiencing a three-phase physical short and one lane operating and the other experiencing a single MosFET failure).

#### A) Max power with no failure:

The measured results (Figure 214) show the superiority of the SPM design over the other designs, especially in constant power region. The d-axis inductance plays a crucial role in this region as it is the main component that enables field weakening. The

motor also has a lower winding resistance that makes more supply voltage available and increases the knee point speed. This could be enhanced by further shortening the motor and increasing the input current by 5% to match the baseline motor input. This will push the knee point further by having a lower back-emf and lower voltage drop due to winding resistance, for the supply voltage to overcome.

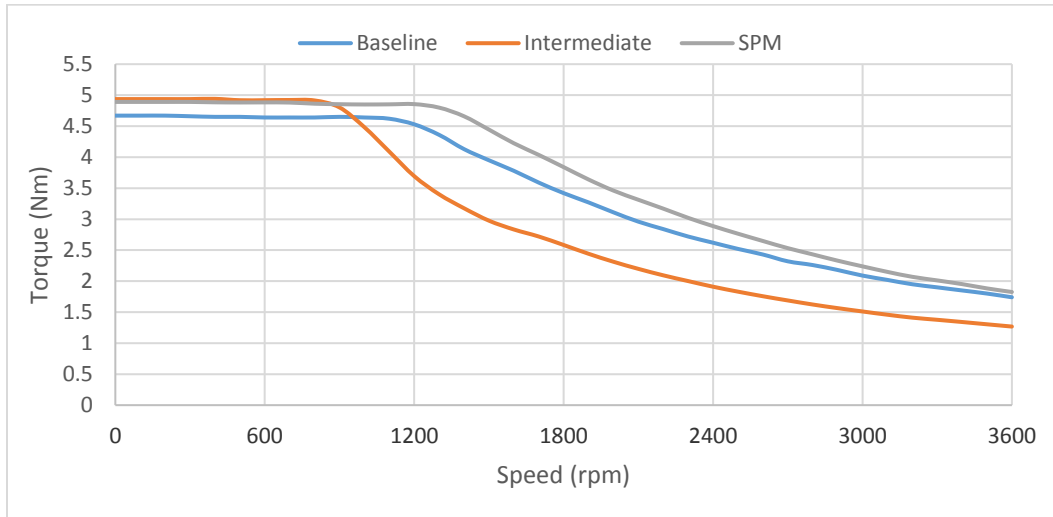


Figure 214: Comparison between torque-speed characteristics of all the motor designs for max power tuning.

Figure 215 shows the difference between harmonic content of the motors' torque across the torque-speed range. There is a fixed vertical line at 450 Hz, which corresponds to rig resonance and can be seen in all the figures of this section and other sections. Figure 215.A shows the baseline motor's harmonic content in which 8<sup>th</sup>, 12<sup>th</sup> and 24<sup>th</sup> orders are dominant and can be seen clearly. The lower orders are not predicted from simulations and may be due to assembly and manufacturing tolerances. However, both modular stators show similar behaviour despite having different rotors (Figure 215. B and C). The SPM motor has a higher ripple content as the stator has push-in teeth, which can be seen as 8<sup>th</sup> order and different even orders. Markedly, the baseline's 24<sup>th</sup> order that comes from the interaction between the stator MMF and the rotor magnetic field and slotting effect is higher than both the new developed designs.

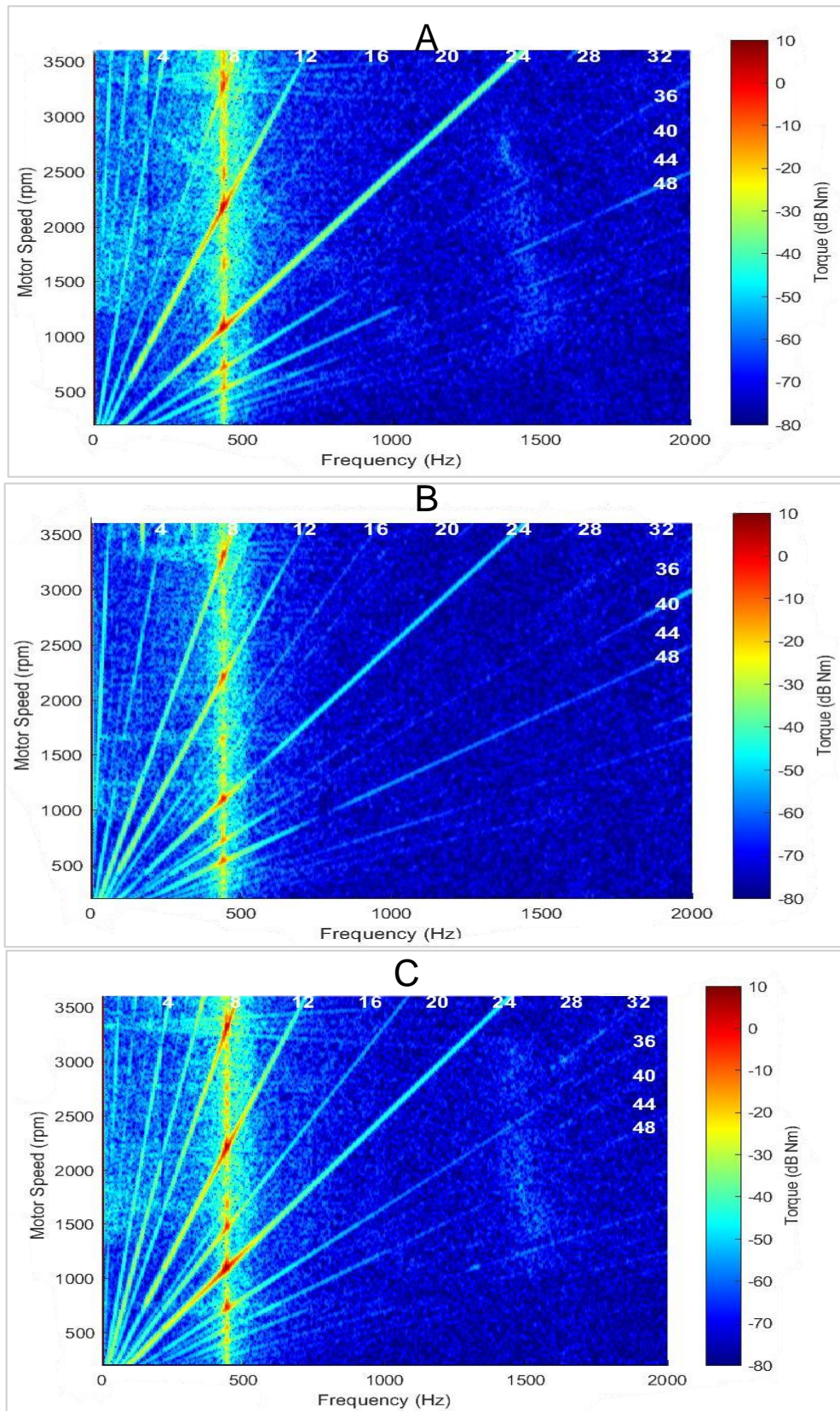


Figure 215: colour map of torque ripple harmonic content for different motors: A) baseline, B) intermediate, and C) SPM.

**B) One lane operating, and one lane inactive:**

As explained earlier, all the motor designs have a dual-lane stator split in two equal halves (half-half arrangement). One-lane of the motors was connected to an ECU and the other lane was left inactive, leaving all the coil terminals unconnected. This approach is to replicate the condition when one of the two motor inverters is disconnected from the motor using a solid-state switch between the inverter and the motor. Both SPM and intermediate designs operate with half the capability of when both lanes are excited. They have an identical knee point speed, as shown in Figure 217. This is due to low transformer coupling between the motor lanes, as they both have modular windings.

On the other hand, the torque speed curve knee point of the baseline motor is increased due to high transformer coupling between the coils. This is due to interaction between the loaded coils of the excited lane. Figure 216 shows that with lane 2 inactive, coils 2 and 3 in the highlighted green circles are only affected by one coil. However, both coils 2 and 3 highlighted in the yellow circle are affected through transformer coupling.

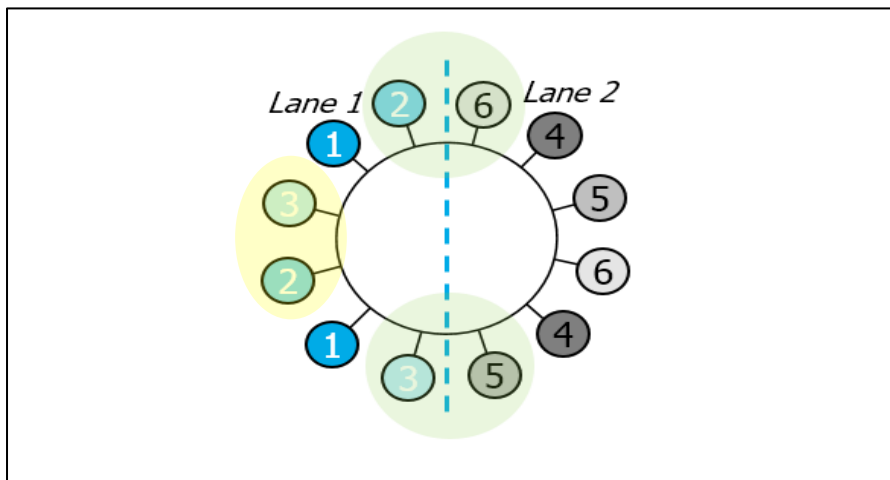


Figure 216: Interaction between motor lanes for Half-half arrangement.

The transformer coupling affects the motors' harmonic content as it affects the flux linking individual stator coils.

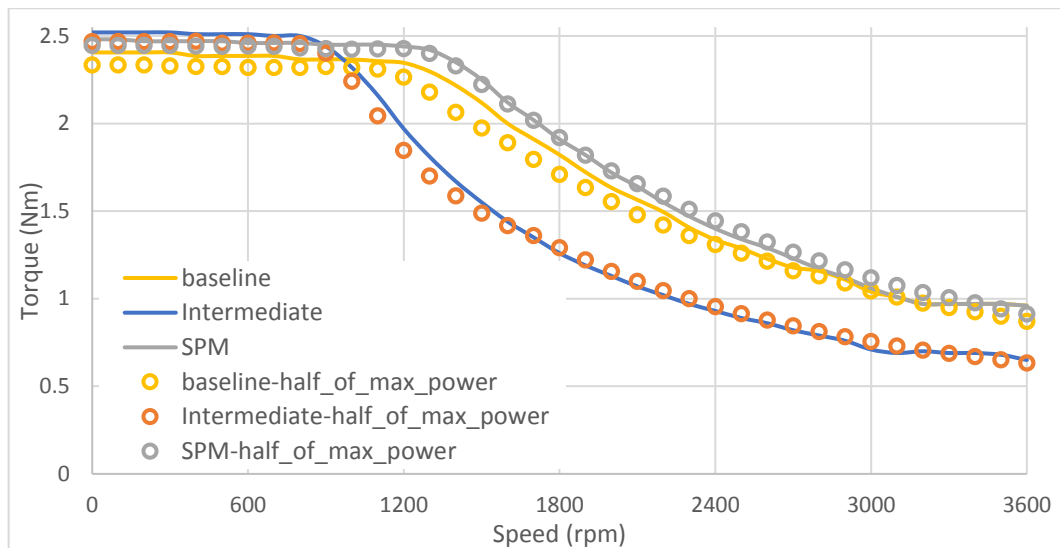


Figure 217: torque-speed characteristics of all the motor designs when one lane is operated, and one lane is inactive.

The baseline motor colour map of Figure 218.A. shows that there are both 8<sup>th</sup> and 16<sup>th</sup> harmonics present due to high mutual coupling between the coils. The imbalance between parallel connected coils caused by different mutual couplings is believed to be the main reason for the 8<sup>th</sup> order harmonics.

Expectedly, both the SPM and intermediate designs have negligible 16<sup>th</sup> order harmonic content as there is only one coil per phase. Overall, the intermediate design exhibits lower harmonic content as its stator is unitary. The SPM suffers from extra harmonic orders which are mainly due to the push-in teeth, which were found to move slightly during operation. Despite that, the 8<sup>th</sup> order harmonic is lower than that in the baseline design. The colour maps in Figure 218 show the different behaviour of the all tested motors.

Interestingly, the 24<sup>th</sup> order of both SPM and intermediate designs is significantly lower than the baseline across all the speed range.

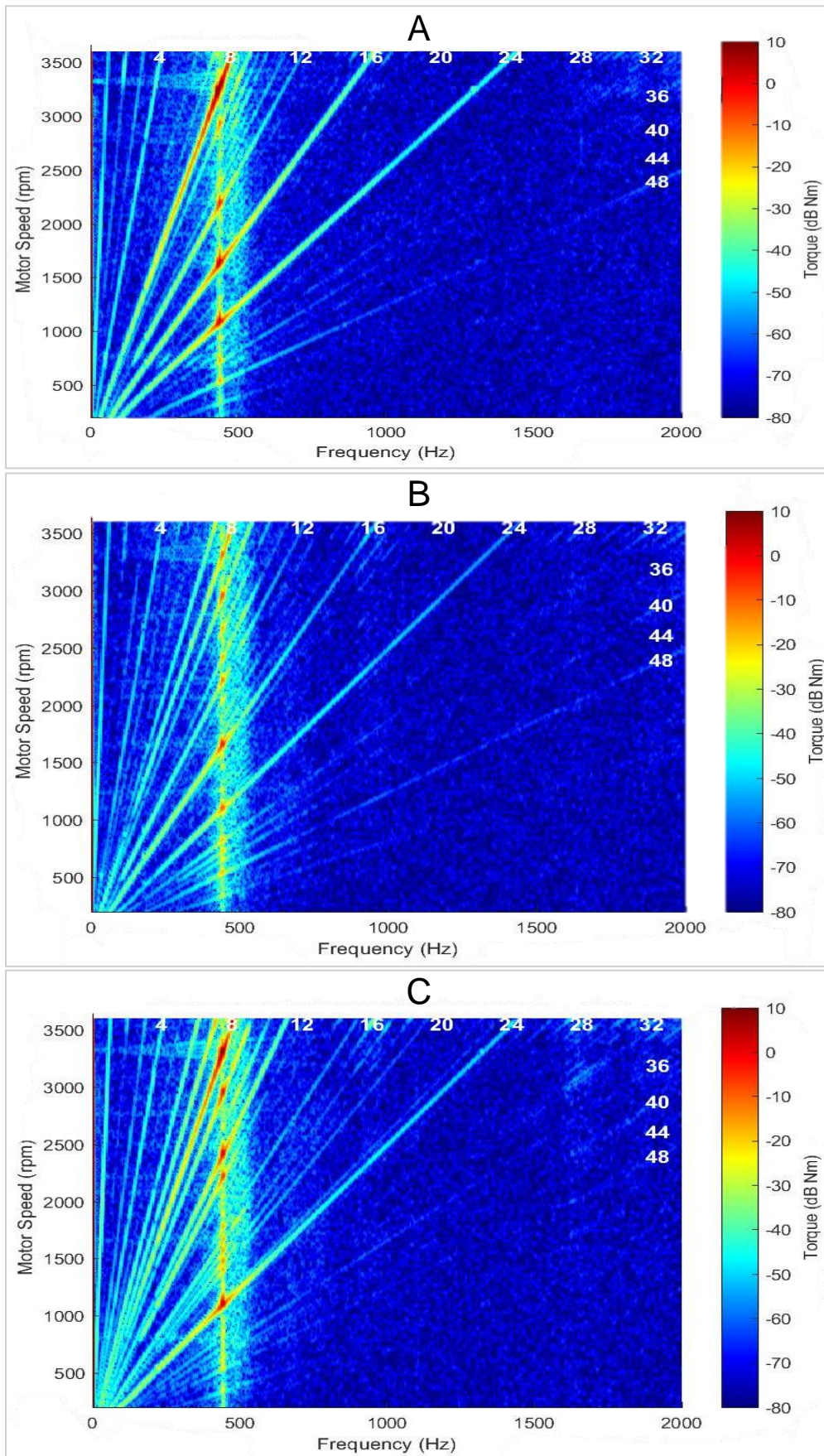


Figure 218: colour map of torque ripple harmonic content for different motors: A) baseline, B) intermediate, and C) SPM.

**C) One lane is operating, and one lane is short-circuited through a power module (Single MosFET failure):**

To create a MosFET short-circuit failure, a power module was used, as shown in Figure 219. The power module was provided by ZF: it can handle 100 Amps RMS for a ramp test of less than 30 seconds. It was placed on a heat sink with a fan attached to the end of the heat sink. Figure 220 shows the power model connected to create a physical short circuit across one MosFET. There are two conditions for this test, termed middle MosFET and Edge MosFET short-circuits.

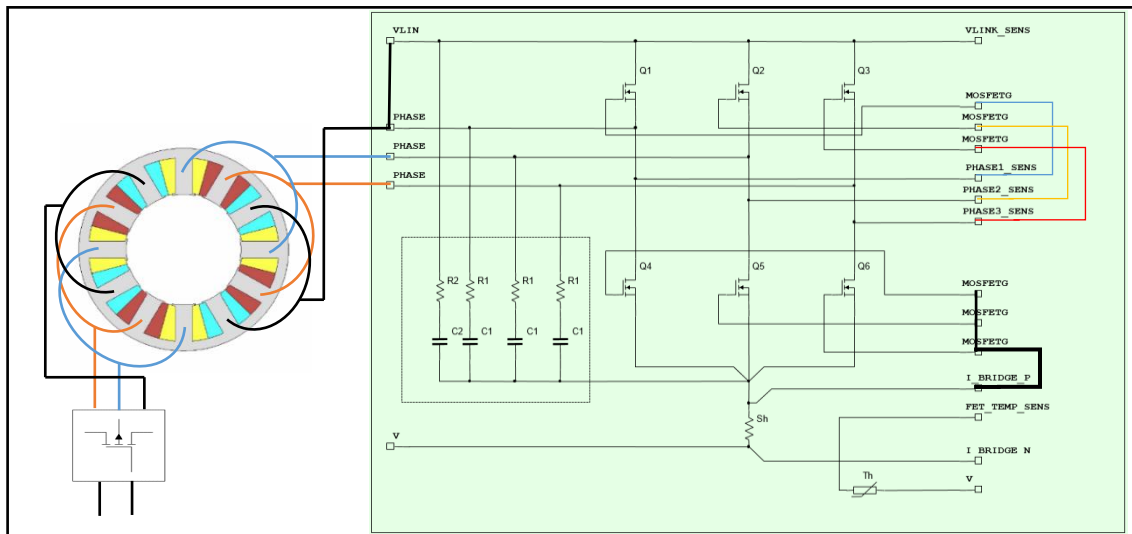


Figure 219: circuit diagram of a power module used to create a single MosFET failure.



Figure 220: power module with reconnected terminals to create a single MosFET failure.

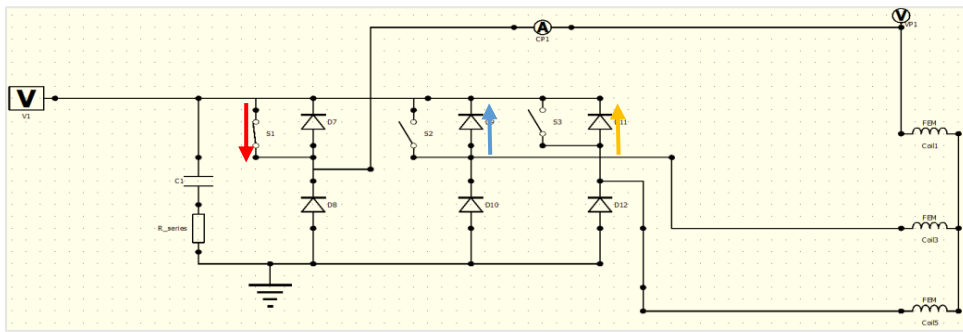


Figure 221: circuit diagram for single MosFET and direction of current flow.

Figure 222 shows the torque signal when the motor has a single MosFET failure. The graph shows two electrical cycles of torque capability for the intermediate design, during which time the ripple repeats four times in one mechanical cycle. Figure 223 shows that the harmonic content of time series waveform contains multiples of 4<sup>th</sup> order. Also, the diodes parallel to the short-circuit MosFET operate in rectifier mode in which the highest current flows through the short-circuit MosFET and returns through the parallel diodes (Figure 221 and Figure 224).

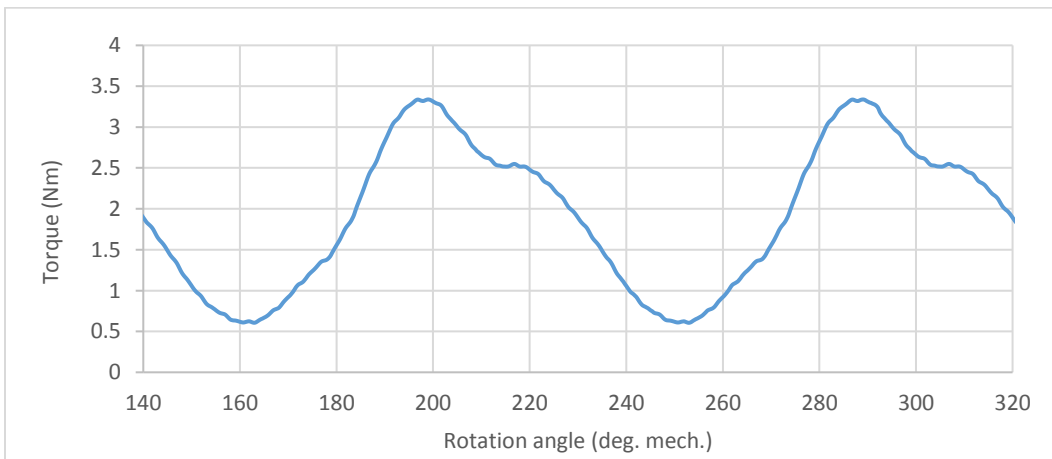


Figure 222: 2D FE simulated single MosFET failure time series torque waveform at 800 rpm.

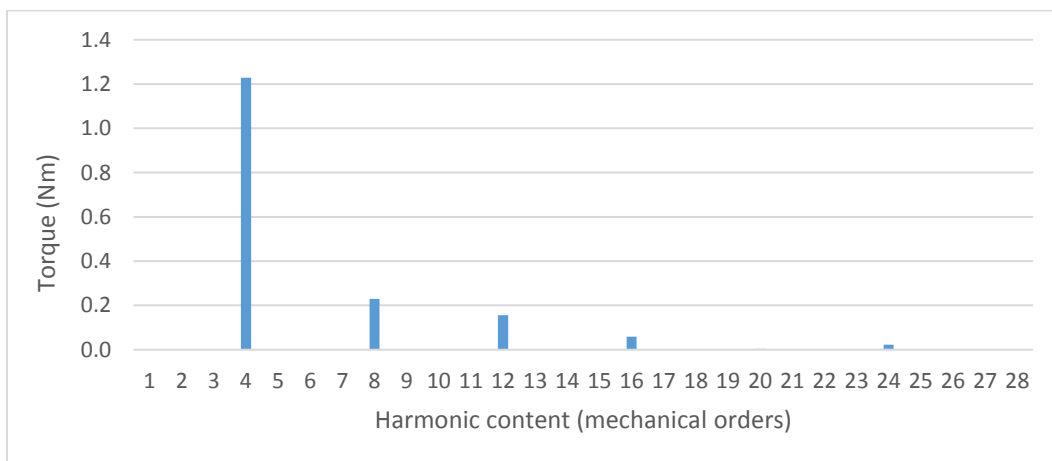


Figure 223: harmonic contents of the simulated single MosFET failure time series waveform.

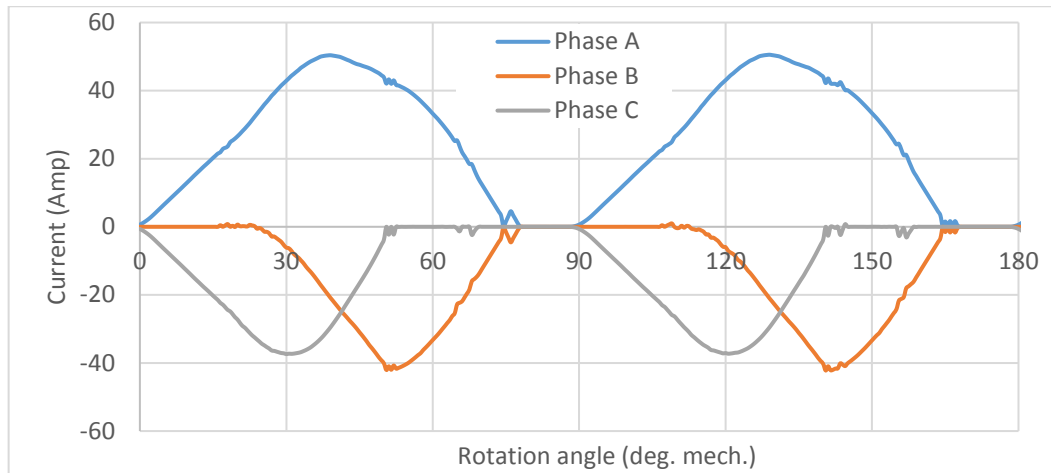


Figure 224: 2D FE simulated single MosFET failure time series current waveform at 800 rpm.

- **Edge coil connected to the shorted MosFET**

During this fault mode, both the motor resistance and inductance limit the short-circuit current and drag torque. The baseline motor is the best compromise under this fault condition. It provides the highest torque capability during high speed operation and medium torque capability below the knee point speed (Figure 225). The SPM design has the lowest torque capability up to the knee and medium capability. This is expected as the resistance is approximately 30% lower, whilst the inductance is similar to that of the baseline motor.

The intermediate design can validate the discussion above as it has similar resistance to the baseline motor. It provides the highest torque capability in the constant torque region due to the motor's inductance. However, the inductance compromises the motor's capability in the constant power region.

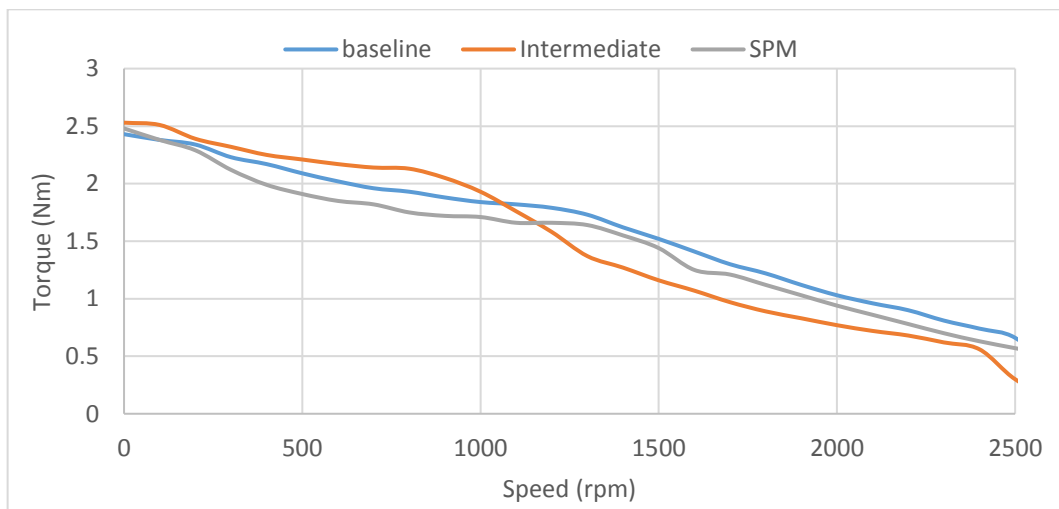


Figure 225: torque comparison under single MosFET short-circuit fault (edge coil) for all the motor designs (measured).

- **Middle coil connected to the shorted MosFET**

In this section the motor terminals (phase A and phase B) connected to the power module were altered. Based on the simulation results in chapter 2, the baseline motor performance was expected to change due to transformer coupling between the lanes when a shorted MosFET is connected to the middle coil. The phase connected to the shorted MosFET is no longer next to the healthy lane (Figure 226), which means that they are not sharing the same slot. This reduces the short-circuit current, which is mainly due to high transformer coupling between the coils.

Figure 227 shows that both intermediate and SPM designs have similar performance as in Figure 225 for the case where the edge coil is connected to a short-circuit MosFET. This is because the motor lanes are well segregated and transformer coupling between coils is at its lowest. However, the baseline motor’s torque performance is higher, and it is very close to the intermediate design’s performance up to the knee point. It also outperforms both the intermediate and SPM designs in the flux-weakening region.

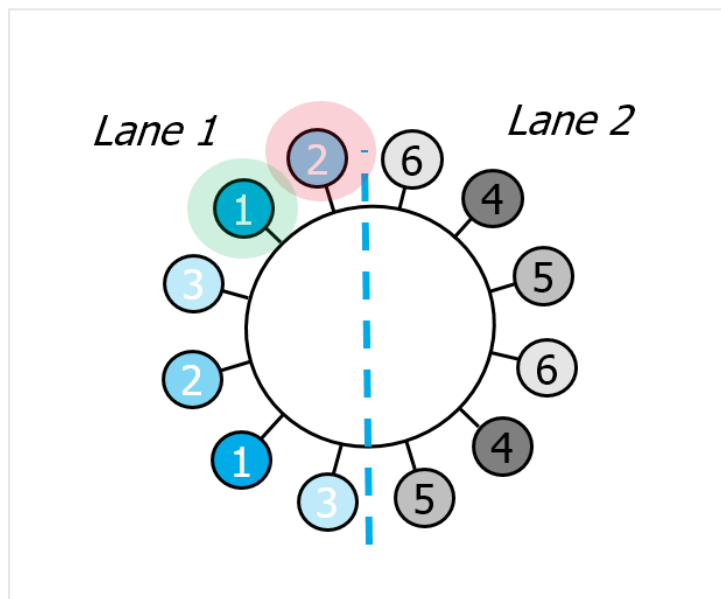


Figure 226: Winding connection layouts and coil highlight for MosFET failure.

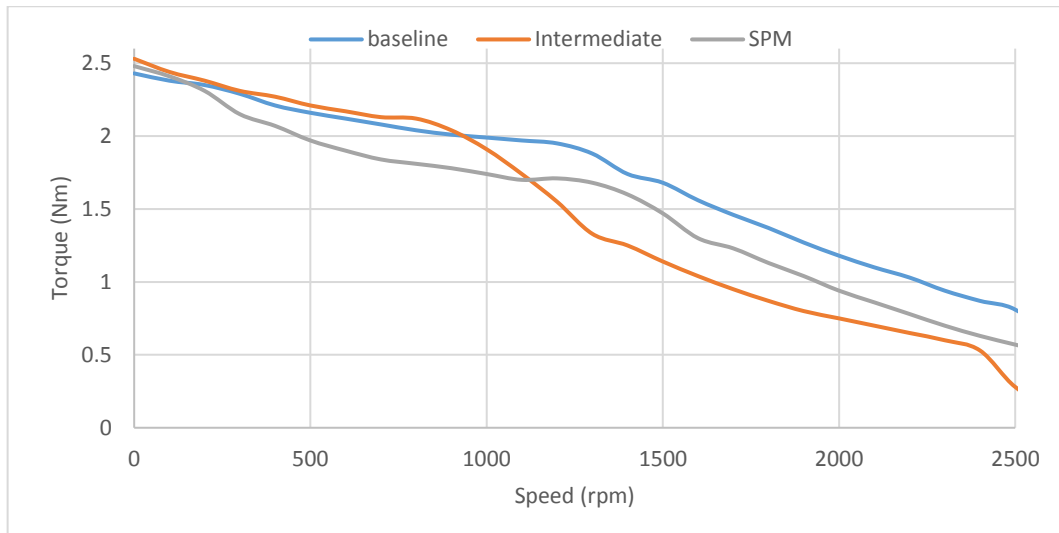
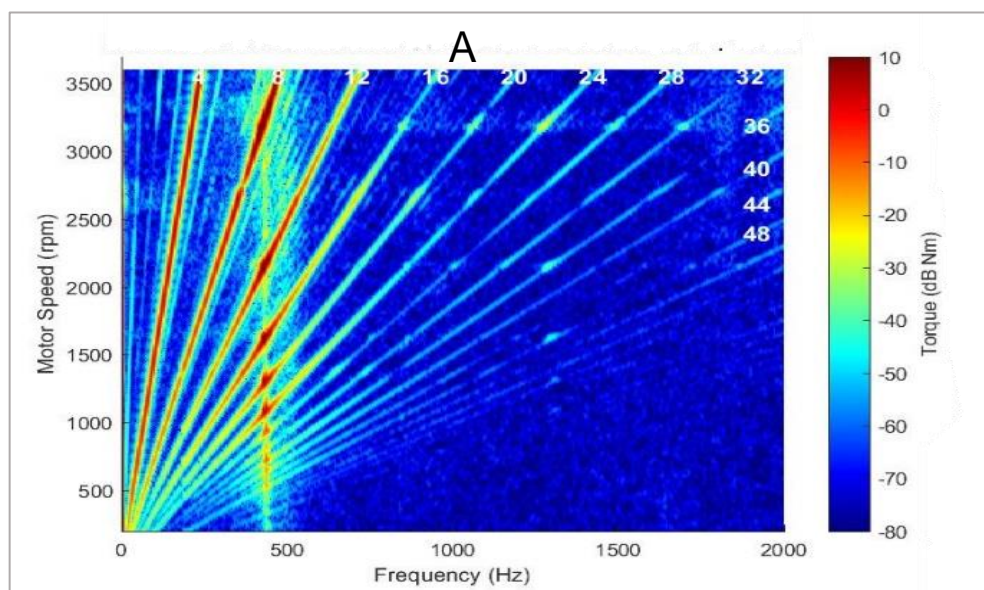


Figure 227: torque comparison under single MosFET short-circuit fault (middle coil) for all the motor designs (measured).

With this failure mode the harmonic content is similar for all the designs, with the amplitude solely dependent on the drag torque. Figure 228 shows that the torque ripple is a multiple of 4<sup>th</sup> order (4<sup>th</sup>, 8<sup>th</sup>, 12<sup>th</sup>, 16<sup>th</sup> and etc.). Due to the very high ripple content for this failure mode, it is very unlikely that the motor will be operated in this mode at very high speeds as both torque ripple and drag torque are high.

A better operating scheme is to turn on other MosFETs to create a three-phase balanced short. The switchover mode could be carried out once the drag torque under three-phase symmetrical short becomes lower than that resulting from a single MosFET failure. This will be covered later.



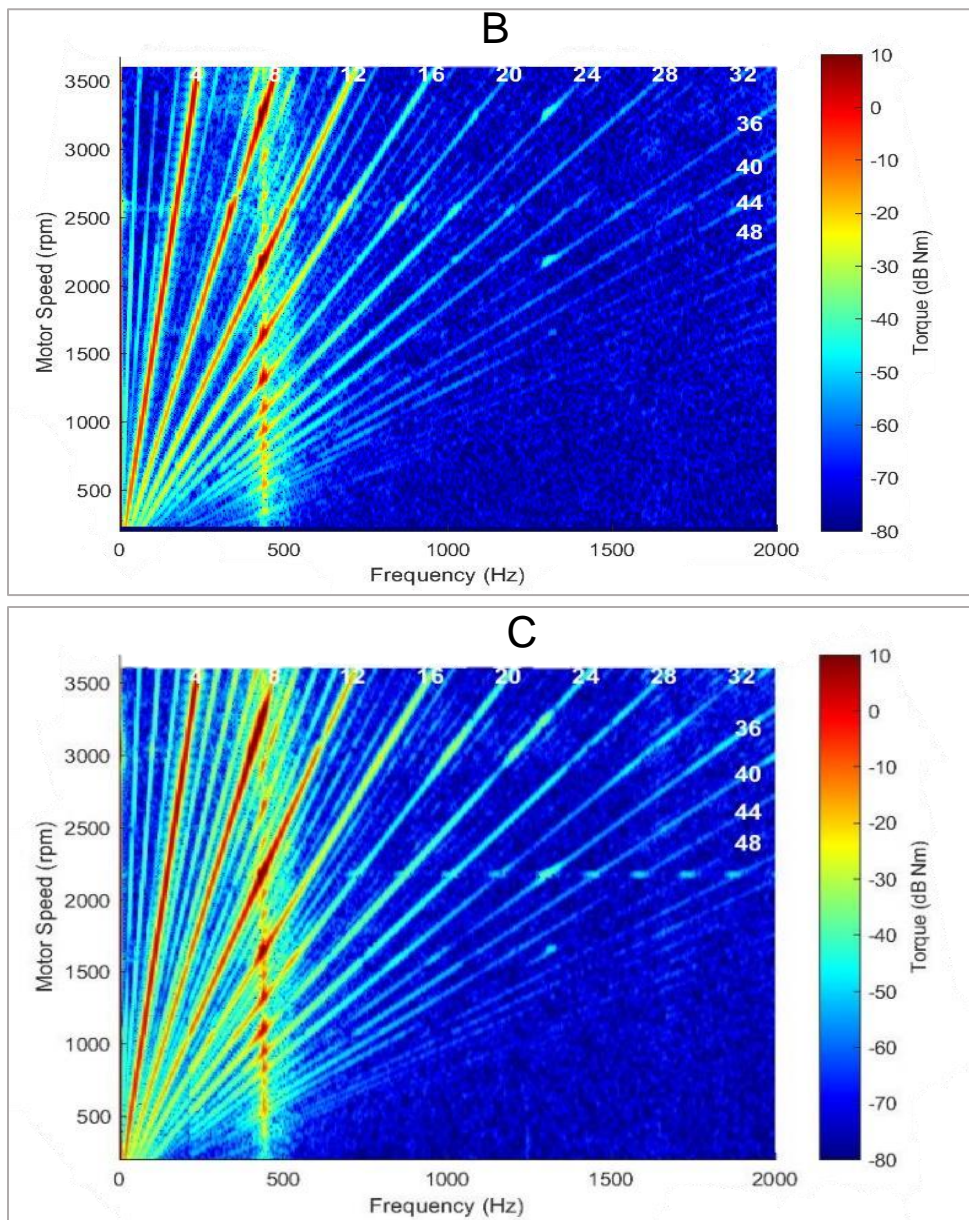


Figure 228: colour map of torque ripple harmonic content for different motors with a single MosFET shorted: A) baseline, B) intermediate, and C) SPM.

**D) One lane operational and one lane short-circuited at its terminals to give a balanced three-phase short-circuit:**

This fault is created by connecting the motors’ coil terminals physically together (for example in a terminal block) for one lane of the motor while operating the other lane normally. A symmetrical three-phase fault is created to reduce drag torque and torque ripple during single MosFET failure by changing it to a symmetrical three-phase fault at higher speeds.

With a three-phase symmetrical short circuit fault, the SPM design offers a compromise between a higher torque capability compared to the intermediate design at high speeds

and a higher torque capability compared to the baseline design at low speeds (Figure 229).

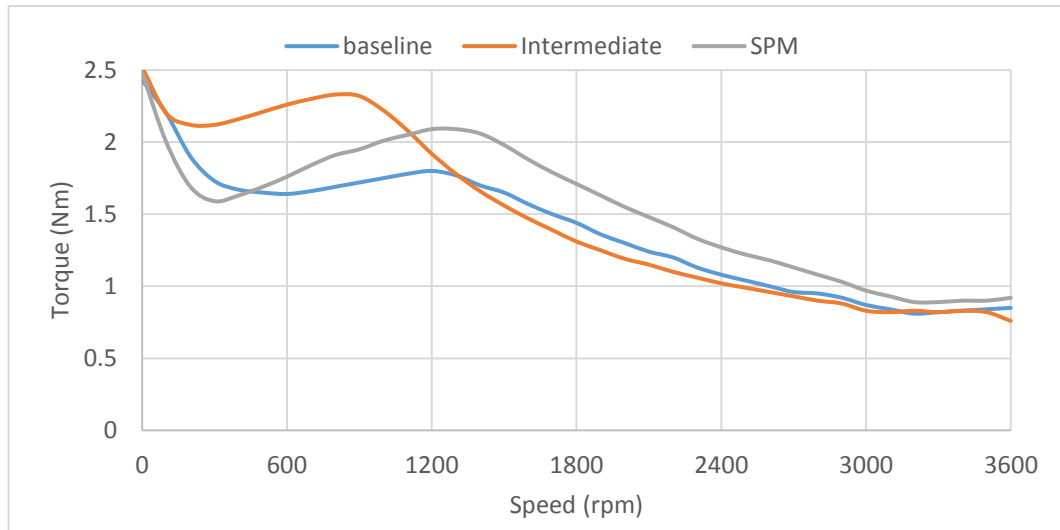


Figure 229: torque capability under three-phase short-circuit in one lane and the other is operated normally (measured).

As described earlier, the baseline motor suffers from high transformer coupling between the phase coils of the different lanes. Figure 229.A shows that transformer coupling results in a very high 8<sup>th</sup> order harmonic along with a 16<sup>th</sup> order. The faulty lane phase coil that shares the same slot with the healthy lane carries the highest short-circuit current and its parallel coil from the parallel path carries the least. This results in high 8<sup>th</sup> and 16<sup>th</sup> orders torque ripple in the drag torque. Both the SPM and intermediate design motors have very low or negligible 16<sup>th</sup> order harmonic as there is only one coil per phase and no parallel path (Figure 230).

The SPM with push-in teeth is chosen for this comparison to compare its high-power capability with the other two motors. The 8<sup>th</sup> harmonic order harmonic remains dominant. It has been stated earlier how this is believed to be due to movement of the inserted teeth. The magnitude does not change much between unfaulted and faulted conditions.

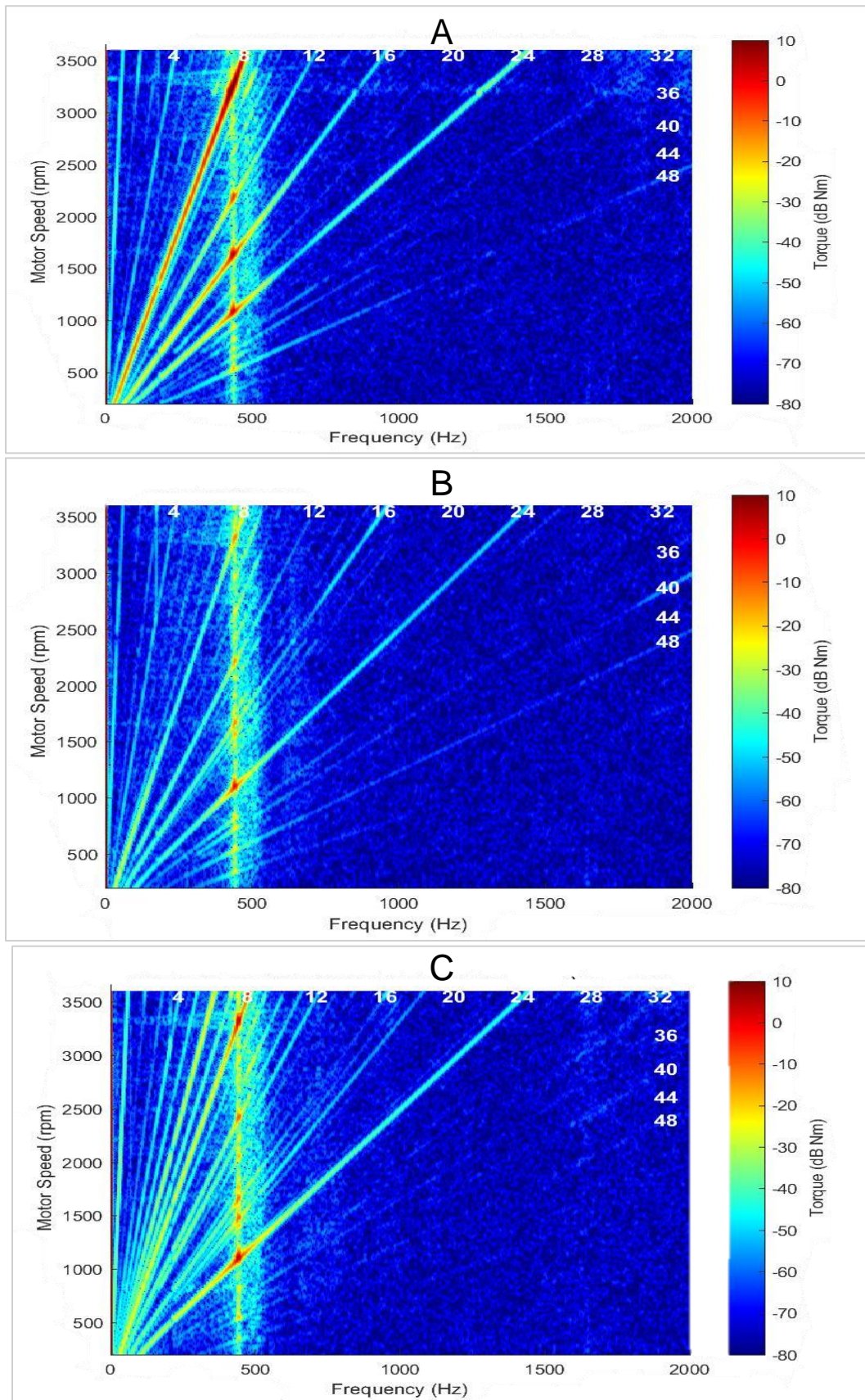


Figure 230: colour map of torque ripple harmonic content for different motors with a symmetrical short circuit of one lane: A) baseline, B) intermediate, and C) SPM.

**E) All fault comparison for the same motor:**

By examining the performance of any one design over a series of faults it is possible to draw some conclusions. For example, as mentioned earlier, it is better to change a single MosFET short-circuit to a symmetrical three-phase fault by switching on the MosFETs in the same (upper/lower) half of the bridge. This helps in reducing the significant torque ripple and drag torque beyond a specific speed.

Figure 231 shows a circuit diagram in JMAG FE software in which a diode bridge is connected the motor coils to replicate the drive being inactive (mode 1), with a single MosFET short-circuit (Mode 2), and three-phase short circuit (mode 3). The simulation includes a lane operating normally and a faulted lane.

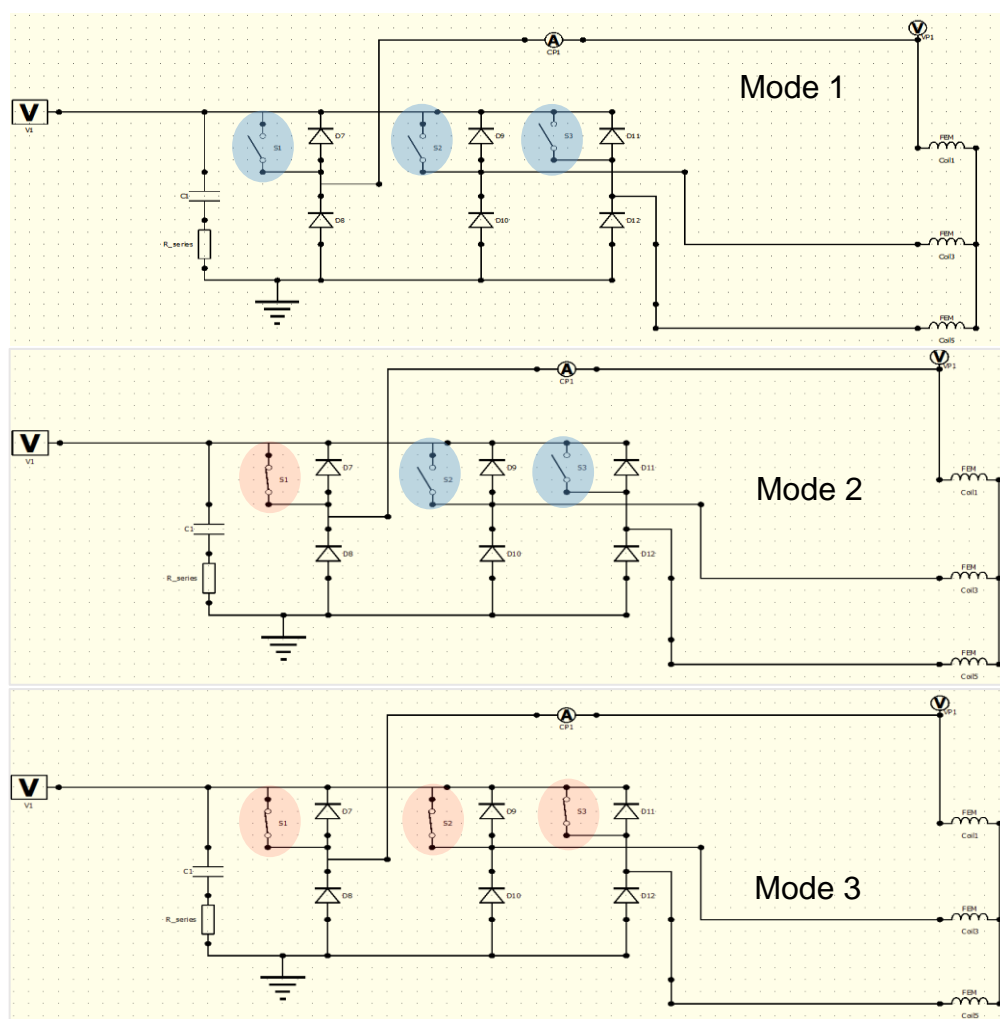


Figure 231: change over modes between single MosFET failure and symmetrical three-phase fault.

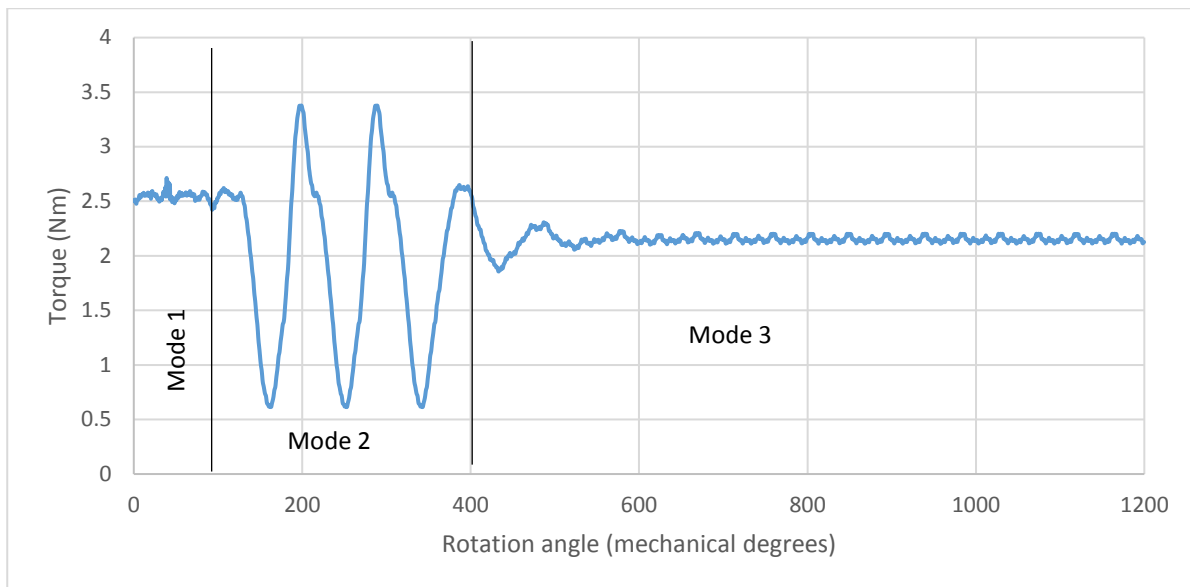


Figure 232: torque capability of the intermediate design a constant speed experiencing different faults (simulation).

Figure 232 shows that at high speeds the motor capability with a single MosFET failure is lower than that with symmetrical three-phase short-circuit. This means that switchover, if control of non-faulted MosFETs is possible, is useful in maximising the average torque-speed capability. It also minimises the peak to peak torque ripple at higher speeds.

The following section will compare a specific motor torque capability under different conditions:

- **Baseline motor:**

Figure 233 shows the baseline motor capability under normal conditions and different fault conditions. The worst torque capability in the constant torque region is 35.5% of the normal torque with a three-phase symmetrical short-circuit. The switchover point between single MosFET and three-phase short circuit faults is highlighted and occurs at 1200 rpm. This enables the motor to operate with higher torque capability in the constant power region.

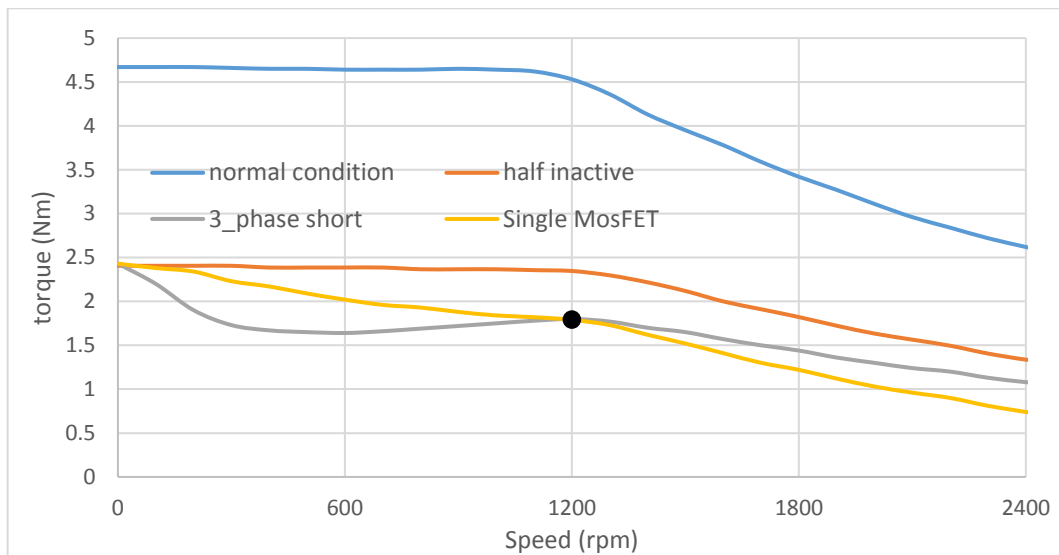


Figure 233: baseline motor's capability under different conditions (measured)

- **Intermediate design:**

Figure 234 shows the intermediate design's torque capability under various operating conditions. The lowest torque capability with a three-phase short-circuit fault is approximately 46% of the baseline motor's stall torque. This also affected the switchover mode speed, which drops to 500 rpm. This is beneficial as the motor will not experience high peak to peak torque ripple over a large speed range. However, the high inductance compromises the power capability at high speed.

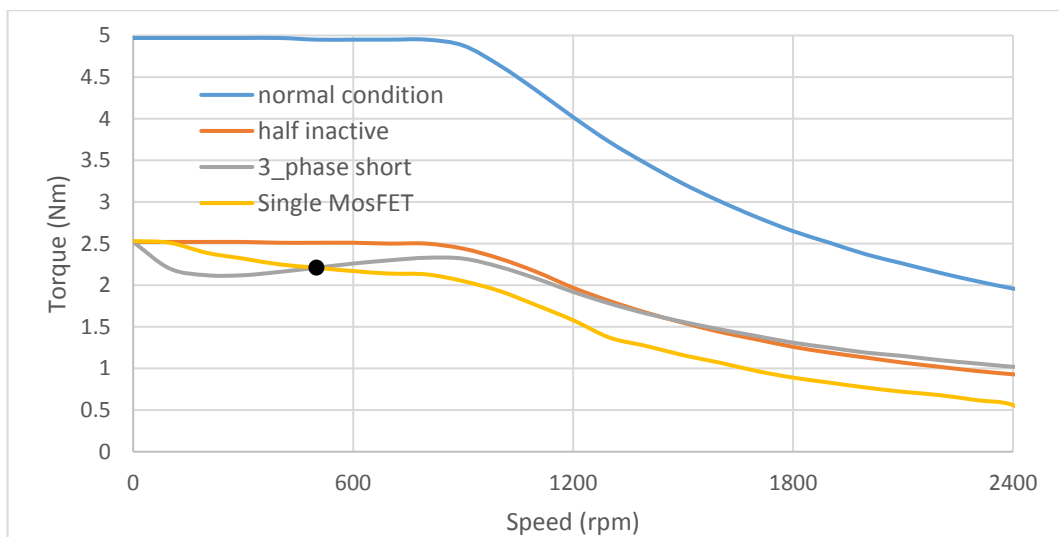


Figure 234: intermediate design's capability under different conditions (measured).

- **SPM motor:**

The SPM motor produces more torque than the baseline motor under normal operating conditions, despite the shorter stack. The worst torque capability of the SPM motor is

34.5% compared to the baseline motor's stall torque (Figure 235). This is approximately 1% lower than the baseline motor's worst capability. However, due to higher d-axis inductance and lower winding resistance, the SPM motor performs better at high speeds. The SPM motor inductance is similar to the baseline motor, with significantly lower winding resistance. This changes the switchover mode speed from 1200 rpm to approximately 700 rpm compared to the baseline design.

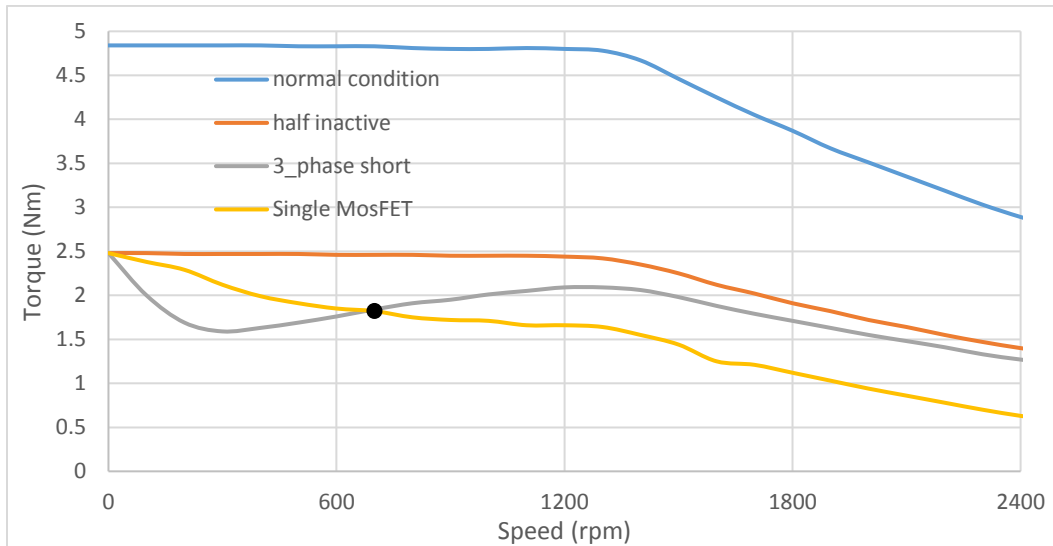


Figure 235: SPM motor's capability under different conditions (measured)

### 5.7. Summary:

The prototyped SPM design has a rotor 31 mm long, combined with a stator stack of 32 mm. these are approximately 14% and 11% shorter than the baseline motor. The rotor is shorter to reduce end-effects. It is a 12 slot 8 pole machine in which the stator teeth are dissimilar (6 thin teeth combined with 6 thick teeth). The thick teeth are wound and intended to be fed from two separate inverters.

The SPM was developed to overcome the issue with the intermediate design of chapter 4, which runs out of voltage due to a high q-axis inductance. Various approaches were taken to minimise the q-axis flux, whilst maintaining torque capability, which reduces the inductance and the magnet demagnetisation.

After finalising both the rotor and stator electromagnetic designs, manufacturing difficulties were one of the main challenges. The segmented rotor has the advantage of having low scrap during manufacturing, but it needs precision assembly.

Two stators were made, one with push in teeth that compromised the torque ripple and the other, a unitary stator that compromised power. The stator with the push-in teeth

was wound with 1.9mm wire gauge. The low resistance provided high-power capability, but higher torque ripple and cogging torque from manufacturing imperfections.

The power and torque density of the SPM motor are significantly higher under normal conditions. Despite the motor's shorter stack (32 vs 36 mm), the SPM is capable of producing 6% and 12% higher torque at full-load and half-load, respectively. This means that the motor can be shortened further, which is very important for packaging in the automotive industry. However, accommodating high end-winding length is a challenge for motors with modular windings.

Under faulted conditions, the SPM is a compromise between the baseline and intermediate design. The inductance is lower than the intermediate design so has a higher drag torque. However, the torque ripple is lower due to segregation between the phase coils. The worst drag torque in constant torque region is 34.5% of the baseline motor's normal capability. However, the SPM motor outperforms both baseline and intermediate designs in the constant power region under normal, half-inactive and symmetrical three-phase fault conditions.

## Chapter 6

---

### Conclusions and further work

A concentrated wound, 12-slot 8-pole interior permanent magnet synchronous motor used in an automotive electric power steering application was used as a focus for this work. This is a safety critical component, where high levels of availability and increasing levels of fault tolerance are desired. The first aim of this work was to analyse and compare the benefits of different potential winding arrangements that could be used when converting the baseline motor from single to dual lane operation. It was observed that the baseline motor suffers from high drag torque and torque ripple under faulted conditions due to high transformer coupling between coils wound around adjacent stator teeth. A new stator with a modular winding was designed and tested with the rotor from the baseline motor. This intermediate arrangement showed improved performance under faulted conditions. However, the high inductance of this arrangement led to a significant reduction in the power the motor could deliver. A surface mounted permanent magnet (SPM) motor with segmented rotor was developed that has a lower q-axis inductance. The SPM design provides higher torque and power density under normal conditions. It is also a compromise between the baseline design and intermediate design under faulted conditions.

#### **6.1. Background:**

Driverless cars are expected to become a reality over the next 20 years. The sub-systems within these vehicles will require increased fault tolerance and capability. This is in addition to the already high reliability, efficiency and performance of today's systems such as Electric Power Steering (EPS). Despite their low inertia, high efficiency, rugged rotor construction and natural fault tolerance capability, switched reluctance machines (SRM) are less likely to be used for EPS systems due to their high acoustic noise and torque ripple. Induction machines have the reputation of having a very rugged rotor, low maintainability and high durability. However, they are not preferred for EPS applications because of their high rotor inertia, poor capability under open circuit conditions and high mutual inductance between phases to limit the short circuit current under faulted conditions. PM motors are the most favoured candidates for this application because of their high torque density, low torque ripple, and balanced radial forces for appropriate slot/pole combinations thereby reducing

acoustic noise and increasing the bearing life. One of the major challenges with PM machines is the drag torque following a short-circuit fault.

Concentrated winding PM machines can be constructed by winding coils around individual stator teeth. This allows for a higher slot fill and greater power density. Through careful mechanical design the coils can often be kept segregated from each other. Modular concentrated winding machines where conductors from one coil are only present in a stator slot are largely preferred for fault tolerant applications as they offer higher inductance and better magnetic and physical separation between the coils compared to double layer windings. However, they introduce higher space harmonics that leads to higher torque ripple.

### **6.2. Baseline design investigation:**

A 12 slot 8 pole interior permanent magnet motor provided by ZF was analysed. There are four coils in parallel per phase that can be connected to the inverter in different ways in a dual-lane system.

In fault tolerant dual lane systems, winding arrangements and connection types affect the motor capability under faulty conditions. This is because of mutual coupling between neighbouring coils. This can be reduced by separating either the phase coils or the motor lanes through different winding layout and connections.

Each lane has two coils in parallel per phase, and the stator coils can be connected in three different ways which are interleaved, half-half, and quarter arrangements (fully covered in chapter 2). It was observed the connecting arrangement significantly affected the drag torque and torque ripple under faulted conditions. Table 4 showed that the half-half arrangement offers the best compromise for the baseline motor providing the highest average torque and medium torque ripple under a symmetrical three-phase short-circuit fault.

### **6.3. Dissimilar teeth stator with modular windings:**

The baseline motor with double-layer winding suffered from high drag torque and torque ripple due to transformer coupling between the coils. The baseline motor was simulated with the double layer windings swapped for modular windings. As the stator of the baseline motor was not designed for a modular winding, significant saturation occurred in the stator teeth and core back. Hence, the stator core became magnetically saturated that led to a considerable torque drop and higher torque ripple.

A new modular stator (chapter 4) was developed to overcome the saturation and minimise torque ripple. The new stator was designed with six thick teeth that would have the coils wound around them and six thin teeth to separate the wound coils. The thick teeth have a wider tooth arc that increases the winding factor. This increased the torque density of the motor compared to the baseline motor. It was observed that the fault tolerance capability was significantly increased as the inductance of the motor was approximately doubled.

However, the motor power was significantly compromised in the constant power region as the motor runs out of voltage at a lower speed. The knee point of the torque-speed curve was significantly affected due to high q-axis inductance.

### **6.4. Segmented rotor SPM motor:**

To restore the power drop in the constant power region, various approaches were considered to reduce either the inductance or only the q-axis inductance (chapter 5). Firstly, it was proposed that by reducing the number of turns and keeping the MMF input unchanged, the power drop can be restored. Two challenges result with this approach. Thicker, less manageable wires are needed for the winding. Secondly, a higher phase current is required that leads to increased ECU losses.

The second approach was to shape the baseline motor's rotor blocking the q-axis flux path. This reduced the power drop, but the torque ripple of the motor was compromised.

A novel segmented SPM rotor was designed to further reduce the q-axis inductance by putting flux barriers in the rotor. It also helps in blocking the stator flux from demagnetising the magnet edges. The overall motor stack length was reduced compared to the baseline by approximately 13%, the current by 5% and the number of turns by 3 turns. The SPM motor provides 6% and 12.5% more torque at full load and half load, respectively. The cogging torque and torque ripple is higher than the baseline design, however, by optimising the design, it is expected that acceptable values could be achieved. Interestingly, it also has a very low rotor inertia, almost half of the baseline motor's inertia. This makes the dynamic response of the motor very high. Finally, the motor output power in the constant power region is higher by approximately 11% and 7% at 2000 rpm and 3000 rpm respectively.

### **6.5. Testing and comparison the designs:**

Initially, the baseline motor was tested and compared to 3D FE analysis to validate the normal operating conditions of the motor. The average torque, cogging torque and torque ripple were used as targets to at least meet, or ideally improve upon with the revised designs.

For the same electric loading and an identical rotor, the measured torque from the new-stator design was significantly higher than the baseline design. This was due to a significantly higher winding factor. However, the test results showed that the motor had a poorer performance in the constant power region. This was due to the higher inductance.

Finally, the SPM was tested and shown to be outperforming both baseline and intermediate designs. The segmented SPM has higher power and torque density than the baseline motor. It also has modular windings that have greater physical, thermal and magnetic segregation than the baseline motor's double layer concentrated winding. The low speed capability of the motor is not significantly improved from that of the baseline motor. However, in applications where high-speed operation is required in a faulted condition, the SPM is able to provide greater average torque with a lower torque ripple.

### **6.6. Segmented surface magnet motor**

Whilst this work set out to look for a motor having higher fault tolerance, the segmented SPM motor that has been designed offers a number of benefits that allow it to be considered for a range of applications. These can be summarised as follows:

- 1- The torque density and power of the SPM is significantly higher compared to the baseline motor. After reducing the motor stack by approximately 13%, it is capable of delivering 6% more average torque.
- 2- The SPM design has a very low rotor inertia, almost half of the baseline design's rotor. This is relevant in high dynamic servo systems. In automotive applications, such as electric power steering, where the driver is making many small movements and frequent changes of direction a high dynamic response is preferred.
- 3- It has high d-axis inductance and lower q-axis inductance with almost 20% lower phase resistance. Therefore, the fault tolerance capability is better than the baseline motor at high speeds, under three-phase short-circuit fault in one lane.

- 4- Unlike the baseline motor, the rotor of the SPM motor is not skewed, which is a benefit.

As the SPM has modular windings, the end windings are longer than that of the baseline motor. If scaling the design, for shorter stack lengths this will increase the proportion of the end winding resistance to the resistance of the active part of the motor as compared to a double layer winding. The increased end winding length can also be harder to accommodate and integrate into the space available. One way to mitigate this is to integrate the end-windings in to space around the bearings supporting the rotor shaft.

### **6.7. Further work:**

The SPM design was developed in steps to restore the power drop of the intermediate design. There are areas that the SPM can be further improved.

#### **6.7.1. Optimising the wound tooth and insert as a push in tooth:**

There is 8% torque drop per amp between half load and full load, which is mainly due to the saturation in the wound teeth and tooth tips. This can be solved in different ways such as:

- Optimising the wound teeth to reduce saturation to recover the torque drop.
- Changing the material of the wound teeth to a material with a higher saturation flux density such as cobalt iron.
- Using the wound teeth as push in teeth, as they can be wound externally and then pushed in. This might help in increasing the winding slot fill, reducing the winding resistance, and hence the power drop.
- changing the tooth tip material to cobalt iron and pushing it onto the body of the larger stator teeth. This might increase assembly difficulties, but it would allow the stator coils to be form wound, and the amount of cobalt iron would be relatively low.

#### **6.7.2. Compressed coils:**

The modular winding has a longer end-winding length compared to the double-layer winding. This leads to increase overall motors length which might affect the motor size and packaging.

Compressed coils can be used to shape the coils and reduce the winding resistance. However, care is needed with these to ensure that the coils are not mechanically damaged during the compression process thereby comprising the integrity of the coils.

**6.7.3. Sleeve material and sleeve thickness:**

Mechanical clearance is required between the rotor and stator to allow for tolerances and free rotation of the rotor. A sleeve is also required in the SPM to provide secondary retention of the magnets. If a thinner sleeve such as shrink wrap could be used, the magnetic air gap could be reduced without affecting the mechanical air gap. This would allow a small improvement in the torque density. An intense electro-mechanical study is required for this to assess both magnetic and structural feasibility.

**6.7.4. Vibration and structural analysis:**

The SPM design has been investigated only from the electromagnetic design point of view. The baseline motor is a 12 slot 8 pole combination that is expected to have 4<sup>th</sup> order vibration mode [49]. Similar to 12 slot 10 pole motor combination, the modular stator of the SPM design is expected to have 2<sup>nd</sup> order vibration mode as diametrically opposite coils are energised at the same time. Structural analysis is important to show the robustness of this design against vibration and noise, or to identify where changes are needed to stiffen the assembly to achieve acceptable performance.

## References

- [1] A. Marouf, C. Sentouh, M. Djemai, and P. Pudlo, "Control of an electric power assisted steering system using reference model," in *Decision and Control and European Control Conference (CDC-ECC), 2011 50th IEEE Conference on*, 2011, pp. 6684-6690.
- [2] N. Bianchi, M. D. Pre, and S. Bolognani, "Design of a fault-tolerant IPM motor for electric power steering," *Vehicular Technology, IEEE Transactions on*, vol. 55, pp. 1102-1111, 2006.
- [3] A. W. Burton, "Innovation drivers for electric power-assisted steering," *Control Systems, IEEE*, vol. 23, pp. 30-39, 2003.
- [4] H. Akhondi, J. Milimonfared, and K. Malekian, "Performance evaluation of electric power steering with IPM motor and drive system," in *Power Electronics and Motion Control Conference, 2008. EPE-PEMC 2008. 13th*, 2008, pp. 2071-2075.
- [5] C. Oprea, C. Martis, and B. Karoly, "Six-phase brushless DC motor for fault tolerant electric power steering systems," in *Electrical Machines and Power Electronics, 2007. ACEMP'07. International Aegean Conference on*, 2007, pp. 457-462.
- [6] H. Yaohua, Y. Can, and L. Fangfang, "Study of linear electric powered steering system," in *Electric Information and Control Engineering (ICEICE), 2011 International Conference on*, 2011, pp. 2705-2710.
- [7] G. Cosulich, M. Fracchia, A. Mariscotti, and S. Savio, "Comparative dependability analysis of electric ship propulsion systems. In proc. of EPE'95," in *6th European Conference on Power Electronics and Applications*, 1995, pp. 328-33.
- [8] J. A. Haylock, "Fault tolerant drives for safety critical applications," Thesis (Ph. D.)--University of Newcastle upon Tyne, 1998., Newcastle upon Tyne, 1998.
- [9] R. Caplen, *A practical approach to reliability*. London: London, Business Books, 1972.
- [10] G. W. A. Dummer, *An elementary guide to reliability*, 5th ed. ed. Oxford, England ; Boston: Oxford, England: Oxford, England ; Boston : Butterworth-Heinemann, 1997.
- [11] R. Pietrantuono and S. Russo, "Introduction to Safety Critical Systems," in *Innovative Technologies for Dependable OTS-Based Critical Systems*, ed: Springer, 2013, pp. 17-27.
- [12] R. V. White, "Fault tolerance in distributed power systems," in *Power Electronics Congress, 1995. Technical Proceedings. CIEP 95., IV IEEE International*, 1995, pp. 121-128.
- [13] G. J. Atkinson, "High power fault tolerant motors for aerospace applications," Thesis (Eng. D.)--University of Newcastle upon Tyne, 2007., Newcastle upon Tyne, 2007.
- [14] P. H. Mellor, T. J. Allen, R. Ong, and Z. Rahma, "Faulted behaviour of permanent magnet electric vehicle traction drives," in *Electric Machines and Drives Conference, 2003. IEMDC'03. IEEE International*, 2003, pp. 554-558.
- [15] C. J. Ifedi, B. C. Mecrow, S. T. M. Brockway, G. S. Boast, G. J. Atkinson, and D. Kostic-Perovic, "Fault tolerant in-wheel motor topologies for high performance electric vehicles," in *Electric Machines & Drives Conference (IEMDC), 2011 IEEE International*, 2011, pp. 1310-1315.
- [16] J. W. Bennett, B. C. Mecrow, D. J. Atkinson, C. Maxwell, and M. Benarous, "Fault-tolerant electric drive for an aircraft nose wheel steering actuator," *IET Electrical Systems in Transportation*, vol. 1, pp. 117-125, 2011.
- [17] P. Andrada, B. Blanque, E. Martinez, J. Perat, J. Sanchez, and M. Torrent, "Switched reluctance motor for electric power-assisted steering," in *Power Electronics and Applications, 2009. EPE'09. 13th European Conference on*, 2009, pp. 1-9.
- [18] B. C. Mecrow, A. G. Jack, J. A. Haylock, and J. Coles, "Fault-tolerant permanent magnet machine drives," *IEE Proceedings-Electric Power Applications*, vol. 143, pp. 437-442, 1996.
- [19] A. J. Mitcham, G. Antonopoulos, and J. J. A. Cullen, "Favourable slot and pole number combinations for fault-tolerant PM machines," *IEE Proceedings-Electric Power Applications*, vol. 151, pp. 520-525, 2004.
- [20] A. G. Jack and B. C. Mecrow, "Safety critical drives for aerospace applications," in *Proceedings of ICEM Conference, Paris, France*, 1994.
- [21] J. Larminie and J. Lowry, *Electric vehicle technology explained*: John Wiley & Sons, 2012.

## References

---

- [22] D. A. Torrey and J. M. Kokernak, "Power Steering: Brushless DC or Switched-Reluctance?," *Power Electronics Technology*, vol. 28, pp. 24-33, 2002.
- [23] T. Tanaka, "Motors for electric power steering," *Motor Technologies for Industry and Daily Life Edition*, 2003.
- [24] J. R. Hendershot and T. J. E. Miller, *Design of brushless permanent-magnet machines*: Motor Design Books, 2010.
- [25] D.-Y. Pang, B.-C. Jang, and S.-C. Lee, "Steering wheel torque control of electric power steering by PD-control," *제어로봇시스템학회 국제학술대회 논문집*, pp. 1366-1370, 2005.
- [26] B. Mecrow, E. El-Kharashi, J. Finch, and A. Jack, "Segmental rotor switched reluctance motors with single-tooth windings," *IEE Proceedings-Electric Power Applications*, vol. 150, pp. 591-599, 2003.
- [27] S. Ullah, "A magnet assisted segmental rotor switched reluctance machine suitable for fault tolerant aerospace applications," Thesis (Ph. D.)--Newcastle University, 2016., Newcastle upon Tyne, England, 2016.
- [28] D. Lee and H.-C. Jung, "Cost Pattern Value Method for Local Search Algorithms Applied to Optimal FEA-Based Design of Induction Motors," *IEEE Transactions on Magnetics*, 2018.
- [29] G. Lee, S. Min, and J.-P. Hong, "Optimal shape design of rotor slot in squirrel-cage induction motor considering torque characteristics," *IEEE Transactions on Magnetics*, vol. 49, pp. 2197-2200, 2013.
- [30] D. Zhang, C. S. Park, and C. S. Koh, "A new optimal design method of rotor slot of three-phase squirrel cage induction motor for NEMA class D speed-torque characteristic using multi-objective optimization algorithm," *IEEE transactions on magnetics*, vol. 48, pp. 879-882, 2012.
- [31] G. Aroquiadassou, H. Henao, V. Lanfranchi, F. Betin, B. Nahidmobarakeh, G.-A. Capolino, *et al.*, "Design comparison of two rotating electrical machines for 42 V electric power steering," in *Electric Machines and Drives, 2005 IEEE International Conference on*, 2005, pp. 431-436.
- [32] B. A. Welchko and T. A. Lipo, "A novel variable-frequency three-phase induction motor drive system using only three controlled switches," *IEEE Transactions on Industry Applications*, vol. 37, pp. 1739-1745, 2001.
- [33] R. F. Schiferl and T. A. Lipo, "Power capability of salient pole permanent magnet synchronous motors in variable speed drive applications," *Industry Applications, IEEE Transactions on*, vol. 26, pp. 115-123, 1990.
- [34] B. C. McCrow, A. G. Jack, D. J. Atkinson, and J. A. Haylock, "Fault tolerant drives for safety critical applications," 1997.
- [35] Z. Q. Zhu and C. C. Chan, "Electrical machine topologies and technologies for electric, hybrid, and fuel cell vehicles," in *Vehicle Power and Propulsion Conference, 2008. VPPC'08. IEEE*, 2008, pp. 1-6.
- [36] T. M. Jahns, G. B. Kliman, and T. W. Neumann, "Interior Permanent-Magnet Synchronous Motors for Adjustable-Speed Drives," *Industry Applications, IEEE Transactions on*, vol. IA-22, pp. 738-747, 1986.
- [37] T. M. Jahns, "Flux-Weakening Regime Operation of an Interior Permanent-Magnet Synchronous Motor Drive," *Industry Applications, IEEE Transactions on*, vol. IA-23, pp. 681-689, 1987.
- [38] A. M. El-Refaie, "Fractional-Slot Concentrated-Windings Synchronous Permanent Magnet Machines: Opportunities and Challenges," *Industrial Electronics, IEEE Transactions on*, vol. 57, pp. 107-121, 2010.
- [39] W. Jiabin, K. Atallah, Z. Q. Zhu, and D. Howe, "Modular Three-Phase Permanent-Magnet Brushless Machines for In-Wheel Applications," *Vehicular Technology, IEEE Transactions on*, vol. 57, pp. 2714-2720, 2008.
- [40] C. M. Spargo, B. C. Mecrow, J. D. Widmer, and C. Morton, "Application of Fractional-Slot Concentrated Windings to Synchronous Reluctance Motors," *Industry Applications, IEEE Transactions on*, vol. 51, pp. 1446-1455, 2015.

## References

---

- [41] N. Bianchi, S. Bolognani, Pre, x, M. D., and G. Grezzani, "Design considerations for fractional-slot winding configurations of synchronous machines," *Industry Applications, IEEE Transactions on*, vol. 42, pp. 997-1006, 2006.
- [42] C.-Z. Liaw, W. L. Soong, B. A. Welchko, and N. Ertugrul, "Uncontrolled generation in interior permanent-magnet machines," *Industry Applications, IEEE Transactions on*, vol. 41, pp. 945-954, 2005.
- [43] T. M. Jahns and V. Caliskan, "Uncontrolled generator operation of interior PM synchronous machines following high-speed inverter shutdown," *Industry Applications, IEEE Transactions on*, vol. 35, pp. 1347-1357, 1999.
- [44] G. J. Atkinson, J. W. Bennett, B. C. Mecrow, D. J. Atkinson, A. G. Jack, and V. Pickert, "Fault tolerant drives for aerospace applications," in *Integrated Power Electronics Systems (CIPS), 2010 6th International Conference on*, 2010, pp. 1-7.
- [45] N. Bianchi and S. Bolognani, "Performance analysis of an IPM motor with segmented rotor for flux-weakening applications," 1999.
- [46] D. Gerling, "Comparison of different fe calculation methods for the electromagnetic torque of pm machines," in *NAFEMS Seminar. "Numerical Simulations of Electromechanical Systems*, 2005.
- [47] T. M. Jahns, "Improved reliability in solid-state AC drives by means of multiple independent phase drive units," *IEEE Transactions on Industry Applications*, pp. 321-331, 1980.
- [48] W. Chu and Z. Zhu, "Average torque separation in permanent magnet synchronous machines using frozen permeability," *IEEE Trans. Magn.*, vol. 49, pp. 1202-1210, 2013.
- [49] B. Aslan, E. Semail, J. Korecki, and J. Legranger, "Slot/pole combinations choice for concentrated multiphase machines dedicated to mild-hybrid applications," in *IECON 2011-37th Annual Conference of the IEEE Industrial Electronics Society*, 2011, pp. 3698-3703.
- [50] W. Wang, J. Zhang, M. Cheng, and S. Li, "Fault-tolerant control of dual three-phase permanent-magnet synchronous machine drives under open-phase faults," *IEEE Transactions on Power Electronics*, vol. 32, pp. 2052-2063, 2017.
- [51] M. Barcaro, "Design and analysis of interior permanent magnet synchronous machines for electric vehicles," 2011.
- [52] R. Dutta, L. Chong, and M. F. Rahman, "Design and Experimental Verification of an 18-Slot/14-pole Fractional-Slot Concentrated Winding Interior Permanent Magnet Machine," *Energy Conversion, IEEE Transactions on*, vol. 28, pp. 181-190, 2013.
- [53] N. Bianchi and S. Bolognani, "Design techniques for reducing the cogging torque in surface-mounted PM motors," *Industry Applications, IEEE Transactions on*, vol. 38, pp. 1259-1265, 2002.
- [54] Z. Q. Zhu, S. Ruangsinchaiwanich, N. Schofield, and D. Howe, "Reduction of cogging torque in interior-magnet brushless machines," *Magnetics, IEEE Transactions on*, vol. 39, pp. 3238-3240, 2003.
- [55] C. Studer, A. Keyhani, T. Sebastian, and S. K. Murthy, "Study of cogging torque in permanent magnet machines," in *Industry Applications Conference, 1997. Thirty-Second IAS Annual Meeting, IAS '97., Conference Record of the 1997 IEEE*, 1997, pp. 42-49 vol.1.
- [56] L. Zhu, S. Z. Jiang, Z. Q. Zhu, and C. C. Chan, "Analytical methods for minimizing cogging torque in permanent-magnet machines," *Magnetics, IEEE Transactions on*, vol. 45, pp. 2023-2031, 2009.
- [57] Z. Q. Zhu and D. Howe, "Influence of design parameters on cogging torque in permanent magnet machines," *Energy Conversion, IEEE Transactions on*, vol. 15, pp. 407-412, 2000.
- [58] W. Q. Chu and Z. Q. Zhu, "Investigation of torque ripples in permanent magnet synchronous machines with skewing," *Magnetics, IEEE Transactions on*, vol. 49, pp. 1211-1220, 2013.
- [59] X. Ge, Z. Zhu, G. Kemp, D. Moule, and C. Williams, "Optimal step-skew methods for cogging torque reduction accounting for three-dimensional effect of interior permanent magnet machines," *IEEE Transactions on Energy Conversion*, vol. 32, pp. 222-232, 2017.
- [60] S. Schulte and K. Hameyer, "Inductances as Dynamic Exchange Parameters for Electrical Machine Computation based on the Method of Frozen Permeabilities."

## References

---

- [61] N. Bianchi, S. Bolognani, and B. J. Chalmers, "Salient-rotor PM synchronous motors for an extended flux-weakening operation range," *IEEE Transactions on industry applications*, vol. 36, pp. 1118-1125, 2000.

# Appendix

## 1. Appendix A:

All motors' torque-speed characteristics were investigated using a dyno (Figure 236) in the lab facilities at ZF. The ECU that is described in Figure 31, was connected to the motors and the external encoder were aligned to find the right axis of the input current to the rotor. Additionally, the motors need to be tuned to obtain maximum power. The tuning process is carried out by testing the motor at different advance angle using a ramp test across the speed range. By using a MATLAB based software, all the torque-speed curves for the different advance angles were loaded to obtain the optimum torque across the speed range. The results out of the tuning process are input current value and advance angle for the speed range. the parameters were later fed to the controller and the dyno to validate the torque speed map through experiment.

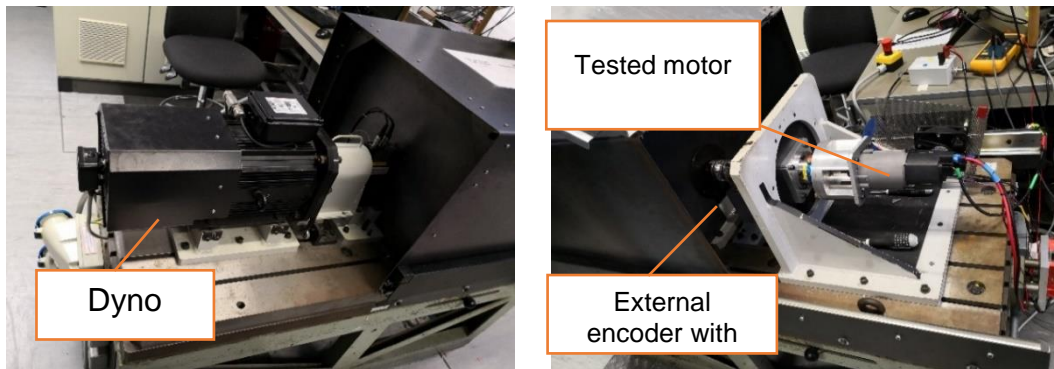


Figure 236: dynamometer to test torque-speed curve using ramp tests.

## 2. Appendix B:

The core material property that is used in all the motor designs is provided by ZF. Figure 237 shows the material characteristics.

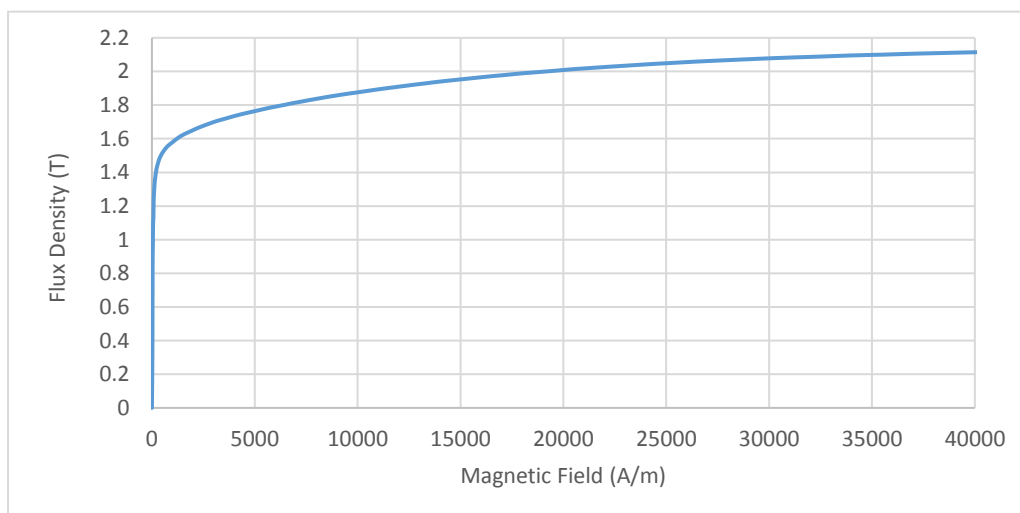


Figure 237: B - H characteristic of the steel material used for all the motor